Fatigue characteristics of concrete subjected to compressive cyclic loading: laboratory testing and numerical simulation

To the Faculty of Geosciences, Geoengineering and Mining

of the Technische Universität Bergakademie Freiberg

Approved

THESIS

to attain the academic degree of

Doctor of Engineering

Dr.-Ing.

submitted

by M. Sc. Zhengyang Song

born on March 18, 1991 in Shandong, China

Reviewers: Prof. Dr.-Ing. habil. Heinz Konietzky, Freiberg, Germany

Prof. Dr.-Ing. Viktor Mechtcherine, Dresden, Germany

Prof. Dr.-Ing. Yixin Zhao, Beijing, China

Date of the award: 11.02.2020, Freiberg

Acknowledgement

Time flies, the last page of this thesis is finished on a sunny summer afternoon in Freiberg. At the same time, it reminds me that it seems to be soon to say goodbye to such a wonderful place and such a perfect research group.

First, I would like to express my sincere gratitude to Prof. Heinz Konietzky, my Ph.D. supervisor. During my 3-year Ph.D. career, I am always inspired by Professor's scientific and hardworking attitude. His quick, accurate and responsible feedback is a big motivation for me to complete my research task.

I am grateful to all my dear colleagues at the Geotechnical Institute of TU Bergakademie Freiberg. I want to give special thanks to Dr. Herbst, Dr. Frühwirt, Mr. Münzberger, Mrs. Griebsch and Mr. Weber for the technical assistance during research and kind help at daily life. The support and help from Chinese colleges is a huge encouragement for me. The special care from my good friend and also my best roommate Mr. Fei Wang is greatly appreciated.

I want to sincerely thank my parents and my girlfriend for their unconditional support.

Abstract

The cyclic loading induced damage of geo-materials is quite common in geo-engineering. Therefore, the investigation on the fatigue behaviour of concrete subjected to cyclic loading is of great significance in terms of structure safety and stability. Also, due to the similar structure and properties, knowledge obtained from concrete can be transferred to rock material. In this thesis, the fatigue characteristics of concrete are studied based on laboratory tests and numerical simulations. The main content of the thesis can be summarized as follows:

1. A series of single-level and multi-level compressive cyclic loading tests have been carried out on concrete samples. The effects of maximum and minimum load level on the evolution of axial strain rate, radial strain rate, energy dissipation, acoustic emissions (AE) and P-wave speed are analysed.

2. Based on particle based numerical simulations, damage models corresponding to single-level and multi-level cyclic loading tests are proposed. The damage variable in the numerical model is time- and stress-dependent and is characterized by the progressive reduction of the bond diameter. The numerical simulations are calibrated based on laboratory test results, and the mechanical behaviour of concrete during cyclic loading tests is well reproduced.

3. A real time fatigue failure prediction method is proposed based on the hysteresis occurrence ratio and hysteresis energy ratio. This real time prediction method can be used to monitor the fatigue failure of constructions in-situ.

4. The AE characteristics during the laboratory tests are reproduced by the numerical simulations. AE counts and energy are characterized by broken bonds and released bond strain energy, respectively.

5. The dynamic characteristics of concrete are analysed based on laboratory tests. The relation of hysteresis time and dynamic response ratio with respect to cyclic load levels are analysed.

IV

Table of Contents

List of Figures

IX

XII

XIV

List of Tables

Nomenclature

a	half-length of a crack
a_{maj}	semi major axis of an elliptical crack
A	bond cross-section area in LPBM
d	displacement vector in LPBM
D	damage variable
D_c	critical damage at failure
D_i	initial damage
E_c	elastic modulus after the initial cycle
E_i	elastic modulus of the initial cycle
E_k	bond strain energy in LPBM
E_l	elastic modulus for the linear interface in LPBM
E_p	elastic modulus for the parallel bond interface in LPBM
E^*	apparent activation energy
E^+	stress-free activation energy
F	force vector in LPBM
F_c	contact force in LPBM
F_d	dashpot force in LPBM
F_{dn}	normal dashpot force in LPBM
F_{ds}	shear dashpot force in LPBM
F_l	linear force in LPBM
F_{ln}	normal linear force in LPBM
F_{ls}	shear linear force in LPBM
F_{ln0}	linear normal force at the beginning of the time step in LPBM
F_{ls0}	linear shear force at the beginning of the time step in LPBM
F_p	parallel bond force in LPBM
F_{pn}	parallel bond normal force in LPBM
F_{ps}	parallel bond shear force in LPBM
G	shear modulus
H	concrete sample height
I	moment of inertia of the parallel bond cross section
J	polar moment of inertia of the parallel bond cross section

$\boldsymbol{k}$	stiffness matrix in LPBM
$\boldsymbol{k_d}$	stiffness matrix after damage in LPBM
k_n	linear normal stiffness
k_s	linear shear stiffness
$k_n{}'$	normal stiffness of parallel bond interface
$k_s{}'$	shear stiffness of parallel bond interface
K_I, K_{II}, K_{III}	Mode-I, Mode-II, Mode-III stress intensity factor
K_a	stress intensity factor of stress amplitude
K_{ave}	stress intensity factor of the average stress
K_f	effective fatigue stress intensity factor
K_{max}, K_{min}	stress intensity factor of maximum and minimum stress, respectively
ΔK	range of the stress intensity factor
l_m	measuring length of LVDT
l_w	axial deformation measured by loading platen
m_1, m_2	masses of the two contact particles in LPBM
M_b	bending moment in LPBM
M_c	parallel bond moment in LPBM
M_t	twisting moment in LPBM
N, N_f	fatigue life
N_h	number of cycles with hysteresis occurrence
N_w	total selected cycle number
R	universal gas constant
$S_i\ (i = 1,\ 2)$	series number of concrete samples
t	time or hysteresis time
T	absolute temperature
U_a	accumulated dissipated energy density
U_{at}	accumulated dissipated energy density at the top of the sample
U_{am}	accumulated dissipated energy density at the middle of the sample
U_{ab}	accumulated dissipated energy density at the bottom of the sample
U_d	dissipated energy density
U_n	normal displacement between the two bonded particles in LPBM
U_s	shear displacement between the two bonded particles in LPBM
v_x, v_y, v_z	displacements in x, y, z axis direction, respectively
V_m	ultrasonic P-wave speed measured at the middle part of the sample

V_t	ultrasonic P-wave speed measured at the top part of the sample
α_1, α_2	curve slope or material constants that vary with temperature
β_1, β_2	damage rate constants
β_n	normal critical damping ratio
β_s	shear critical damping ratio
ε_a	axial strain
ε_{ap}	peak strain during a single cycle
ε_{ar}	residual strain during a single cycle
ε_{at}	axial strain measured at the top of the sample by strain gauge
ε_{am}	axial strain measured at the middle of the sample by strain gauge
ε_{ab}	axial strain measured at the bottom of the sample by strain gauge
ε_c	axial strain measured by LVDT at the middle of the sample
ε_l	lateral strain measured by chain-strain gauge at the middle of the sample
ε_{lt}	lateral strain measured at the top of the sample by strain gauge
ε_{lm}	lateral strain measured at the middle of the sample by strain gauge
ε_{lb}	lateral strain measured at the bottom of the sample by strain gauge
ε_p	plastic axial strain of each cycle during cyclic loading
ε_{pt}	total plastic axial strain during cyclic loading
ε_r	radial strain
ε_t	axial strain measured by loading platen
μ	friction coefficient in LPBM
ρ_1	fictitious radius of a crack tip
σ_c	maximum normal bond strength in LPBM
σ_{eff}	effective stress
σ_{th}	fatigue stress threshold
$\sigma_{max}, \sigma_{min}$	maximum and minimum load level during cyclic loading, respectively
θ_n	normal rotations between two bonded particles in LPBM
θ_s	shear rotations between two bonded particles in LPBM
τ_c	maximum shear bond strength in LPBM
λ	bond radius multiplier in LPBM
ϕ	concrete sample diameter
ς_c	moment contribution factor in LPBM
υ_M	molar volume of the glass
γ	interfacial surface energy between the glass and the reaction products

Abbreviation

AE	Acoustic Emission
AHE	Accumulated Hysteresis Energy
BEM	Boundary Element Method
CDT	Continuum Damage Theory
DCB	Dense Clump Block
DEA	Dissipated Energy Approach
DEM	Discrete Element Method
DRR	Dynamic Response Ratio
FBD	Flattened Brazilian Disc
FDM	Finite Difference Method
FEM	Finite Element Method
HCF	High Cycle Fatigue
HED	Hysteresis Energy Density
HER	Hysteresis Energy Ratio
HOR	Hysteresis Occurrence Ratio
LCF	Low Cycle Fatigue
LPBM	Linear Parallel Bonded Model
LURR	Loading/Unloading Response Ratio
LVDT	Linear Variable Differential Transformer
MSC	Multi-level Stress Corrosion
NDT	Non-Destructive Testing
NPSC	Nonlinear Parallel-bonded Stress Corrosion
PFC	Particle Flow Code
P-M	Preisach-Mayergoyz
PSC	Parallel-bonded Stress Corrosion
SIF	Stress Intensity Factor
UCS	Uniaxial Compressive Strength
XFEM	Extended Finite Element Method

1. Introduction

1.1 Research background

1.1.1 What is fatigue?

Fatigue is a common mechanical behaviour in nature and engineering. Currently, the most general definition of fatigue in material science refers to the weakening and deterioration of materials when exposed to repetitive loading. The research on fatigue was initiated by investigations of metal materials in the early 19th century. Figure 1.1 briefly illustrates the history of fatigue research and documents some important milestones and researchers who have made major contributions to fatigue investigations. The fatigue behaviour was first scientifically reported by the German mining engineer Albert (1838). He found the conveyor chains used in the mine can easily fail even if the external load is much smaller than the material strength (Schütz 1996). After Albert, in the 19th century many other researchers (Rankine 1842; York 1842; McConnell 1850; Braithwaite 1854) continuously reported about the fatigue behaviours in water pumps, propeller shafts, crankshafts, railway axles, and cranes. From that time on, the fatigue problem has become a hotspot. The German railway engineer August Wöhler put the fatigue research on a higher level by introducing the S-N curve (also known as Wöhler curve). This was the first quantitative characterization of the relation between fatigue life and applied loads (Wöhler 1870). Nowadays, the S-N curve is still an important reference for production standards in construction and material sciences. With science development in the 20th century, more micro/mesoscopic research became available. With the aid of precision instruments, the evolution of cracks at the surface of materials can be precisely captured. The Paris' law was proposed by Paris et al. (1963) to relate the stress intensity factor to sub-critical crack growth under a fatigue stress regime. This equation is still the most popular crack growth criteria for fatigue loading. At present, the fatigue research is not only limited to metal and alloy materials. Geo- and bio-materials also have a risk of fatigue failure. The well-developed acoustic emission (AE) technology and non-destructive testing (NDT) are efficient to predict fatigue failure. High and extremely high cycle fatigue testing (more than 10^{10} cycles) can be performed using reliable fatigue testing systems (Shimadzu 2017). Therefore, the fatigue behaviour of some high durable materials used in aerospace and railway engineering can be reliably tested.
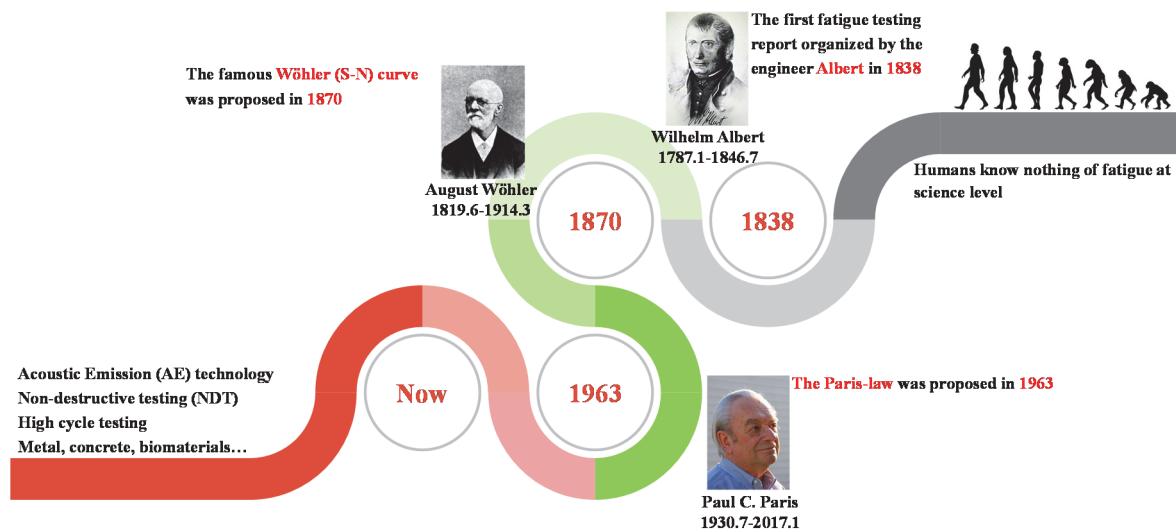
Figure 1.1 The development of fatigue research incl. important milestones and researchers

1.1.2 Classification of fatigue

Based on different parameters, different fatigue classification exist. Here only the classification schemes based on frequency, loading scheme, stress state and fatigue life are presented.

1.1.2.1 Classification based on frequency

According to the different cyclic loading frequencies, the fatigue can be categorised as follows (Xu 2016): 1. High frequency fatigue (frequency > 10 Hz); 2. Medium frequency fatigue (10 Hz > frequency > 0.1 Hz); 3. Low frequency fatigue (frequency < 0.1 Hz); 4. Static fatigue (constant load), see Figure 1.2.
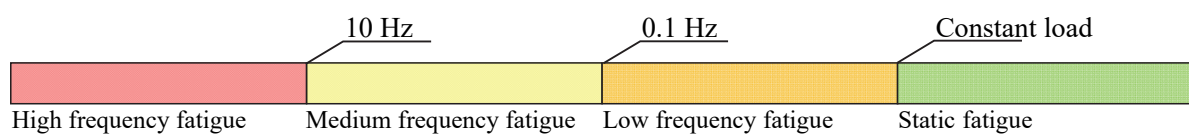
Figure 1.2 Fatigue classification based on loading frequency

1.1.2.2 Classification based on loading scheme

According to the loading scheme, fatigue can be categorised as follows: 1. Strain-controlled fatigue; 2. Stress-controlled fatigue. In strain-controlled fatigue testing, the amplitude of strain during each cycle is constant, the elastic modulus will gradually reduce until failure, see Figure 1.3a; in stress-controlled fatigue testing, the maximum and minimum load level of each cycle remain the same, the axial strain usually acts as a variable and evolves with loading time, the elastic modulus almost doesn't change when sample remains stable, see Figure 1.3b.

2
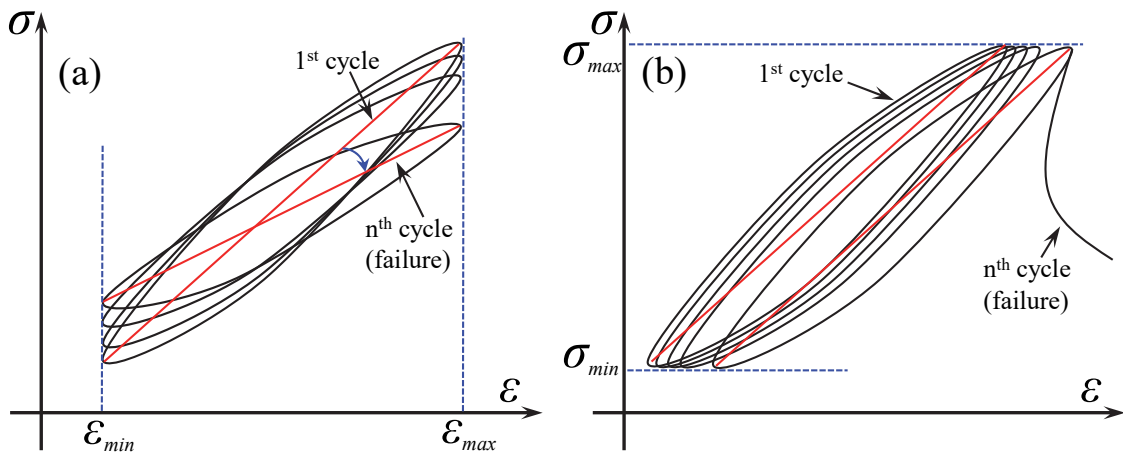
Figure 1.3 Fatigue classification based on loading scheme (a) strain-controlled fatigue (b) stress-controlled fatigue

1.1.2.3 Classification based on stress state

Based on the stress state, the fatigue can be classified as follows: 1. Uniaxial fatigue; 2. Multi-axial fatigue. The uniaxial fatigue is quite common in nature and engineering, such as bridge foundations, pavements and highways.

1.1.2.4 Classification based on fatigue life

Based on the number of cycles up to failure, the fatigue can be categorized as: 1. High cycle fatigue (HCF); 2. Low cycle fatigue (LCF). 10^4 cycles are always considered as limit for HCF, but there is no consensus about the limit value for LCF. The most obvious characteristic for LCF is that plastic deformation is quite large during each cycle. This indicates that LCF usually corresponds to a higher load level. Figure 1.4 illustrates the range of fatigue life corresponding to different natural and human-induced activities. The crustal plate (earth) movement can lead to the most serious damage in quite short time. The aerospace-related materials usually have the most stringent requirements on fatigue life (larger than 10^8 cycles).
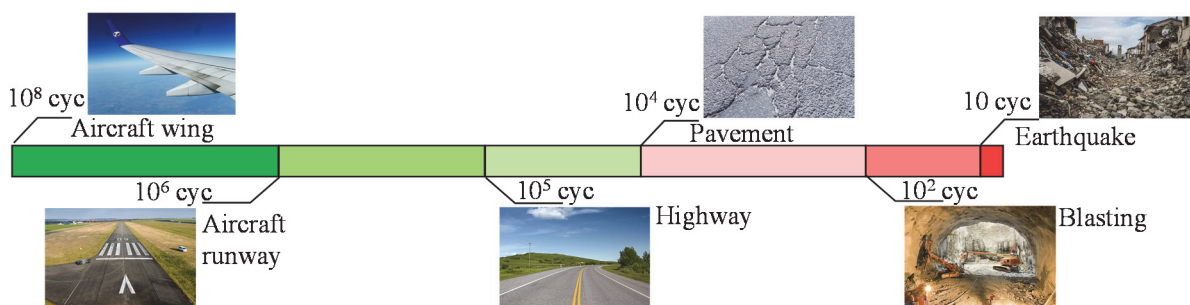
Figure 1.4 Range of fatigue life of natural and human-induced activities

1.1.3 Fatigue in geotechnical engineering

Geo- and construction materials, such as soils and rocks or concrete, always act as load bearing structures and foundations. The applied loads acting on man-made constructions are always cyclic (fatigue load) in nature (Lee and Barr 2004; Cerfontaine and Collin 2018). The geo-materials are easily susceptible to fatigue load. This kind of load always results in premature failure of constructions. According to statistics, over 80% of structure failures in engineering are fatigue damage related (Suresh 1998).
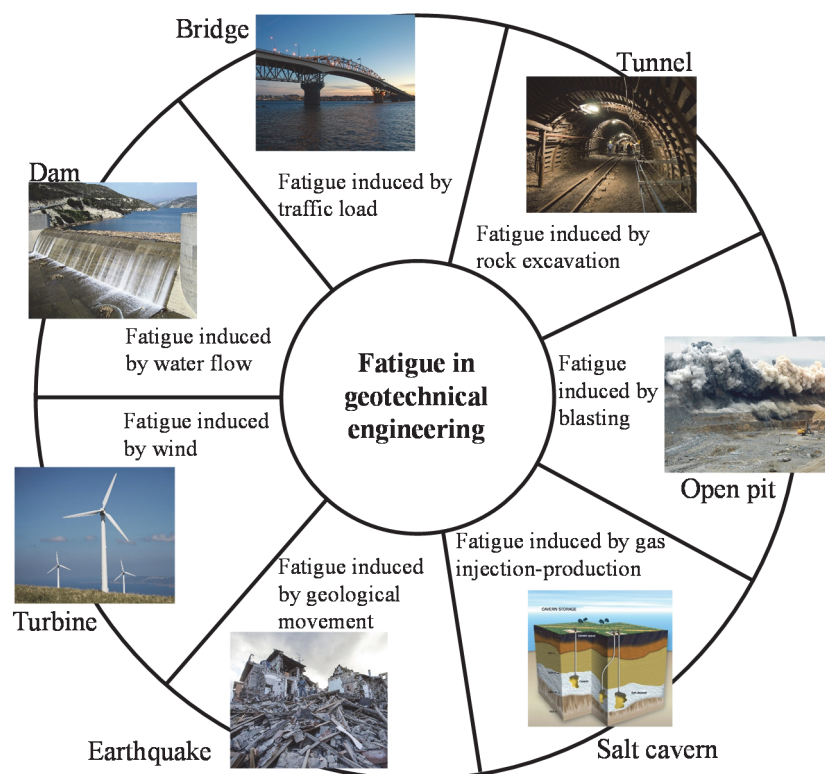
Figure 1.5 Fatigue in geotechnical engineering

Figure 1.5 illustrates the problem of fatigue in geotechnical engineering. It covers the stability of underground openings, such as tunnels or caverns or surface constructions, such as bridges and dams. All these constructions experience fatigue loading induced by blasting, wind, water flow, traffic load, etc. Therefore, the fatigue problem is important and quite general in geotechnical engineering. Compared with metal and alloy materials, geo-materials are obviously more heterogeneous and anisotropic. These characteristics lead to a more complex and scattered fatigue behaviour of geo-materials. The classical S-N curve may have less precision in terms of fatigue evaluation when applied to geo-materials. Considering this fact, some instant monitoring methods (Ling et al. 2011; Dib et al. 2019), AE and NDT (Feng et al. 2019) technologies are better suited in-situ to predict fatigue failure.

1.2 Work objective

This thesis presents laboratory and numerical investigations about the fatigue behaviour of a typical brittle construction material: concrete. Multi-level compressive cyclic loading tests were conducted to acquire the mechanical fatigue characteristics of concrete. Energy dissipation, strain evolution, stress-strain loop, AE characteristics and ultrasonic P-wave speed evolution are analysed. The detection of effective precursors of fatigue failure is also an important objective. Based on the **P**article **F**low **C**ode (PFC), the fatigue behaviour of concrete subjected to single and multi-level cyclic loading is reproduced by numerical simulations. The corresponding fatigue damage model relates the damage rate of the particle assembly to the applied load levels. The AE characteristics obtained from laboratory testing are replicated by the released bond strain energy in the simulation. A stress-time-dependent fatigue damage model is proposed and implemented into PFC to characterize the strain evolution and the stress-strain (hysteresis) loop for different load levels. The dynamic response characteristics of concrete in cyclic loading are also discussed. A relation between dynamic response, AE and ultrasonic wave speed evolution is also established.

1.3 Structure of thesis

This thesis includes six chapters in total, the content of each chapter is briefly listed below.

Chapter 1. Research background of fatigue, objective and main structure of the thesis.

Chapter 2. Review on fatigue research based on mechanical theory, laboratory testing and numerical approaches.

Chapter 3. Analysis of laboratory tests based on classical damage variables and energy dissipation, dynamic response features.

Chapter 4. Proposal of two numerical fatigue models, calibration of numerical simulations based on laboratory testing, PFC based simulation of AE monitoring.

Chapter 5. Proposal of a real time fatigue failure prediction method.

Chapter 6. Main conclusions and outlook.

2. State of the art

2.1 Fatigue research based on mechanical theories

Fracture mechanics, continuum mechanics and damage mechanics are the three basic mechanical theories to solve fatigue problems. Fatigue exist in a quite complex manner in engineering and from the theoretical point of view, the three mechanical concepts have their own advantages and limitations of handle these fatigue problems.

2.1.1 Fracture mechanics

2.1.1.1 Fracture modes and stress intensity factor (SIF)

The prerequisite for fracture mechanics to solve fatigue problems is the assumption of real or artificial cracks (Zerbst et al. 2018). Based on the work of Inglis (1913), Griffith (1921) and Irwin (1956, 1957), the concept of SIF was introduced to develop analytical solutions for stresses and displacements at the crack tips for brittle materials like concrete. Figure 2.1 plots the three typical modes of fractures. The corresponding SIF are expressed as K_I, K_{II} and K_{III}. The equations for the stress and displacement fields at the crack tip are given by Equations 2.1 to 2.6.
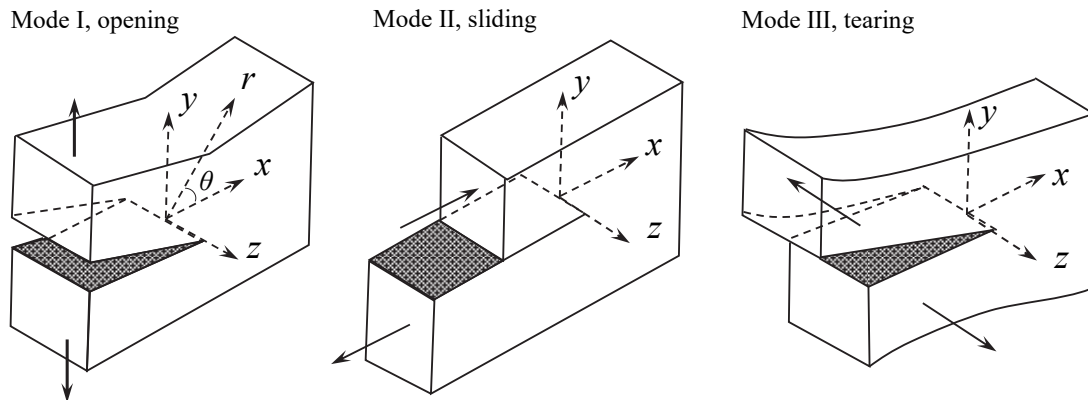
Figure 2.1 Three modes of fracture (Kanninen et al. 1988)

For Mode I:

$$\begin{Bmatrix} \sigma_{xx} \\ \sigma_{yy} \\ \tau_{xy} \end{Bmatrix} = \frac{K_I}{\sqrt{2\pi r}} \cos(\theta/2) \begin{Bmatrix} 1 - \sin(\theta/2)\sin(3\theta/2) \\ 1 + \sin(\theta/2)\sin(3\theta/2) \\ \sin(\theta/2)\sin(3\theta/2) \end{Bmatrix}$$

(2.1)

$$\begin{Bmatrix} v_x \\ v_y \end{Bmatrix} = \frac{K_{\mathrm{I}}}{2G}\sqrt{\frac{r}{2\pi}}(\kappa - \cos\theta)\begin{Bmatrix} \cos(\theta/2) \\ \sin(\theta/2) \end{Bmatrix}$$

(2.2)

For Mode II:

$$\begin{Bmatrix} \sigma_{xx} \\ \sigma_{yy} \\ \tau_{xy} \end{Bmatrix} = \frac{K_{\mathrm{II}}}{\sqrt{2\pi r}}\cos(\theta/2)\begin{Bmatrix} -\sin(\theta/2)[2+\cos(\theta/2)\cos(3\theta/2)] \\ \sin(\theta/2)\cos(\theta/2)\cos(3\theta/2) \\ \cos(\theta/2)[1-\sin(\theta/2)\sin(3\theta/2)] \end{Bmatrix}$$

(2.3)

$$\begin{Bmatrix} v_x \\ v_y \end{Bmatrix} = \frac{K_{\mathrm{II}}}{2G}\sqrt{\frac{r}{2\pi}}\begin{Bmatrix} \sin(\theta/2)[\kappa+2+\cos\theta] \\ \cos(\theta/2)[\kappa-2+\cos\theta] \end{Bmatrix}$$

(2.4)

For Mode III:

$$\begin{Bmatrix} \tau_{xz} \\ \tau_{yz} \end{Bmatrix} = \frac{K_{\mathrm{III}}}{\sqrt{2\pi r}}\begin{Bmatrix} -\sin(\theta/2) \\ \cos(\theta/2) \end{Bmatrix}$$

(2.5)

$$v_z = \frac{K_{\mathrm{III}}}{2G}\sqrt{\frac{r}{2\pi}}\{\sin(\theta/2)\}$$

(2.6)

The SIF of the three modes are shown in Equation 2.7.

$$K_{\mathrm{I}} = \lim_{r\to 0}\sqrt{2\pi r}\,\sigma_{yy}(r,0)$$
$$K_{\mathrm{II}} = \lim_{r\to 0}\sqrt{2\pi r}\,\tau_{yx}(r,0)$$
$$K_{\mathrm{III}} = \lim_{r\to 0}\sqrt{2\pi r}\,\tau_{yz}(r,0)$$

(2.7)

v_x, v_y, v_z are the displacements in x, y, z axis direction. G is the shear modulus. κ has different expressions under plane strain and plane stress conditions. For plane stress condition $\kappa = (3-\mu)/(1+\mu)$, for plane strain condition $\kappa = 3 - 4\mu$. μ is the Poisson's ratio and r is the distance in polar coordinates. Equations 2.1 to 2.7 provide the stress and displacement fields at the crack tips of solid materials subjected to quasi-static loads. For fatigue load, the SIF can be expressed as shown by Equation 2.8. K_f is the effective fatigue SIF, K_{ave} is the SIF at average stress, K_a is the SIF for stress amplitude, w is the angular frequency and t is the time. K_{max} and K_{min} are SIFs of maximum and minimum stress.

$$K_f = K_{ave} + K_a \sin wt$$
$$K_a = (K_{max} - K_{min})/2 \tag{2.8}$$

Systematically, the specific fatigue crack analysis was initiated in the middle of the 20th century. Head (1953) first proposed a crack-propagation law (Head's law). His model considers rigid plastic work hardening elements ahead of the crack tip. The model is shown in Equation 2.9.

$$\frac{\mathrm{d}a}{\mathrm{d}N} = \frac{C_1 \sigma^3 a^{3/2}}{(C_2 - \sigma) w_0^{1/2}} \tag{2.9}$$

C_1 is a material constant related to yield stress and elastic modulus, C_2 is the yield stress. w_0 is the size of the plastic zone near to the crack tip. In Head's law, w_0 is a constant during crack propagation and a is the half length of the crack. Frost and Dugdale (1958) pointed out that the size of the plastic zone is proportional to the size of the crack. Irwin (1957) quantitatively characterized the relation between plastic zone and crack length, see Equation 2.10. Considering this correction, Head's law is modified as shown in Equation 2.11

$$w_0 = \sigma a^2 \tag{2.10}$$

$$\frac{\mathrm{d}a}{\mathrm{d}N} = \frac{C_1 \sigma^2 a}{(C_2 - \sigma)} \tag{2.11}$$

McEvily and Illg (1958) proposed a fatigue crack law based on the elastic stress-concentration factor k_c, see Equation 2.12. This model assumes that the crack tip has a fictitious radius ρ_1. σ_{con} is the concentrated stress and σ_{uni} is the uniform stress in an infinite plate. a_{maj} is the semi major axis of the elliptical hole. The damage rate of the crack is characterized by Equation 2.13. With crack propagation, a_{maj} increases as well as the corresponding damage rate.

$$\sigma_{con} = k_c \sigma_{uni}$$
$$k_c = 1 + 2(a_{maj}/\rho_1)^{1/2} \tag{2.12}$$

$$\frac{\mathrm{d}a}{\mathrm{d}N} = f\left\{ \sigma_{uni} \left[1 + 2(a_{maj}/\rho_1)^{1/2} \right] \right\} \tag{2.13}$$

Paris et al. (1963) proposed the famous Paris' law as shown in Equation 2.14.

$$\frac{\mathrm{d}a}{\mathrm{d}N} = C\Delta K^m \tag{2.14}$$

da/dN denotes the crack growth rate (increase of crack length per cycle N) during fatigue load. C and m are material constants related to material properties and stress level. ΔK is the range of the SIF and is equal to $\Delta K = K_{max} - K_{min}$. Paris' law characterizes the linear part of the crack growth rate as shown in Figure 2.2. On a log-log plot, the two model parameters of Paris' law, C and m, can be determined according to the procedure illustrated in Fig. 2.2.
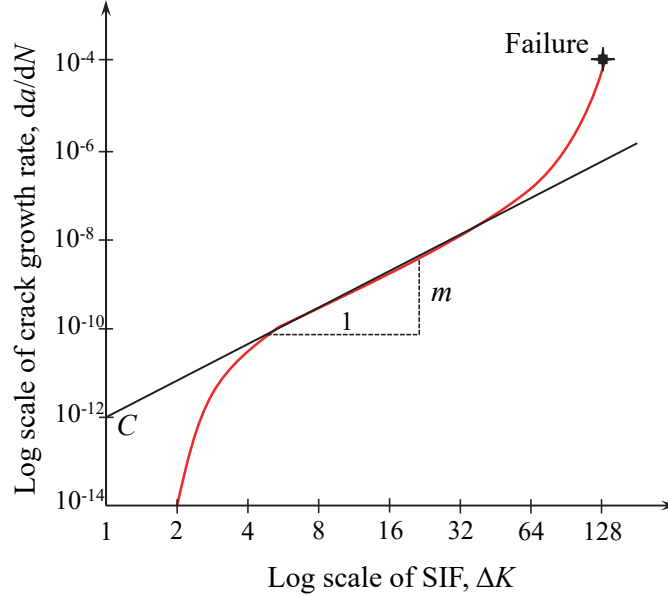
Figure 2.2 Crack growth rate vs. SIF and parameter determination for Paris' law

Based on Paris' law, the fatigue life N can be calculated for a given crack size. Here we define a cyclic SIF, ΔK, as given by Equation 2.15. $\Delta \sigma$ is the amplitude of cyclic load. a is the crack size. The fatigue life can be calculated by substituting Equation 2.15 into Paris' law. The differential equation can be solved via separation of variables, see Equation 2.16. a_i is the initial crack size and a_c is the critical crack size up to failure. After integration, the fatigue life is obtained by Equation 2.17, here C and m are assumed to be constant during the whole process.

$$\Delta K = \Delta \sigma \sqrt{\pi a} \tag{2.15}$$

$$\int_{0}^{N_f} \mathrm{d}N = \int_{a_i}^{a_c} \frac{\mathrm{d}a}{C(\Delta \sigma \sqrt{\pi a})^m} = \frac{1}{C(\Delta \sigma \sqrt{\pi a})^m} \int_{a_i}^{a_c} a^{\frac{-m}{2}} \, \mathrm{d}a \tag{2.16}$$

$$N_f = \frac{2(a_c^{\frac{2-m}{2}} - a_i^{\frac{2-m}{2}})}{(2-m)C(\Delta \sigma \sqrt{\pi})^m} \tag{2.17}$$

Paris' law only characterizes the linear part of the curve shown in Figure 2.2. Erdogan and Ratwani (1970) extended the classical Paris' law as shown in Equation 2.18. This model can characterize all three parts of the curve shown in Figure 2.2.

$$\frac{\mathrm{d}a}{\mathrm{d}N} = \frac{C(1+\beta)^m(\Delta K - K_t)^n}{K_c - (1+\beta)\Delta K}$$

$$\beta = \frac{K_{max} + K_{min}}{K_{max} - K_{min}}$$

(2.18)

In Equation 2.18, K_t is the threshold value of SIF where crack propagation starts. K_c is a critical SIF at which the crack propagation rate becomes infinite or quite large. C, m and n are material constants. K_{max} and K_{min} are SIF at maximum and minimum load level, respectively. The effect of maximum and minimum stress is reflected by β.

2.1.2 Continuum mechanics

The continuum mechanical approach considers fatigue more from a phenomenological point of view. A classic approach is the S-N curve. The S-N curve describes the quantitative relation of stress amplitude with respect to fatigue life. A typical S-N curve is shown in Figure 2.3. The threshold limit σ_{th} can be defined according to the percentage of maximum load level σ_{max} or average cyclic load amplitude $(\sigma_{max} - \sigma_{min})/2$. If the applied load level is smaller than σ_{th}, the fatigue life will be close to infinite and the "run out" happens. A fatigue threshold exists in many materials such as, metals (Pantelides 2014; Li and Rosa 2016; Tazoe et al. 2017; Vojtek et al. 2018), brittle geo-materials (Horii et al. 1992; Wang et al. 2015; Song et al. 2018a; Zheng et al. 2019) and composites (Alderliesten and Rans 2009; Turon et al. 2015; Vassilopoulos et al. 2015). σ_{th} is an important parameter for design in engineering applications. σ_{up} is also an important parameter (see Figure 2.3): when the load level is larger than σ_{up}, the material will fail after quite a small number of cycles. When the load level is between σ_{th} and σ_{up}, the relation between σ and N_f is approximately linear. This linear relation can give a reliable reference in terms of material durability for engineering applications.
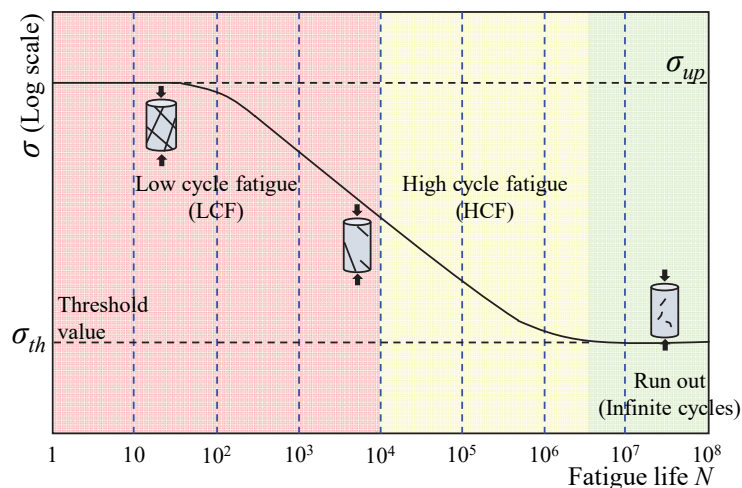
Figure 2.3 Typical S-N curve

The Miner's law (Miner 1945) (Equation 2.19) is another classical approach in continuum mechanics. If a material subjected k kinds of stress magnitudes in a spectrum, each kind contributing n_i cycles during cyclic loading. If N_i is the fatigue life of the material exposed to a single stress amplitude, failure occurs under the following condition:

$$\sum_{i=1}^{k} \frac{n_i}{N_i} = 1$$

(2.19)

However, Miner's law has some limitations in fatigue life prediction:

1. It ignores the probabilistic nature of fatigue. The scatter in fatigue life cannot be reflected.

2. The effect of cyclic loading sequence on fatigue life is not considered. Under certain conditions, for instance low cyclic stress followed by high cyclic stress, Miner's law will underestimate the damage (Eskandari and Kim 2017). On the other side, high stress followed by low stress may produce less damage due to the presence of compressive residual stresses.

2.1.3 Damage mechanics

Compared with fracture and continuum mechanics, damage mechanical theory considers internal state variables, so-called damage variables. A damage variable gradually evolves, and can be used to continuously characterize the deterioration and degradation of the material properties. Damage mechanics is able to model damage growth under initial "defect-free" conditions, unlike fracture mechanics that needs an initial crack (Bhattacharya and Ellingwood 1998).
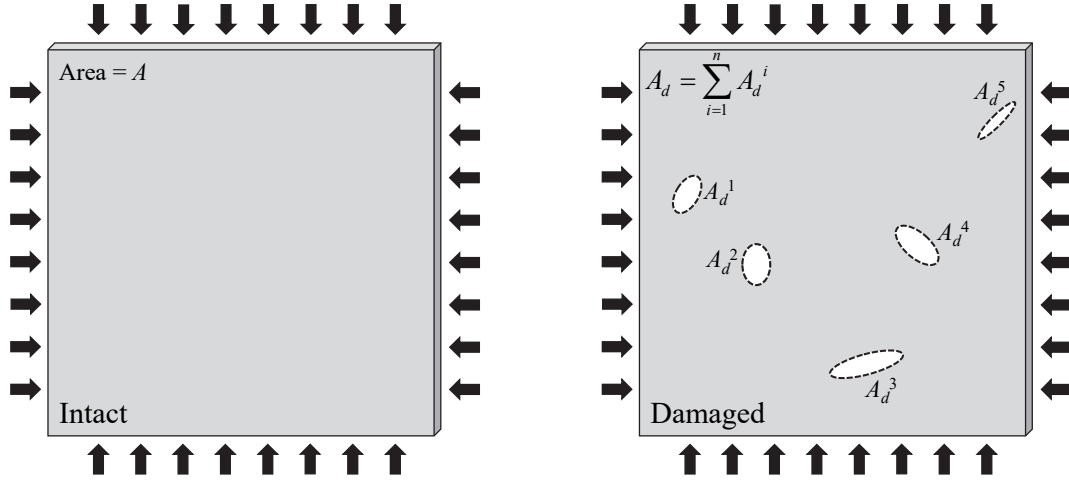
Figure 2.4 Schematic of damage mechanics

In a given volume or area of the material (see Figure 2.4, area = A), some elements of the selected area do not meet the bearing capacity. The sum of these elements is A_d. The damage is given by Equation 2.20. Due to the damage, the effective stress is given by Equation 2.21

$$D = \frac{A_d}{A} = \frac{A - A_c}{A}$$

(2.20)

$$\sigma_{eff} = \frac{F}{A - A_d} = \frac{\sigma}{1 - D}$$

(2.21)

Based on damage mechanics, Chaboche (2009a, b) proposed a rule to characterize the fatigue damage evolution under uniaxial cyclic loading, see Equation 2.22,

$$\frac{dD}{dN} = [1 - (1-D)^{B+1}]^{A(\bar{\sigma})} \left(\frac{\sigma_a}{M(\bar{\sigma})(1-D)} \right)^B$$

(2.22)

Where B is a material constant related to temperature, $M(\bar{\sigma})$ is a function about the average stress. $A(\tilde{\sigma})$ is a function related to both, temperature and stress.

$$A(\tilde{\sigma}) = 1 - a(T) \frac{\sigma_{max} - h(\bar{\sigma})}{\sigma_b - \sigma_{max}}$$

$$h(\bar{\sigma}) = \bar{\sigma} + \sigma_{-1} \left(1 - \frac{b(T)(\bar{\sigma})}{\sigma_b} \right)$$

$$M(\bar{\sigma}) = M_0(T) \left(1 - \frac{b(T)(\bar{\sigma})}{\sigma_b} \right)$$

(2.23)

Whereby, $\sigma_a = (\sigma_{max} - \sigma_{min})/2$ and $\overline{\sigma} = (\sigma_{max} + \sigma_{min})/2$. σ_{-1} is the fatigue strength under symmetric cyclic loading and σ_b is the static tensile strength. a, b, M_0 and B are coefficients with respect to the temperature and can be determined through laboratory tests. The fatigue life can be calculated by the integral of Equation 2.22. The integration result is shown in Equation 2.24, where D_i is the initial damage and D_c is the critical damage or final damage at failure.

$$N_f = \left(\frac{M(\overline{\sigma})}{\sigma_a}\right)^B \int_{D_i}^{D_c} \frac{(1-D)^B}{[1-(1-D)^{B+1}]^{A(\tilde{\sigma})}} \mathrm{d}D$$

$$N_f = \left(\frac{M(\overline{\sigma})}{\sigma_a}\right)^B \frac{1}{(B+1)[1-A(\tilde{\sigma})]}\left[[1-(1-D_c)^{B+1}]^{1-A(\tilde{\sigma})} - [1-(1-D_i)^{B+1}]^{1-A(\tilde{\sigma})}\right]$$

(2.24)

It is assumed that the initial damage D_i is 0 and final damage D_c is 1. Then, Equation 2.24 can be simplified as shown in Equation 2.25:

$$N_f = \left(\frac{M(\overline{\sigma})}{\sigma_a}\right)^B \frac{1}{(B+1)-[1-A(\tilde{\sigma})]}$$

(2.25)

Lee et al. (2000) compared the differences in solving fatigue failure problems in damage mechanics and fracture mechanics (see Table 2.1). In fracture mechanics, a measureable fracture is a prerequisite, whereas the damage mechanical concept is based on thermodynamics.

Table 2.1 Fracture mechanics versus continuum damage mechanics (Lee et al. 2000)

Type of approaches	Fracture mechanics	Damage mechanics
Crack/damage driving force	$G = -\partial W/\partial a$ = energy release rate	$f = -\partial W/\partial S$ = thermos dynamic force
Crack/damage resistance	$G_c = -\partial W_c/\partial a$	$f_c = -\partial W_s/\partial S$
Damage initiation condition	$G = G_c$	$f = f_c$

Note: a = crack length; W = strain energy; W_c, W_s = dissipated energy; S = internal state variable

2.2 Fatigue research based on laboratory tests

2.2.1 Compressive fatigue tests

The uniaxial compressive fatigue test is a common and typical test especially for geo- and construction materials, such as rocks (Bagde and Petroš 2005; Xiao et al. 2009; Liu et al. 2015; Geranmayeh Vaneghi et al. 2018; Jia et al. 2019; Li et al. 2019), soils (Leng et al. 2018; Oliveira et al. 2018), asphalt (Wang et al. 2017; Isailović and Wistuba 2018) and concrete (Lei et al. 2017; Hu et al. 2018; Song et al. 2018a, 2019b). This kind of test often corresponds to

the actual stress condition of engineering structures exposed to one dimensional load, such as bridge foundations or pavements. This test is also a fundamental approach to obtain S-N curves. The triaxial compressive fatigue test is specifically designed for materials which are usually deeply buried in the underground, such as in mines, tunnels, or hydropower stations. Under these conditions, the lateral strain of the material is usually confined and a pronounced triaxial state of stress develops. Many triaxial fatigue tests on brittle geo-materials (Liu et al. 2011; Liu and He 2012; Ma et al. 2013; Jia et al. 2018; Zhao et al. 2018) document, that with increased confining pressure residual axial and volumetric strain become larger. The materials subjected to cyclic load behave significantly stiffer at higher confining pressure compared to uniaxial load. When the samples show dilatant behaviour, the corresponding axial strain is greater for cyclic load than under static triaxial load. Compared with static load under the same confining stress, the localized failure bands are wider under cyclic loading.

2.2.2 Tensile fatigue tests

For geo-materials, the direct tensile fatigue test is not that often used due to the difficulties in sample preparation, but in the last years, more and more direct tensile fatigue tests are carried out (Reinhardt and Cornelissen 1984; Fan et al. 2016; Chen et al. 2017). Figure 2.5 shows a typical direct tensile fatigue test by using concrete material. In this test (Chen et al. 2017), two cylindrical discs (steel plates) are pasted with the ends of the specimen by a structural adhesive. The other sides of the discs are connected to the test device by spherical hinges and screws. The spherical hinges reduce the eccentricity. The device stretches the plates and then the force is transmitted to the specimen.
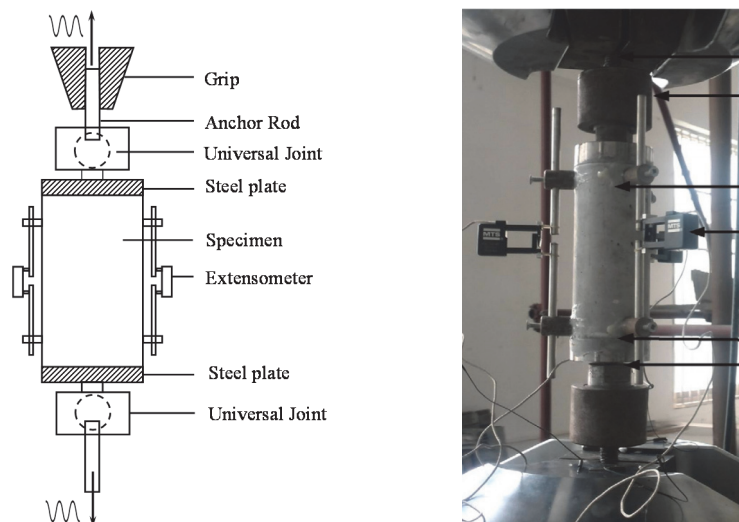
Figure 2.5 Direct tensile fatigue test: scheme and experimental setup (Chen et al. 2017)

Considering the difficulties with device operation and sample preparation in direct tensile fatigue tests, indirect methods like the Brazilian test (Vicentini et al. 2014; Liu et al. 2018b) are becoming popular. According to the ISRM suggested methods (ISRM 1978), a thin circular-shaped disc is vertically compressed in the diametrical direction, which leads to tensile failure. Theoretically, the tensile failure should be initiated at the central point of the disc where the tensile stress has the maximum value. However in laboratory tests, sometimes the crack initiates at the contact between loading platens and sample due to stress concentrations (Fairhurst 1964; Hudson et al. 1972; Swab et al. 2011). Some efforts have been made to ensure a reasonable failure mode of the tested discs. These modifications are: 1. change of the shape of loading platen, see Figure 2.6 (Li and Wong 2013) and, 2. change of Brazilian disc shape, see Fig. 2.7 (Wang and Xing 1999; Wang et al. 2004).
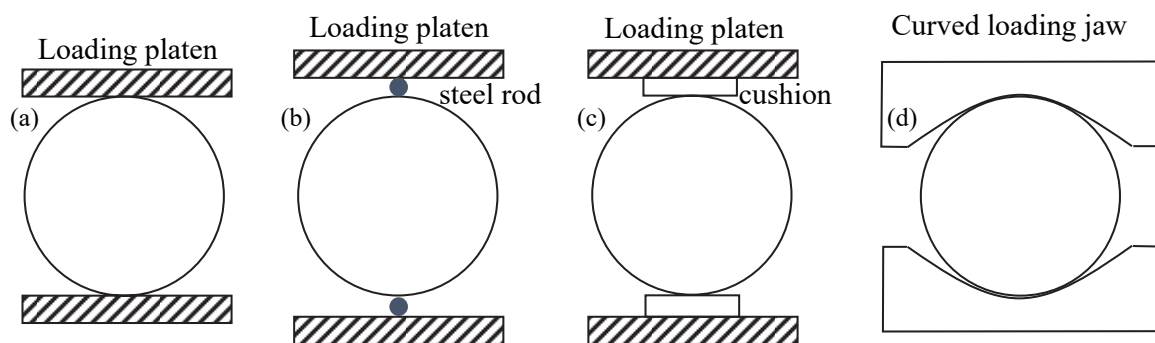
Figure 2.6 Typical Brazilian tensile test loading configurations: (a) flat loading platens (b) flat loading platens with two small-diameter steel rods (c) flat loading platens with cushion and (d) curved loading jaws (Li and Wong 2013)
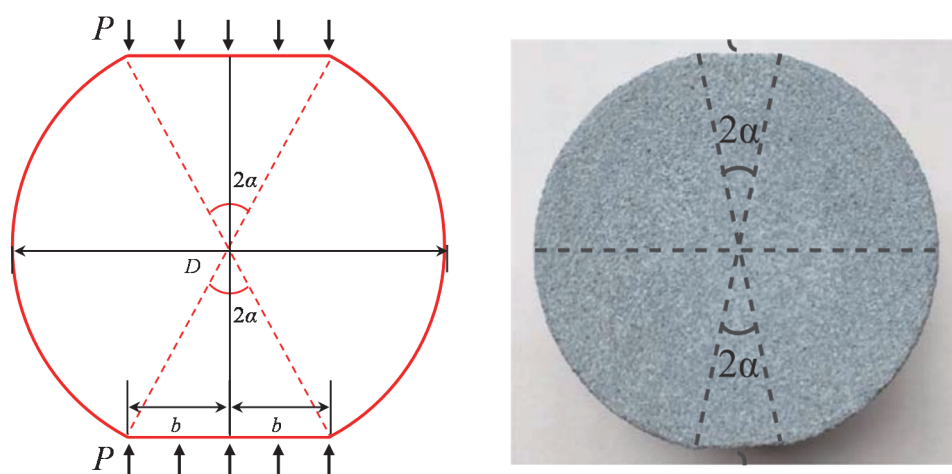
Figure 2.7 Flattened Brazilian disc (FBD)(Liu et al. 2018b)

2.2.3 Shear fatigue tests

Cyclic direct shear tests are often carried out on soils or clay materials (Boukpeti et al. 2014; Kim et al. 2015; Le and Ghayoomi 2017). During the tests, a vertical stress is usually applied on the sample and the cyclic shear stress is controlled by the movement of a tray which is activated by a hydraulically pressurized actuator. Besides cyclic direct shear tests on intact samples, also the cyclic shear fatigue of planar or natural joints can be investigated (Jing et al. 1993; Dang et al. 2016, 2017; Fathi et al. 2016) as shown in Figure 2.8.
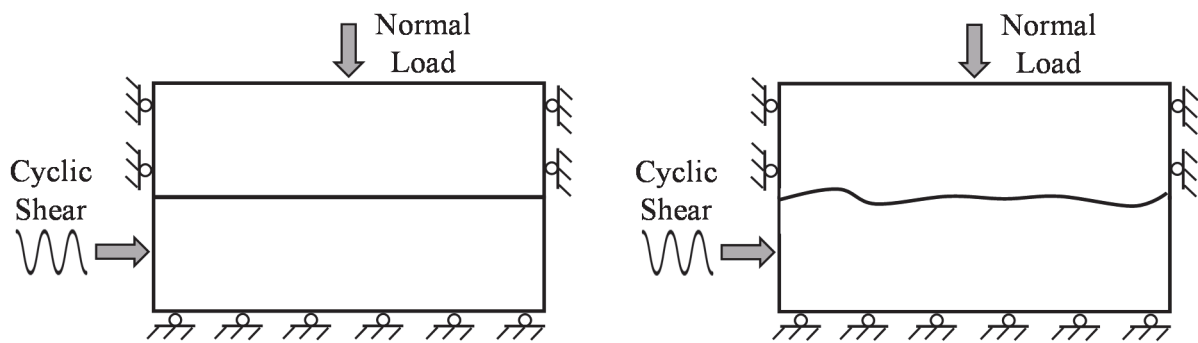
Figure 2.8 Cyclic shear test of planar or natural joints

2.2.4 Torsional fatigue tests

During these tests, a force is applied to the sample via bending moments. The sample rotates so that each surface experiences alternating tensile and compressive stresses. However, due to the difficulties of sample preparation, this kind of test is usually only used to test metal materials (Bernard et al. 2011; Minto et al. 2017; Özdeş et al. 2017) or ceramics (Yassini et al. 2016).

2.2.5 Flexural fatigue tests

In the flexural test, also known as three-point or four-point flexural test, the specimen always has either a semi-circular or rectangular cross-section and is cyclically bent until macroscopic fractures appear and failure happens, see Figure 2.9. The flexural property is an important factor in design of pavement and railways. The detailed procedure in respect to flexural tests with geo-materials is discussed by Singh and Kaushik (2003); Ramakrishnan et al. (2005); Singh and Sharma (2007); Goel et al. (2012); Tarefder et al. (2013); Hanif et al. (2018) and Sohel et al. (2018).
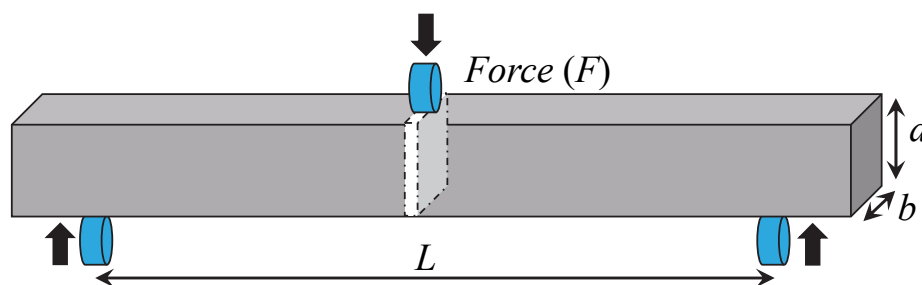
Figure 2.9 Three-point flexure test on rectangular samples

2.2.6 Static fatigue tests

The static fatigue is related to "delayed fracture", referring to the time-dependent behaviour under constant load, e.g. (Chen and Konietzky 2014; Xu et al. 2018). Static fatigue is associated with stress corrosion and creep behaviour. Systematic static fatigue tests were performed for example with Lac du Bonnet granite (Schmidtke and Lajtai 1985), see Figure 2.10. The diagram shows the stress-ratio (ratio of applied stress to UCS) vs. lifetime (duration up to failure).
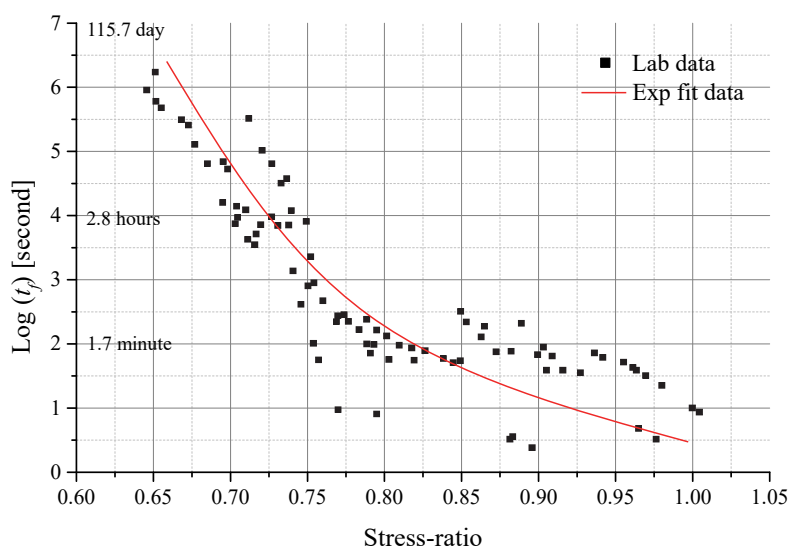
Figure 2.10 Static fatigue lab test of Lac du bonnet granite: lifetime vs. stress ratio

(Schmidtke and Lajtai 1985)

2.2.7 Freezing-thawing cyclic tests

Freezing-thawing cyclic (fatigue) tests aim to explore the effect of cyclic temperature variations (above and below 0 ºC) on material properties of partial or fully saturated materials. Water expands up to about 9% of its original volume when frozen. This expansion induces tensile stress concentration and damages the micro structure. When material is thawed, water flows through the fractured micro pores which can also increases the damage (Chen et al. 2004;
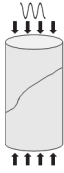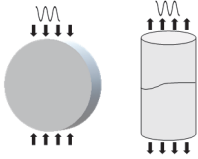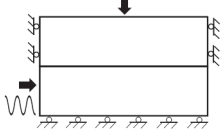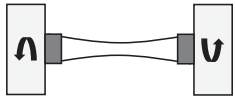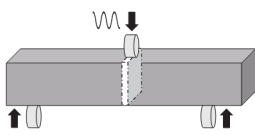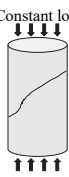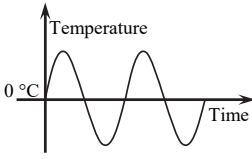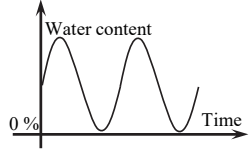
Zhang et al. 2004; Grossi et al. 2007). These effects are of special importance for geo-materials in cold regions, such as soils (Qi et al. 2006; Wang et al. 2007), rocks (Tan et al. 2011) and concretes (Polder and Peelen 2002; Bumanis et al. 2018). During freezing-thawing tests, the samples are stored in temperature and humidity controlled containers undergoing the cyclic change of temperature. Compared to the mechanical fatigue tests, the duration of one cycle in freeze-thaw fatigue tests is much longer and can last 4 - 10 hours (Tan et al. 2011). After cyclic freezing-thawing treatment mechanical testing follows. A literature review about this topic is provided by Aïtcin (2003), Qi et al. (2006) and Henry (2007).

2.2.8 Wetting-drying cyclic tests

The wetting-drying cyclic tests mainly aim to investigate the influence of cyclic change of water content in geo-materials. Wetting and drying leads to changes of properties, including bulk density, weight loss, water absorption (water content), effective porosity and P-wave velocity (Sumner and Loubser 2008; Özbek 2014; Khanlari and Abdilor 2015; Xu et al. 2017). A wetting-drying cycle is generally divided into two phases: saturation (from dry to saturated state) and drying (from saturated to dry state). In each cycle, specimens were submerged into water or other fluids for a given time to reach the saturated state at a constant temperature, and then taken out and getting air-dried at the same temperature (Zhou et al. 2017). After cyclic wetting-drying treatment, the samples experience mechanical testing.

A brief comparison of the eight types of fatigue tests are presented in Table 2.2, each type corresponds to different kind of engineering problems.

Table 2.2 Brief comparison between different fatigue tests

Types of fatigue tests	Fatigue reasons	Common test materials	Test schemes	Corresponding engineering problems
Compressive fatigue tests	Stress induced failure	Rock, Concrete, Soil, Laminate, Asphalt		1. Railway 2. Pavement 3. Foundation 4. Mining 5. …
Tensile fatigue tests	Stress induced failure	1. Direct tensile test: Metal, Alloy, Concrete 2. Brazilian test: Rock, Concrete		1. Crane 2. Bridge 3. Truss 4. Concrete beam 5. …
Shear fatigue tests	Stress induced failure	Metal, Soil, Rock, Concrete		1. Slope 2. Engineering geology 3. Airplane wing 4. …
Torsional fatigue tests	Stress induced failure	Metal, Alloy, Ceramics		1. Windmill 2. Turbine 3. Engine shaft 4. …
Flexural fatigue tests	Stress induced failure	Rock, Concrete, Laminate, Metal		1. Offshore structures 2. Pavement 3. Bridge deck 4. …
Static fatigue tests	Stress induced failure	Rock, Concrete		1. Gas cavern 2. Dam 3. Hydro station 4. …
Freezing-thawing tests	Water/temp. effect	Rock, Concrete, Soil		1. Cold region construction 2. Aerospace material 3. …
Wetting-drying tests	Water effect	Rock, Concrete, Soil		1. Highway 2. Natural rock and soil 3. …

2.3 Fatigue research based on numerical simulations

The numerical simulation of fatigue can be classified into continuum (mesh-based) methods and discontinuum (mesh-free) methods.

2.3.1 Continuum approaches

Continuum method based simulations on fatigue behaviour of geo-materials include the boundary element method (BEM), finite element method (FEM), finite difference method (FDM) and extended finite element method (XFEM), see for instance Liang et al. (2017); Nesládek and Španiel (2017); Chen et al. (2019); Nikfam et al. (2019); Pandey et al. (2019); Shabani et al. (2019) or Surendran et al. (2019). An up-to-date review on continuum based fatigue simulations is provided by Llavori et al. (2018).

Crack propagation in standard FEM is modelled with re-meshing methods around the crack tip to align the element boundaries with the crack faces. Despite this, the mesh should fit the crack geometry and very high resolution of mesh is required. In addition, the re-meshing algorithm is time-consuming and can reduce the simulation accuracy because the model needs to be frequently refreshed from the old to the new and refined mesh.

To solve this shortcoming, XFEM was first introduced by Belytschko and Black (1999) for modelling asymptotic singular fields at the crack tip. Under the regime of XFEM, the scheme is extended by enrichment functions. The domain of a crack-cut element is divided into sub domains and their Gauss points are used for integration of the domain over the enriched elements. XFEM allows the simulation of fatigue crack growth as documented for instance by Kumar et al. (2015); Dirik and Yalçinkaya (2018); Feng and Li (2018); Infante-García et al. (2019); Nikfam et al. (2019) and Pandey et al. (2019). The constitutive laws to characterize the crack direction and propagation are often based on Paris' law and SIF, as shown in Equation 2.26; where a is the crack length, N is the number of load cycles, C and n are material constants, K_1, K_2 and K_3 are SIFs for modes I, II and III, respectively. K_p is the SIF due to primary stress, K_s is the SIF due to secondary stress, v is Poisson's ratio, θ is the direction of the crack growth.

$$\frac{\mathrm{d}a}{\mathrm{d}N} = C\Delta K^n, \Delta K = K_{max} - K_{min}$$

$$K = \sqrt{(K_1^2 + K_2^2 + K_3^2/(1-v))}$$

$$K_i = K_i^p + K_i^s, i = 1,2,3$$

$$\theta = \cos^{-1}\left(\frac{3K_2^2 + \sqrt{K_1^4 + 8K_1^2 K_2^2}}{K_1^2 + 9K_2^2}\right)$$

(2.26)

The continuum method allows to simulate the crack path trajectory and to predict the fatigue failure. The fracture-based method characterizes the fatigue based on the relationship between crack growth rate and fracture mechanical terms such as SIF, fracture energy (Ray and Kishen 2010; Simon and Kishen 2017), or cohesive fracture theory (Yang et al. 2001; Nguyen et al. 2001).

2.3.2 Discontinuum approaches

For the simulation of geo-materials, the DEM approach can better duplicate the following items:

(1) Initial defects and structure, such as voids, crack and porosity.

(2) Load-induced cracks in terms of length, density, aspect ratio and orientation (Potyondy and Cundall 2004).

(3) Actual shape of mineral components and grains (Stahl and Konietzky 2011; Li et al. 2017a).

(4) Interactions between different components at the grain size level, such as mortar and aggregates (Cho et al. 2007; Ding et al. 2017).

The macroscopic behaviour can be well simulated by assigning proper microscopic contact models between basic elements (Cundall and Strack 1979; Potyondy and Cundall 2004). The DEM can be considered as a rational means of incorporating actual physical processes that occur at the grain scale and it usually shows better results than continuum approaches.

However, DEM simulations of fatigue tests are not common compared to continuum methods. This is possibly attributed to the following reasons:

(1) Lack of proper DEM damage models.

(2) More microscopic parameters are needed to assign and to calibrate the macroscopic fatigue behaviour.

(3) Compared with continuum approaches, DEM simulations are much more time consuming and geometry effects (element size, assembly structure, element shape, particle size, shape and distribution) have to be taken into account.

Nevertheless, based on particle models a few DEM simulations to model the fatigue behaviour of geo-materials were already carried out (Potyondy 2007; Ma et al. 2016; Liu et al. 2017, 2018b; Sinaie et al. 2018; Nguyen et al. 2019; Song et al. 2019c).

The basic logic in DEM models to simulate fatigue can be summarized as follow:

(1) The bond between two contacting elements are gradually weakening, which results in more obvious plastic characteristics of the materials. The mechanism is similar to stress corrosion (Potyondy 2007; Song et al. 2019c). Equation 2.27 shows the effect of bond damage based on a linear parallel bond model (LPBM) in PFC^{3D}. The normal/shear strain U_n, U_s after bond weakening will be divided by the square of damage factor β. The relative twist-rotation and bend-rotation θ_n and θ_s will be divided by the fourth power of β. It is clear that the strain and rotation will increase if bond becomes gradually deteriorated.

$$\begin{Bmatrix} U_n' \\ U_s' \\ \theta_n' \\ \theta_s' \end{Bmatrix} = \begin{bmatrix} 1/\beta^2 & 0 & 0 & 0 \\ 0 & 1/\beta^2 & 0 & 0 \\ 0 & 0 & 1/\beta^4 & 0 \\ 0 & 0 & 0 & 1/\beta^4 \end{bmatrix} \begin{Bmatrix} U_n \\ U_s \\ \theta_n \\ \theta_s \end{Bmatrix} = \begin{Bmatrix} U_n/\beta^2 \\ U_s/\beta^2 \\ \theta_n/\beta^4 \\ \theta_s/\beta^4 \end{Bmatrix}, \quad 0<\beta<1$$

(2.27)

(2) The fatigue model is formulated on the basis of the cohesive damage-plastic model (Nguyen et al. 2019). The expressions of the relative displacement between two particles incorporate fatigue displacement variables. The relative displacement μ is equal to the sum of elastic μ_e, plastic μ_p, and fatigue μ_f, displacement components, see Equation 2.28. The contact stress-displacement relationships in normal and shear directions are given by Equation 2.29.

$$\mu = \mu^e + \mu^p + \mu^f$$

(2.28)

$$\sigma_n = k_n^0(1-D)(\mu_n - \mu_n^p - \mu_n^f) - Dk_n^0 \left\langle -(\mu_n - \mu_n^p - \mu_n^f) \right\rangle$$
$$\sigma_s = k_s^0(1-D)(\mu_s - \mu_s^p - \mu_s^f)$$

(2.29)

23

Where k_n^0 and k_s^0 are initial normal and shear stiffness; D is the damage variable. Equation 2.30 shows the expression of D. The Macaulay brackets are used in terms of normal stress update to impose the full recovery of normal stiffness under compression.

$$D = \sum_{i=1}^{n} \delta D = \sum_{i=1}^{n} [(1 - f_i) \delta D_p + f_i \delta D_f]$$

(2.30)

f_i is the shift factor, which equals 0 or 1 if the stress reaches or is below the yield surface. δD_p and δD_f are increments of plastic and fatigue damage variables.

(3) A gradual reduction of strength and stiffness is acting during the cyclic loading process. The key logic is that bond strength and stiffness vary during the loading, unloading and reloading stages (Sadd et al. 1993; Liu et al. 2017). Equation 2.31 describes the variation of bond strength and stiffness.

$$\sigma = \begin{Bmatrix} \pi C_i \left(\dfrac{\mu_l}{\mu_i} \right)^p, \dfrac{d\mu}{dt} > 0 \\[2ex] \pi C_i \left(\dfrac{\mu_u}{\mu_i} \right)^q, \dfrac{d\mu}{dt} < 0 \\[2ex] \pi C_i \left(\dfrac{\mu_{rl}}{\mu_i} \right)^r, \dfrac{d\mu}{dt} > 0 \end{Bmatrix} \qquad K_n = \begin{Bmatrix} \pi E_i \left(\dfrac{\mu_l}{\mu_i} \right)^s, \dfrac{d\mu}{dt} > 0 \\[2ex] \pi E_i \left(\dfrac{\mu_u}{\mu_i} \right)^t, \dfrac{d\mu}{dt} < 0 \\[2ex] \pi E_i \left(\dfrac{\mu_{rl}}{\mu_i} \right)^m, \dfrac{d\mu}{dt} > 0 \end{Bmatrix}$$

(2.31)

Where $d\mu/dt > 0$ and $d\mu/dt < 0$ represent the loading and unloading stages, respectively. σ and K_n are bond strength and stiffness. C_i and E_i are initial bond strength and elastic modulus. μ_i is the initial height of sample, and μ_l, μ_u and μ_{rl} are axial height of the sample during the loading, unloading and reloading stages, respectively. p, q, r, s, t and m are reduction coefficients.

3. Laboratory fatigue testing

3.1 Fatigue testing set-up

3.1.1 Specimen preparation

The specimens (125 mm height (H) and 50 mm diameter (ϕ)) are made of plain concrete of type C25/30 XC4 XF1. The specimens are in two series (Series 1: S1 and Series 2: S2) according to the production date, see Figure 3.1. Before fatigue testing, ultrasonic wave speed and dynamic elastic modulus were measured to evaluate magnitude and scatter of the physical properties, see Figure 3.2. The specimen properties are presented in Table 3.1. S1-1 indicates the sample No. #1 in series 1 and so on. S1-4 and S1-9 are selected to measure the uniaxial compressive strength (UCS) representative for S1. S2-15 and S2-16 are selected to measure UCS representative for S2. The loading rate in UCS tests is 5 MPa/min for S1-4 and S1-9 and 0.125 mm/min for S2-15 and S2-16. In order to avoid early failure during the fatigue testing, the smaller reference values of 18.0 MPa and 19.0 MPa are adopted as UCS for S1 and S2 samples, respectively.
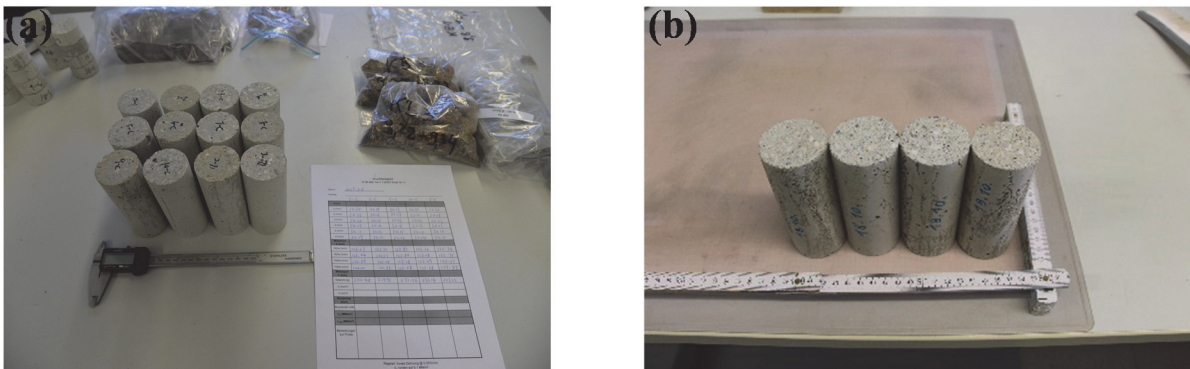
Figure 3.1 Concrete samples (a) series 1 (b) series 2

Figure 3.2 (a) ultrasonic wave speed measurement (b) data acquisition

Table 3.1 Properties of cyclically loaded concrete samples

Sample	Wave velocity [m/s]		Dyn. Young's modulus	Length	Diameter	Density	UCS
No.	P-wave	S-wave	[GPa]	[mm]	[mm]	[g/cm^3]	[MPa]
S1-1	3481	2129	22.86	125.31	50.14	2.10	
S1-2	3536	2196	23.99	126.07	50.21	2.10	
S1-3	3606	2229	24.88	125.60	50.21	2.10	
S1-4	3631	2272	25.81	125.88	50.06	2.13	18.04
S1-5	3657	2260	25.83	125.74	50.17	2.12	
S1-6	3674	2259	25.88	126.03	50.21	2.12	
S1-7	3730	2265	26.08	125.51	50.22	2.10	
S1-8	3731	2331	27.39	126.31	50.08	2.14	
S1-9	3774	2313	27.48	125.85	50.15	2.14	19.28
S1-10	3790	2432	29.52	125.76	50.14	2.17	
S1-11	3791	2274	27.00	125.66	50.21	2.14	
S1-12	3832	2459	30.11	126.09	50.18	2.17	
S2-13	4096	2289	28.75	123.74	50.31	2.16	
S2-14	4046	2323	28.63	123.70	50.45	2.11	
S2-15	4173	2416	31.75	123.46	50.31	2.18	21.01
S2-16	3760	2165	25.02	123.69	50.36	2.13	19.27

* The loading rate for S1-3, S1-4 is 5.00 MPa/min, for S2-15, S2-16 is 0.125 mm/min

3.1.2 Experimental apparatus

3.1.2.1 Testing system

The uniaxial compression testing was conducted with a MTS 20/M machine, see Figure 3.3a. The loading frame stiffness of MTS 20/M is 5E8 N/m and the maximum load is 100 kN. The fatigue testing was carried out with TIRA 28500 test system illustrated in Figure 3.3b. The system is able to perform both, static and dynamic compression tests. It has a compression capacity of 500 kN, with a piston stroke length of 1300 mm and a maximum loading velocity of 200 mm/min. The external measuring system which consists of vertical and radial strain measurement is shown in Figure 3.3c. The axial deformation of the whole specimen l_w is measured directly through displacement of loading platen of the TIRA test system. The external axial strain measurement (ε_a) is performed by linear variable differential transformer (LVDT) located at the central part of the sample and has a measuring length l_m of 50 mm. Radial strain ε_r was measured through radial chain strain gauge also placed at the central part of the specimen. For the purpose of measuring the strains at different sections (top, middle and bottom) of the specimen, strain gauges are glued at the different parts of specimen surface to measure the axial and radial strain, see Figure 3.3d.
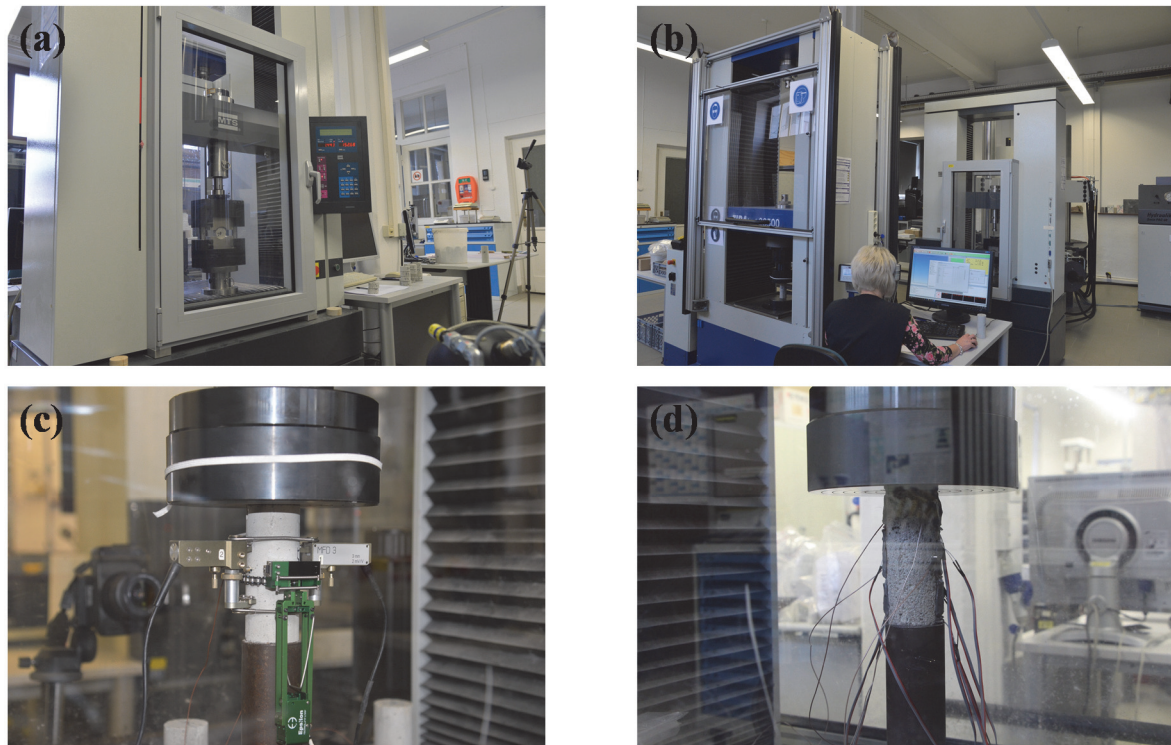
Figure 3.3 (a) MTS 20/M (b) TIRA 28500 (c) LVDT and radial chain strain gauge (d) strain gauges to measure the strain at different parts of the specimen

3.1.2.2 Acoustic emission and ultrasonic wave speed measuring system

Figure 3.4a illustrates the setup of the ultrasonic wave senders and receivers. An AMSY-6 multi-channel AE measurement system with parallel measurement channels is used in this study. Small-scale piezoelectric AE sensors with full metal housing are attached directly to the specimen surface using thermoplastic glue. Due to their small size of approximately 5 mm diameter and their frequency response showing characteristic resonance at approximately 600 kHz, the sensors are well suited to trace local AE events at a laboratory scale. Utilizing the inverse piezoelectric effect, the AE sensors can be stimulated to act as ultrasonic senders by converting an electrical pulse into a mechanical pulse. Therefore, the same sensor array can be used alternately to monitor AE and to determine ultrasonic wave speed, respectively. A limitation of this bimodal use of the sensors is, of course, that the AE monitoring system cannot detect signals while acting as an ultrasonic sender in active mode. Therefore, some AE events might be missed and are not included in our evaluation. Figure 3.4b illustrates the four AE sensors, which allow for parallel recording of AE events, such as AE counts and AE energy, at four parallel channels. The two groups of ultrasonic sensors are positioned at the top and middle part of the specimen, respectively, to independently measure the P-wave speed along the top and middle profiles.
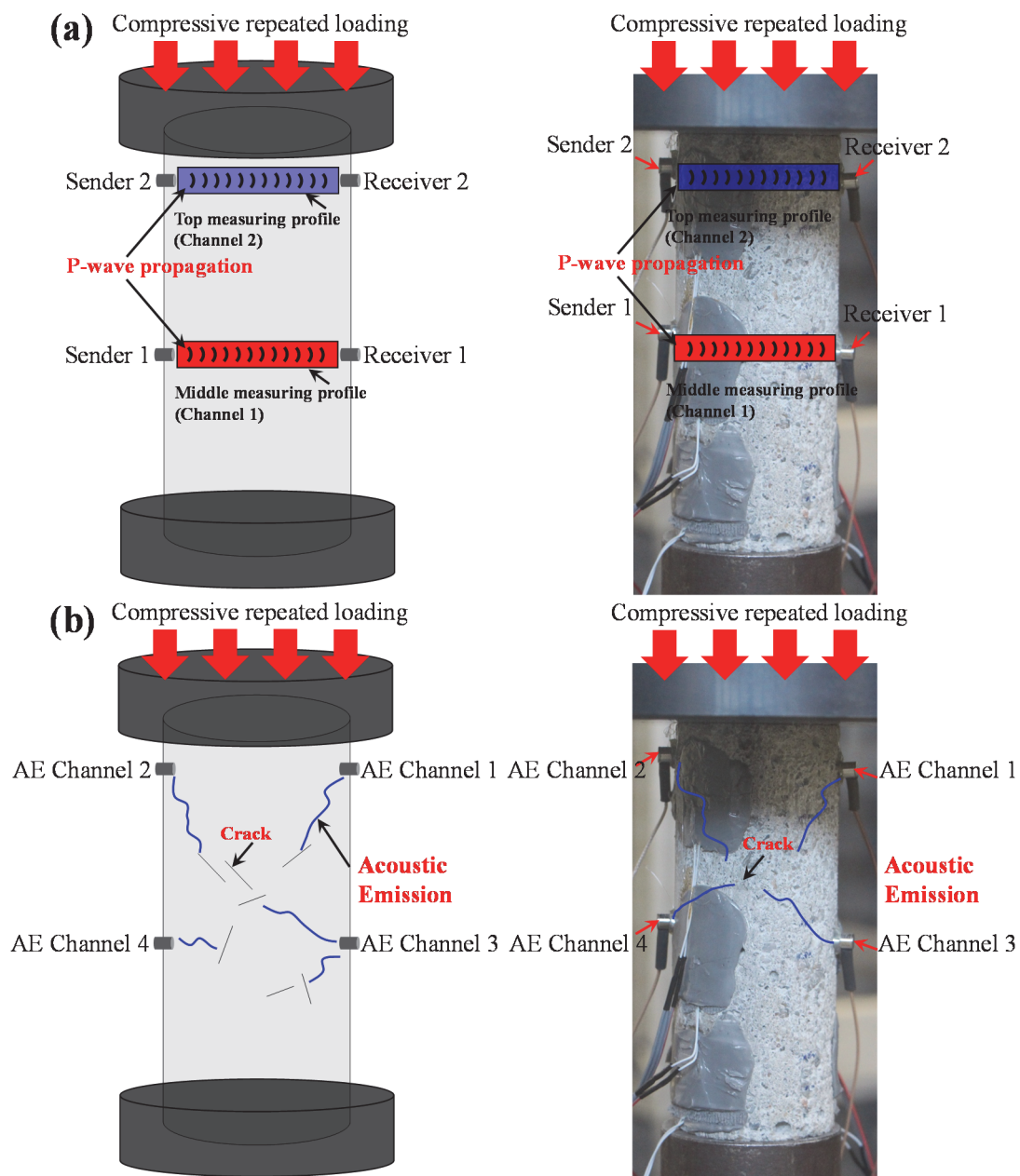
Figure 3.4 Layout of (a) ultrasonic wave speed monitoring (b) AE monitoring system

3.1.3 Testing scheme

Fatigue loading is applied as standard sinusoidal wave with constant peak-to-peak-amplitude during one loading stage. The fatigue loading schemes and the fatigue life (number of cycles up to failure) are listed in Table 3.2 and Table 3.3, respectively. According to the loading frequencies and the fatigue life, all the testing can be characterized as low frequency and low cyclic fatigue testing. The cyclic load level 40-80 means 40% UCS - 80% UCS, UCS for S1 = 18 MPa, UCS for S2 = 19 MPa. According to Table 3.2, the variations of both, maximum load stress σ_{max} and minimum load stress σ_{min} are considered.

Table 3.2 Fatigue testing scheme

Sample	Stage1	Stage2	Stage3	Stage4	Stage5	Stage6	Stage7	Stage8	Stage9	Stage10	Stage11
	Cyclic load level normalized to %UCS										
S1-1	40-80	40-90									
S1-2	40-80	40-85	30-90								
S1-3	40-65	40-85	40-95								
S1-5	40-75	40-85	40-87.5	40-90	40-92.5						
S1-6	40-90										
S1-7	40-95										
S1-11*	40-90										
S1-12	40-90	40-95	40-97.5	40-100	40-102	40-105	40-107				
S1-8	50-90	40-90	30-90	25-90	20-90	15-90	10-90	10-95	10-97.5	10-100	
S1-10	30-90	20-90	10-90	10-95	10-97.5	10-100					
S2-13	40-60	40-65	40-70	40-75	40-80						
S2-14	40-75	35-75	30-75	25-75	20-75	15-75	10-75	5-75	5-80	5-85	5-90

* Sample unexpectedly broke during fatigue test and data is not available

Table 3.3 Number of cycles in each cyclic loading stage

Sample	Stage1	Stage2	Stage3	Stage4	Stage5	Stage6	Stage7	Stage8	Stage9	Stage10	Stage11	f
	Cycle number											
Unit	Cycles	Cycles	Cycles	Cycles	Cycles	Cycles	Cycles	Cycles	Cycles	Cycles	Cycles	[Hz]
S1-1	50	3 F										0.4
S1-2	50	50	2 F									0.4
S1-3	2490	50	5 F									0.4
S1-5	2880	150	150	150	97 F							0.4
S1-6	34 F											0.4
S1-7	11 F											0.4
S1-11*	1 F											0.2
S1-12	500	150	150	150	150	150	53 F					0.8
S1-8	1250	150	150	150	150	150	150	150	150	52 F		0.4
S1-10	500	150	150	150	150	150	250 F					0.4
S2-13	150	150	150	150	11 F							0.5
S2-14	150	150	150	150	150	150	150	150	150	150	126 F	0.5

* Sample unexpectedly broke during fatigue test and data is not available; F: The sample failed in the current stage

3.2 Characteristics of dissipated energy

The continuum damage theory (CDT) and dissipated energy approach (DEA) are the two important approaches to investigate fatigue damage (Lei et al. 2017). Researchers adopted CDT to establish constitutive equations between the selected variables and damage evolution. A continuum damage model for fatigue load of concrete was established by Alliche (2004). This damage model can describe the material degradation under fatigue load by introducing tensorial damage parameters. Xiao et al. (2010) suggested that the damage variables should have a distinct physical meaning and should be measured and applied conveniently. The authors stated that axial residual strain is the most appropriate variable to reflect the damage evolution. Oneschkow (2016) investigated the evolution of strain and stiffness of high-strength concrete subjected to fatigue load. She found that the change of waveform from sinusoidal to

triangular leads to larger values of strain and an increasing loss of stiffness. Baluch et al. (2003) established a damage model based on CDT for predicting the fatigue properties of concrete subjected to cyclic loading, which is able to predict the residual strength of concrete subjected to initial damage induced by a given number of stress cycles. Lee et al. (2000) proposed a fatigue prediction model for asphalt concrete based on the elasto-visco-elastic correspondence principle. This model can account for the effects of loading rate and stress level on fatigue features. Generally, CDT can describe the evolution of damage based on constitutive equations. However, the damage variables selected in CDT always reflect single aspects, such as axial/radial strain or elastic modulus.

The DEA is able to reflect damage of materials during cyclic loading by considering the energy dissipated or absorbed by the sample. Compared to CDT, DEA has the following advantages: 1. DEA can consider strain and stress concurrently and is more precise compared to the CDT which only considers a single damage variable; 2. During the stationary stage of fatigue test, the increment of strain is hard to measure to characterize the damage due to the extremely small change of strain. The DEA can still clearly reflect the dissipated energy in the stationary stage, and continuously represent the progressive damage. Bagde and Petroš (2009) found that the dissipated energy is increasing with frequency and load amplitude. The energy dissipated by the rock could be treated as an inherent characteristic. Lei et al. (2017) proposed a concrete fatigue life prediction method, which is based on accumulated dissipated energy. It was concluded that the dissipated energy within each cycle has a direct relationship with stress levels. Tepfers et al. (1984) investigated the energy absorption of plain concrete in fatigue tests and found that the absorbed energy at failure under uniaxial compression seems to be the same for static load as well as for fatigue load. Xie et al. (2004, 2005) discussed the intrinsic relations between dissipated energy, energy release, and structural failure of rocks during loading and unloading stages and stated that dissipated energy acts as an internal factor connected with damage and irreversible deformation. Naderi and Khonsari (2013) performed a series of fatigue tests on glass/epoxy laminates. He concluded that when the load is relatively low, the dissipated energy due to damage is small compared to dissipated energy due to heat. With increasing load level, the proportion of dissipated energy due to damage increases. Jiang et al. (1994) and Tong et al. (1989) suggested that the accumulated dissipated energy can be used as a proper variable to reflect the damage of materials because there is no discontinuity in the curve. Shadman and Ziari (2017) proposed an approach based on dissipated energy to predict fatigue life of porous asphalt. The authors found that the total dissipated energy at failure can be forecasted by

regression equations relating cycle number and total dissipated energy. Shen et al. (2006) pointed out that the fluctuation of energy dissipation between two consecutive cycles can indicate the development of damage.

Many researchers found that maximum load level during cyclic loading has an influence on fatigue of the material. Ge et al. (2003) investigated the threshold value (endurance limit) of load level during fatigue tests. He mentioned that in case the maximum load level is smaller than the threshold value, the axial, radial and volumetric irreversible strain tend to be constant. However, when maximum load level is larger than the threshold value, axial, radial and volumetric irreversible strain increase with increasing number of load cycles. Rao and Ramana (1992) conducted fatigue tests on Hyderabad granites. They concluded that when load level is larger than threshold value, the Kaiser Effect and AE events are more pronounced and that the threshold value is comparable to the dilatancy limit. Concrete as quasi-brittle material is always exchanging (absorbing and releasing) energy with its surrounding system during cyclic loading (Dattoma and Giancane 2013; Lei et al. 2017; He et al. 2018). The amount of dissipated energy during one single cycle reflects the ability of the material to resist damage induced by external loading. The more energy during one cycle is dissipated the more damage is generated inside the material. The total dissipated energy of a sample can be generally divided into two parts: one is dissipated by heat convection, conduction and radiation of seismic energy, the other part includes defect formation, crack propagation and plastic deformation. The dissipated energy by heat convection and conduction remains almost constant during cyclic loading (Dattoma and Giancane 2013), therefore the change in dissipated energy is directly related to fatigue evolution.

This chapter is based on DEA to investigate the characteristics of dissipated energy of concrete samples subjected to stress-controlled uniaxial cyclic loading. The effect of cyclic load levels on characteristics of dissipated energy is quantitatively investigated. The dissipated energy within the DEA concept is compared with variables used in CDT and the evolution of damage variables in the two approaches is analysed.

In this thesis, the dissipated energy density U_d within one single cycle is defined as the area of the hysteresis loop in the stress (σ) - axial strain (ε_a) - diagram (Tepfers et al. 1984; Lei et al. 2017; He et al. 2018; Song et al. 2018a). The unit of U_d is J/m^3 and it represents the dissipated energy in a unit volume. The accumulated dissipated energy density U_a is the sum of single cycles U_d from the beginning of cyclic loading until the current cycle N. The axial strain ε_a is

measured through axial strain gauge placed at the central part of the sample. U_d and U_a are defined by Equation 3.1 and Equation 3.2.

$$U_d = \oiint \sigma d\varepsilon_a \tag{3.1}$$

$$U_a = \sum_{i=1}^{N} U_d \tag{3.2}$$

3.2.1 Effect of maximum cyclic load level on energy dissipation

3.2.1.1 U_d for different maximum cyclic load levels

U_d for different maximum cyclic load levels is plotted in Figure 3.5. Among the six samples (S1-1, S1-2, S1-3, S1-5, S1-6 and S1-7), only S1-6 and S1-7 experienced cyclic loading at one stage only until failure (40% - 90% UCS and 40% - 95% UCS, respectively). The first 50 cycles at different load levels were used to analyse U_d. Like shown in Figure 3.5, the curves for U_d of S1-6 and S1-7 are "U"-shaped. The fatigue life of S1-6 and S1-7 are 34 and 11 cycles, respectively. U_d of S1-6 and S1-7 is almost symmetrical along the middle point of fatigue life (17th cycle and 5th cycle). The minimum value of U_d is also observed at the 17th and 5th cycle, respectively. Considering these characteristics, the minimum value of U_d can be used to predict the fatigue life of materials under cyclic loading with only one loading stage.

According to Table 3.2, S1-1 and S1-2 experienced cyclic loading between 40% - 80% UCS in the first stage (without any former cyclic loading stages). U_d of S1-1 and S1-2 is plotted in Figure 3.6a. The values of U_d are highly coincident, which demonstrates the same material has similar characteristics of energy dissipation under the same loading strategy. In addition, from Figure 3.6a to Figure 3.6d, it can be observed that U_d is sensitive to the change of cyclic load level and can be selected as an inherent damage variable.

According to Table 3.2, S1-2, S1-3 and S1-5 experienced loading between 40% - 85% UCS with different cyclic loading stages before. In detail, the S1-2, S1-3 and S1-5 experienced 40% - 80% UCS, 40% - 65% UCS, and 40% - 75% UCS in first stage before cyclic loading between 40% - 85% UCS was applied. U_d of S1-2, S1-3 and S1-5 are plotted in Figure 3.6b. In terms of U_d it holds: S1-2 > S1-3 > S1-5. Rao and Ramana (1992) stated that the threshold value for fatigue is comparable to the dilatancy limit. This limit usually corresponds to about 80% UCS (Ge and Lu 1992; He et al. 2014). Consequently, the first cyclic loading stage for

S1-2 (40% - 80% UCS) can already result in massive fatigue damage inside the sample. Therefore, compared to S1-3 and S1-5, S1-2 is more damaged. In addition, from the first to the second cyclic loading stage, the increments of load amplitude for S1-3 and S1-5 are 20% UCS and 10% UCS, respectively. Therefore, U_d of S1-3 is significantly larger than that of S1-5.

Different from S1-1 and S1-2, S1-5 and S1-6 experienced the same cyclic load level but applied in different loading strategies (see Table 3.2). S1-5 experienced cyclic loading between 40% - 90% UCS after three former cyclic loading stages (40% - 75% UCS, 40% - 85%UCS, and 40% - 87.5% UCS). S1-6 experienced only a single cyclic loading stage between 40% - 90% UCS until failure. U_d is represented in Figure 3.6c. S1-5 did not fail after 50 cycles whereas S1-6 broke after only 34 cycles at same cyclic load level. Figure 3.6c documents that U_d of S1-6 is significantly larger than that of S1-5. U_d of S1-6 reveals a "U" shape. This demonstrates, that samples can have a different amount of dissipated energy in the same cyclic load level. The loading strategy can influence the amount of dissipated energy. Progressively increasing maximum load, for example the maximum load level of S1-5 increased from 75% UCS to 90% UCS, will lead to less dissipated energy compared to cyclic loading at only one stage, for example for S1-6. This phenomenon may be explained by energy transmission and crack propagation. The moderate increasing of load level in cyclic loading, such as for sample S1-5, can result in more evenly distributed micro cracks and more even transmission of energy. This can avoid the rupture of sample in extremely short time due to initial large load level. According to Table 3.2, S1-5 experienced 5 cyclic loading stages. U_d for S1-5 is illustrated in Figure 3.6d. With increasing maximum load level from 75% UCS to 92.5% UCS, the evolution of U_d changes. As shown in Figure 3.6d, it becomes obvious that U_d increases with increasing of load level from 40% - 75% UCS to 40% - 92.5% UCS.
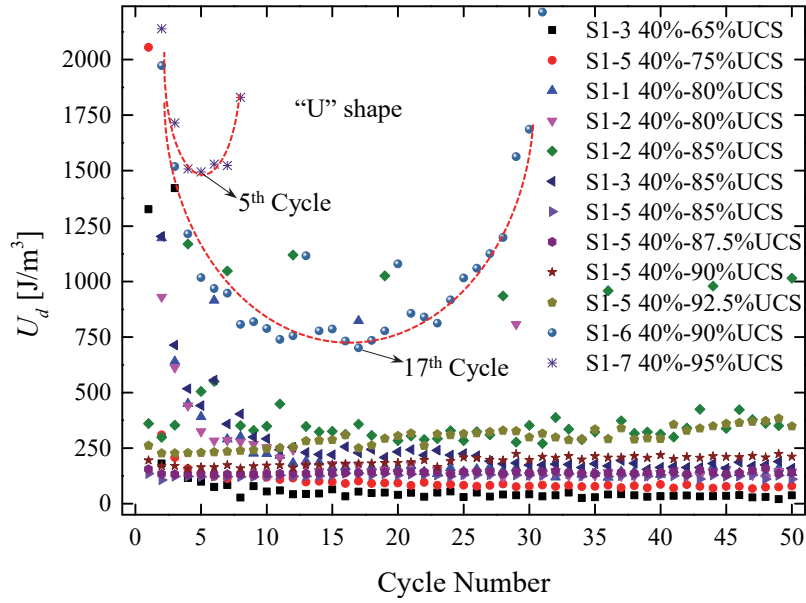
Figure 3.5 U_d for different maximum cyclic load levels
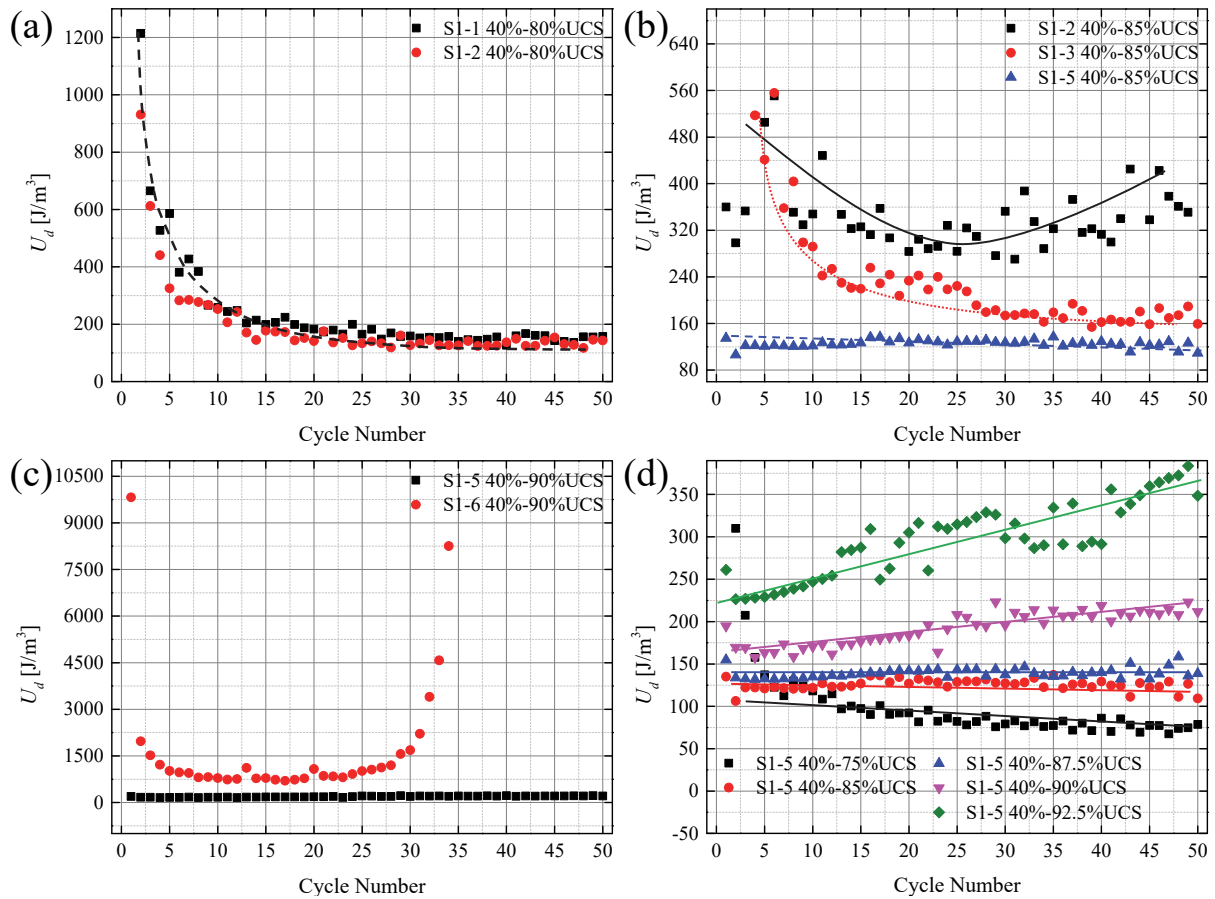
Figure 3.6 (a) U_d between 40% and 80% UCS (b) U_d between 40% and 85% UCS (c) U_d between 40% and 90% UCS (d) U_d of S1-5 (5 cyclic loading stages)

3.2.1.2 *U_a* for different maximum cyclic load levels

U_a registered in different cyclic load levels is illustrated in Figure 3.7. S1-6 and S1-7 broke within one single cyclic load level. *U_a* of S1-6 and S1-7 are "inverted-S" shaped and can be divided into three phases: 1. decelerating phase 2. stationary phase 3. accelerating phase - similar to the evolution of residual axial strain in fatigue tests (Xiao et al. 2009) and also common in classical creep tests. The cycle number in phase 1 is almost equal to the cycle number in phase 3. The slope of the curve of S1-7 is larger than that of S1-6 for the same number of cycles. Apart from S1-6 and S1-7, all other samples show only the first or the second phase during the first 50 cycles.

U_a of S1-1 and S1-2 is illustrated in Figure 3.8a. The slope of *U_a* during the stationary phase reflects the speed of energy dissipation. The load level in the first cyclic stage of S1-1 and S1-2 are both 40% - 80% UCS. According to Figure 3.8a, the slope of *U_a* during the first 10 cycles show some scatter, which is caused by small differences in the physical properties of the samples. However, the slope for *U_a* of S1-1 and S1-2 are nearly identical (see values of β_1, β_2) for same cycle number during the stationary phase, hereon the stationary phase is designated as the phase in which the slope of *U_a* curve remains constant, as plotted in Figure 3.8a. S1-1 and S1-2 entered the stationary phase after nearly the same number of cycles (around 12 cycles). This demonstrates that the speed of energy dissipation in the stationary phase is constant for a certain cyclic loading strategy and can therefore be selected as variable to represent fatigue damage of materials.

U_a of S1-2, S1-3 and S1-5 in 40% - 85% UCS cyclic load level is illustrated in Figure 3.8b. As shown in Figure 3.8b, S1-2 and S1-5 do not have a decelerating phase but only the stationary phase. However, S1-3 shows both, the decelerating and stationary phase. As can be seen from Figure 3.7 and Figure 3.8a, the curves of *U_a* during the first cyclic loading stage show at least the first two or all three phases, like for S1-6 and S1-7. Curves of *U_a* after the first cyclic loading stage usually only show the stationary phase. This phenomenon can also be observed in Figure 3.8c and Figure 3.8d. As Figure 3.8b documents, S1-2 has the largest slope (see β_1) due to massive damage resulting from former cyclic loading stage (40% - 80% UCS) in which the maximum load level is close to the fatigue threshold value. Due to the damage in former cyclic loading stage, the ability of S1-2 to resist external load decreases and consequently the speed of energy dissipation is larger than that of S1-3 and S1-5. The load increments for S1-3

35

and S1-5 are 20% UCS (from 65% to 85%) and 10% UCS (from 75% to 85%), respectively. Larger increments can result in larger slope values for U_a (see Figure 3.8b).

U_a of S1-5 and S1-6 in the 40% - 90% UCS cyclic load level is illustrated in Figure 3.8c. The slope of U_a curve for S1-6 in the stationary phase is consistently larger than that of S1-5. S1-6 experienced only one cyclic load level (40% - 90% UCS) up to failure and the curve shows all three phases. However, due to former cyclic loading stages, S1-5 shows only the stationary phase. This indicates that the former cyclic loading stages with small load level lead to less energy dissipation compared to samples that only experience one single cyclic load level. The reason might be that the former cyclic loading stages with small load level progressively consolidated the sample which improves the ability to resist external load. U_a of S1-5 for five consecutive cyclic loading stages are illustrated in Figure 3.8d. As shown in Figure 3.8d, only the first cyclic loading stage (40% - 75% UCS) shows the decelerating phase, the latter four stages only show the stationary phase. By progressively increasing the maximum load, the slope of U_a increases. This confirms that during cyclic loading the maximum load directly influences the release of dissipated energy (Tepfers et al. 1984; Lei et al. 2017).
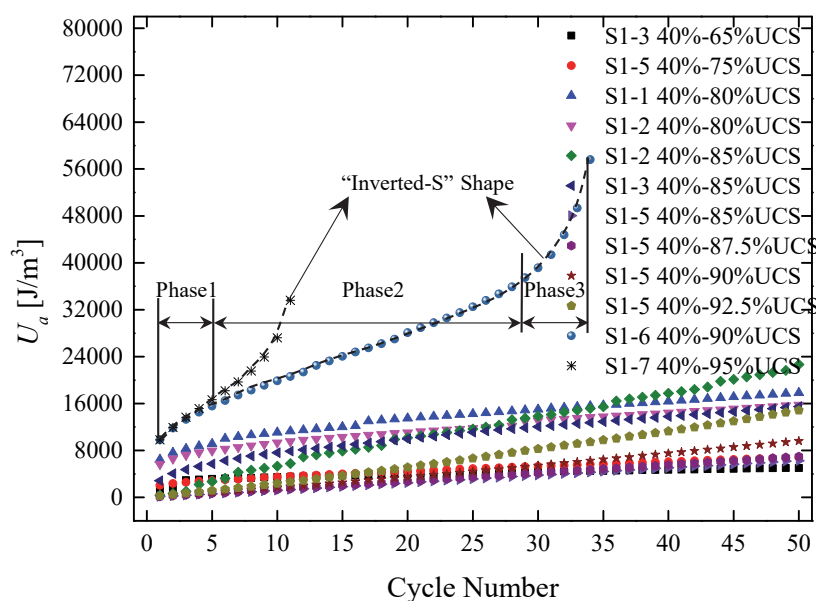
Figure 3.7 U_a for different maximum cyclic load levels
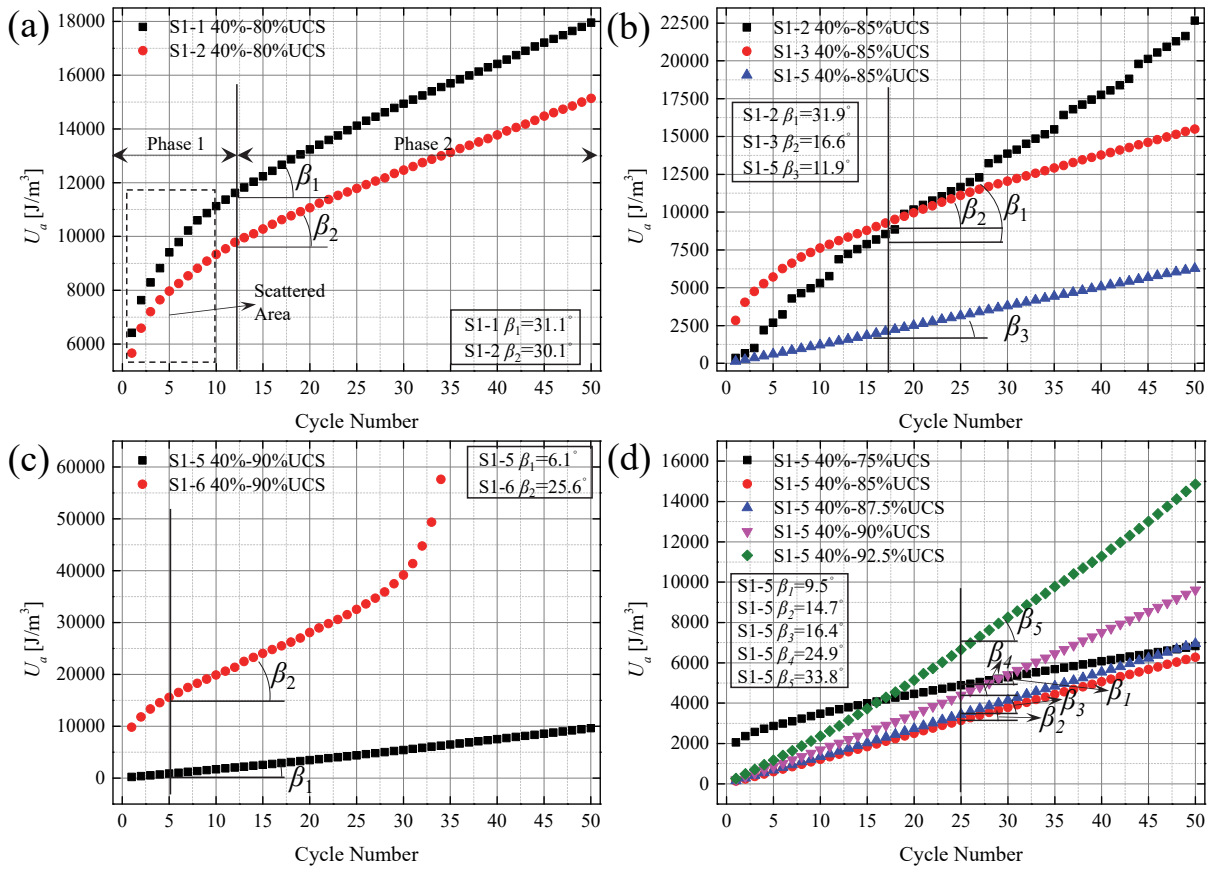
Figure 3.8 (a) U_a between 40% and 80% UCS (b) U_a between 40% and 85% UCS (c) U_a between 40% and 90% UCS (d) U_a of S1-5 (5 cyclic loading stages)

3.2.1.3 Effect of maximum cyclic load level on damage indicator

The residual axial strain and residual radial strain are often used as damage indicators to reflect fatigue damage evolution in CDT (Xiao et al. 2009, 2010; Sun et al. 2017), while the accumulated dissipated energy (U_a) is usually used as damage indicator in DEA (Naderi and Khonsari 2013; Lei et al. 2017; He et al. 2018). The effects of maximum cyclic load level on the evolution of the damage indicators during fatigue tests are investigated in the framework of CDT and DEA. A growth rate of damage (dV/dN) is observed in the stationary phase. V stands for the selected damage indicators (U_a, l_w, ε_a, ε_r) and N is cycle number. In Table 3.4, the development of the damage indicators is listed.

Table 3.4 Damage indicators for different maximum cyclic load levels

Sample	Load level	U_a/N	l_w/N	ε_a/N	ε_r/N	Note	
Unit	[% UCS]	[J/m³/N]	[mm/N]	[mm/mm/N]	[mm/mm/N]		
S1-3	40 – 65	3.85×1E1	6.00×1E-6	2.00×1E-7	-1.00×1E-8	1st	load stage
S1-5	40 – 75	8.18×1E1	2.00×1E-5	5.00×1E-7	-2.00×1E-8	1st	load stage
S1-2	40 – 80	1.61×1E1	3.00×1E-4	2.00×1E-6	-1.00×1E-6	1st	load stage
S1-1	40 – 80	1.62×1E2	3.00×1E-4	2.00×1E-6	-9.00×1E-7	1st	load stage
S1-1	40 – 85	4.05×1E2	1.20×1E-3	2.00×1E-5	-3.00×1E-5	2nd	load stage
S1-3	40 – 85	1.92×1E2	2.00×1E-4	2.00×1E-6	-3.00×1E-6	2nd	load stage
S1-5	40 – 85	1.27×1E2	5.00×1E-5	6.00×1E-7	-2.00×1E-7	2nd	load stage
S1-5	40 – 87.5	1.40×1E2	1.00×1E-4	6.00×1E-7	-2.00×1E-7	3rd	load stage
S1-5	40 – 90	2.00×1E2	2.00×1E-4	1.00×1E-6	-1.00×1E-6	4th	load stage
S1-6	40 – 90	8.42×1E2	3.40×1E-3	3.00×1E-5	-3.00×1E-5	1st	load stage
S1-5	40 – 92.5	3.11×1E2	8.00×1E-4	6.00×1E-6	-5.00×1E-6	5th	load stage
S1-7	40 – 95	1.80×1E3	9.90×1E-3	7.00×1E-5	-2.00×1E-4	1st	load stage

*ε_a/N, ε_r/N are shown in one digit

The growth rate of damage indicators in the first cyclic loading stage is fitted by black solid lines (fitting line 1) in Figure 3.9. It is observed that all four indicators follow an exponential function in relation to the maximum cyclic load level according to Equation 3.3. V includes U_a, l_w, ε_a and ε_r. σ_{max} is the maximum cyclic loading, a and b are fitting coefficients. According to Table 3.4, the damage indicators using U_a, l_w, ε_a and ε_r for S1-5 considering all five consecutive cyclic loading stages were also determined (red dashed fitting line 2 in Figure 3.9). It is apparent that all indicators can be fitted well again by an exponential relationship. The fitting parameters for fitting line 1 and 2 in Figure 3.9 are listed in Table 3.5. According to this, the damage evolution using U_a, l_w, ε_a, ε_r can be obtained by Equation 3.3 also for other load levels.

$$V = a \cdot \exp(b \cdot \sigma_{max})$$

(3.3)

The evolution of damage indicators in the first cyclic loading stage (black solid lines) can be compared with those obtained under gradually increasing maximum loading conditions (red dashed lines). It demonstrates that the damage evolution under progressively increasing maximum load is much smaller than those observed in the first cyclic loading stage. This can be also observed from the area encircled by blue dashed-dot lines in Figure 3.9. The speed of damage increase can be different under the same cyclic load level for different loading strategies (see 85% UCS and 90% UCS conditions). The progressively increasing maximum load can slow down the damage evolution. This again verifies the conclusion that the loading strategy has influence on the damage evolution.
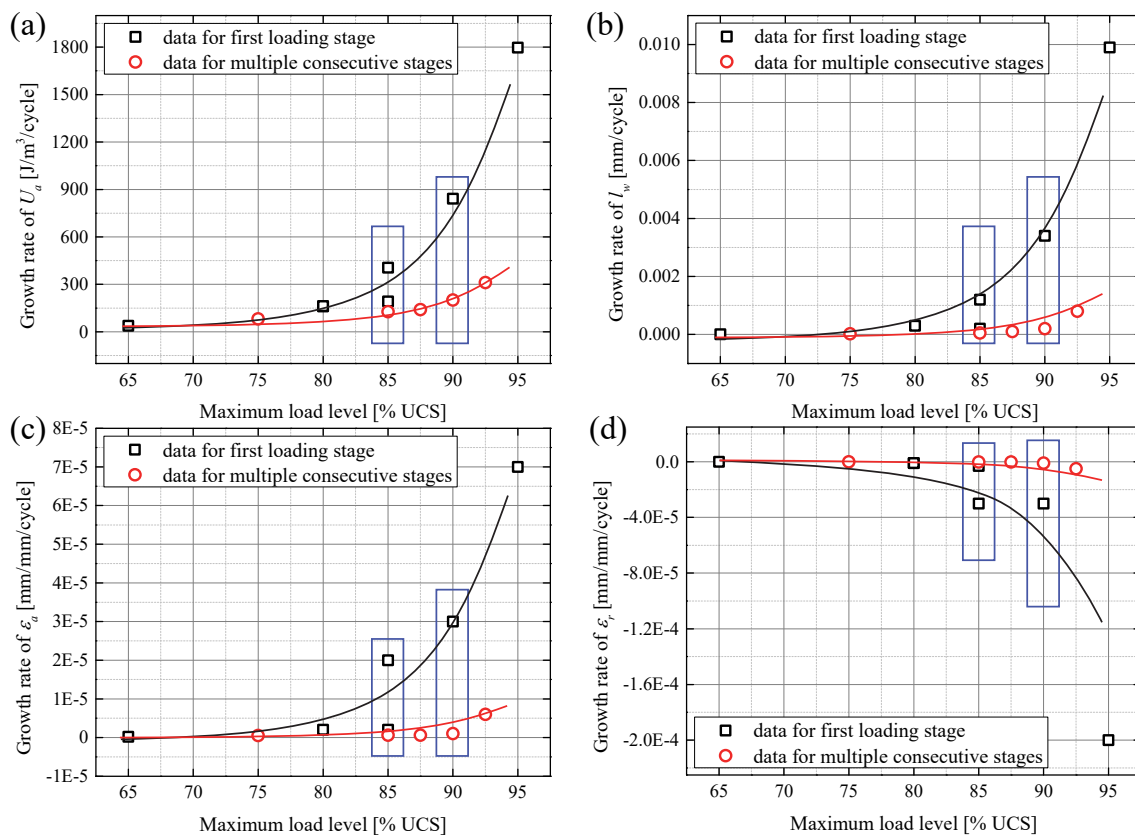
Figure 3.9 (a) U_a/N (b) l_w/N (c) ε_a/N (d) ε_r/N for different maximum cyclic load levels

Table 3.5 Fitting parameters (see Figure 3.9)

Fitting line number	Damage indicators	a	b	R^2	Maximum load level range
Fitting-1	U_a	4.80×1E-3	1.33×1E-1	0.9697	65% UCS – 95% UCS
Fitting-2	U_a	4.00×1E-1	6.93×1E-2	0.8667	75% UCS – 92.5% UCS
Fitting-1	l_w	2.00×1E-13	2.62×1E-1	0.9629	65% UCS – 95% UCS
Fitting-2	l_w	9.00×1E-12	1.90×1E-1	0.8418	75% UCS – 92.5% UCS
Fitting-1	ε_a	1.00×1E-13	2.10×1E-1	0.9625	65% UCS – 95% UCS
Fitting-2	ε_a	9.00×1E-16	2.39×1E-1	0.9547	75% UCS – 92.5% UCS
Fitting-1	ε_r	-4.00×1E-19	3.54×1E-1	0.9391	65% UCS – 95% UCS
Fitting-2	ε_r	-4.00×1E-18	2.92×1E-1	0.9321	75% UCS – 92.5% UCS

(a)

(b)
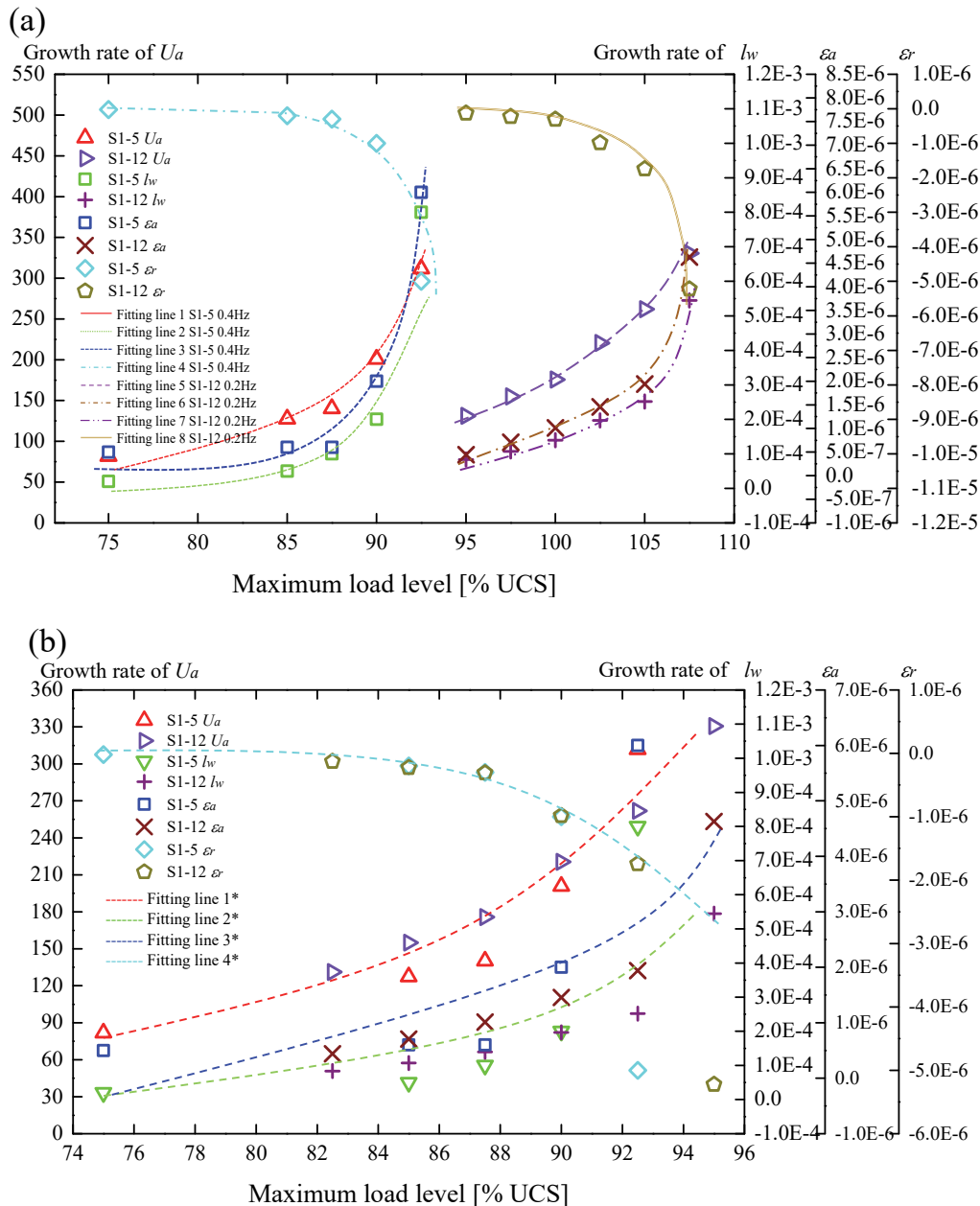
Figure 3.10 (a) original (b) shifted data: U_a/N, l_w/N, ε_a/N and ε_r/N versus maximum load level for S1-5 and S1-12

The loading frequency was changed from 0.4 Hz to 0.8 Hz and 0.2 Hz for S1-11 and S1-12 according to Table 3.2. Due to unexpected pre-failure of S1-11, only data of S1-12 can be used. The loading strategies of S1-12 and S1-5 are similar. The damage indicators for S1-12 and S1-5 are plotted in Figure 3.10a: the fitting lines 1 to 4 belong to S1-5 called Fitting-2 in Table 3.5, the fitting lines 5 to 8 belong to S1-12 called Fitting lines 1 to 4 in Table 3.6. Figure 3.10a shows the obtained exponential relationships according to Equation 3.3. It becomes obvious, that the evolution of damage indicators show a very similar trend. Therefore, it can be concluded, that at least a relatively small change in loading frequency by a factor of 2 does not

alter the damage evolution. Test results indicate that S1-12 has a significant higher strength than S1-5. Therefore, values for S1-12 were shifted (reduced) by a value of 12.5% UCS (best fitting), which leads to a nearly perfect fit with results for S1-5 as shown in Figure 3.10. The parameters of fitting lines 1* to 4* in Figure 3.10b are listed in Table 3.6. It indicates that an exponential relationship holds for different values of short term strength.

Table 3.6 Fitting parameters (see Figure 3.10)

Fitting lines number	Damage indicators	*a*	*b*	R^2	Maximum load level range
Fitting line 1	U_a	1.20×1E-1	7.34×1E-2	0.9924	95% UCS – 107.5% UCS
Fitting line 2	l_w	1.00×1E-10	1.40×1E-1	0.9491	95% UCS – 107.5% UCS
Fitting line 3	ε_a	3.00×1E-14	1.73×1E-1	0.9686	95% UCS – 107.5% UCS
Fitting line 4	ε_r	-7.00×1E-20	2.95×1E-1	0.9732	95% UCS – 107.5% UCS
Fitting line 1*	U_a	3.20×1E-1	7.25×1E-2	0.9153	82.5% UCS – 95% UCS
Fitting line 2*	l_w	4.00×1E-11	1.72×1E-1	0.8583	82.5% UCS – 95% UCS
Fitting line 3*	ε_a	1.00×1E-11	1.32×1E-1	0.6855	82.5% UCS – 95% UCS
Fitting line 4*	ε_r	-5.00×1E-18	2.88×1E-1	0.9453	82.5% UCS – 95% UCS

3.2.2 Effect of minimum cyclic load level on energy dissipation

3.2.2.1 U_d for different minimum cyclic load levels

U_d for different minimum cyclic load levels is plotted in Figure 3.11a. The first 100 cycles in the different cyclic load levels are used to analyse U_d. It should be noted that the samples did not break during loading process listed in Table 3.2, therefore the maximum load level is enhanced to obtain sample failure. 30% - 90% UCS is used for the first cyclic loading stage for S1-10. S1-8 has experienced four preceding cyclic loading stages until a load level at 30% - 90% UCS is reached. After cyclic loading at 30% - 90% UCS, both samples experienced the same cyclic loading at 20% - 90% UCS and later at 10% - 90%. As shown in Figure 3.11a, S1-10 shows smaller values of U_d than S1-8 in the same stage. During cyclic loading at 20% - 90% UCS and 10% - 90% UCS, the difference of U_d is obviously. This also verifies: when maximum load is larger than threshold value of fatigue (80% UCS), massive damage is induced. Therefore, the damage of S1-8 (four former loading stages with maximum load larger than 90% UCS) will be more serious than S1-10. U_d for different minimum cyclic load levels of S1-8 are plotted in Figure 3.11b. U_d increases with decreasing values of minimum cyclic load level. The decrease of minimum cyclic load level in the first four cyclic loading stages is 5% UCS and later one 10% UCS. Figure 3.11b indicates a non-linear increase in energy release with decreasing minimum cyclic load level.
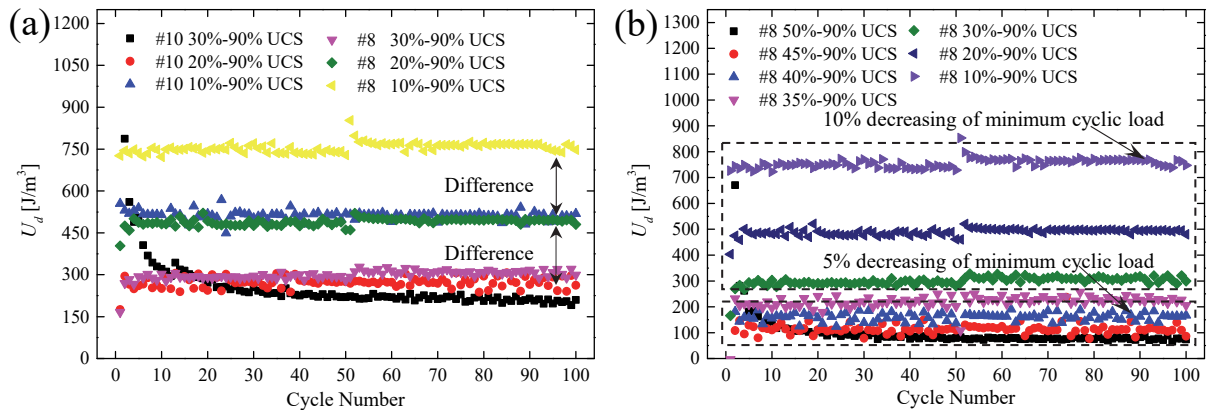
Figure 3.11 (a) U_d of S1-8, S1-10 (b) U_d of S1-8 versus cycle number for different minimum cyclic load levels

3.2.2.2 U_a for different minimum cyclic load levels

U_a for different minimum cyclic load levels is plotted in Figure 3.12a. The two later cyclic loading stages (20% UCS - 90% UCS and 10% UCS - 90% UCS) show obviously different slopes for S1-8 and S1-10 which represents different speed of damage evolution. According to loading strategies shown in Table 3.2, this indicates again: due to the fact that S1-8 experienced four former loading stages and the maximum load levels in all four former stages are larger than threshold value of fatigue damage (80% UCS), the speed of damage evolution for S1-8 is larger than that of S1-10 in 20% UCS - 90% UCS and 10% UCS - 90% UCS stages. U_a for sample S1-8 at different minimum cyclic load levels and fixed maximum load level of 90% UCS is plotted in Figure 3.12b. A clear trend becomes obvious: the cumulative speed of dissipated energy increases if span between maximum and minimum load level increases. This also verifies the effect of minimum cyclic load level on cumulative dissipated energy. It shows that both maximum and minimum load have obvious effect on amount of dissipated energy.
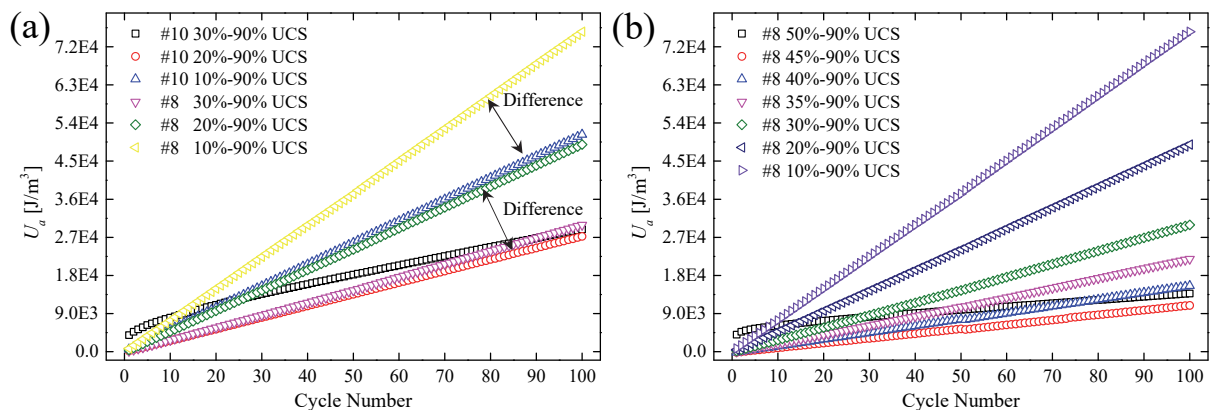
Figure 3.12 (a) U_a of S1-8, S1-10 (b) U_a of S1-8 versus cycle number for different minimum cyclic load levels

3.2.2.3 Effect of minimum cyclic load level on damage indicators

A growth rate of damage (dV/dN) in the stationary phase is documented with decreasing minimum cyclic load level. Table 3.7 shows the corresponding damage indicators. Figure 3.13 illustrates the development of the damage indicators together with corresponding fitting functions. It can be seen that, apart from ε_r (difficult to measure), the other three indicators (U_a, l_w, ε_a) are well fitted by a logarithmic function in respect to the minimum cyclic load level according to Equation 3.4. σ_{min} is the minimum cyclic load level, a and b are fitting coefficients. The fitting parameters are listed in Table 3.7.

$$V = a \cdot \ln\left(\sigma_{min}\right) + b$$

(3.4)

Equations 3.3 and 3.4 consider the effect of maximum and minimum cyclic load level on damage speed in different quantitative form. The first cyclic loading phase (encircled with blue dotted lines and marked as special data points) in Figure 3.13b and 3.13c does not fit into the general trend. This is very likely caused by the fact, that sample incl. interface between sample and loading plate have to overcome an initial phase of 'setting'. Therefore, the first cyclic loading stage is ignored in the evaluation.
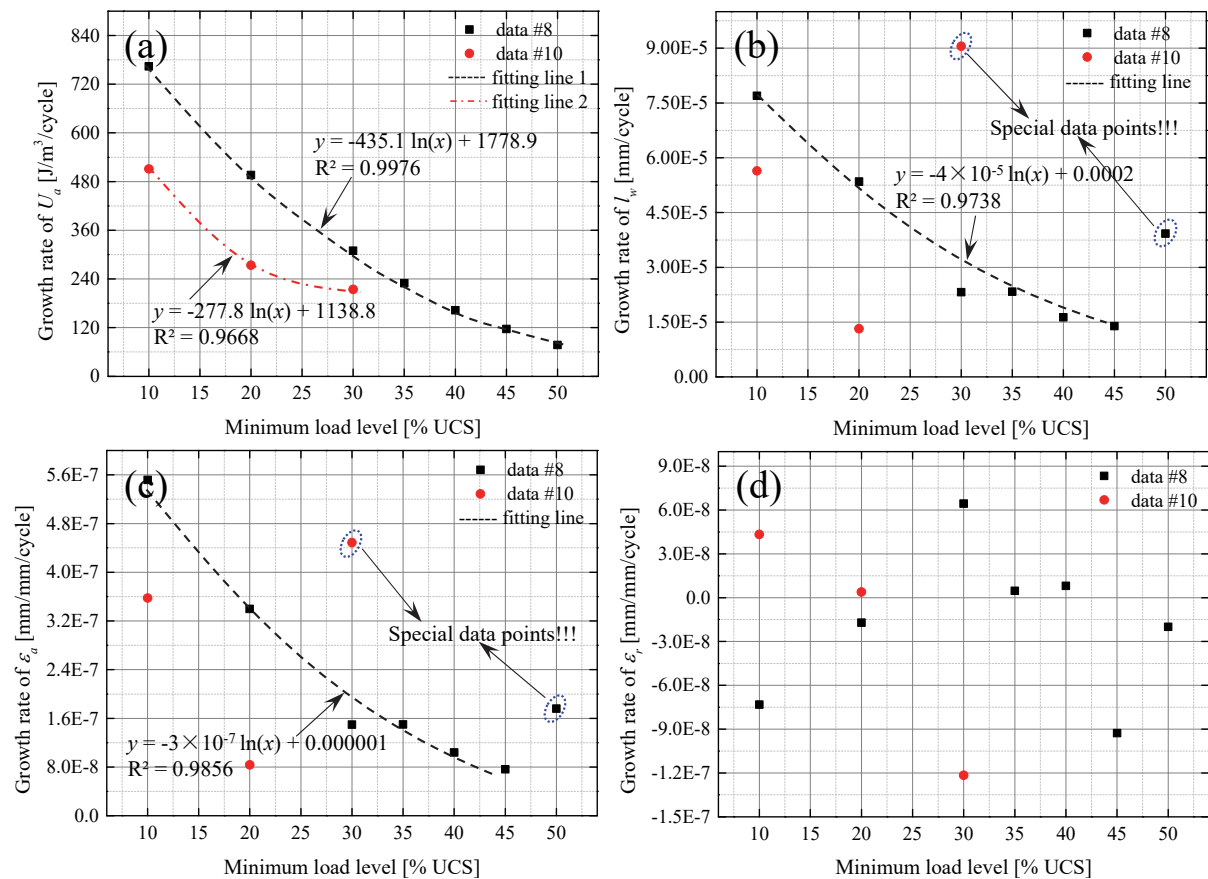
Figure 3.13 (a) U_a/N (b) l_w/N (c) ε_a/N and (d) ε_r/N for different minimum cyclic load levels

43

Table 3.7 Damage indicators for different minimum cyclic load levels

Sample No.	Load level [% UCS]	U_a/N [J/m³/N]	l_w/N [mm/N]	ε_a/N [mm/mm/N]	ε_r/N [mm/mm/N]	Note	
S1-8	50 – 90	7.71×1E1	3.93×1E-5	1.76×1E-7	-2.00×1E-8	1st	load stage
S1-8	45 – 90	1.17×1E2	1.40×1E-5	7.65×1E-8	-9.27×1E-8	2nd	load stage
S1-8	40 – 90	1.63×1E2	1.63×1E-5	1.04×1E-7	8.00×1E-9	3rd	load stage
S1-8	35 – 90	2.30×1E2	2.33×1E-5	1.50×1E-7	4.70×1E-9	4th	load stage
S1-8	30 – 90	3.10×1E2	2.32×1E-5	1.49×1E-7	6.44×1E-8	5th	load stage
S1-8	20 – 90	4.96×1E2	5.35×1E-5	3.40×1E-7	-1.71×1E-8	6th	load stage
S1-8	10 – 90	7.64×1E2	7.70×1E-5	5.52×1E-7	-7.32×1E-8	7th	load stage
S1-10	30 – 90	2.14×1E2	9.05×1E-5	4.49×1E-7	-1.22×1E-7	1st	load stage
S1-10	20 – 90	2.74×1E2	1.32×1E-5	8.36×1E-8	3.09×1E-9	2nd	load stage
S1-10	10 – 90	5.11×1E2	5.64×1E-5	3.58×1E-7	4.33×1E-8	3rd	load stage

3.2.3 Inhomogeneous characteristics of strain evolution and energy dissipation

In order to investigate whether the strain evolution and energy dissipation are inhomogeneous or not at different parts of the sample during cyclic loading, six strain gauges are used for Series 2 concrete specimens to measure the strain and cumulative dissipated energy at different sections (top, middle and bottom) of the sample. The measuring layout is illustrated in Figure 3.14 (Song et al. 2019a).
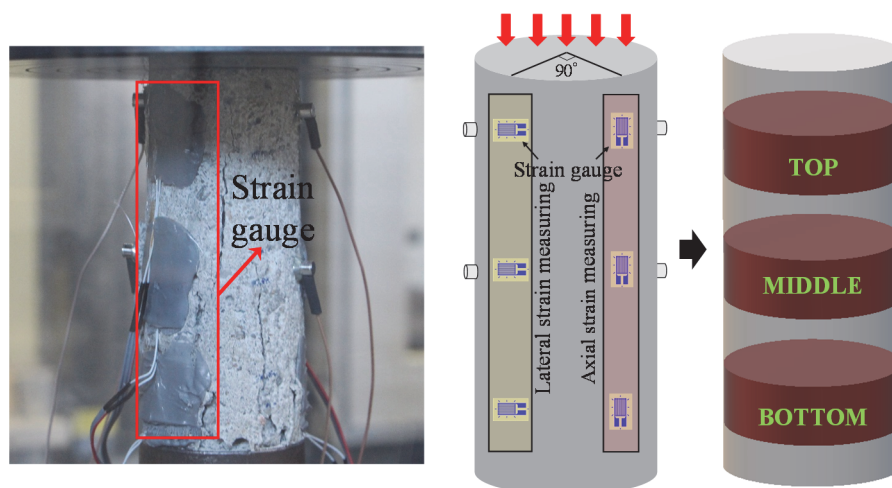
Figure 3.14 Strain measurement system for Series 2 concrete samples

As indicated in Figure 3.14, quantities were measured at 3 different locations via strain gauges: axial strain, lateral strain and dissipated energy at top (ε_{at}, ε_{lt}, U_{at}), middle (ε_{am}, ε_{lm}, U_{am}) and bottom (ε_{ab}, ε_{lb}, U_{ab}) parts of the concrete sample. The first 50 cycles are selected to analyse the evolution l.of strain and cumulative dissipated energy. The detailed growth rates of strain and energy dissipation are listed in Table 3.8 and Table 3.9, respectively.

Table 3.8 Growth rate of residual strain in each cyclic stage for Series 2

Sample No.	Load level	$d\varepsilon_{at}/dN$	$d\varepsilon_{am}/dN$	$d\varepsilon_{ab}/dN$	$d\varepsilon_{lt}/dN$	$d\varepsilon_{lm}/dN$	$d\varepsilon_{lb}/dN$	Select Cycles
Unit	[%UCS]	[mm/mm/N]	[mm/mm/N]	[mm/mm/N]	[mm/mm/N]	[mm/mm/N]	[mm/mm/N]	
S2-13	40-60	1.355E-06	5.308E-07	1.051E-06	-1.225E-06	-7.710E-08	-2.512E-07	1-50
S2-13	40-65	1.325E-06	6.690E-07	8.305E-07	-1.465E-06	-1.592E-07	-2.534E-07	1-50
S2-13	40-70	2.242E-06	1.614E-06	1.303E-06	-2.317E-06	-5.660E-07	-4.346E-07	1-50
S2-13	40-75	2.154E-06	4.931E-06	1.708E-06	-5.695E-06	-1.535E-06	-4.769E-07	1-50
S2-13	40-80	2.071E-06	5.248E-05	1.258E-05	-2.011E-05	-9.540E-06	-1.684E-06	1-50
S2-14	40-75	7.853E-07	1.636E-06	8.316E-07	-3.280E-07	-1.144E-06	-6.616E-07	1-50
S2-14	35-75	1.220E-07	2.720E-07	1.454E-07	-4.570E-08	-1.573E-07	-8.000E-08	1-50
S2-14	30-75	1.033E-07	2.266E-07	1.308E-07	-3.570E-08	-1.214E-07	-7.050E-08	1-50
S2-14	25-75	8.340E-08	2.072E-07	1.185E-07	-3.610E-08	-1.152E-07	-7.410E-08	1-50
S2-14	20-75	2.365E-07	3.999E-07	2.696E-07	-7.260E-08	-1.801E-07	-1.343E-07	1-50
S2-14	15-75	1.827E-07	3.486E-07	2.250E-07	-5.830E-08	-1.731E-07	-1.703E-07	1-50
S2-14	10-75	6.550E-08	1.901E-07	1.044E-07	-3.970E-08	-1.565E-07	-1.837E-07	1-50
S2-14	5-75	1.945E-07	3.890E-07	2.380E-07	-7.490E-08	-2.474E-07	-2.397E-07	1-50
S2-14	5-80	4.278E-07	1.043E-06	5.120E-07	-1.919E-07	-1.108E-06	-9.660E-07	1-50
S2-14	5-85	7.845E-07	2.251E-06	1.031E-06	-3.017E-07	-3.302E-06	-2.102E-06	1-50
S2-14	5-90	1.318E-06	5.555E-06	2.914E-06	-2.308E-07	-1.337E-05	-5.712E-06	1-50

Table 3.9 Growth rate of cumulative dissipated energy in each cyclic stage for Series 2

Sample No.	Load level	U_{at}/N	U_{am}/N	U_{ab}/N	Select Cycles
Unit	[%UCS]	[J/m³/N]	[J/m³/N]	[J/m³/N]	
S2-13	40-60	53.60	35.49	49.63	1-50
S2-13	40-65	399.99	335.32	383.53	1-50
S2-13	40-70	993.92	866.02	953.72	1-50
S2-13	40-75	1739.50	1568.63	1634.90	1-50
S2-13	40-80	2390.83	2865.91	2327.44	1-50
S2-14	40-75	105.81	171.15	117.82	1-50
S2-14	35-75	120.95	180.67	128.86	1-50
S2-14	30-75	211.99	315.05	230.72	1-50
S2-14	25-75	277.47	413.42	301.72	1-50
S2-14	20-75	330.54	501.86	362.40	1-50
S2-14	15-75	534.92	787.21	573.48	1-50
S2-14	10-75	1113.75	1562.25	1163.32	1-50
S2-14	5-75	1425.06	2031.84	1499.80	1-50
S2-14	5-80	1924.43	2766.17	2045.21	1-50
S2-14	5-85	2621.25	3883.99	2860.96	1-50
S2-14	5-90	3729.47	5891.42	4432.76	1-50

3.2.3.1 Effect of maximum load level on strain and energy dissipation
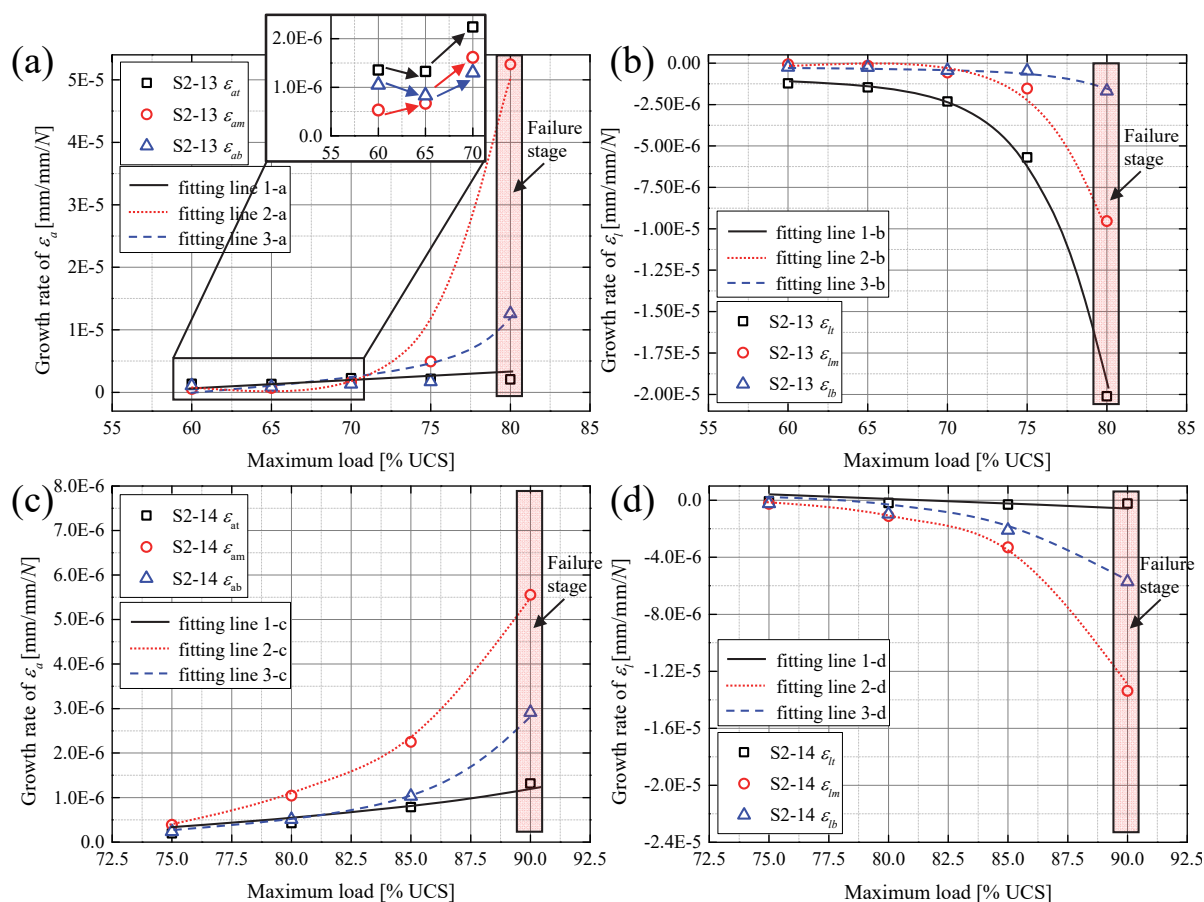
Figure 3.15 (a) relation between σ_{max} and growth rate of ε_a for S2-13 (b) relation between σ_{max} and growth rate of ε_l for S2-13 (c) relation between σ_{max} and growth rate of ε_a for S2-14 (d) relation between σ_{max} and growth rate of ε_l for S2-14

According to Table 3.2, sample S2-13 experienced consecutive multi-loading stages with gradual increasing σ_{max} at fixed σ_{min}. The quantitative relation between growth rate of residual strain and σ_{max} for sample S2-13 is illustrated in Figure 3.15a and Figure 3.15b. The growth rate of strain and σ_{max} follows an exponential function as shown by Equation 3.3. The fitting parameters according to Figure 3.15a and Figure 3.15b are listed in Table 3.10. An exponential function can well describe the relation between growth rate of residual strain and σ_{max}. For S2-13 an initial decrease is observed for ε_{at} and ε_{ab} from the first to the second loading stage (see black square and blue triangle symbols in Figure 3.15a). However, ε_{am} does not show such a characteristic. This demonstrates that top and bottom parts of the sample exhibit a larger growth rate of axial strain in the first loading stage, where σ_{max} is smaller than in the second loading stage. This observation can be explained by the stiffness platen effect. Due to the stiffness difference between the loading platen and the specimen, the top and bottom parts first show obvious plasticity and softening and large axial strain rate can be observed. The middle part of

the concrete sample is not affected by platen effect and the growth rate of axial strain increases with σ_{max} during the first two loading stages. The platen effect may induce some initial damage in the top and bottom parts of the sample in the first loading stage. With gradual increase of σ_{max}, the axial strain rate in the middle part (see red round symbols in Figure 3.15a) rises to an obvious larger value than ε_{at} and ε_{ab}. The smaller confinement at the middle part of the concrete sample may lead to this behaviour, the friction induced by the interface between sample and loading platen restricts the deformation. The lateral strain rate also increases with σ_{max}, however, the initial drop shown in Figure 3.15a is not observed. This indicates that a weakening effect in the early loading stage is not pronounced in lateral direction. This may be caused by the lateral strengthening effect of specimen end sections due to the stiffness contrast between loading platens (steel) and specimen (concrete). Sample S2-14 experienced two loading strategies: (1) σ_{max} is fixed and σ_{min} gradually decreases; (2) σ_{min} is fixed and σ_{max} gradually increases. Figure 3.15c and Figure 3.15d illustrate the relation between strain rate and σ_{max} for samples S2-14 for the second loading strategy. The fitting parameters according to Figure 3.15c and Figure 3.15d are given in Table 3.10. The growth rates of ε_{am} and ε_{lm} are apparently larger than the corresponding value in the top and bottom parts when close to peak strength. It can be concluded from Figure 3.15 that an exponential function can well describe the relation between σ_{max} and growth rate of strain in both, single loading strategies (S2-13) and multi-loading strategies (S2-14). The strain rate evolution is not homogenous in the different parts of the sample during the cyclic loading. The difference in strain growth rate between the middle and top/bottom parts obviously increases close to peak strength. Therefore, the sudden rise of axial/lateral strain rate observed at the middle part of the sample may serve as damage precursor for concrete under cyclic loading.

Table 3.10 Fitting parameters (see Figure 3.15)

Fitting lines	Variable	Sample	a	b	R^2	Range of σ_{max}	Frequency
Fit line 1-a	ε_{at}	S2-13	3E-7	0.0267	0.6499	60% UCS – 80% UCS	0.5
Fit line 2-a	ε_{am}	S2-13	4E-13	0.2237	0.8921	60% UCS – 80% UCS	0.5
Fit line 3-a	ε_{ab}	S2-13	7E-10	0.1137	0.6789	60% UCS – 80% UCS	0.5
Fit line 1-b	ε_{lt}	S2-13	-2E-10	0.1391	0.9086	60% UCS – 80% UCS	0.5
Fit line 2-b	ε_{lm}	S2-13	-4E-14	0.2381	0.9774	60% UCS – 80% UCS	0.5
Fit line 3-b	ε_{lb}	S2-13	-9E-10	0.0888	0.8175	60% UCS – 80% UCS	0.5
Fit line 1-c	ε_{at}	S2-14	2E-11	0.1269	0.9909	75% UCS – 90% UCS	0.5
Fit line 2-c	ε_{am}	S2-14	8E-13	0.1749	0.9979	75% UCS – 90% UCS	0.5
Fit line 3-c	ε_{ab}	S2-14	1E-12	0.1643	0.9921	75% UCS – 90% UCS	0.5
Fit line 1-d	ε_{lt}	S2-14	-3E-10	0.0766	0.6658	75% UCS – 90% UCS	0.5
Fit line 2-d	ε_{lm}	S2-14	-8E-16	0.2612	0.9967	75% UCS – 90% UCS	0.5
Fit line 3-d	ε_{lb}	S2-14	-5E-14	0.2058	0.9862	75% UCS – 90% UCS	0.5
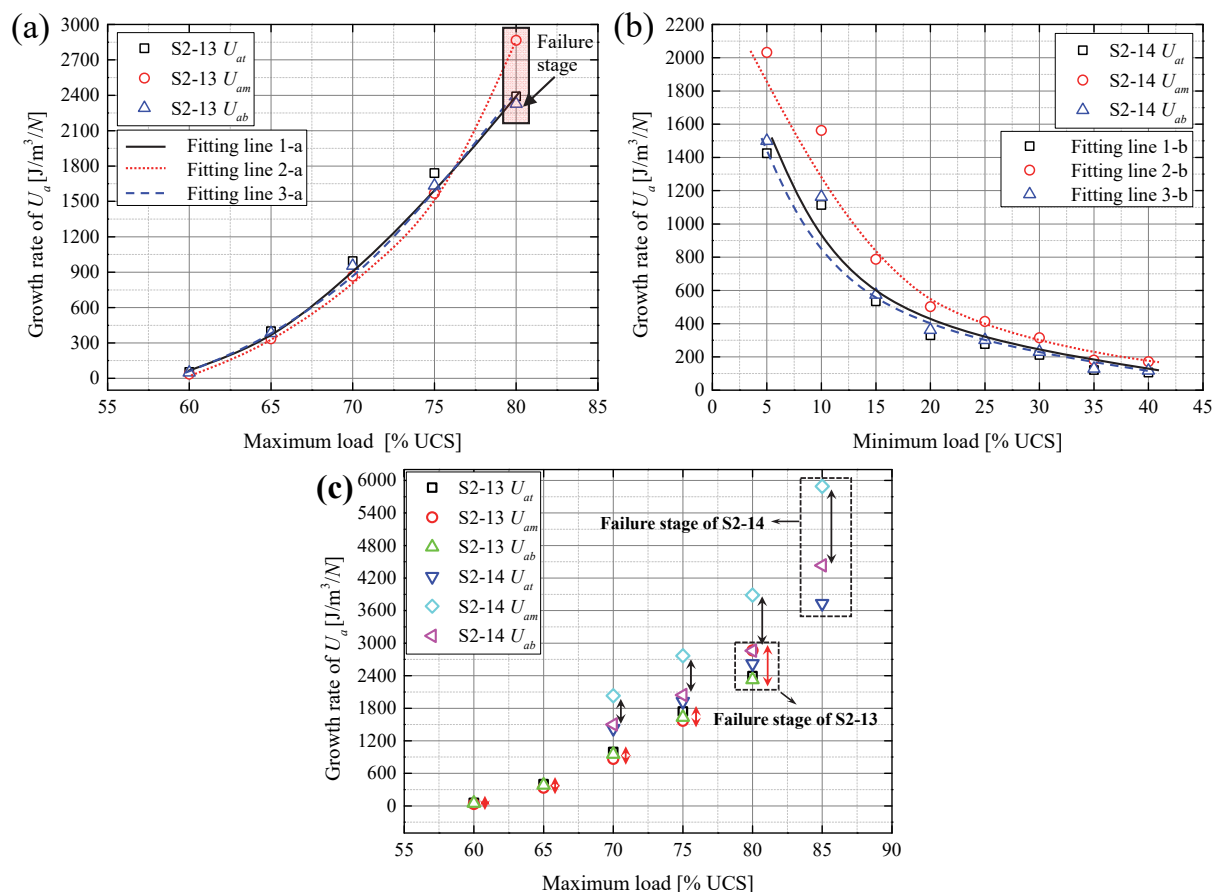
Figure 3.16 (a) relation between σ_{max} and growth rate of cumulative dissipated energy for S2-13 (b) relation between σ_{min} and growth rate of cumulative dissipated energy for S2-14 (c) inhomogeneous characteristic of energy dissipation for S2-13 and S2-14

The effect of σ_{max} on energy dissipation is plotted in Figure 3.16a. With increase of σ_{max}, growth rate of U_a increases in an exponential manner as shown by Equation 3.3. The detailed fitting parameters are listed in Table 3.11. As documented by the data of sample S2-13, the growth rate of U_a in different parts of one sample are almost the same in the first several loading stages. With the increase of σ_{max}, the growth rate of U_a in the middle part of the sample (U_{am}) grows obviously faster than in the top (U_{at}) and bottom parts (U_{ab}). The disparity between the growth rates of U_{am} and U_{at}, U_{ab} for sample S2-13 reaches the peak at ultimate strength. This indicates that with an increase of σ_{max}, the inhomogeneity of energy dissipation becomes more obvious: in the middle part of the specimen the energy dissipation is larger than in the top and bottom parts. This is consistent with the strain evolution as discussed in former sections. The inhomogeneous energy dissipation is documented in Figure 3.16c. The data in Figure 3.16c are based on sample S2-13 and the second loading stage of sample S2-14. Both samples experienced a gradual increase in σ_{max} while σ_{min} is fixed during these stages. It becomes obvious that for both samples the disparity between growth rate of U_{am} and U_{at}, U_{ab} increases

with σ_{max}. The disparity at failure is significantly large. Therefore, it can be concluded that the energy dissipation of concrete subjected to cyclic loading is inhomogeneous, and the middle parts have larger energy dissipation close to peak strength.

Table 3.11 Fitting parameters (see Figure 3.16)

Fitting lines	Variable	Sample	a	b	R^2	Range of σ_{max}	Frequency
Fitting line 1-a	U_{at}	S2-13	0.0019	0.1813	0.8843	60% UCS - 80% UCS	0.5
Fitting line 2-a	U_{am}	S2-13	0.0003	0.2065	0.9048	60% UCS - 80% UCS	0.5
Fitting line 3-a	U_{ab}	S2-13	0.0016	0.1829	0.8836	60% UCS - 80% UCS	0.5
Fitting lines	Variable	Sample	a	b	R^2	Range of σ_{min}	Frequency
Fitting line 1-b	U_{at}	S2-14	-682.1	2571.0	0.9523	40% UCS - 5% UCS	0.5
Fitting line 2-b	U_{am}	S2-14	-959.8	3562.6	0.9589	40% UCS - 5% UCS	0.5
Fitting line 3-b	U_{ab}	S2-14	-731.2	2640.5	0.9565	40% UCS - 5% UCS	0.5

3.2.3.2 Effect of minimum load level on energy dissipation

The effect of σ_{min} on energy dissipation is shown in Figure 3.16b. The relation between σ_{min} and growth rate of U_a is obvious and can be described by a logarithmic equation (Equation 3.4). The corresponding fitting parameters according to Figure 3.16b are presented in Table 3.11. The inhomogeneity of energy dissipation can be seen in Figure 3.16b: with decrease of σ_{min} the growth rate of U_{am} is significantly larger than U_{at} and U_{ab}. This demonstrates that an inhomogeneous energy dissipation is a general feature during uniaxial cyclic loading tests.

Both, σ_{max} and σ_{min} have a pronounced effect on energy dissipation. Whether the effect of both are equivalent or not is not yet known. Figure 3.17 illustrates and compares the effect of σ_{max} and σ_{min} on the energy dissipation. According to Table 3.2, samples S1-8, S-10 and S2-14 experienced two loading strategies: (1) fixed σ_{max} and gradual reduction of σ_{min}; (2) fixed σ_{min} and gradual increase of σ_{max}. As $\Delta\sigma = \sigma_{max} - \sigma_{min}$ consistently increases during the two loading strategies, this measure is selected to investigate which loading effect (increase of σ_{max} or decrease of σ_{min}) has a more pronounced effect on energy dissipation. The effect of σ_{min} on energy dissipation is obtained from the first loading strategy (see black square symbols in Figure 3.17). The effect of σ_{max} on energy dissipation is obtained from the second loading strategy (see red round symbols in Figure 3.17). It can be observed (see Figure 3.17), that for all three samples the fitting lines for strategy 2 are steeper than those for strategy 1. A kink in growth rate evolution is observed in all cases when switching from strategy 1 to strategy 2. There always exists an angle (see hatched area) between fitting lines 1 and 2. Thus - in terms of energy dissipation: σ_{max} has a more pronounced effect than σ_{min}.
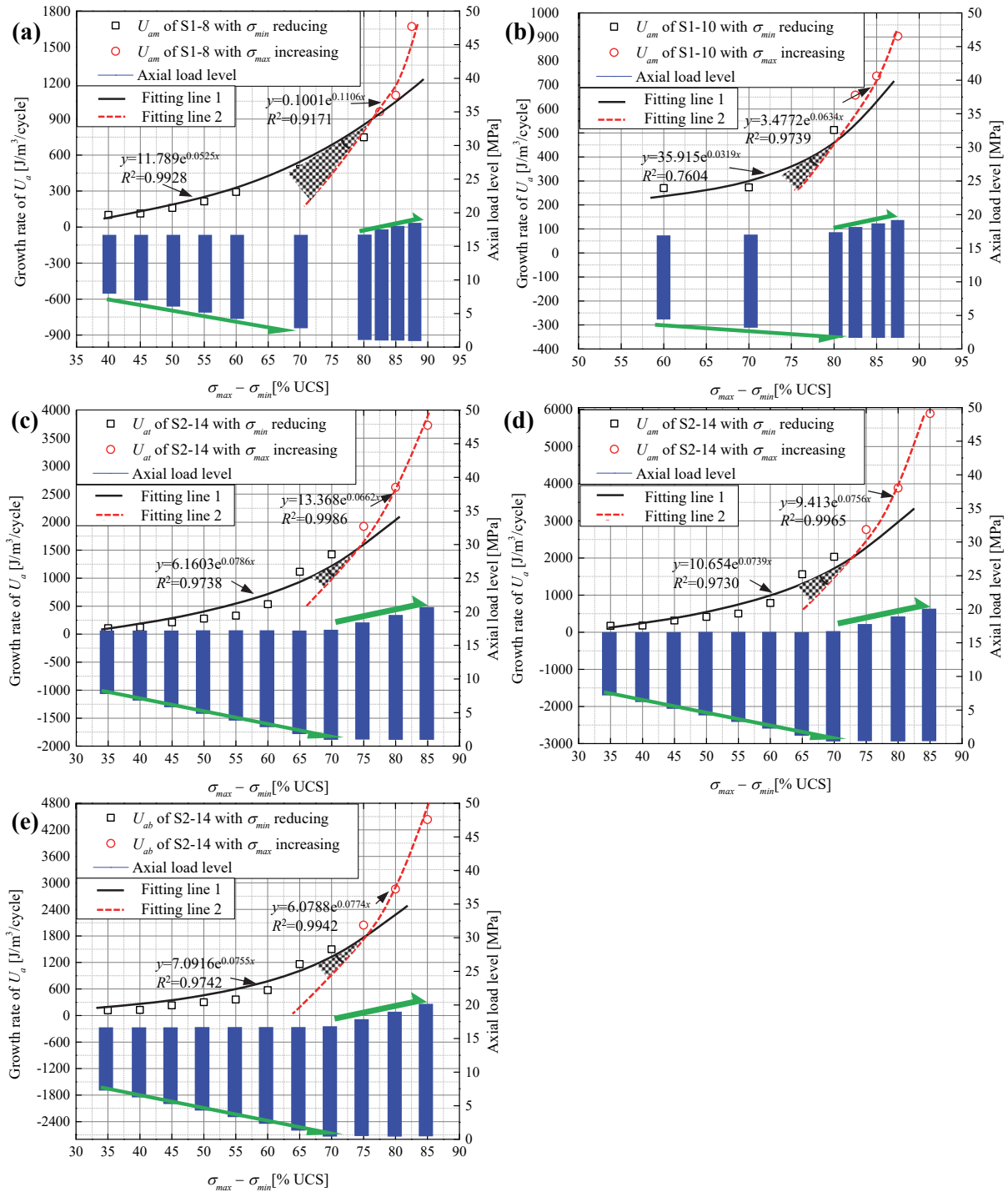
Figure 3.17 (a) growth rate of U_{am} for S1-8 (b) growth rate of U_{am} for S1-10 (c) growth rate of U_{at} for S2-14 (d) growth rate of U_{am} for S2-14 (e) growth rate of U_{ab} for S2-14

3.3 P-wave speed evolution and AE characteristics

3.3.1 P-wave speed evolution

The monitoring of P-wave speed is a practical approach to characterize the damage of a sample during an experiment. In order to draw general conclusions of P-wave speed evolution during fatigue loading, four cyclically-loaded samples of Series 1 and Series 2 (S2-13, S2-14, S1-10, S1-8) are selected for detailed analysis, see Figure 3.18. The measurements of P-wave speed are conducted along two different profiles, which represent the damage evolution at the top and middle part of the concrete samples, see Figure 3.4. Sample S2-13 undergoes the following loading strategy: σ_{min} is fixed to 40% UCS and σ_{max} is gradually increased from 60% UCS to 80% UCS. However, samples S2-14, S1-10 and S1-8 experience a different loading strategy: first σ_{max} is fixed and σ_{min} is reduced, then σ_{min} is fixed and σ_{max} is gradually increased.

It can be observed from Figure 3.18a that the evolution of P-wave speed for sample S2-13 shows three distinct phases, whereas the other three samples show four phases (Figure 3.18b - Figure 3.18d). This is due to the fact that sample S2-13 does not experience the loading stage where σ_{min} decreases and σ_{max} is fixed. In respect to the P-wave-speed the four stages are characterized by:

(1) Initial strong drop

(2) Constant phase

(3) Decreasing phase

(4) Sharp decline and failure

The four-stage feature is visible for formerly tested samples S1-8 and S1-10 as well as S2-14. The effect of σ_{min} on the P-wave speed evolution can be deduced from the second stage. It is obvious that the P-wave speed for both profiles remains almost constant even when σ_{min} reduces by a large amount (for S1-8: from 50% to 10% UCS and for S2-14 from 40% to 5% UCS), whereas σ_{max} is fixed. This indicates that σ_{min} has very limited (insignificant) impact on P-wave speed evolution during cyclic loading. The missing of the second stage for sample S2-13 also indirectly confirms this observation. By increasing σ_{max} of S1-8, S1-10 and S2-14 the third stage with its typical decrease of P-wave speed is started. Considering both measuring profiles, all the four samples experience a more noticeable damage at the top part during the first stage. This can be attributed to the stiffness effect of loading platen and direct, dynamic loading by

51

the moving upper loading platen. The stiffness contrast between the platen and top part of the sample will result in local crack propagation. This effect is consistent with the "initial drop" documented in Figure 3.15a. When the samples are close to failure - typically at the end of the third stage or at the begin of the fourth stage, the P-wave speed in the middle part decreases more pronounced than in the top part and the P-wave speed of the two profiles reach an approximately identical value which is defined as "equal point" in Figure 3.18. The equal point as shown in Figure 3.18 is a precursor to predict the fatigue failure of concrete.

To characterize the evolution of the P-wave speed along the two profiles, a P-wave ratio is defined as: V_m/V_t, where V_m is the P-wave speed measured at the middle part of the sample and V_t is the P-wave speed measured at the top part of the sample. The evolution of P-wave ratio for samples S2-13, S2-14, S1-10 and S1-8 is illustrated in Figure 3.19. The P-wave ratio of the four concrete samples reveal three stages:

(1) Slow increase

(2) Obvious increase reaching peak point at the end

(3) Sharp decline and failure

The P-wave ratio is small (usually only slightly larger than 1) in the first stage. This is induced by the more pronounced reduction of the P-wave speed in the top part of the sample. During this stage, the top profile shows a slightly larger P-wave speed reduction than the middle profile and this leads to the slight increase of the P-wave ratio. The first stage covers both two kinds of loading strategies: (1) fixed σ_{max} and gradual reduction of σ_{min}; (2) fixed σ_{min} and gradual increase of σ_{max}. The second stage includes the peak value of the P-wave ratio. The P-wave speed reduction rate of the two profiles are equal at the peak point. After the peak point, the reducing speed of the middle part is larger than that of the top part leading to a decrease of P-wave ratio. Failure of the sample usually happens shortly after the peak point. The value of the P-wave ratio at failure is close to 0.3 (the value for sample S2-13 is larger, maybe induced by applying loading strategy number one). Compared with the P-wave speed, the P-wave ratio is more general applicable. The peak point as shown in Figure 3.19 is more convenient to be used as failure precursor than the equal point in Figure 3.18.
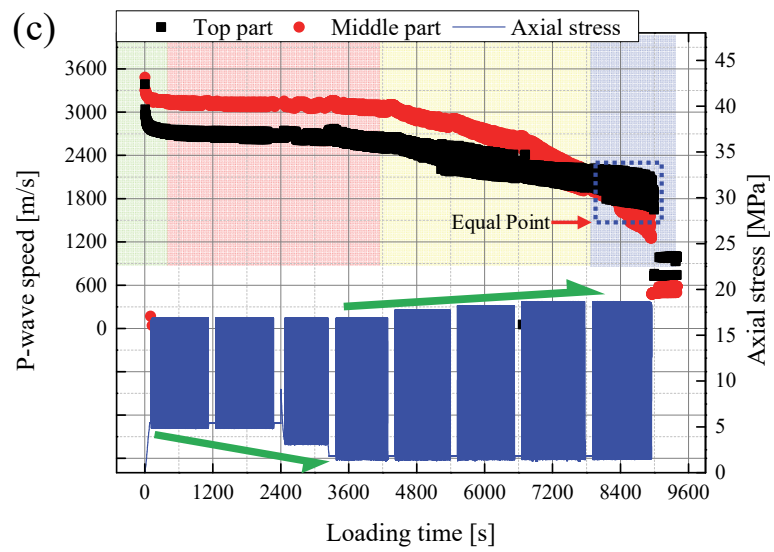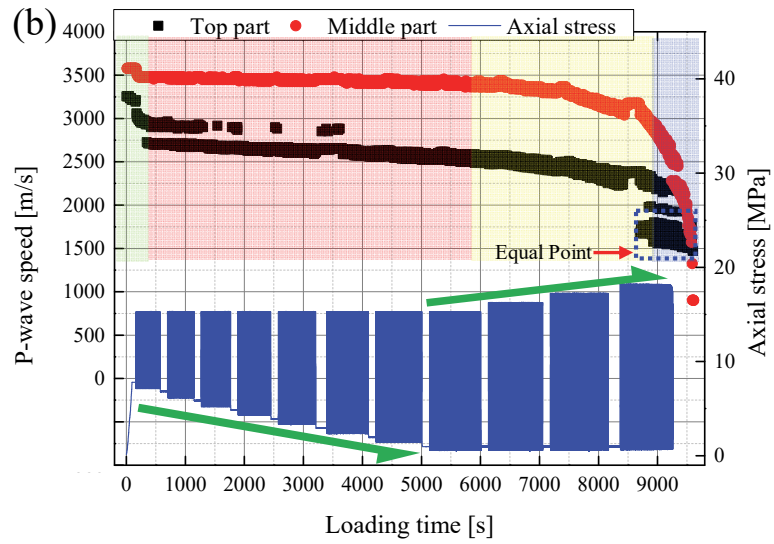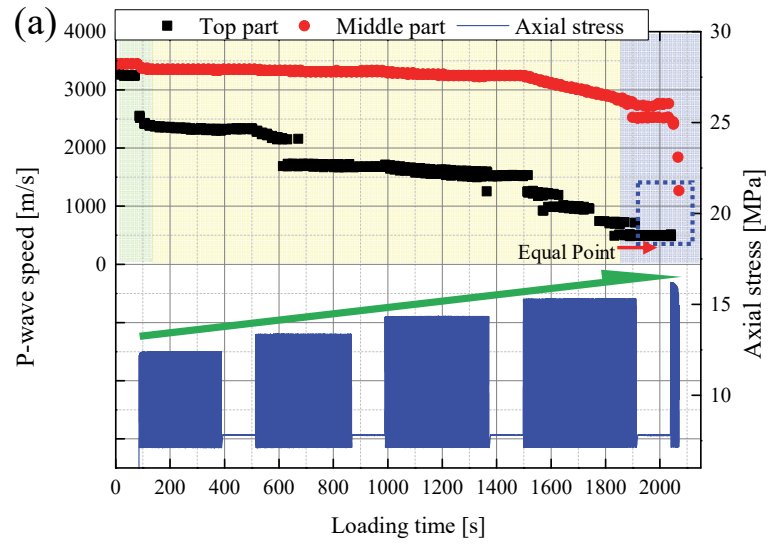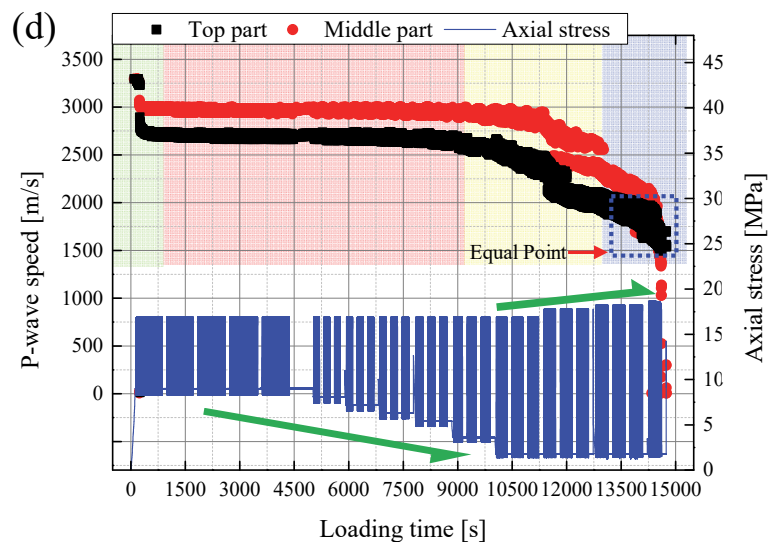
Figure 3.18 P-wave speed evolution for (a) S2-13 (b) S2-14 (c) S1-10 (d) S1-8
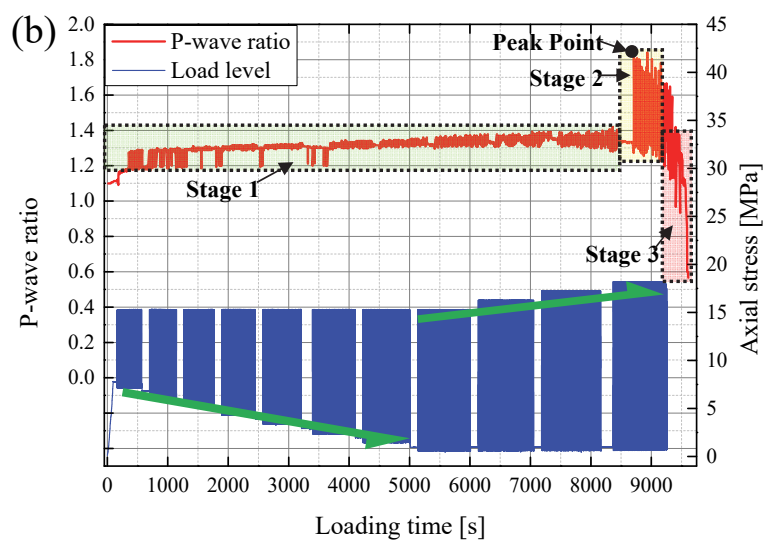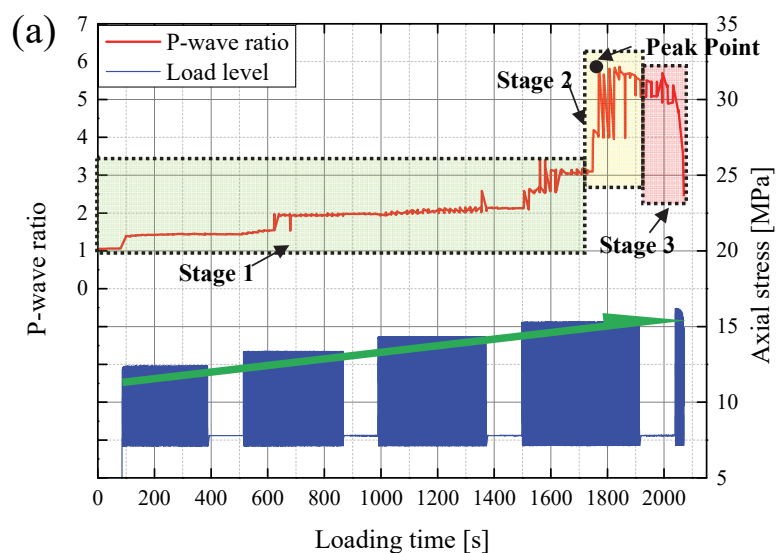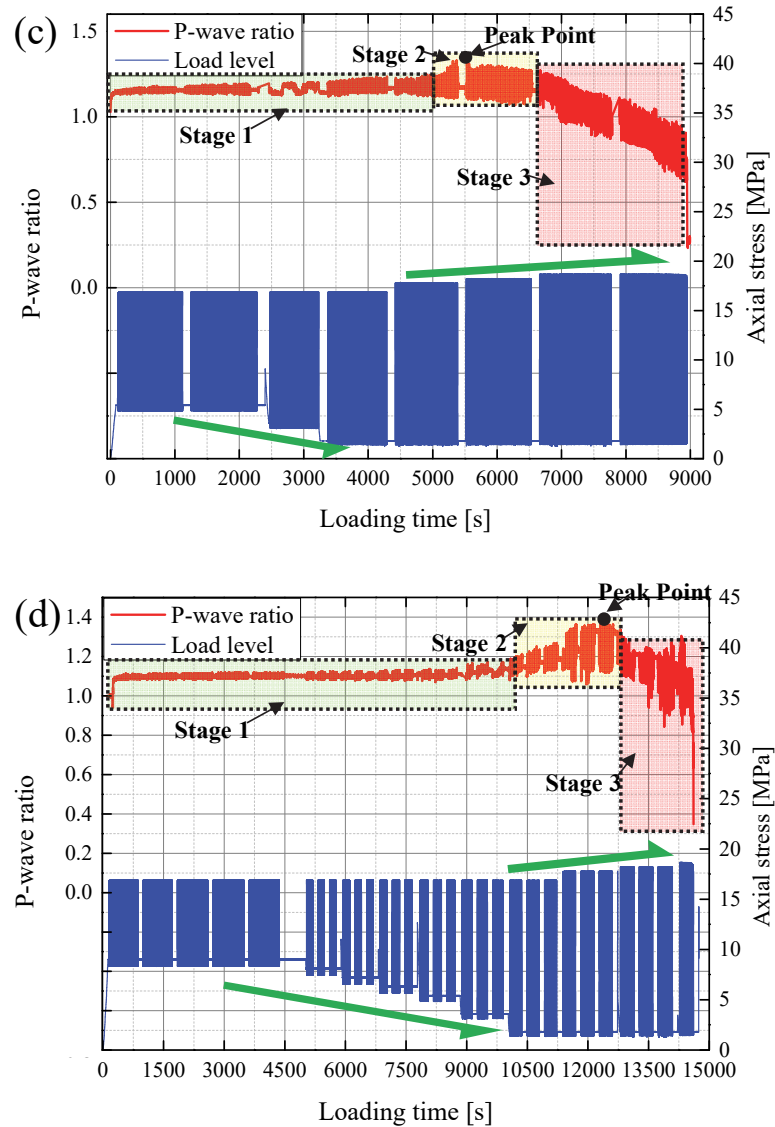
Figure 3.19 P-wave ratio evolution for (a) S2-13 (b) S2-14 (c) S1-10 (d) S1-8

3.3.2 AE characteristics

The AE events are analysed in terms of cumulative AE counts and AE energy. Figure 3.20 and Figure 3.21 illustrate that the four-stage characteristic also fits to describe the evolution of cumulative AE counts and energy when the samples experienced two loading strategies.

(1) Short initial phase with strong non-linear increase in AE activity

(2) Phase with moderate, nearly linear increase in AE activity

(3) Phase of significant accelerating of AE activity

(4) Failure

The effect of σ_{min} on AE counts and energy is also minimal, similar to the effect on P-wave speed. Due to the fact that sample S2-13 has experienced only one loading strategy (σ_{min} is fixed and σ_{max} is gradually increased), the rate of AE counts and energy is gradually rising and stage 2 is missing. The increasing rate in stage 3 for sample S2-13 is larger than for the other three samples, which indicates that the decrease of σ_{min} in former loading stages may be beneficial to reduce the increasing rate of AE counts and energy. This can also be interpreted as follows: stage 2 is acting as a "cushion" role before stage 3, so the increasing rate in stage 3 is smaller compared with the stage 3 without experiencing stage 2 before.
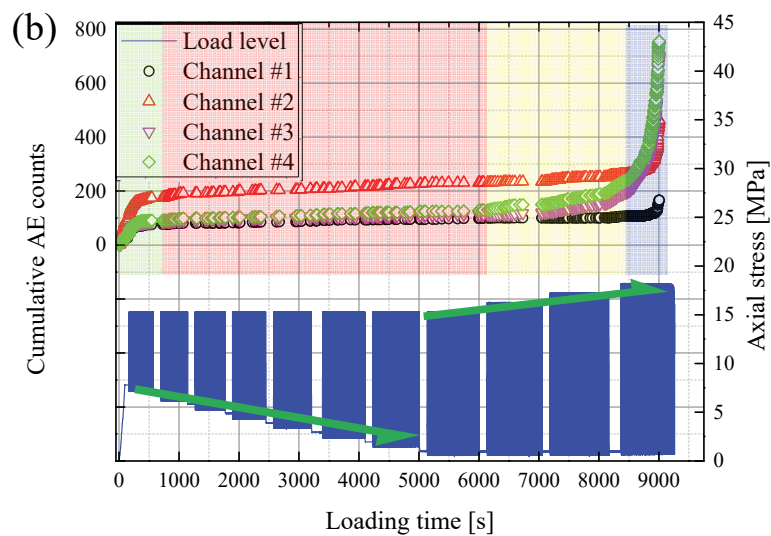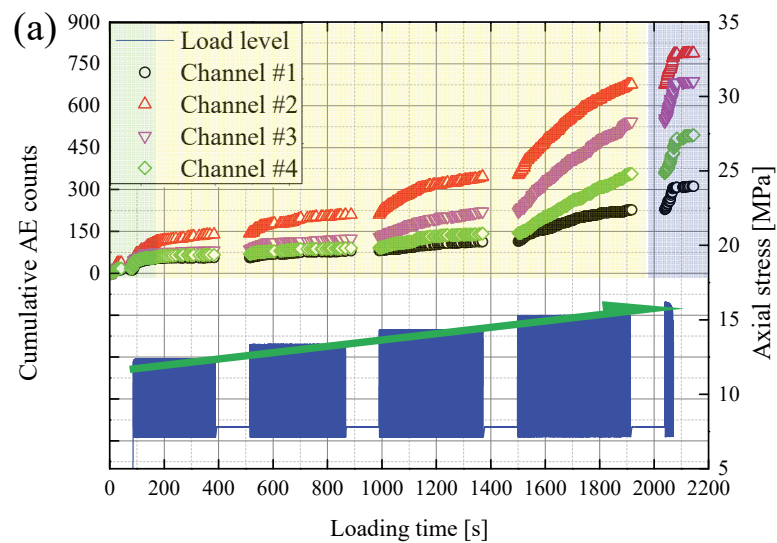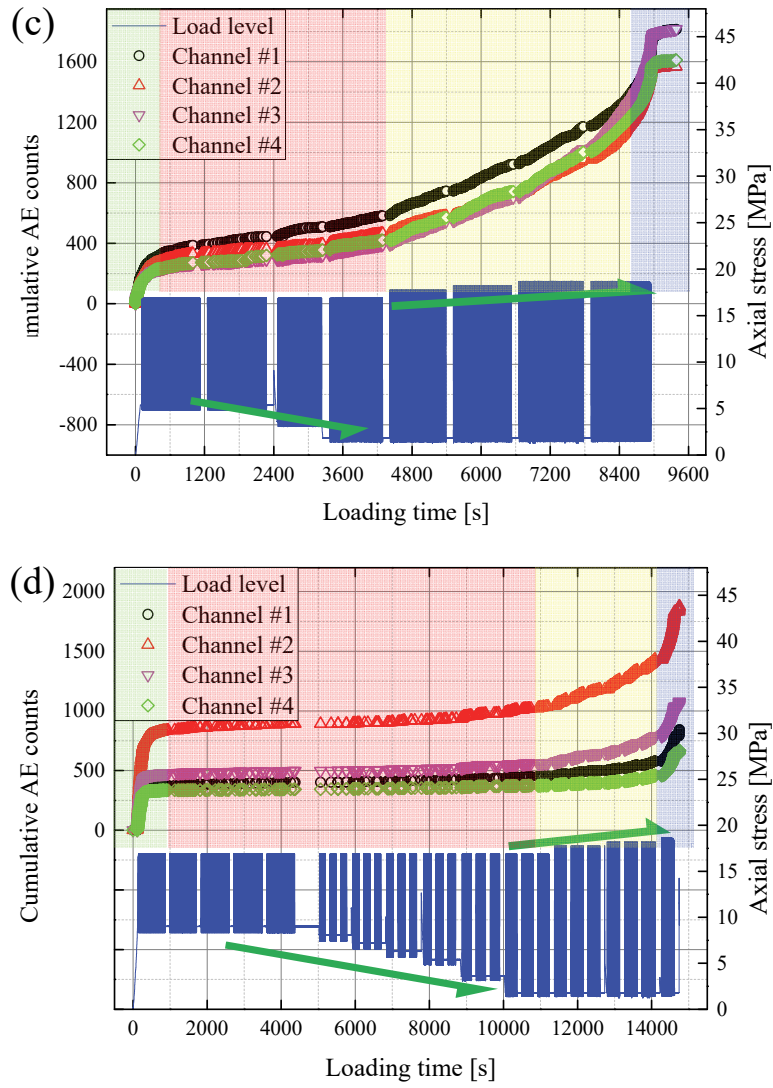
Figure 3.20 Cumulative AE counts for (a) S2-13 (b) S2-14 (c) S1-10 (d) S1-8
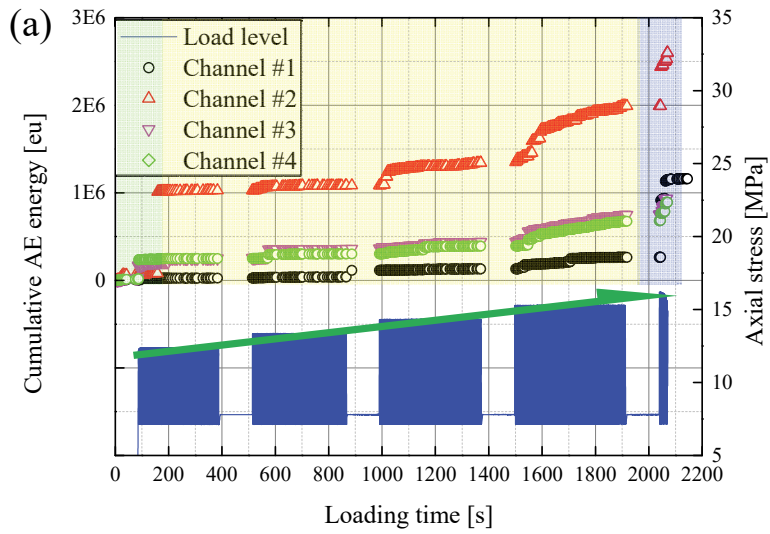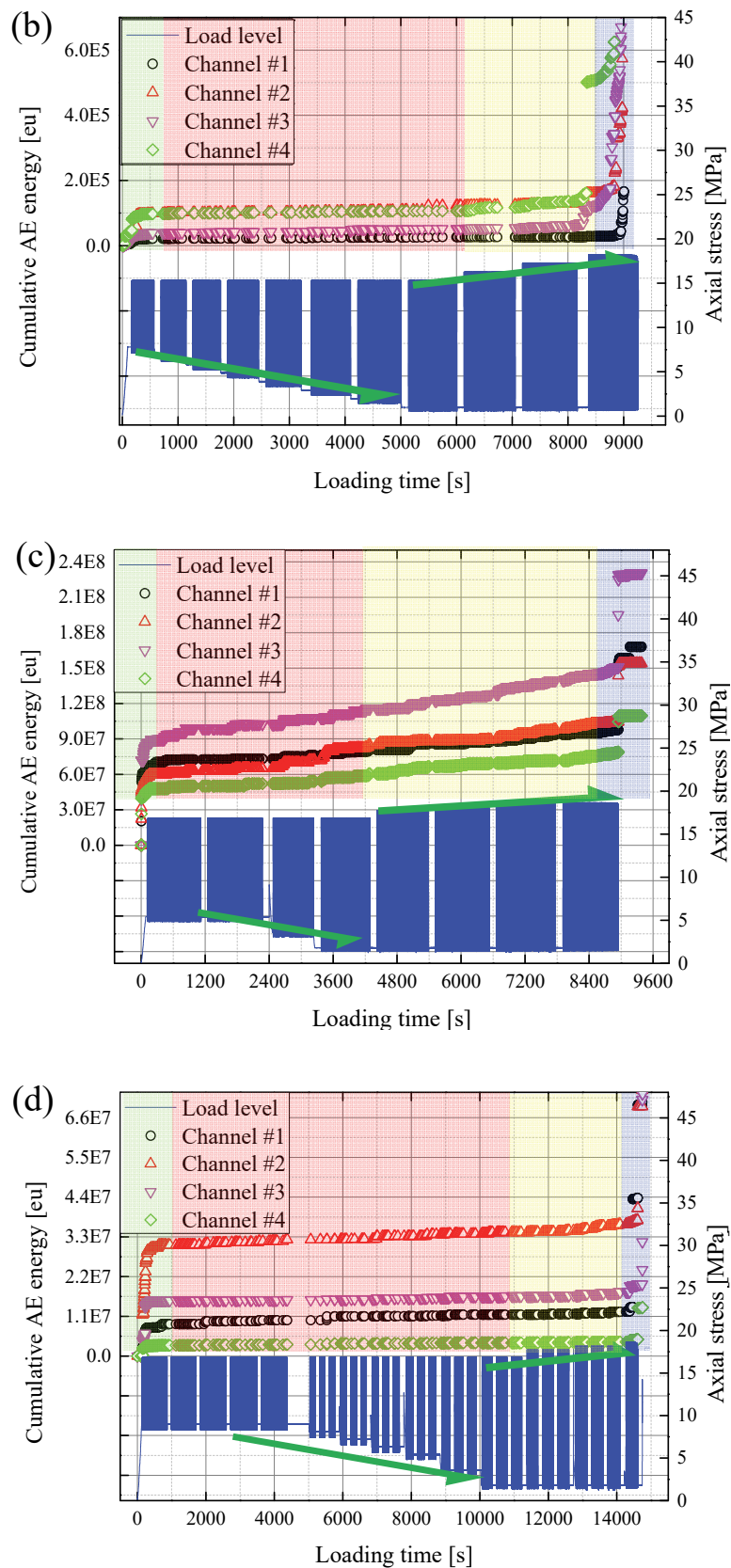
Figure 3.21 Cumulative AE energy for (a) S2-13 (b) S2-14 (c) S1-10 (d) S1-8

3.4 Hysteresis and dynamic response during fatigue loading

The hysteresis is a typical non-linear physical phenomenon, which refers to a dynamic lag between an input and an output variable (Mayergoyz 2003). Some early scientific work about hysteresis in mechanical systems was performed by Maxwell (1865). The hysteresis is often associated with irreversible thermo-dynamic change and microscopic internal damage (Love 1906). The dissipated energy calculated by the energy method is also related to hysteresis. The amount of the dissipated energy during a cycle is defined as the area encircled by a hysteresis loop. During cyclic loading, hysteresis is a common phenomenon. Vasseva (1993) conducted a nonlinear hysteresis analysis for concrete frames under seismic excitation and found that the ratio of hysteresis energy and input energy is a significant safety index. Dowell et al. (1998) proposed a hysteresis model which can reproduce the nonlinear behaviour of concrete in terms of a force-displacement relation and provided meaningful suggestions for bridge design. Sengupta and Li (2014) proposed a hysteresis model for concrete walls and reproduced observed structural degradation. Zhang et al. (2017) found that the deformation of a concrete dam lags behind the air temperature variation and showed that temperature of air and water flow can influence the hysteresis time. Chen et al. (2017) investigated the hysteresis phenomenon of concrete subjected to uniaxial tensile loading by using the Preisach-Mayergoyz (P-M) model. So far the relation between the internal damage of concrete and hysteresis is not quite clear in a quantitative manner. The so-called dynamic response ratio (DRR) and especially the loading/unloading response ratio (LURR) is often associated with cyclic loading and vibration. The dynamic response ratio is used as an important and effective precursor for prediction of failure of geo-materials during earthquakes (Yin et al. 2004, 2008; Feng et al. 2008; Zhang and Zhuang 2011). The analysis of dynamic response on concrete material subjected to multi-level cyclic loading is not common.

Within this section the hysteresis and dynamic response characteristics of concrete subjected to multi-level cyclic loading is analysed. The relation between cyclic load levels and hysteresis time and DRR is discussed.

Usually, stress and strain in cyclic loading tests are normalized for convenient evaluation (value range from 0 - 1). The typical hysteresis phenomenon during the fatigue loading is illustrated in Figure 3.22a. The hysteresis time (t) of phase shift between axial stress (σ), axial strain (ε_a) and lateral strain (ε_l) can be quantified as hysteresis degree. As shown in Figure 3.22b, DRR is defined as the ratio of unloading slope ($\tan \alpha_2$, $\tan \beta_2$) to loading slope ($\tan \alpha_1$, $\tan \beta_1$) in respect

to strain versus time. In this section, σ, ε_c, ε_t, ε_l are used as variables to analyse the hysteresis time and the DRR. σ is the uniaxial stress, ε_c is the axial strain measured by LVDT located at the central part of the sample with measuring range of 50 mm, ε_t is the axial strain measured at top loading plate, ε_l is the lateral strain measured by the chain-strain gauge at the middle of the sample.
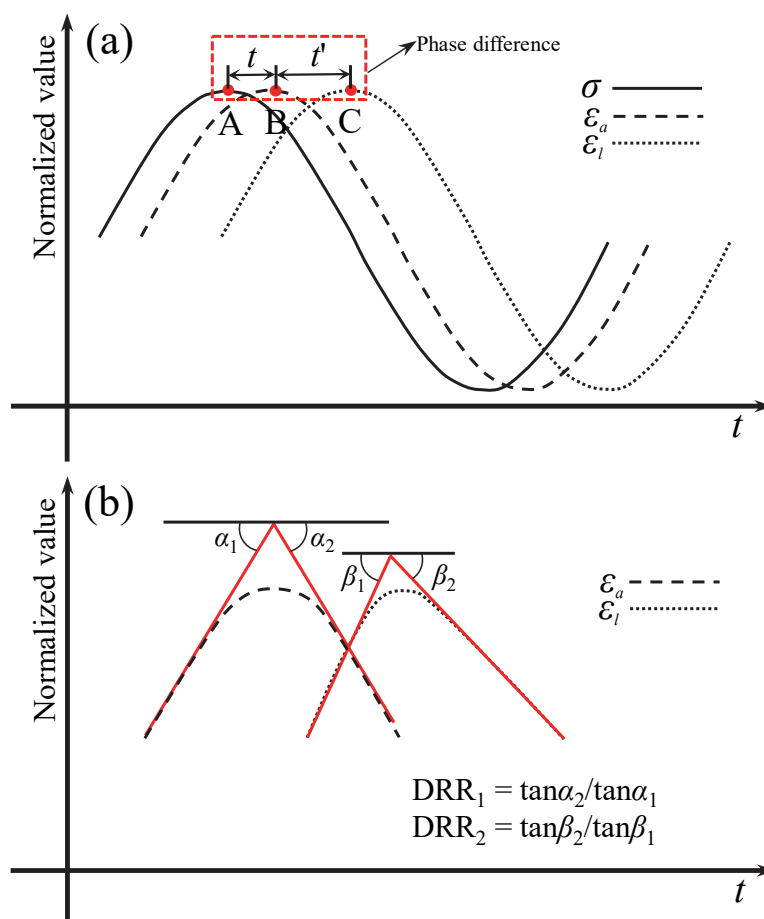
Figure 3.22 (a) hysteresis during fatigue loading (b) definition of DRR

3.4.1 Hysteresis and DRR characteristics of specimens failed within only one loading stage

Specimens S1-6 and S1-7 failed within one fatigue loading stage. The number of cycles (N) up to failure for S1-6 and S1-7 are 11 and 34, respectively. In order to more comprehensively reflect the evolution of hysteresis and dynamic response, four cycles with almost the same intervals (for S1-6: 1st, 4th, 7th and 11st cycle, for S1-7: 1st, 11st, 22nd and 34th cycle) during the loading process are selected for analysis. Figure 3.23 illustrates the normalized stresses and strains versus loading time for different cycles. It is obvious in all eight figures, that ε_l always lags behind σ, ε_c and ε_t. The detailed quantitative relations are shown in Figure 3.24. The hysteresis time (time lagged behind σ) of ε_c, ε_t and ε_l nonlinearly increases with N. It indicates

that for those specimens which failed in one loading stage, the hysteresis of axial and lateral strain are more pronounced with increasing number of cycles. Close to the failure cycle, the hysteresis time is strongly increasing. This is similar to the trend of axial strain and accumulated dissipated energy of concrete subjected to fatigue loading (Lei et al. 2017; Song et al. 2018a). For both, S1-6 and S1-7, the hysteresis time of ε_l is always larger than that of ε_c and ε_t. This demonstrates that the lateral deformation has a more obvious hysteresis than deformation along the axial direction (loading direction). The hysteresis time of ε_c is a little bit larger than that of ε_t. It can be concluded that closer to the loading platen the hysteresis is less pronounced. The disparity between ε_l and ε_c, ε_t for S1-6 is smaller than that for S1-7. This is possibly due to the reduction of maximum load level (95% UCS of S1-7 reduces to 90% UCS of S1-6). The trend of DRR versus N is a little bit more complex. As plotted in Figure 3.24c and Figure 3.24d, DRR of S1-6 and S1-7 first experiences an increase, the peak value is reached at half of the total number of cycles and the value of DRR is close to 1.1. Then, DRR drops to a certain value (for ε_l close to 0 and for ε_c, ε_t close to 0.3) at failure. Contrary to the trend of hysteresis time shown in Figure 3.24a and Figure 3.24b, DRR of ε_l is smaller than that of ε_c and ε_t. DRR of ε_t is bigger than those of ε_l and ε_c. Similar to hysteresis time, the disparity between ε_l, ε_c and ε_t decreases with reduction of maximum load level. It can be concluded that DRR is inversely proportional to the hysteresis time. Specimens with less hysteresis time have a larger value of DRR.
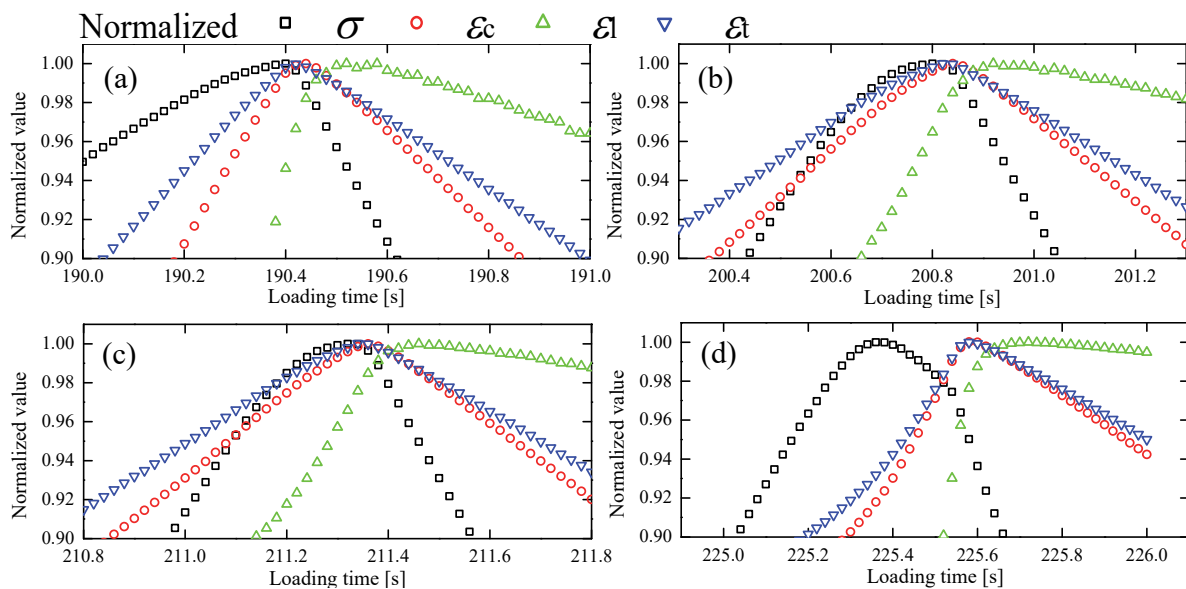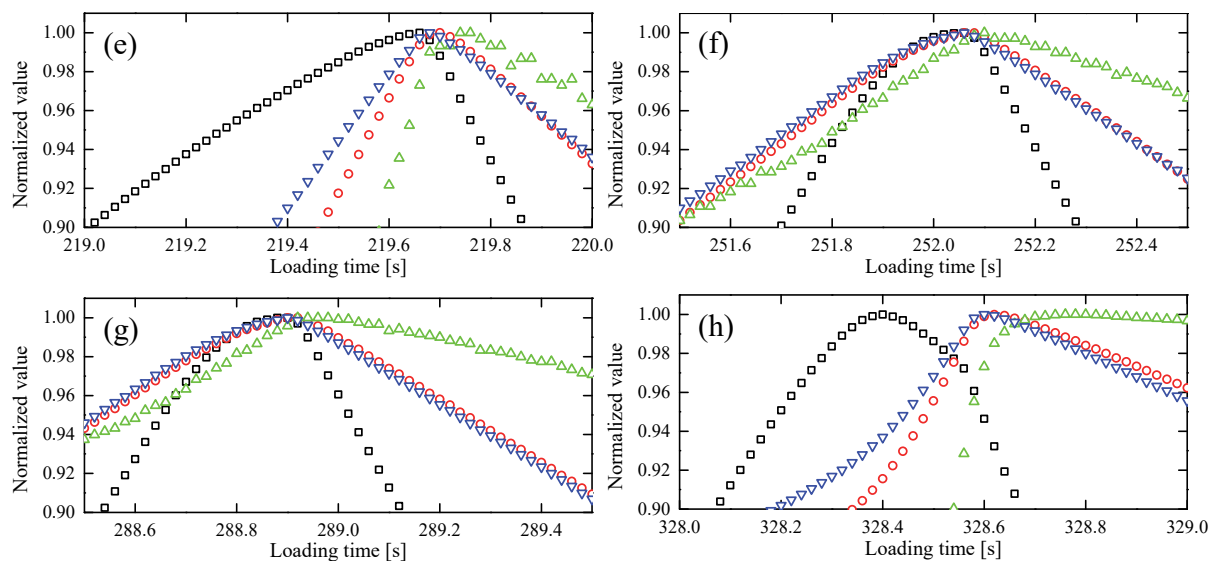
Figure 3.23 Normalized stresses and strains versus loading time for (a) 1st cycle of S1-7 (b) 4th cycle of S1-7 (c) 7th cycle of S1-7 (d) 11st cycle of S1-7 (e) 1st cycle of S1-6 (f) 11st cycle of S1-6 (g) 22nd cycle of S1-6 (h) 34th cycle of S1-6
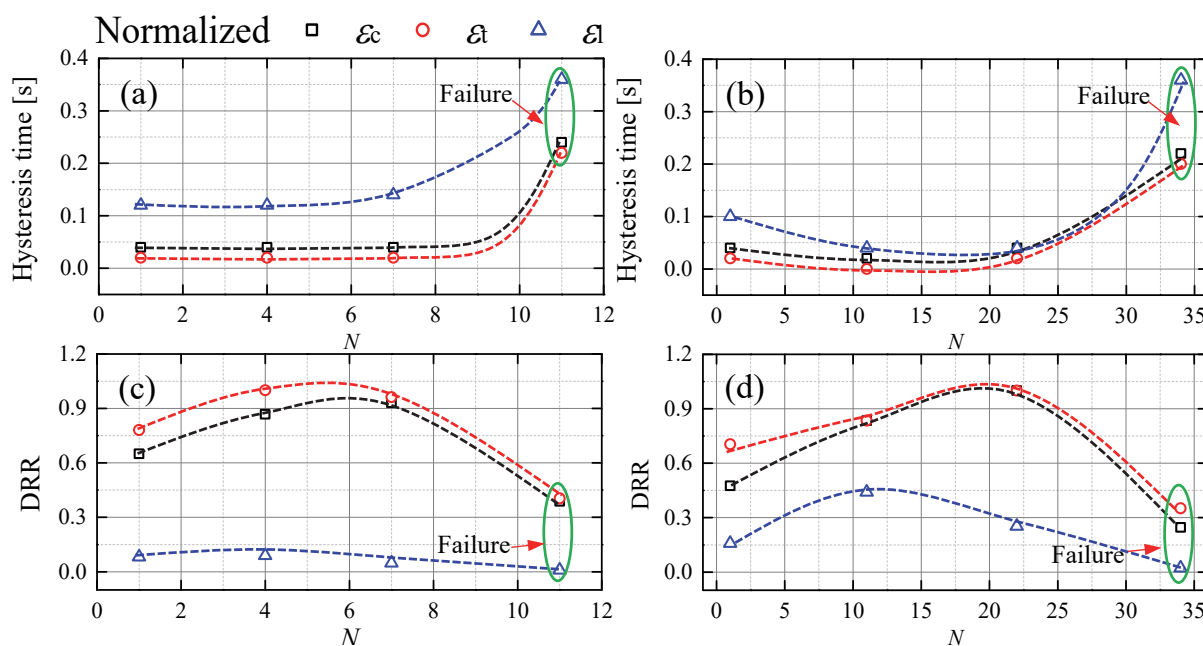
Figure 3.24 (a) hysteresis time versus *N* for S1-6 (b) hysteresis time versus *N* for S1-7 (c) DRR versus *N* for S1-6 (d) DRR versus *N* for S1-7

3.4.2 Effect of maximum load level on hysteresis time and DRR

Many laboratory tests (e.g. Bagde and Petroš 2005; Ghuzlan and Carpenter 2006) have confirmed that the maximum load level has an obvious effect on the evolution of axial strain and dissipated energy during cyclic loading. The first loading stages of samples S1-1, S1-3, S1-5, S1-6 and S1-7 have different maximum load levels while the minimum load levels are

all fixed to 40% UCS. The 5th or 6th cycle of the first loading stages of S1-1, S1-3, S1-5, S1-6 and S1-7 are selected to compare and to analyse the effect of maximum load level on hysteresis time and DRR (see Figure 3.25). The quantitative relations between hysteresis time, DRR and maximum load level are shown in Figure 3.26. As visible in Figure 3.25, the hysteresis becomes more pronounced with increasing maximum load level. The hysteresis time approximately follows a linear relation with the maximum load level (Figure 3.26a). Evaluation of ε_l gives larger hysteresis time than using ε_c and ε_t. The hysteresis time of ε_c is slightly larger than that of ε_t. Figure 3.26b shows the trend of DRR: a linear reduction with maximum load level. DRR of ε_l has the steepest slope and is consistently smaller than those of ε_c and ε_t. Figure 3.26 indicates that hysteresis time and DRR have opposite trend during cyclic loading.
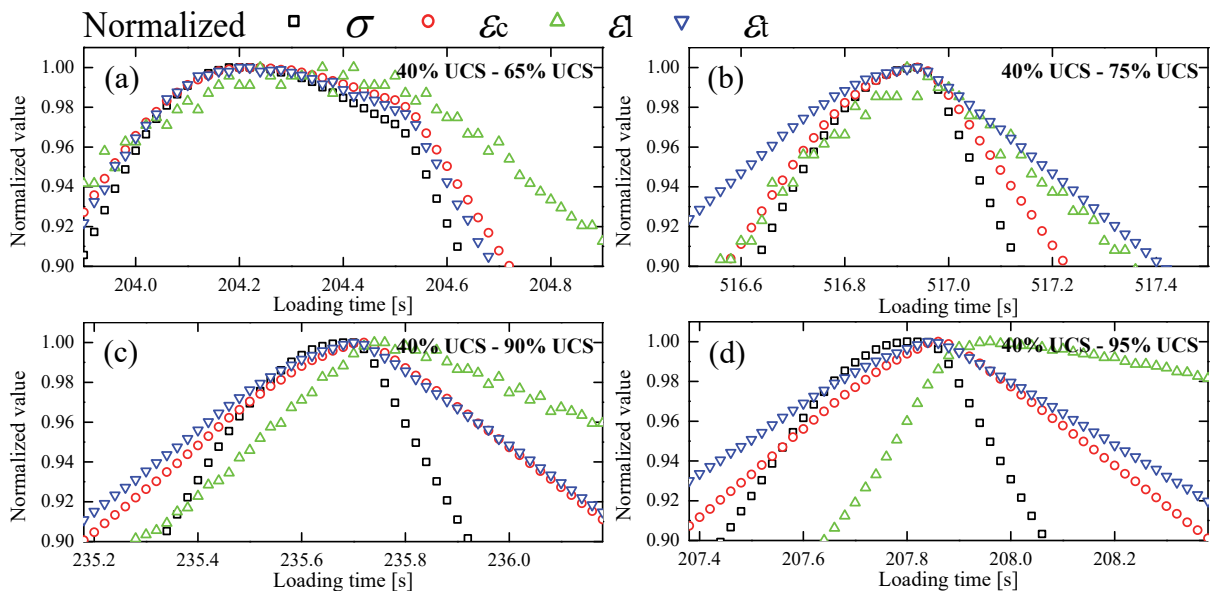
Figure 3.25 Normalized stresses and strains for (a) 5th cycle of S1-3 (b) 5th cycle of S1-5 (c) 6th cycle of S1-6 (d) 6th cycle of S1-7
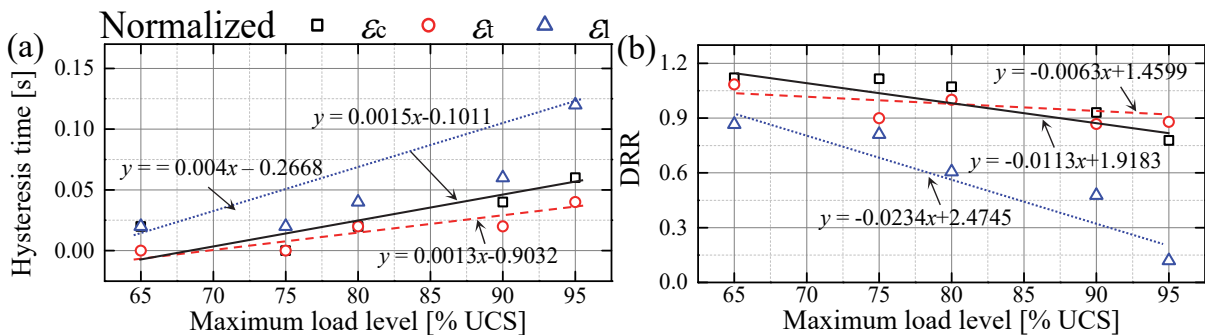
Figure 3.26 (a) hysteresis time versus maximum load levels (b) DRR versus maximum load levels

According to Table 3.2, S1-5 and S1-12 experienced 5 and 7 continuous loading stages, respectively. With gradually increasing maximum load levels, S1-5 and S1-12 experienced different loading frequencies, S1-5: 0.4 Hz, S1-12: 0.8 Hz. The 5th cycle of each loading stage is selected to compare hysteresis time and DRR. The normalized stresses and strains versus loading time of S1-5 and S1-12 are illustrated in Figure 3.27. The relation between hysteresis time, DRR and maximum load levels are shown in Figure 3.28. Figure 3.28a shows the effect of maximum load level on hysteresis time of S1-5. The hysteresis time of ε_l, ε_c and ε_t remains almost constant when the maximum load level is less than 90% UCS. When the stress is larger than 90% UCS, the hysteresis time of ε_l and ε_c shows a sudden rise. The evolution of DRR for S1-5 is plotted in Figure 3.28b. Three phases can be observed: (1) decrease (2) increase and (3) decrease. The first decrease results from the increase of maximum load level by 10% UCS. A slight increase of DRR can be observed shortly after the initial decrease. This is due to the gentle increase of load level (2.5% UCS). It indicates that a smaller increase of maximum load level after former huge increase can reduce the damage rate. A similar conclusion can be dawn in terms of accumulated dissipated energy (Song et al. 2018a). The second decrease of DRR is induced by the continuous increase of maximum load level of 2.5% UCS. The second decrease of DRR corresponds to the obvious increase of hysteresis when the load level is larger than 90% UCS. For S1-12, the frequency is double that of S1-5. The symmetry of normalized stresses and strains versus loading time for S1-12 is more pronounced than that of S1-5 (Figure 3.27). As shown in Figure 3.28c, the hysteresis time at the first loading stage shows a larger value. This is possibly due to the closure of intrinsic cracks. After the first loading stage, the hysteresis time reaches a stable value which is close to 0. An obvious increase is observed during the last two loading stages (similar to Figure 3.28a). DRR of S1-12 (Figure 3.28d) shows a different trend compared to S1-5 (Figure 3.28b). The DRR of ε_c and ε_t remains almost constant during the whole loading process. It shows that the increase of frequency may result in a more stable evolution of DRR. However, DRR of ε_l is still sensitive to the maximum load level. With increasing maximum load level, DRR of ε_l first experiences a slight rise followed by a linear reduction.
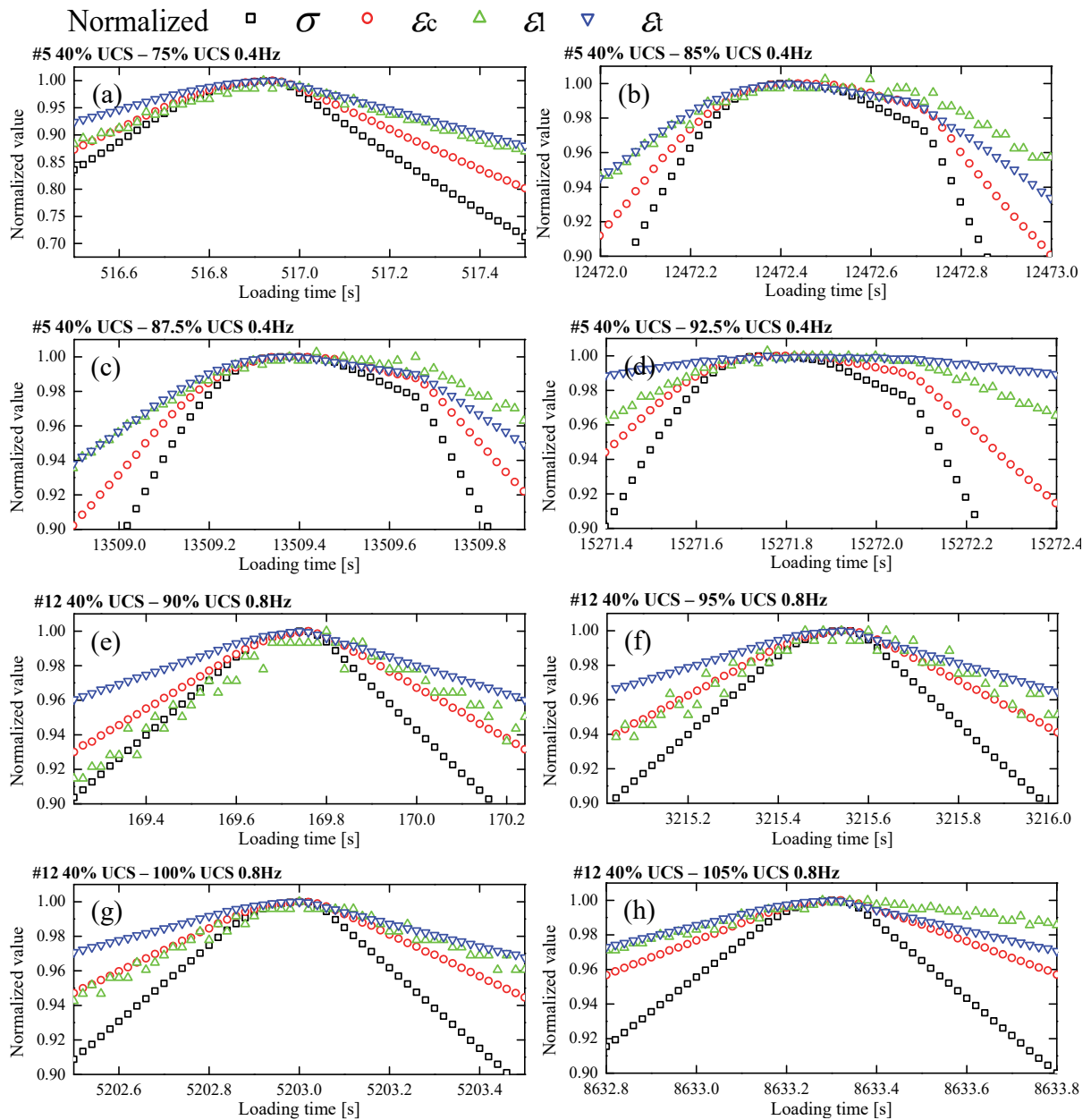
Figure 3.27 Normalized stresses and strains versus loading time for (a) 5th cycle of S1-5 (40% - 75% UCS) (b) 5th cycle of S1-5 (40% - 85% UCS) (c) 5th cycle of S1-6 (40% - 87.5% UCS) (d) 5th cycle of S1-7 (45% - 92.5% UCS) (e) 5th cycle of S1-12 (40% - 90% UCS) (f) 5th cycle of S1-12 (40% - 95% UCS) (g) 5th cycle of S1-12 (40% - 100% UCS) (h) 5th cycle of S1-12 (45% - 105% UCS)
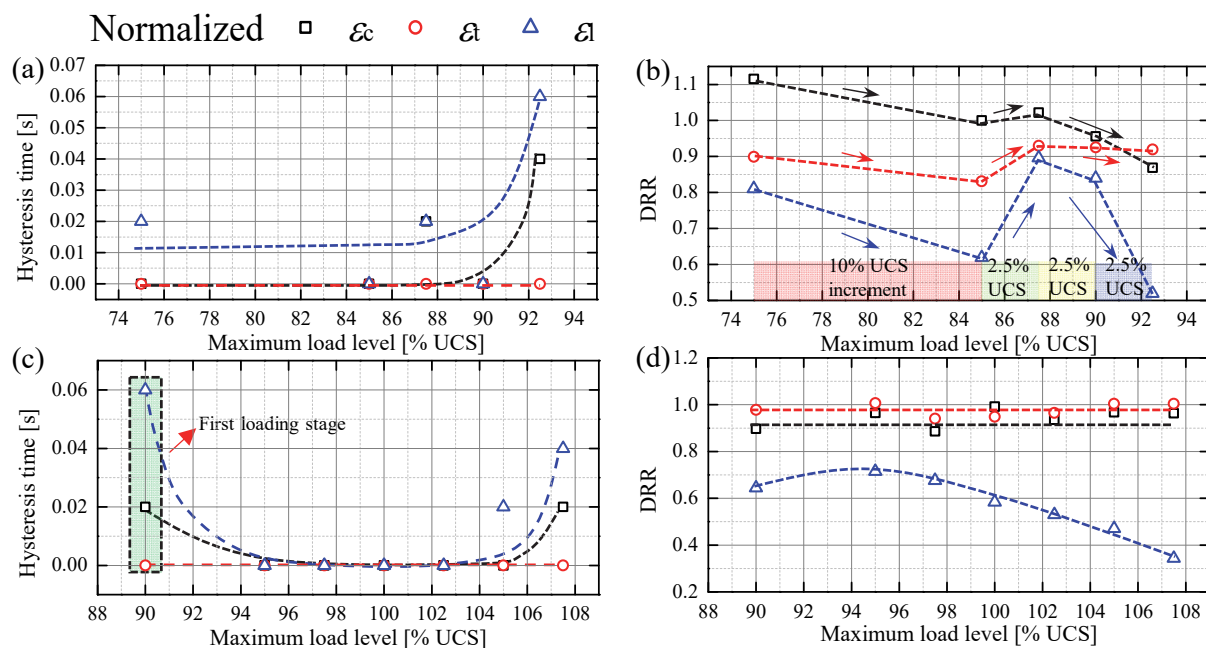
Figure 3.28 (a) hysteresis time versus maximum load level for S1-5 (b) DRR versus maximum load level for S1-5 (c) hysteresis time versus maximum load level for S1-12 (d) DRR versus maximum load level for S1-12

3.4.3 Effect of minimum load level on hysteresis time and DRR

S1-8 and S1-10 experienced fatigue loading stages with gradually decreasing minimum load levels (Table 3.2). The 5th cycle of different loading stages are again selected to compare and to analyse the effect of minimum load level on hysteresis time and DRR. Figure 3.29 illustrates the normalized stresses and strains versus loading time for different loading stages. The quantitative relations between DRR, hysteresis time and minimum load levels are plotted in Figure 3.30. Figure 3.30a shows the relation between hysteresis time and minimum load level for S1-8, which indicates that the effect of minimum load level on hysteresis time for S1-8 is limited. The hysteresis time shows only slight fluctuations with decreasing minimum load level. The relation between DRR and minimum load level for S1-8 is given in Figure 3.30b, which shows that DRR slightly fluctuates with decreasing minimum load level. It seems that no obvious effect of minimum load level on DRR can be observed according to Figure 3.30b. For specimen S1-10, Figure 3.30c shows that the hysteresis time decreases with reducing minimum load level. The larger value of hysteresis time with respect to 30% UCS minimum load level is likely due to the effect of cyclic loading on the closure of internal cracks during the first several cycles. Consistent with the former conclusion, DRR for S1-10 (Figure 3.30d) shows the opposite trend compared to hysteresis time shown in Figure 3.30c. More data are necessary to verify the effect of minimum load level on hysteresis time and DRR in detail. At least, it can

be stated that the effect of minimum load level on hysteresis time and DRR is not that pronounced as the effect of maximum load level.
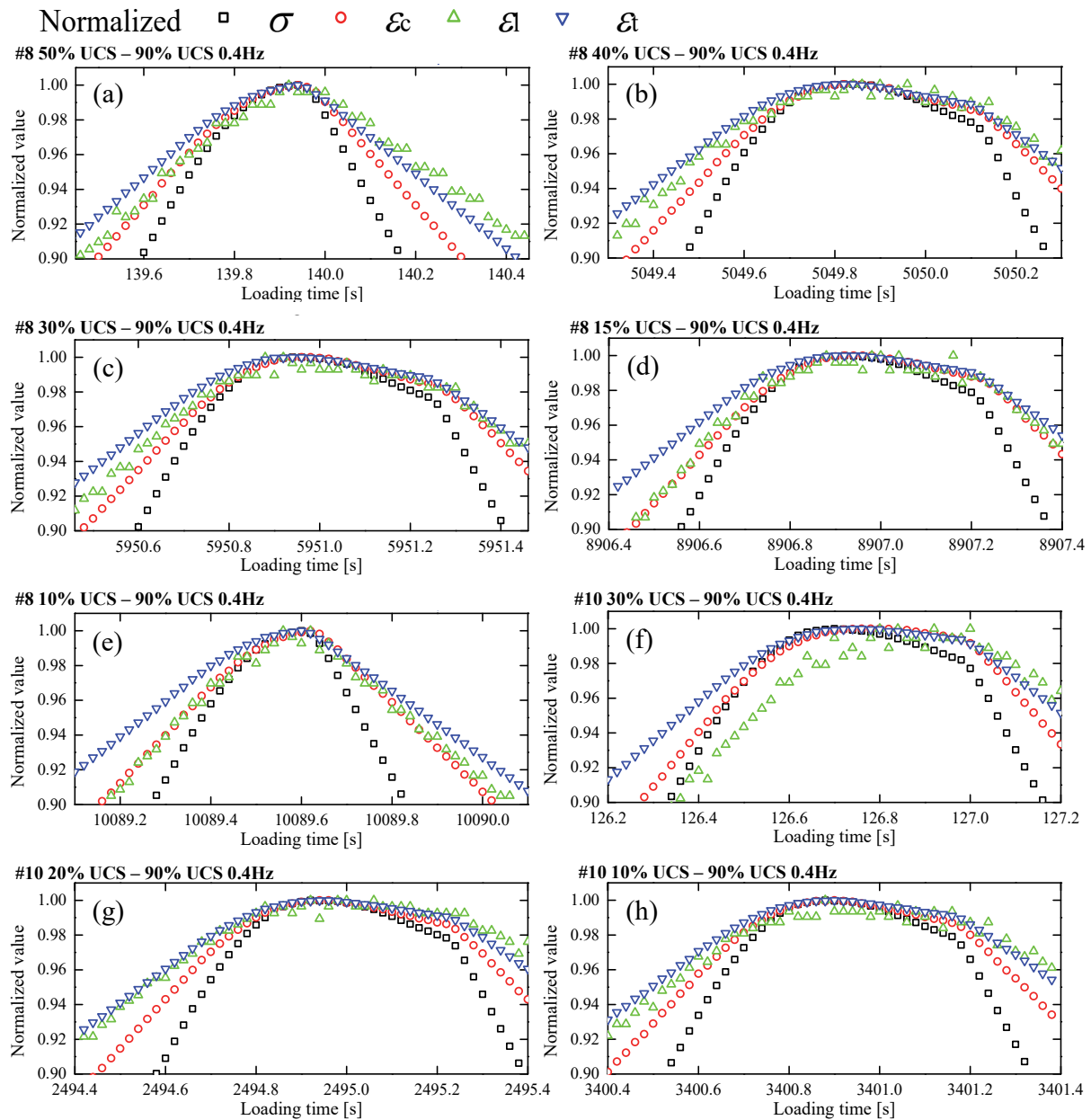
Figure 3.29 Normalized stresses and strains versus loading time (a) 5th cycle of S1-8 (50% - 90% UCS) (b) 5th cycle of S1-8 (40% - 90% UCS) (c) 5th cycle of S1-8 (30% - 90% UCS) (d) 5th cycle of S1-8 (15% - 90% UCS) (e) 5th cycle of S1-8 (10% - 90% UCS) (f) 5th cycle of S1-10 (30% - 90% UCS) (g) 5th cycle of S1-10 (20% - 90% UCS) (h) 5th cycle of S1-10 (10% - 90% UCS)
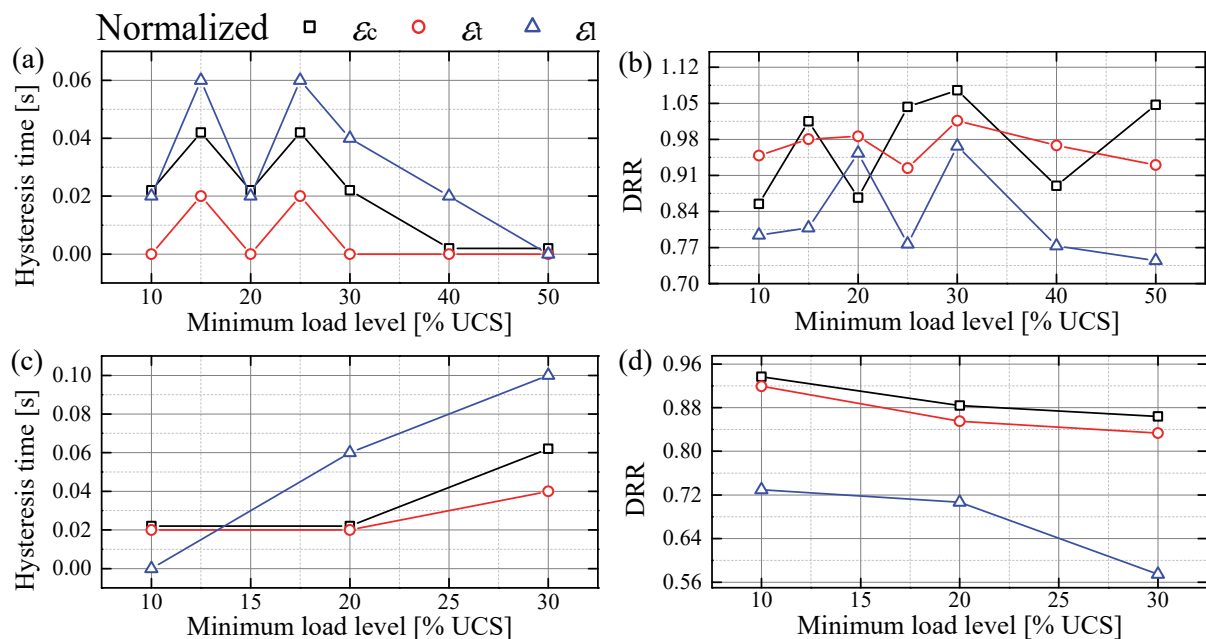
Figure 3.30 (a) hysteresis time versus minimum load level for S1-8 (b) DRR versus minimum load level for S1-8 (c) hysteresis time versus minimum load level for S1-10 (d) DRR versus minimum load level for S1-10

3.4.4 Hysteresis and dynamic response with respect to AE and P-wave speed evolution

Hysteresis time and DRR of the cycles before failure for the 9 specimens are accumulated to obtain more general insight (Figure 3.31). ε_l has a larger hysteresis time than ε_c and ε_t at failure (Figure 3.31a). ε_l has a smaller DRR than ε_c and ε_t at failure (Figure 3.31b). It is obvious that specimens with larger hysteresis time have a smaller DRR value (see the red circles in Figure 3.31a and blue circles in Figure 3.31b). S1-12, S1-8 and S1-10 have a larger hysteresis time and smaller DRR compared to other specimens. S1-12 has a larger loading frequency (0.8 Hz). S1-8 and S1-10 have experienced cyclic loading stages with gradually reducing minimum load level. It indicates that the increase of loading frequency and gradual decrease of minimum load level may result in a more obvious hysteresis and smaller DRR value at failure.
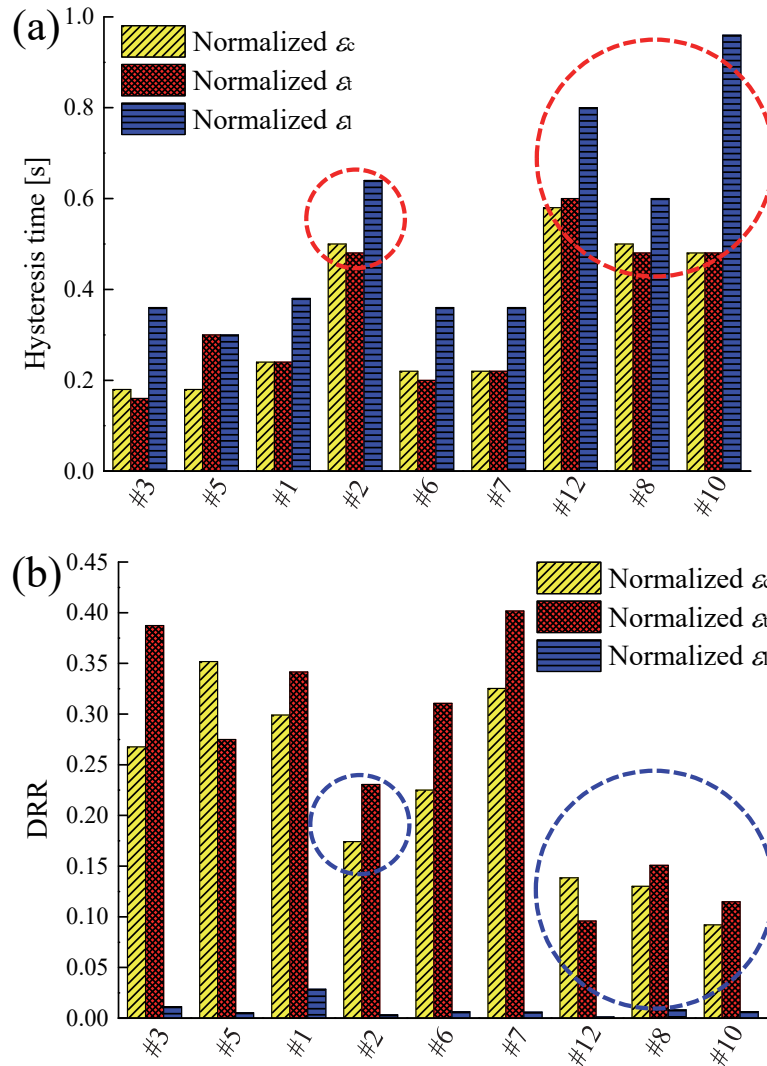
Figure 3.31 (a) hysteresis time before failure (b) DRR before failure for different samples

AE monitoring and ultrasonic wave speed measuring were applied during the cyclic loading process as shown in Figure 3.4. The evolution of P-wave speed and cumulative AE counts are commonly used to investigate the progressive damage during the loading process (Rao and Ramana 1992; Ohtsu and Watanabe 2001; Fan et al. 2017). S1-8 and S1-10 are selected for the monitoring. Both, S1-8 and S1-10, experienced multi-loading stages with variable maximum and minimum load levels. The value of DRR and hysteresis time for different points in time are also registered to reflect the continuous evolution of DRR and hysteresis time.

Figure 3.32 shows the evolution of DRR and P-wave speed for S1-8 and S1-10. It is obvious that four phases can be observed in terms of P-wave speed evolution:

(1) initial drop

(2) stationary phase

(3) obvious decrease and

(4) failure.

The evolution of DRR for ε_c, ε_t and ε_l are also plotted in the same figure. For ε_c and ε_t, three phases can be observed:

(1) initial increase

(2) stationary phase

(3) failure.

The phase of obvious decrease is missing compared with P-wave evolution. However, the evolution of ε_l has a good consistency with the P-wave speed. The four-phase characteristic is also observed in the trend of ε_l. A small difference between the trend of P-wave speed and DRR is observed in the initial phase: the P-wave speed shows an initial decrease whereas DRR shows an increase. This is due to the effect of dynamic loading. The closure of intrinsic cracks of concrete results in a lower DRR value during the first several cycles. The obvious decreasing trend of DRR in the third phase is well consistent with the P-wave speed. It is suggested that when ultrasonic monitoring is not available during cyclic loading, DRR of ε_l can be used as a variable to reflect the evolution trend of P-wave speed.

Figure 3.33 illustrates the evolution of hysteresis time and cumulative AE counts for S1-8 and S1-10. Similar to the trend of P-wave speed, the four-phase feature is observed in terms of cumulative AE counts. The four phases are:

(1) initial increase

(2) stationary phase

(3) obvious increase

(4) failure.

The trends of hysteresis time for ε_c, ε_t and ε_l are plotted in the same figure. For ε_c and ε_t, three phases can be observed:

(1) initial decrease

(2) stationary phase

(3) failure.

The evolution of ε_l shows four phases similar to the trend of cumulative AE counts. The closure of intrinsic cracks due to the effect of cyclic loading also results in different trends for cumulative AE counts and hysteresis time during the first phase (the first phase of S1-10 is not obvious). The trend of hysteresis time for ε_l can best fit the evolution of cumulative AE counts. It indicates that the hysteresis of ε_l can be used as a variable to represent the evolution of cumulative AE counts when AE monitoring is not available.
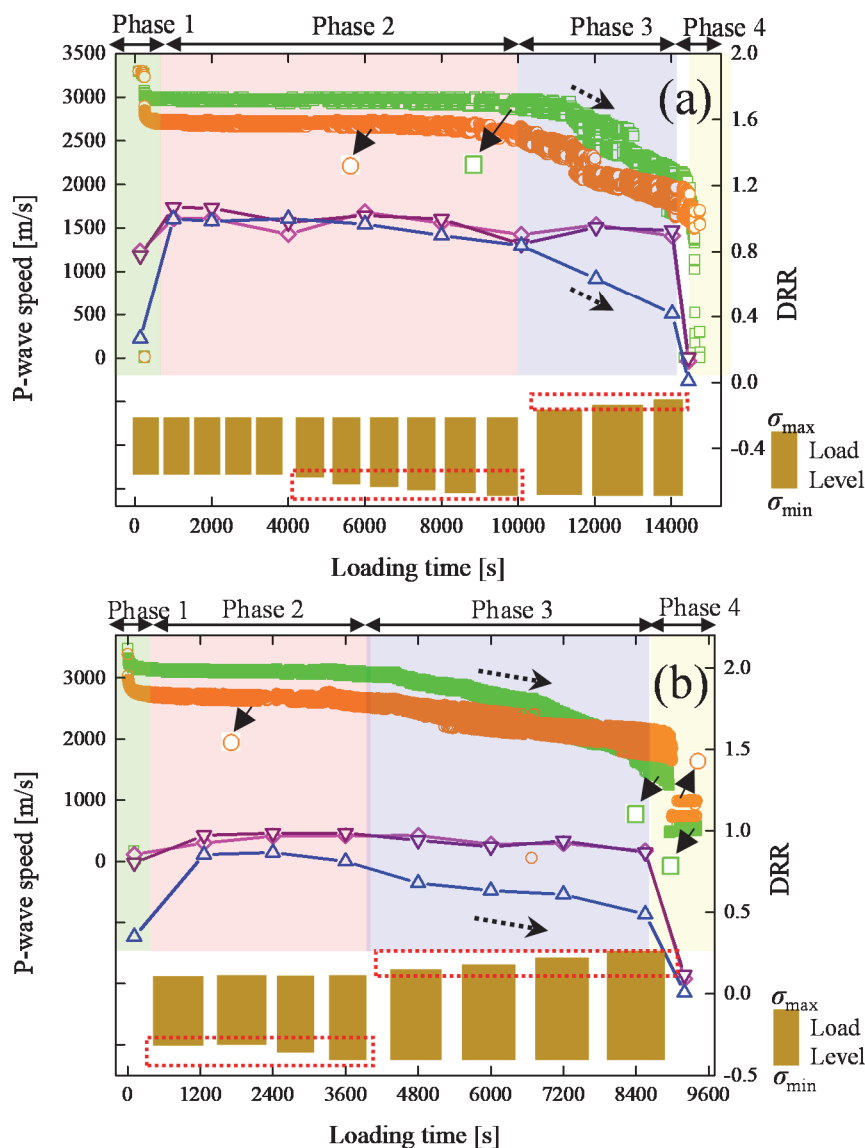
Figure 3.32 Evolution of DRR and P-wave speed versus loading time for (a) sample S1-8 and (b) sample S1-10
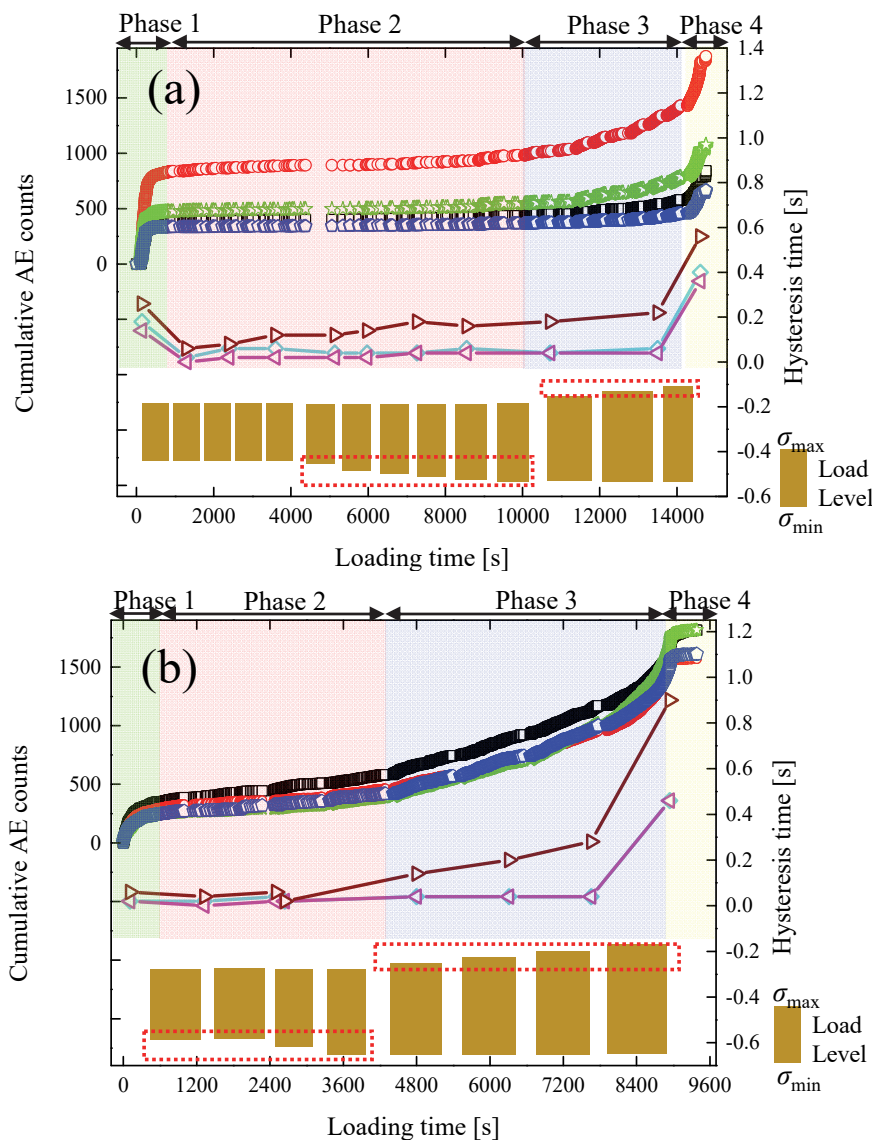
Figure 3.33 Evolution of hysteresis time and cumulative AE counts versus loading time for (a) sample S1-8 and (b) sample S1-10

3.5 Failure patterns of concrete specimens

Crack growth processes and failure patterns of brittle materials like concrete or rocks are different if they experience either monotonic or cyclic loading (Zhang and Zhao 2014; Cerfontaine and Collin 2018). It is found that under monotonic loading, almost all grains on the failure surface are highly cracked and failure pattern is brittle (Erarslan et al. 2014; Yang et al. 2015). Under cyclic loading, most grains are crack-free and failure develops mainly along grain boundaries. The failure patterns of concrete samples we have tested are shown in Figure

3.34. The eight samples are categorized into four groups according to the loading strategies. The samples S2-15 and S2-16 (Group 1) are monotonically loaded with loading speed of 0.125 mm/min. The samples S1-6 and S1-7 (Group 2) are cyclically loaded, and both samples failed within only one cyclic loading stage. The samples S1-3 and S1-5 (Group 3) are cyclically loaded, and both samples failed after multi-level cyclic loading stages. During these stages, σ_{min} is fixed and σ_{max} is gradually increased. The samples S2-13 and S2-14 (Group 4) are cyclically loaded. These samples underwent two loading strategies: (1) σ_{max} is fixed and σ_{min} is gradually decreased, (2) σ_{min} is fixed and σ_{max} gradually increased. Note that the surface of samples of Group 4 are roughened to stick the strain gauges.
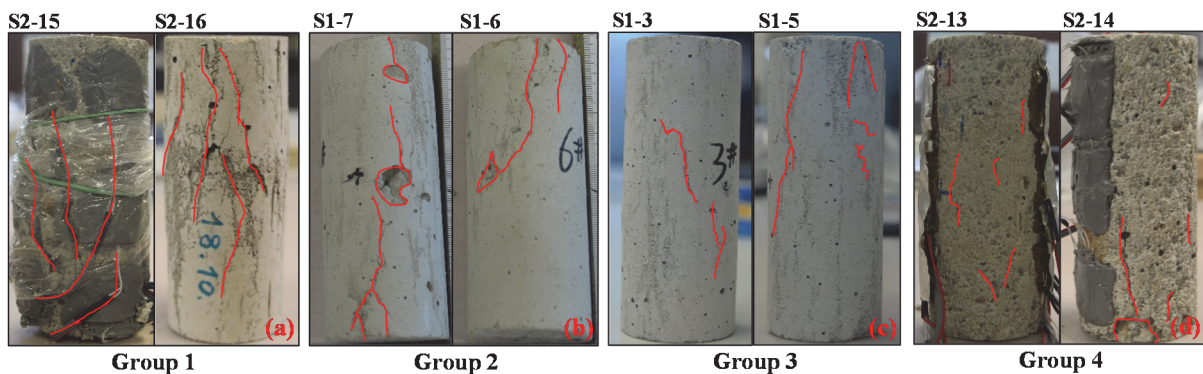
Figure 3.34 Failure patterns of samples (a) Group 1 (b) Group 2 (c) Group 3 (d) Group 4

From the viewpoint of mechanics, the failure of concrete or rocks subjected to external load, such as earthquakes or rockbursts, is connected with a rapid release of energy (Yin et al. 2004, 2008; Zhang and Zhuang 2011). Monotonic loading is characterized by dominant absorption of energy produced by external load. This will lead to macroscopic persistent cracks or sample splitting, see Figure 3.34a. The samples S1-7 and S1-6 undergo 11 and 34 cycles, respectively, up to failure within only one cyclic loading stage. The low cycle number is caused by the higher level of σ_{max} which results in larger energy absorption in each cycle. Some persistent cracks can be observed in Figure 3.34b and small concrete pieces are spalled from the sample. Compared to Group 1 and Group 2, the crack sizes observed in samples of Group 3 and Group 4 are much smaller, no persistent cracks are observed (see Figure 3.34c and Figure 3.34d). The samples of Group 3 and Group 4 experienced more than 600 loading cycles. The internal smaller cracks (micro-cracks) are evenly distributed over the whole sample. The axial and lateral strain at peak stress of the last cycle for the eight samples are shown in Figure 3.35. The monotonically loaded samples show an obviously smaller axial strain (see Figure 3.35a) and lateral strain (see Figure 3.35b) than the cyclically loading samples. This illustrates that the unloading stages in cyclic loading enable the samples to experience larger axial and lateral

strain than under monotonic loading. Thus, the unloading stages in cyclic loading can be beneficial to enhance the energy absorption and reduce the rapid release of energy typically leading to violent failure with macroscopic persistent cracks or sample splitting.
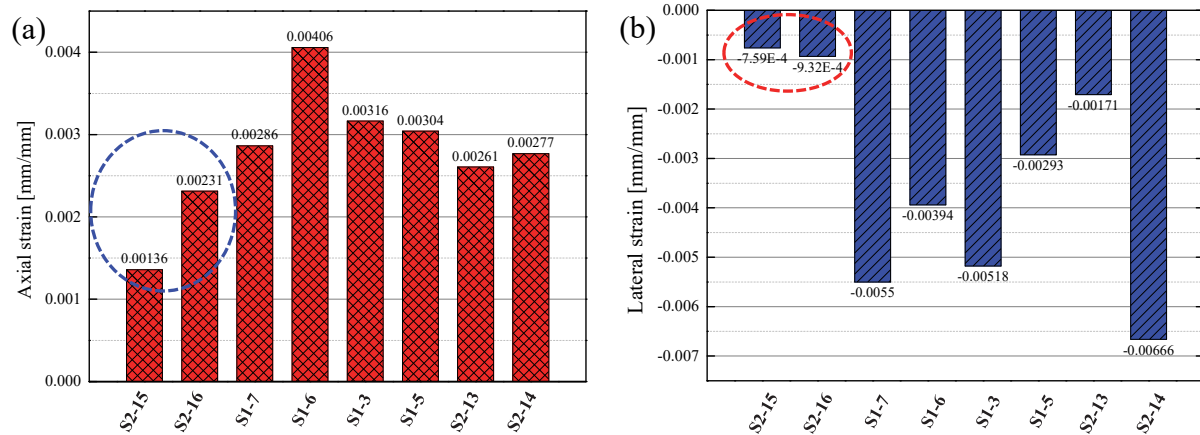
Figure 3.35 (a) axial strain at peak stress of the last cycle (b) lateral strain at peak stress of the last cycle

3.6 Conclusions

The evolution of damage indicators in terms of continuum damage mechanics and dissipated energy can be well described by an exponential relation in case of fixed minimum load level and varying maximum load level and can be well fitted by a logarithmic relation for a fixed maximum load level and varying minimum load level. The effect of maximum load level on cumulative AE counts and P-wave speed is more obvious than the minimum load level. The axial strain for cyclically loaded concrete specimens is inhomogeneous. Top and bottom parts of the samples are influenced by the stiffness contrast and the dynamic effect of direct loading, whereas the middle part is less influenced. The maximum load level has an obvious effect on axial and lateral strain rate and follows an exponential relation. At peak strength the strain rate in the middle part is larger than that in the top and bottom parts. The energy dissipation of samples is also inhomogeneous when subjected to cyclic loading. At small load levels, top, middle and bottom parts have almost the same amount of dissipated energy. The disparity of energy dissipation between middle part and top/bottom part increases with increasing load level and reaches the peak value at ultimate strength. The negligible confinement at the middle part of the sample leads to such a behaviour. The frictional contact between sample surface and loading platen will restrict the deformation of the samples at the ends. The maximum load level has a more pronounced effect on energy dissipation than the minimum load level does.

A P-wave ratio is proposed as ratio of P-wave speed measured at the middle and top part of the concrete sample, respectively. The P-wave ratio evolution shows three stages and its peak point is an effective precursor to predict the fatigue failure of concrete. Monotonically loaded concrete specimens show smaller axial and lateral strain compared to cyclically loaded samples at peak strength of the last cycle. The release of stored energy for samples failing after monotonic loading leads to larger macroscopic and persistent cracks. Due to enhanced energy absorption during cyclic loading the failure patterns of cyclically loaded concrete samples typically show smaller and more evenly distributed cracks.

This chapter also presents the hysteresis and dynamic response characteristics of concrete samples exposed to multi-level fatigue loading. For specimens which failed during the first fatigue loading stage, hysteresis in the direction vertical to loading is more obvious than in loading directions. The hysteresis time shows a sudden rise when the specimen is close to failure. DRR experiences an initial increase and then drops to a lower value at failure. The maximum load level of the first cyclic loading stage has an approximately linear relation with DRR and hysteresis time. The hysteresis time increases with maximum load level whereas DRR shows an opposite trend. For specimens which experienced multi-loading stages, a slight increase of the maximum load level can reduce the hysteresis time and increase DRR. The hysteresis time shows a strong nonlinear rise when the maximum load level is close to the fatigue strength. The evolution with respect to the DRR of lateral strain is well consistent with the four-phase trend of P-wave speed during the cyclic loading. The trend with respect to hysteresis time of lateral strain has strong similarity with the evolution of cumulative AE counts. DRR and hysteresis time of lateral strain can be used as damage variables when ultrasonic and AE monitoring are not available. The maximum load level has more pronounced effect on DRR and hysteresis time than the minimum load level.

4. Numerical simulation of fatigue testing

This chapter presents particle based numerical simulations to replicate the mechanical behaviour of concrete specimens tested in the laboratory as documented in Chapter 3. The linear parallel bonded model (LPBM) implemented in **P**article **F**low **C**ode (PFC) is the basic microscopic contact mode, which was extended to simulate cyclic fatigue. The LPBM was first proposed by Potyondy and Cundall (2004). A brittle geo-material can be represented by a dense packing of non-uniform-sized circular or spherical particles that are bonded together at their contact points. The LPBM has been developed and modified by many scholars to simulate the complex mechanical behaviour of cemented solids (Li et al. 2017b), hydro-fracturing (Komoróczi et al. 2013; Ju et al. 2018; Liu et al. 2018a), and crack propagation of geo-materials (Park and Min 2015; Han et al. 2017; Shang et al. 2018). As a typical DEM approach, PFC has the advantage to replicate the micro structure itself and the micro structural interactions between grains. The model can more naturally reproduce the macroscopic behaviour of brittle geo-materials, such as plasticity and viscosity when subjected to various loading conditions (Potyondy and Cundall 2004; Potyondy 2007). The breakage of a bond between two connected particles can explicitly represent the damage to demonstrate the formation and coalescence of micro fractures (Chang et al. 2002; Schöpfer and Childs 2013). The microstructures of plain concrete and a real rock (shale) are illustrated by SEM photos in Figure 4.1 (Shang et al. 2014; Semnani and Borja 2017).
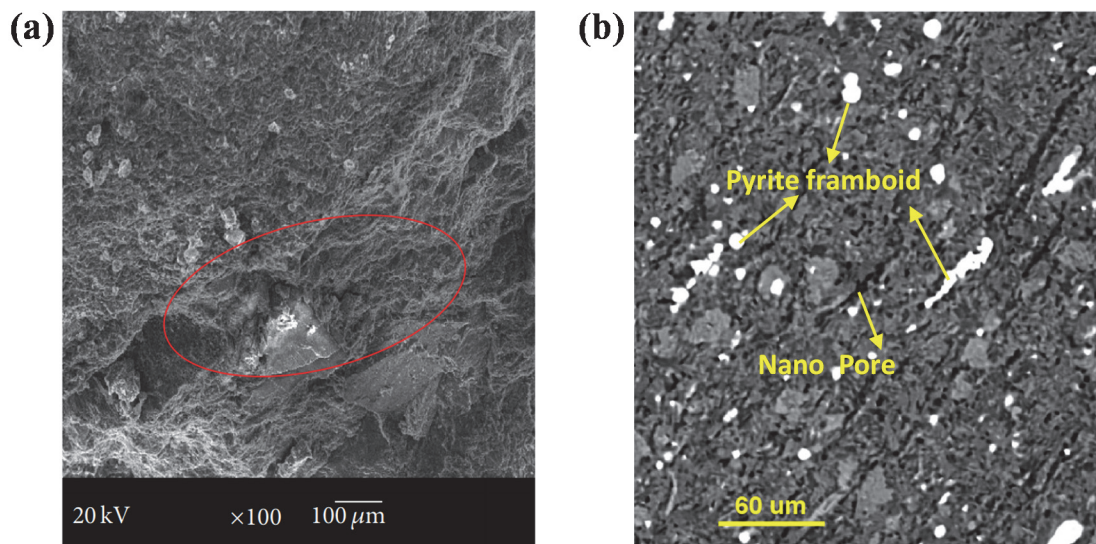
Figure 4.1 SEM photos of (a) plain concrete (Shang et al. 2014) (b) natural shale rock (Semnani and Borja 2017)

77

As shown in Figure 4.1, compared to plain concrete, the structures of rocks are coarser and more heterogeneous in general. There are several options to consider the heterogeneity in particle based methods: use of spheres with different diameters, use of non-spherical particles such as clumps or clusters (Stahl and Konietzky 2011; Li et al. 2017a; Song et al. 2018c; Song and Konietzky 2019) or use of bonds with different diameters and property distributions. Also, alone the random placement of particles in an assembly creates heterogeneity which creates complex force and moment transmission networks. Therefore, the adoption of PFC can well characterize the heterogeneity of typical geo-materials. In addition, the released strain energy at the connected bonds at failure can also be monitored and related to physical mechanisms of AE events.

4.1 Introduction of LPBM

LPBM is an ideal model to mimic the cemented material which can exhibit a rich set of emergent behaviours that correspond evert well with rocklike materials, at the same time the dominate fracture and failure behaviours of rocklike materials can be well simulated. Due to the fact that the LPBM is the basic microscopic contact model used in the numerical simulation, a comprehensive understanding of the force, moment and displacement update in LPBM is important to understand the simulations of fatigue testing.
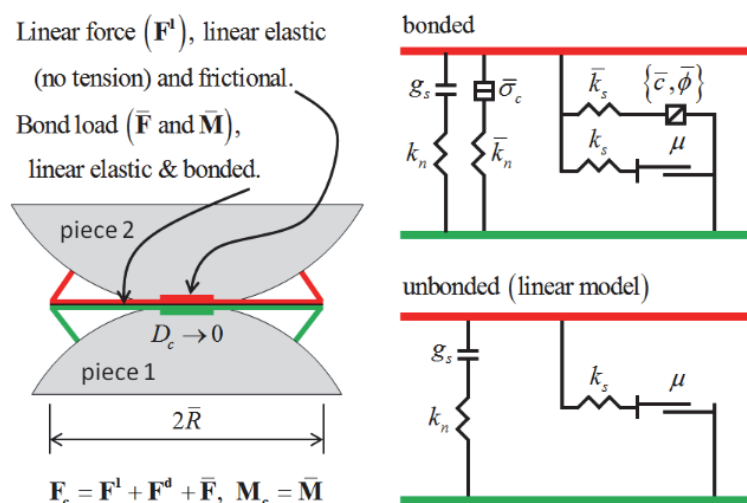
Figure 4.2 Concept and rheological components of the LPBM

As shown in Figure 4.2, the LPBM provides the behaviour of two interfaces:

(1) The first interface is called linear elastic interface, it is equivalent to the linear model: it does not resist relative rotation, and slip is accommodated by imposing a Coulomb limit on the shear force and it cannot bear tensile stresses.

(2) The second interface is called a parallel bond interface. When bonded, it acts in parallel with the first interface. When the second interface is bonded, it resists relative rotation, and its behaviour is linear elastic until the strength limit is exceeded and the bond breaks, making it unbonded. When the second interface is unbonded, it carries no load. The unbonded linear parallel bond model is equivalent to the linear model.

The update of the localized contact force and contact moment for LPBM is shown in Equation 4.1

$$F_c = F_l + F_d + F_p \quad M_c = M_p$$

(4.1)

Where F_c is the contact force, F_l is the linear force, F_d is the dashpot force, F_p is the parallel bond force, M_c is the parallel bond moment which is equal to the moment of parallel bond interface M_p because the linear group doesn't contribute to the moment transmission. The update of linear contact force is shown in Equation 4.2

$$F_{ln} = \min\left(\left(F_{ln}\right)_0 + k_n \Delta \delta_n, 0\right) \quad \text{incremental update}$$

$$F_{ls} = \begin{cases} \min\left(\left(F_{ls}\right)_0 - k_s \Delta \delta_s, 0\right) & \text{when } \min\left(\left(F_{ls}\right)_0 - k_s \Delta \delta_s, 0\right) < -\mu F_{ln} \\ -\mu F_{ln} \end{cases}$$

(4.2)

Where F_{ln} and F_{ls} are linear normal and shear forces. k_n and k_s are linear normal and shear stiffness. $\Delta \delta_n$ and $\Delta \delta_s$ are relative normal and shear displacement increments. $(F_{ln})_0$ and $(F_{ls})_0$ are linear normal and shear forces at the beginning of the time step. μ is the friction coefficient. The update of the dashpot force is shown in Equation 4.3. 'Full normal' means that the normal force can be either compressive or tensile. 'No-tension normal' means that normal force is always compressive. 'Slip-cut' means that F_{ds} is set to zero if the linear spring is sliding, 'full shear' means F_{ds} sliding resistance.

$$F_d = -F_{dn}\hat{n}_c + F_{ds}$$

$$F_{ls} = \begin{cases} \left(2\beta_n\sqrt{m_c k_s}\right)\dot{\delta}_n & \text{(full normal)} \\ \min\left(\left(2\beta_n\sqrt{m_c k_s}\right)\dot{\delta}_n, -F_{ln}\right) & \text{(no-tension normal)} \end{cases}$$

$$F_{ls} = \begin{cases} \left(2\beta_s\sqrt{m_c k_s}\right)\dot{\delta}_s & \text{(full shear)} \\ 0 & \text{(slip-cut)} \end{cases}$$

$$m_c = \frac{m_1 m_2}{m_1 + m_2}$$

(4.3)

Where F_{dn} and F_{ds} are normal and shear dashpot forces, $d\delta_n$ and $d\delta_s$ are relative normal and shear velocities, β_n and β_s are normal and shear critical damping ratios, m_1 and m_2 are the masses of the two particles in contact.

The update of the parallel bond force is shown in Equation 4.4. Where F_{pn} and F_{ps} are parallel bond normal and shear forces, k_n' and k_s' are normal and shear stiffness of the parallel bond interface.

$$F_p = -F_{pn}\hat{n}_c + F_{ps}$$
$$F_{pn} = (F_{pn})_0 + k_n' A\Delta\delta_n$$
$$F_{ps} = (F_{ps})_0 - k_s' A\Delta\delta_s$$

(4.4)

The update of the parallel bond moment is shown in Equation 4.5. Where M_t and M_b are twisting and bending moments. I is the moment of inertia of the parallel bond cross-section. J is the polar moment of inertia of the parallel bond cross section. $\Delta\theta_t$ and $\Delta\theta_b$ are relative twist and bend rotation increments.

$$M_p = -M_t\hat{n}_c + M_b$$
$$M_t = M_t - k_s' J\Delta\theta_t$$
$$M_b = M_b - k_n' I\Delta\theta_b$$

(4.5)

The update of the maximum normal stresses and shear stresses at the parallel-bond periphery are shown in Equation 4.6. Where ς_c is the moment-contribution factor.

$$\sigma = \frac{F_{pn}}{A} + \varsigma_c \frac{M_b R}{I}$$

$$\tau = \frac{F_{ps}}{A} + \varsigma_c \frac{M_t R}{J}$$

(4.6)

The relation between normal and shear strength of the parallel bond interface is shown in Figure 4.3. When for two particles in contact, either the maximum normal strength σ_c or the shear strength τ_c is exceeded, force, moment and stiffness belonging to the parallel bond interface will be removed and the LPBM will become a linear elastic model, see Equation 4.7.

$$\left\{ F_{pn}, F_{ps}, M_p, K_n', K_s' \right\} = 0$$

(4.7)
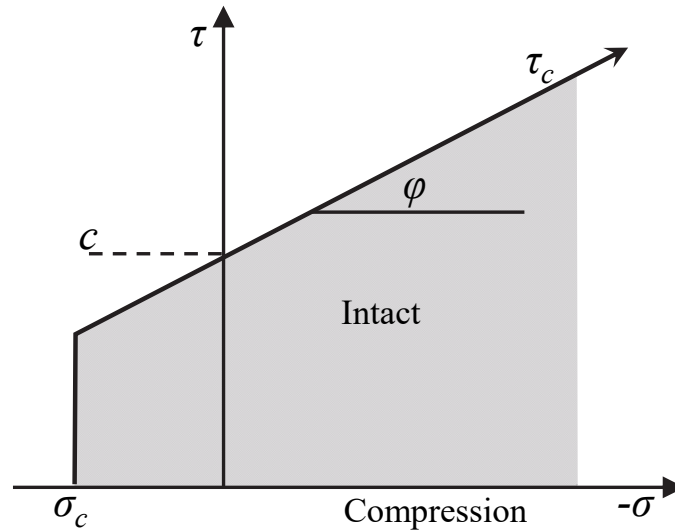
Figure 4.3 Failure envelope for the parallel bond

4.2 Numerical simulation of static fatigue testing

4.2.1 Parallel-bonded Stress Corrosion (PSC) model

The PSC model was proposed to simulate the time-dependent stress corrosion effect that occurred in wet silicate rocks subjected to static fatigue loading (Potyondy 2007).
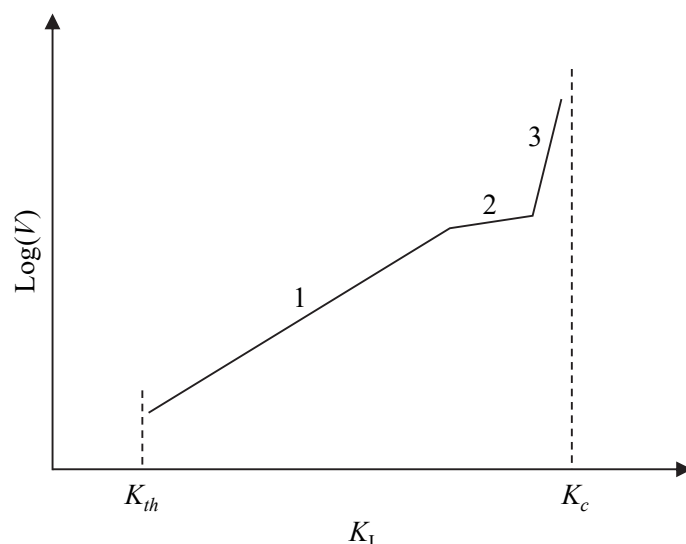
Figure 4.4 Typical crack-growth curve for glasses and ceramics tested in air at a constant temperature and chemical environment (Freiman 1984)

The mechanism of the PSC model originates from the crack growth of glass material. The glass can be treated as an ideal material to apply the concepts of brittle fracturing, because it is homogeneous in terms of composition and structure, isotropic in its properties, and shows brittle crack growth (Wiederhorn et al. 1980). Thus, the conditions at the crack tip can be well described by the theory of **L**inear **E**lastic **F**racture **M**echanics (LEFM) (Anderson 2005). During the loading, the crack-tip stresses are proportional to the mode-I SIF, K_I, which is an appropriate parameter to characterize the "driving force" for the crack growth process in tension. Each crack grows stable with a finite velocity V for SIF less than the fracture toughness, K_c. This phenomenon is known as subcritical crack growth. A typical V - K_I diagram for glasses is shown in Figure 4.4. In region 1, the velocity of crack growth is controlled by the rate of stress corrosion reactions at crack tips. In region 2, the velocity of crack growth is controlled by the rate of transport of reactive species to the crack tips. In region 3, crack growth is controlled mainly by mechanical rupture and is relatively insensitive to the chemical environment. In this plot, K_{th} is a stress corrosion threshold, below which no crack growth is observed.

In the PSC model it is assumed that time-dependent behaviour of silicate rock is controlled by a stress corrosion effect (the existence of water can weaken the Si-O bonds of the material) and that this reaction can be represented using the reaction-rate theory, for which the reaction kinetics are embedded in the chemical reaction rate, see Equation 4.8.

$$V = V_0 \exp\left(\frac{-E^* + \upsilon^+ \sigma}{RT}\right), \quad E^* = E^+ + \upsilon_M \gamma / \rho$$

(4.8)

Where V_0 is an experimental damage constant, E^* is the apparent activation energy, υ^+ is the activation volume, σ is the crack-tip stress, R the universal gas constant and T is the absolute temperature. The apparent activation energy contains the following terms: E^+ is the stress-free activation energy, υ_M is the molar volume of the glass, γ is the interfacial surface energy between the glass and the reaction products and ρ is the radius of curvature of the crack tip. This Equation 4.8 is the basic logic for the damage-rate law of the PSC model, by introducing Equation 4.8 into the PSC model and considering the following four assumptions:

(1) The stress corrosion effect just weakens the connected cement (bond) of two grains. However, it does not affect the grain (stiffness, volume, shape) itself.

(2) The uniform remove rate of bond material is proportional to the crack velocity in Equation 4.8. The rate of material removal is defined as corrosion rate.

(3) The corrosion rate is stress-dependent.

(4) Stress corrosion happens only when the applied stress is larger than the threshold level.

By integrating Equation 4.8, the corrosion rate of diameter, dD/dt, can be expressed by Equation 4.9.

$$\frac{dD}{dt} = \left(-\alpha V_0 \exp\left(-E^* / RT\right)\right) \exp\left(\upsilon^+ \sigma / RT\right)$$

(4.9)

Where α is the constant of proportionality between corrosion rate and reaction rate. Therefore, Equation 4.9 can be expressed as Equation 4.10 when threshold value σ_a is considered.

$$\frac{dD}{dt} = \begin{cases} 0 & \sigma < \sigma_a \\ -\beta_1 e^{\beta_2(\sigma/\sigma_c)} & \sigma_a < \sigma < \sigma_c \\ -\infty & \sigma > \sigma_c \end{cases}$$

(4.10)

Where σ is the applied stress, σ_c is the critical stress or tensile strength. β_1, β_2 are damage rate constants. The damage rate in PSC is similar to LEFM, as shown in Equation 4.11.

$$V = \begin{cases} 0 & \sigma < \sigma_a \\ -\beta_1 e^{\beta_2(\sigma/\sigma_c)} & \sigma_a < \sigma < \sigma_c \\ -\infty & \sigma > \sigma_c \end{cases} \quad \text{PSC}$$

$$V = \begin{cases} 0 & K_I < K_{th} \\ \alpha_1 e^{\alpha_2(K_I/K_c)} & K_{th} < K_I < K_c \\ \infty & K_I > \sigma_c \end{cases} \quad \text{LEFM}$$

(4.11)

Where K_c is the fracture toughness, K_{th} is the stress corrosion threshold, and α_1 and α_2 are material constants that vary with temperature and chemical environment. Figure 4.5 illustrates the bond weakening (stress corrosion) process in the PSC model.
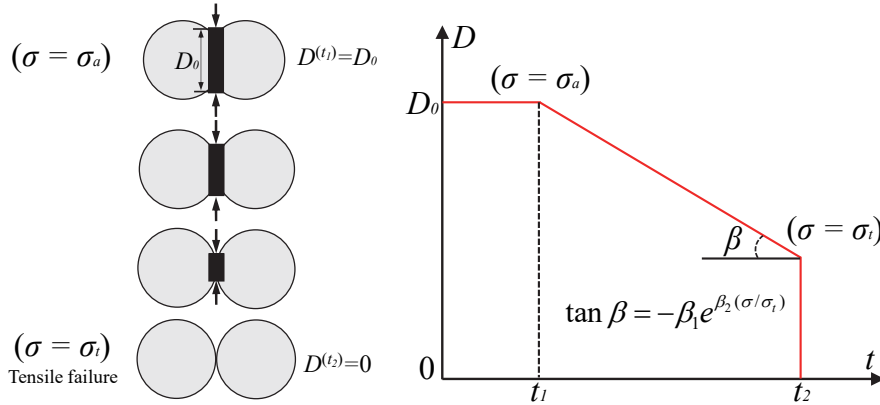
Figure 4.5 PSC model: bond diameter reduction rate

Forces and moments belonging to the parallel bond are transmitted through the parallel bond interface. The bond forces are related to the relative bond displacements. This relation can be expressed by stiffness matrix **k**, force vector **F** and displacement vector **d**, see Equation 4.12 and Equation 4.13.

$$\{F\} = [k]\{d\}$$

(4.12)

$$\begin{Bmatrix} F_{pn} \\ F_{ps} \\ M_{pn} \\ M_{ps} \end{Bmatrix} = \begin{bmatrix} K_n'A & 0 & 0 & 0 \\ 0 & -K_s'A & 0 & 0 \\ 0 & 0 & -K_s'J & 0 \\ 0 & 0 & 0 & -K_n'I \end{bmatrix} \begin{Bmatrix} U_n \\ U_s \\ \theta_n \\ \theta_s \end{Bmatrix}$$

(4.13)

Where U_n, U_s, θ_n, θ_s are normal and shear displacements and rotations between the two bonded particles.

When the external load is larger than the damage threshold, the bond diameter starts to reduce from the original value D_0. When the bond diameter is reduced to λD_0 (λ is the bond radius multiplier, $0 < \lambda < 1$), both the effective stiffness and the bond force are correspondingly reduced. The stiffness which is represented by stiffness matrix k is reduced because of the effect of reduction in the bond cross-sectional properties A, I and J. Where A is the bond cross-section area. I is the moment of inertia of the parallel bond cross-section. J is the polar moment of inertia of the parallel bond cross section. A, I and J after damage are given by Equation 4.14.

$$A' = A\begin{cases} \lambda, & \text{PFC2D} \\ \lambda^2, & \text{PFC3D} \end{cases} \quad I' = I\begin{cases} \lambda^3, & \text{PFC2D} \\ \lambda^4, & \text{PFC3D} \end{cases} \quad J' = J\begin{cases} \text{NA}, & \text{PFC2D} \\ \lambda^4, & \text{PFC3D} \end{cases}$$

(4.14)

Equation 4.12 is transferred into Equation 4.15 with damage involved in stiffness matrix k_d. Equation 4.16 shows the damage of stiffness matrix in 2D and 3D.

$$\{F\} = [k_d]\{d\}$$

(4.15)

$$\begin{Bmatrix} F_{pn} \\ F_{ps} \\ M_{pn} \\ M_{ps} \end{Bmatrix} = \begin{bmatrix} K_n' A\begin{cases} \lambda, & 2D \\ \lambda^2, & 3D \end{cases} & 0 & 0 & 0 \\ 0 & -K_s' A\begin{cases} \lambda, & 2D \\ \lambda^2, & 3D \end{cases} & 0 & 0 \\ 0 & 0 & -K_s' J\begin{cases} \text{NA}, & 2D \\ \lambda^4, & 3D \end{cases} & 0 \\ 0 & 0 & 0 & -K_n' I\begin{cases} \lambda^3, & 2D \\ \lambda^4, & 3D \end{cases} \end{bmatrix} \begin{Bmatrix} U_n \\ U_s \\ \theta_n \\ \theta_s \end{Bmatrix}$$

(4.16)

4.2.2 Application of PSC model for static fatigue simulation

In literature (Potyondy 2007), the PSC model is used to replicate the static fatigue behaviour of Lac du Bonnet granite (Schmidtke and Lajtai 1985). Figure 4.6 illustrates numerical simulation results and corresponding data from static fatigue tests of Lac du Bonnet granite at a confinement of 0.1 MPa. The two bond reducing parameters β_1 and β_2 in Equation 4.10 are assigned with different values in 2D and 3D models, see Equation 4.17. Figure 4.6 shows that the numerical simulations can well replicate the relation between lifetime and stress ratio. Because this thesis concentrate on cyclic fatigue, the numerical simulations of static fatigue tests are not discussed further.
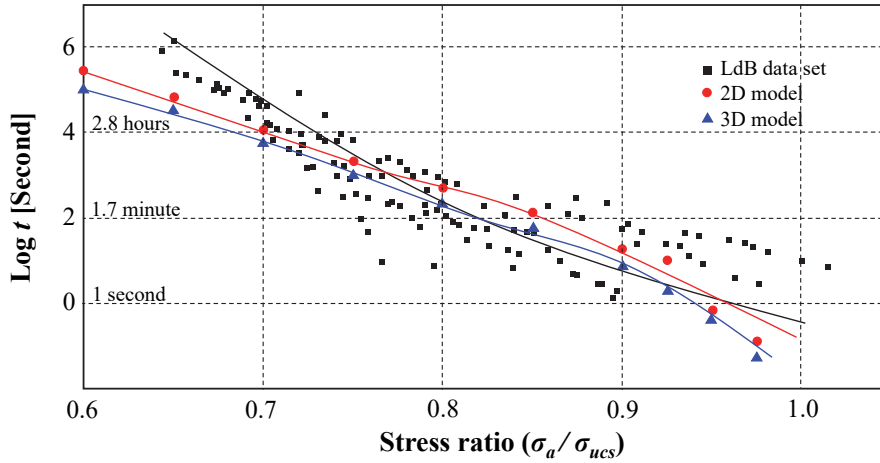
Figure 4.6 Application of PSC model for static fatigue testing (Potyondy 2007)

$$\beta_1 = \begin{cases} 5\times10^{-17}\,\text{m/s}, & 2D \\ 4\times10^{-15}\,\text{m/s}, & 3D \end{cases} \qquad \beta_2 = \begin{cases} 30, & 2D \\ 30, & 3D \end{cases}$$

(4.17)

4.3 Numerical simulation of single-level fatigue testing

4.3.1 Nonlinear Parallel-bonded Stress Corrosion (NPSC) model
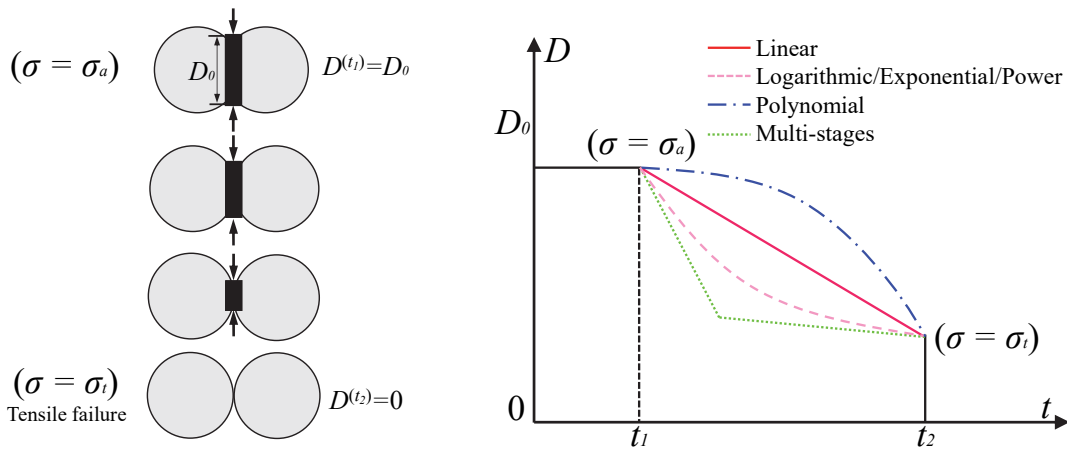
Figure 4.7 Potential NPSC models (Bond diameter versus loading time)

Compared to constant load in static fatigue simulations, cyclic loading is characterized by a more complex transmission process of forces and moments. According to the PSC model, the damage rate, which is represented by the reduction speed of the bond diameter, is constant in the PSC model. However, for cyclic loading it is necessary to describe the damage speed in a more complex manner in order to reproduce the observed laboratory test results. Therefore, nonlinear parallel-bonded stress corrosion (NPSC) models are proposed to simulate cyclic loading. Figure 4.7 illustrates some potential NPSC models. In this thesis, we focus only on the 2-dimensional implementation of NPSC models for single-level fatigue testing.

86

4.3.2 Application of NPSC model for single-level fatigue testing

4.3.2.1 Modelling of stress-controlled cyclic loading

For rock-like materials, the stress-controlled loading strategy is often adopted for fatigue testing (Xiao et al. 2009, 2010; Liu and He 2012; Lei et al. 2017). Stress-controlled laboratory tests were used to calibrate the numerical simulations.

In numerical modelling, loading strategies commonly use boundary walls to run strain-controlled experiments. A wall is usually used as loading platen in PFC (Kulatilake et al. 2001; Potyondy 2007, 2015; Bahaaddini et al. 2013; Park and Min 2015; Zhao et al. 2015). However, here we present a uniaxial stress-controlled loading method. This can be properly implemented through so-called clumps (a clump refers to a fixed unbreakable ball assembly with overlap). In order to make the contact smooth (similar to a wall boundary), the Dense Clump Block wall (DCB-wall) is proposed. The DCB-wall is composed of pebbles with same radii r. The distance between two pebbles of a DCB-wall are $2r$, $0.5r$ and $0.25r$, respectively. With decreasing pebble distance the number of contact points of a DCB-wall increases, see in Figure 4.8.
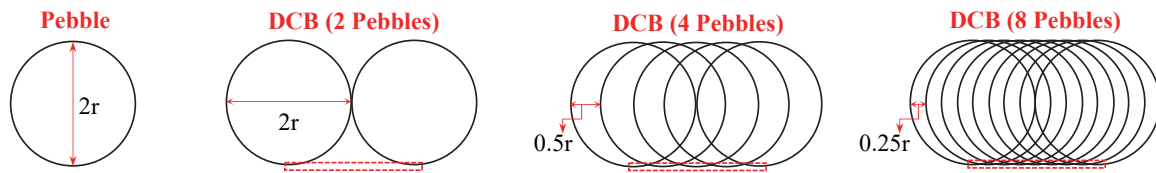
Figure 4.8 DCB-walls with different number of overlapping pebbles

The contacts between the ball assembly and the loading platen serve as force transmission. An uneven contact distribution can result in undesirable stress concentrations. It becomes clear that a DCB-wall with higher number of pebbles generates a smoother force transmission, which is in agreement with loading platen in laboratory tests, see Figure 4.9.
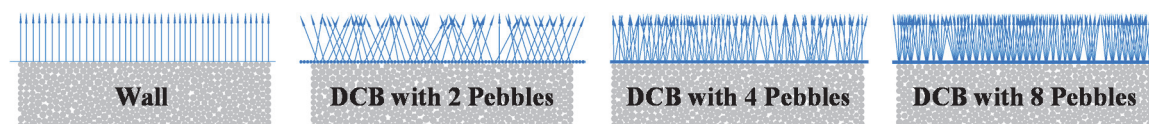
Figure 4.9 Contacts between assembly and DCB-wall

In order to select the most proper DCB-wall as loading platen, a calibration of DCB-wall is needed. The calibration is performed in four steps. First, the ball assemblies are generated with identical micro parameters to guarantee identical properties. Second, uniaxial compressive strength (UCS) tests are conducted with different DCB-walls and loading rates. Third, UCS tests with different loading methods and loading rates are compared like shown in Figure 4.10.

Figure 4.10a illustrates the axial strain rates (solid coloured lines) for DCB loading method and axial strain rates (dash coloured lines) for wall loading method (wall). The curves of axial strain rate under DCB loading and wall loading conditions before failure are highly linear and coincident, which demonstrates elasticity of the assembly before reaching peak stress. Figure 4.10b illustrates typical stress-strain curves of two concrete samples (2.13 g/cm^3 (ρ), 125 mm height (H), 50 mm diameter (ψ), loading rate 5 MPa/min) during uniaxial compressive laboratory tests and numerical simulations. It is obvious that the stress-strain curves of laboratory tests are more coincident with the numerical simulation results using DCB loading conditions (green triangle symbols in Figure 4.10b). Figure 4.10c shows UCS results for assemblies tested under different loading conditions and loading rates. It is observed that the UCS values obtained by a DCB-wall with 4 pebbles is closest to the values obtained by using a wall. Therefore, all further simulations use a DCB-wall with 4 pebbles. The mechanical age refers to the product of time-step and total calculated steps.
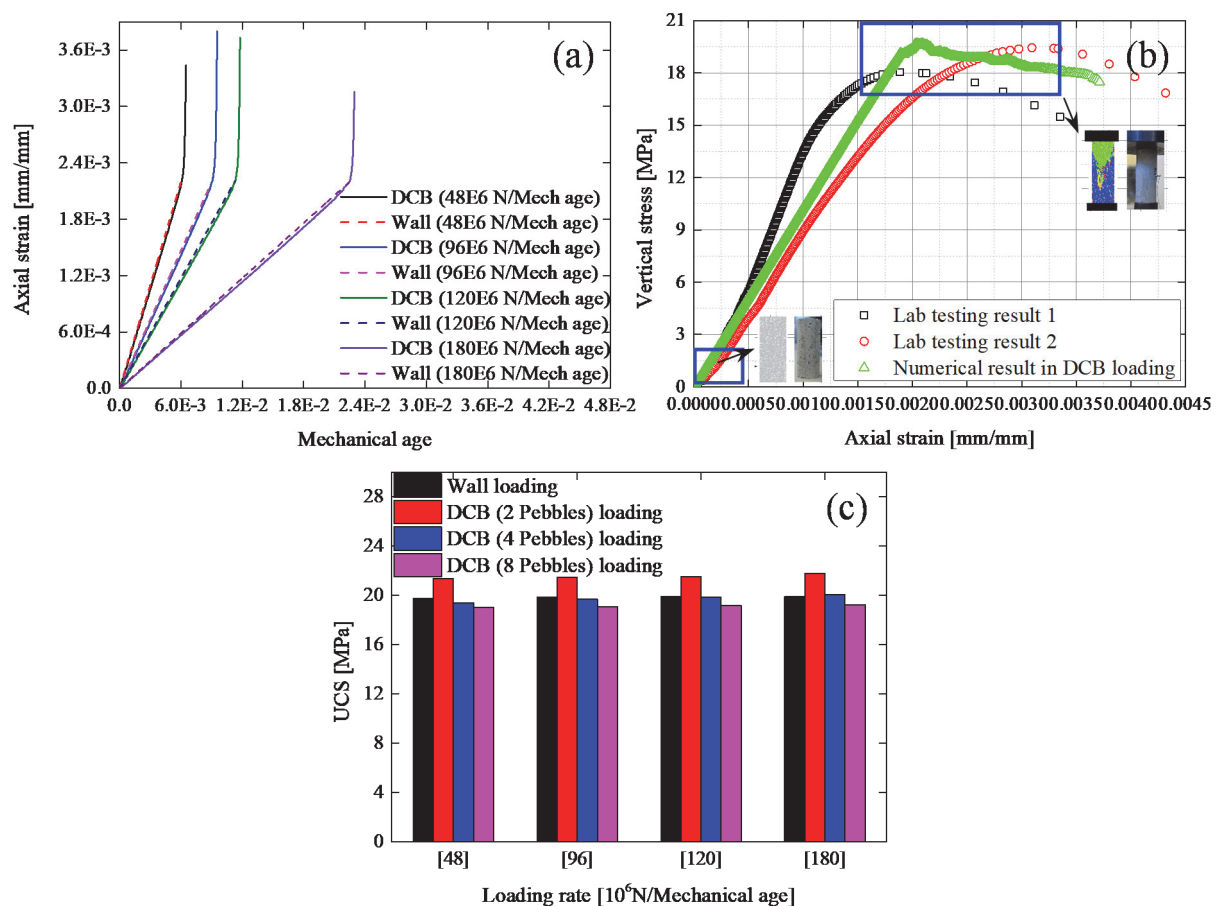
Figure 4.10 (a) axial strain vs. mechanical age: numerical simulations (b) axial stress-strain curves: laboratory tests and numerical simulations with DCB loading (c) UCS obtained with different DCB-walls

A sinusoidal loading (same as in laboratory fatigue tests) is implemented in PFC via the internal programme language FISH (Figure 4.11). Due to hardware limitations, the wave form for the laboratory testing is constructed by only seven sampling points for each cycle, whereas the wave form for the numerical simulation is represented by a continuous sinusoidal equation and a high resolution (sampling rate) of 15 kHz. So little difference of loading wave form can be observed in Figure 4.11, but it doesn't has major influence on the result of the simulations.
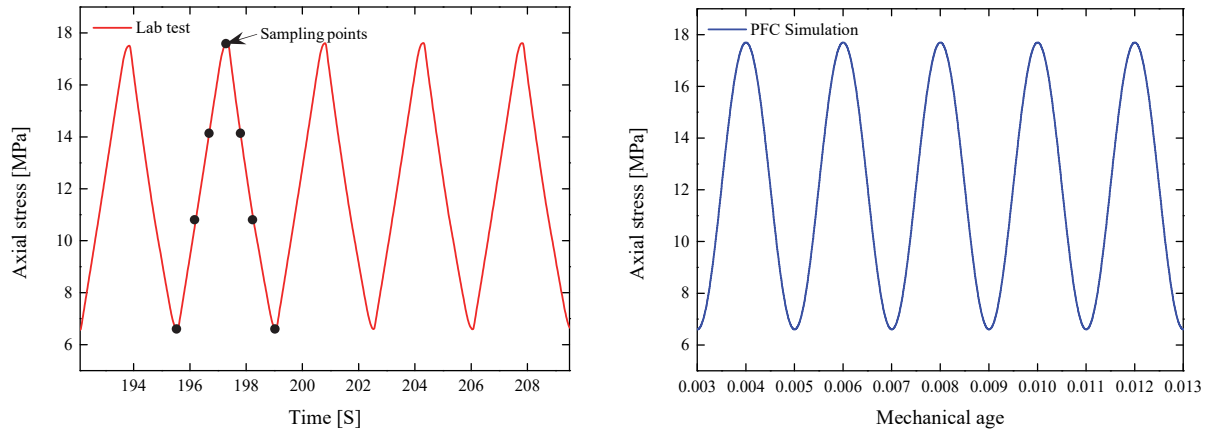
Figure 4.11 Wave form for laboratory tests and numerical simulations

4.3.2.2 Sensitivity analysis and parameter calibration

First of all, the micro mechanical parameters of LPBM have to be calibrated by mechanical laboratory tests. The data of the concrete specimen numbered S1-7 are used for the sensitivity analysis. The physical properties are shown in Table 4.1. The stress-strain curve of S1-7 during the fatigue test is shown in Figure 4.12.

Table 4.1 Geometrical and physical properties as well as loading parameters for S1-7

Length [mm]	Diameter [mm]	Density [g/cm³]	P-wave speed [m/s]	Loading frequency [Hz]	Cyclic load level [% UCS]
125.51	50.22	2.10	3730	0.4	40-95
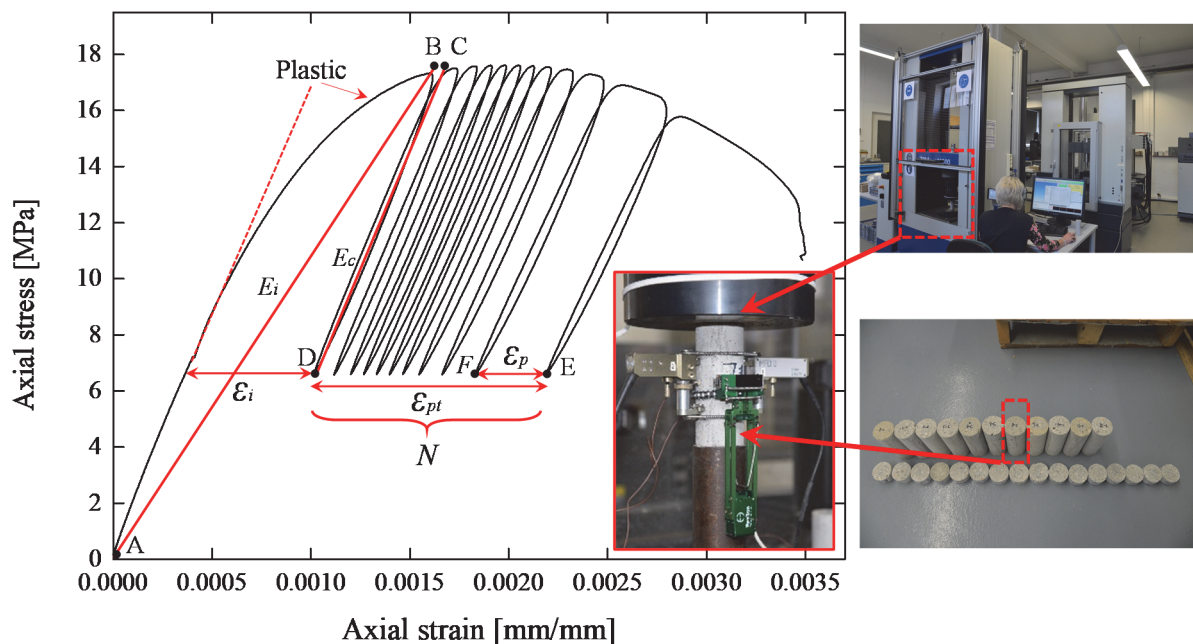
Figure 4.12 Stress-strain curve of sample S1-7 during laboratory fatigue test

The main parameters which have to be calibrated (see Figure 4.12) are: 1. Residual axial strain ε (difference value of the axial strain between two consecutive cycles at the minimum load level); 2. Elastic modulus E (secant modulus between maximum and minimum load points) and 3. Fatigue life N (total number of cycles until failure). The plastic axial strain includes total plastic axial strain ε_{pt} and plastic axial strain of each cycle ε_p. The elastic modulus E includes the elastic modulus of the initial cycle E_i and the elastic modulus after initial cycle E_c. The fatigue life N is a significant parameter directly related to the damage rate in the NPSC model.

4.3.2.3 Calibration of Young's modulus

As visible in Figure 4.12, the stress-strain curve is nonlinear during the loading stage of the initial cycle. This behaviour has been described in many publications (Ge 1987; Ge et al. 2003; Bagde and Petroš 2005; Xiao et al. 2009; Liu and He 2012; Momeni et al. 2015). The nonlinearity indicates that the concrete itself has undergone some plastic deformations from point A to point B (Borja 2013), but even more important are the plastic deformations inside the two interfaces between sample and loading platens. No special attention has been paid to capture the obvious initial phase of plastic deformations. Although this is a general shortcoming and should be overcome in future research, it is of minor importance for the subsequent modelling of cyclic fatigue. The corresponding elastic modulus is equivalent to the secant modulus from point A to point B as shown in Figure 4.12. E_i is determined by two sets of stiffness parameters: 1. the stiffness of linear contact interface k_n and k_s; 2. the stiffness of

parallel bond interface k_n' and k_s'. The subscripts n and s indicate normal and shear direction, respectively. The calibration of E_i should be considered together with the calibration of E_c. The sensitivity analysis revealed that the ratio of k_n/k_n' directly influences both, E_i and E_c when the ratio of k_n/k_s and k_n'/k_s' is fixed. In this thesis a value of 2.5 is used for k_n/k_s and k_n'/k_s' as suggested by Potyondy and Cundall (2004) and Qin and Zhang (2011). The conversions between Young's moduli and normal stiffness are different for linear contact and parallel bond as shown in Equation 4.18. E_l is the elastic modulus for the linear contact and E_p is the elastic modulus for the parallel bond. Where R_1 and R_2 are the radii of the two particles in contact.

$$E_l = k_n L / A$$
$$E_p = k_n' L$$
$$A = 2rq, q = 1$$
$$L = \begin{cases} R_1 + R_2, & \text{ball-ball} \\ R_1, & \text{ball-wall} \end{cases}$$
$$r = \begin{cases} \min(R_1, R_2), & \text{ball-ball} \\ R_1, & \text{ball-wall} \end{cases}$$

(4.18)
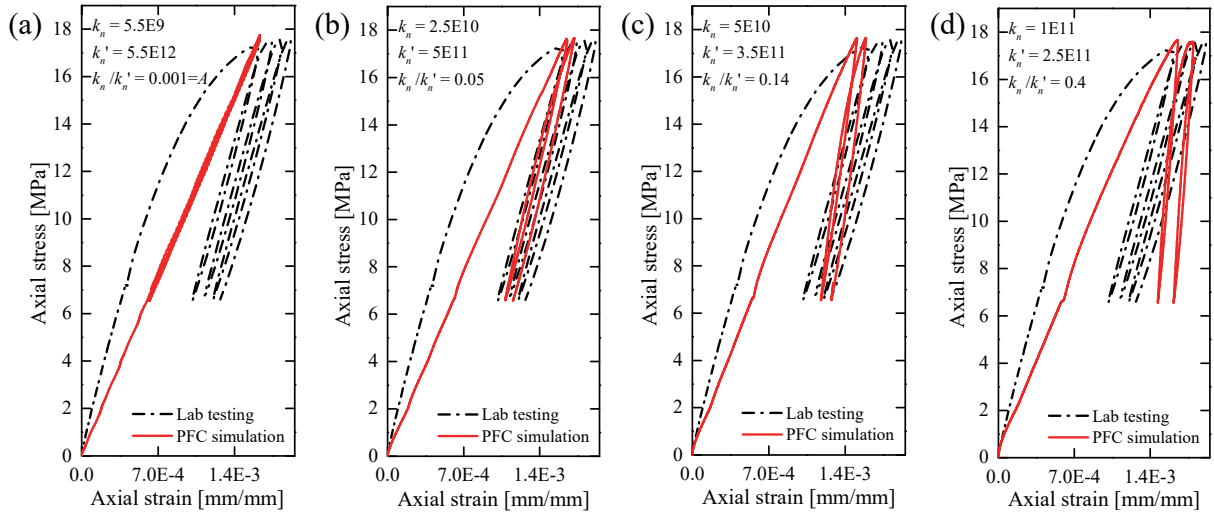
Figure 4.13 Stress-strain curves for different values of k_n/k_n' (a) 0.001 (b) 0.05 (c) 0.14 (d) 0.4

Figure 4.13a-d illustrate the stress-strain curves for different ratio of k_n/k_n'. E_l and E_p are usually suggested to have the same value (Potyondy and Cundall 2004), so the ratio of k_n/k_n' is equal to A for the suggested method. The simulation result for $k_n/k_n' = A$ is shown in Figure 4.13a. Such a simulation cannot simulate the difference in the stress-strain curves between the initial cycle and the later cycles. Furthermore, the residual strain almost remains the same with increasing number of cycles. Therefore, the calibration of Young's moduli should start from

E_c and k_n and is restricted to a reasonable range, then E_i is calibrated based on the effect of k_n and k_n' and the ratio of k_n/k_n'. As Figure 4.13 shows, for k_n/k_n' equal to 0.05, the numerical stress-strain behaviour fits well the laboratory results. So the ratio 0.05 of k_n/k_n' is used in subsequent numerical simulations.

4.3.2.4 Calibration of plastic axial strain

The plastic axial strain is extensively used as damage variable for evaluation of lab tests (Xiao et al. 2010; Sun et al. 2017; Song et al. 2018a) and in numerical simulations (Liu et al. 2017; Sinaie et al. 2018). As shown in Figure 4.12, the plastic strain includes the total plastic axial strain ε_{pt} and plastic axial strain of each cycle ε_p. When the bond tensile or shear strength is reached, force and moment carried by the parallel bond interface are set to zero due to the removal of interactions at the parallel bond interface. Increasing plasticity in the normal direction can be realized by the evolution of bond breakages. The normal contact force ΔF_{cn} is update as shown in Equation 4.19. ΔF_{ln}, ΔF_{dn} and ΔF_{pn} are the increments of linear force, dashpot force, and parallel bond force in normal direction.

$$\Delta F_{cn} = \Delta F_{ln} + \Delta F_{dn} + \Delta F_{pn}$$
$$\Delta F_{ln} = k_n U_n$$
$$\Delta F_{d} = 2\beta_n \sqrt{m_c k_n}(\dot{U}_n)$$
$$\Delta F_{pn} = k_n' A U_n$$

$$(4.19)$$

U_n is the increment of relative normal displacement between two particles; β_n is the normal critical damping ratio; m_c is the mass of the two particles in contact and A is the contact area between the two particles. ΔF_d is extremely small compared to ΔF_{ln} and ΔF_{pn}. Therefore, Equation 4.19 can be transformed into Equation 4.20

$$\Delta F_{cn} = \Delta F_{ln} + \Delta F_{pn} = U_n \left(k_n + k_n' A \right)$$
$$U_n = \Delta F_{cn} / \left(k_n + k_n' A \right)$$

$$(4.20)$$

When the bond is not broken, the relative displacement is calculated by Equation 4.20. When the bond is broken, the update of ΔF_{pn} is removed and Equation 4.20 is transformed into Equation 4.21. The micro plastic deformation U_p in the normal direction induced by bond breakage is equivalent to the difference value of Equation 4.21 and Equation 4.20 when the increment of contact force has not changed (see Equation 4.22).

$$U_n' = \Delta F_{cn} / k_n \tag{4.21}$$

$$U_p = \frac{\Delta F_{cn} k_n' A}{k_n (k_n + k_n' A)} \tag{4.22}$$

This combination of micro plastic deformations between particles can reproduce the macroscopic plastic deformation of an assembly. The total normal plastic deformation of an assembly is calculated by Equation 4.23 for stress-controlled loading conditions, where n is the number of broken bonds. The phenomenon that the number of broken bonds is proportional to the plastic deformation of an assembly can be observed for various loading conditions based on the LPBM (Cho et al. 2007; Yoon et al. 2012; Bahaaddini et al. 2013; Itasca Consulting Group Inc. 2014; Vervoort et al. 2014; Park and Min 2015).

$$\sum_1^n U_p = \frac{\Delta F_{cn} k_n' A}{k_n (k_n + k_n' A)} \tag{4.23}$$

The linear reduction of bond diameter in the PSC model has limited effect in terms of replicating the complex evolution of plastic strain. Therefore, the NPSC model (Figure 4.7) is proposed. In order to choose the most appropriate time-dependent reduction strategy for bond diameter, logarithmic, linear, exponential and multi-stage reduction strategies were evaluated by comparing stress-strain curves and axial plastic strains, see Figure 4.14. The stress-strain curve shows 'loose-dense-loose' characteristics in laboratory tests, also documented by Ge et al. (2003) and Xiao et al. (2009). The simulation strategy shown in Figure 4.14a shows that most distinct features of 'loose-dense-loose' are reproduced according to the laboratory tests. The axial strain evolution is plotted in Figure 4.14e. It is obvious that the observed three-phase characteristic of axial strain in laboratory tests is well reproduced with all four functions. From the viewpoint of axial strain evolution and total residual strain at failure, it can be concluded that the logarithmic function delivers a perfect fit with the laboratory results. Therefore, it is suggested that a logarithmic reduction of the bond diameter should be adopted for numerical simulation of fatigue tests when a sample fails in a single cyclic load level.
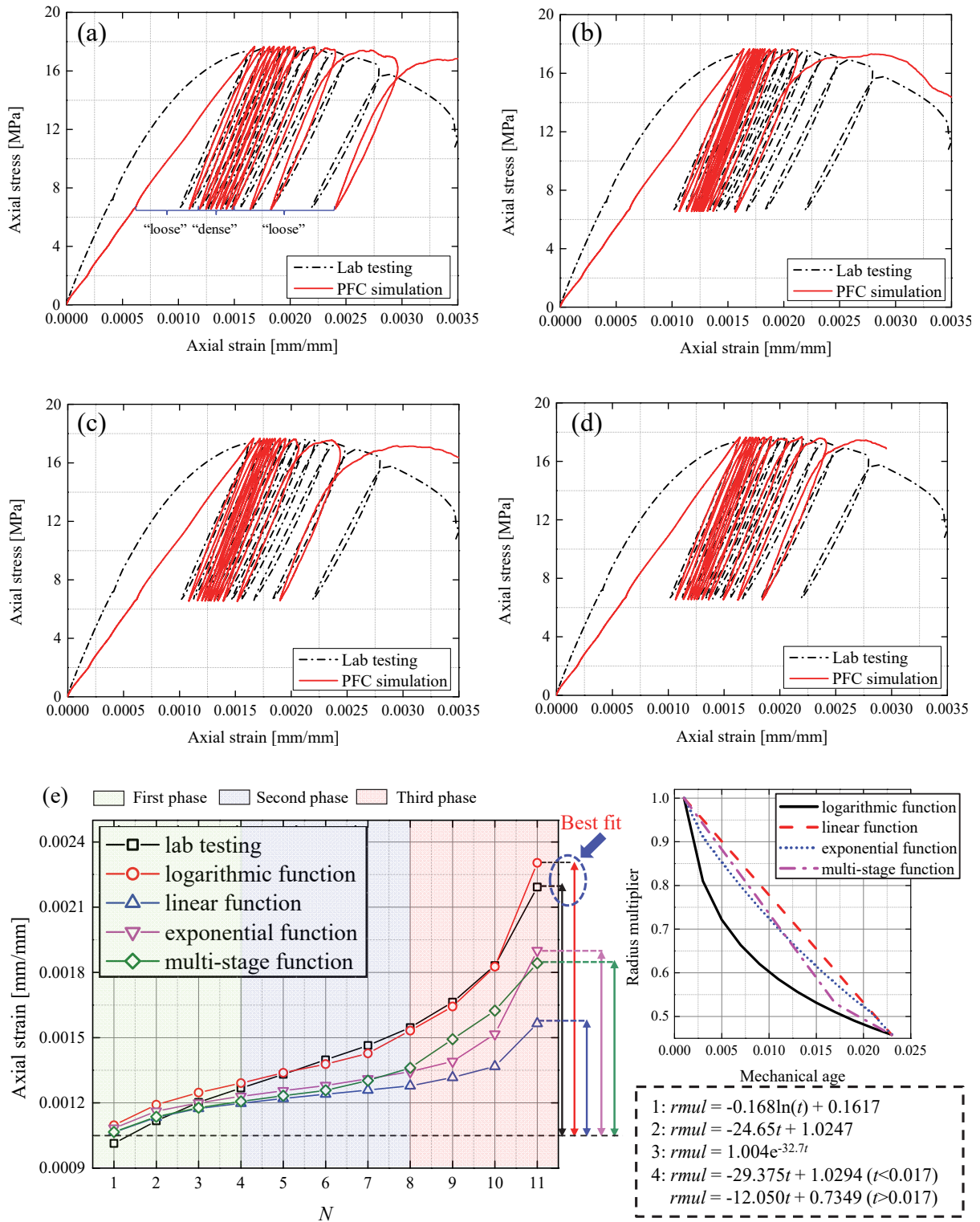
Figure 4.14 Stress-strain curves with different reduction strategies of bond diameter (a) logarithmic function (b) linear function (c) exponential function (d) multi-stage function (e) strain evolution for different reduction strategies of bond diameter

Figure 4.15 shows that the total plastic axial strain at failure ε_{pt} in uniaxial fatigue tests is larger than the corresponding value $\varepsilon_{0.95pk}$ in a uniaxial compressive test. The values of ε_{pk} is also

smaller than ε_{pt}. This result is also observed by other researchers (Ge et al. 2003). This indicates that cyclic loading increases the axial strain at failure compared to static loading. It is essential to reproduce this behaviour also in the simulations. Therefore ε_{pt} has to be calibrated. Figure 4.16 shows the relation between strain evolution and number of bond breakages. Figure 4.16a and Figure 4.16b document, that plastic axial strain at failure (the eleventh cycle) is proportional to the number of bond breakages (like the linear relation shows in Figure 4.16c).
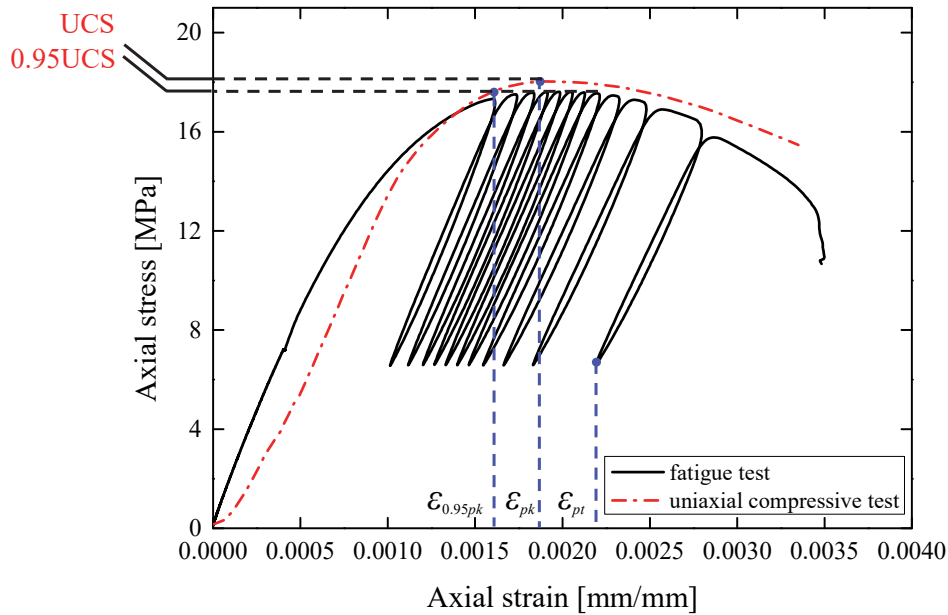
Figure 4.15 Stress-strain curves for uniaxial compressive and fatigue tests
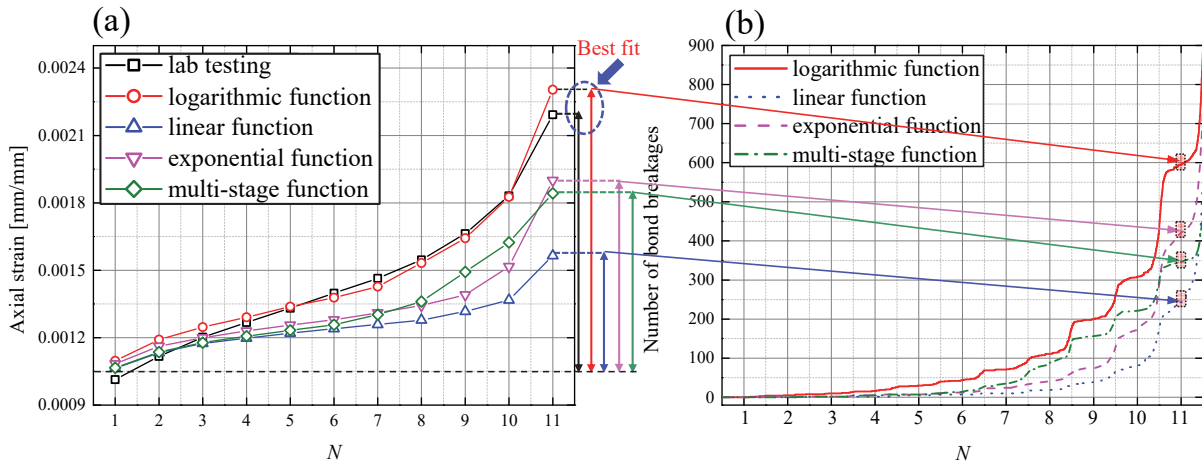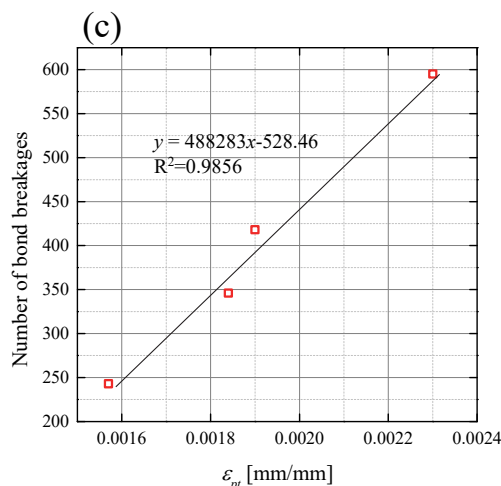
Figure 4.16 Relation between strain evolution and number of bond breakages (number of cracks) (a) axial strain evolution (b) crack evolution (c) plastic axial strain at failure vs. number of bond breakages

The sensitivity analysis documents that ε_{pt} at failure is dominated by bond tensile strength. When a specific tensile strength is applied, number of bond breakages and whole plastic strain are controlled by cyclic load level and critical diameter multiplier λ (value of multiplier at failure). For simulation of monotonic loading, the bond tensile strength is usually calibrated on UCS (Potyondy and Cundall 2004). However, for cyclic loading the maximum axial strain cannot be increased to a value larger than the maximum axial strain in UCS tests, like shown in Figure 4.15. So, bond tensile strength should be assigned according to the calibration of the whole axial strain. Figure 4.17 illustrates the simulated stress-strain curves with different bond tensile strength values compared to the laboratory test of S1-7. Figure 4.17 shows that ε_{pt} decreases with decreasing tensile strength. The relation between bond tensile strength ε_{pt} and critical value of λ is plotted in Figure 4.17e. The relation between bond tensile strength and ε_{pt} is well fitted by a linear function. The relation between bond tensile strength and critical value of λ is well fitted by a logarithmic function. By comparing simulation and laboratory results, the bond tensile strength is suggested to be 1.5e7 Pa.
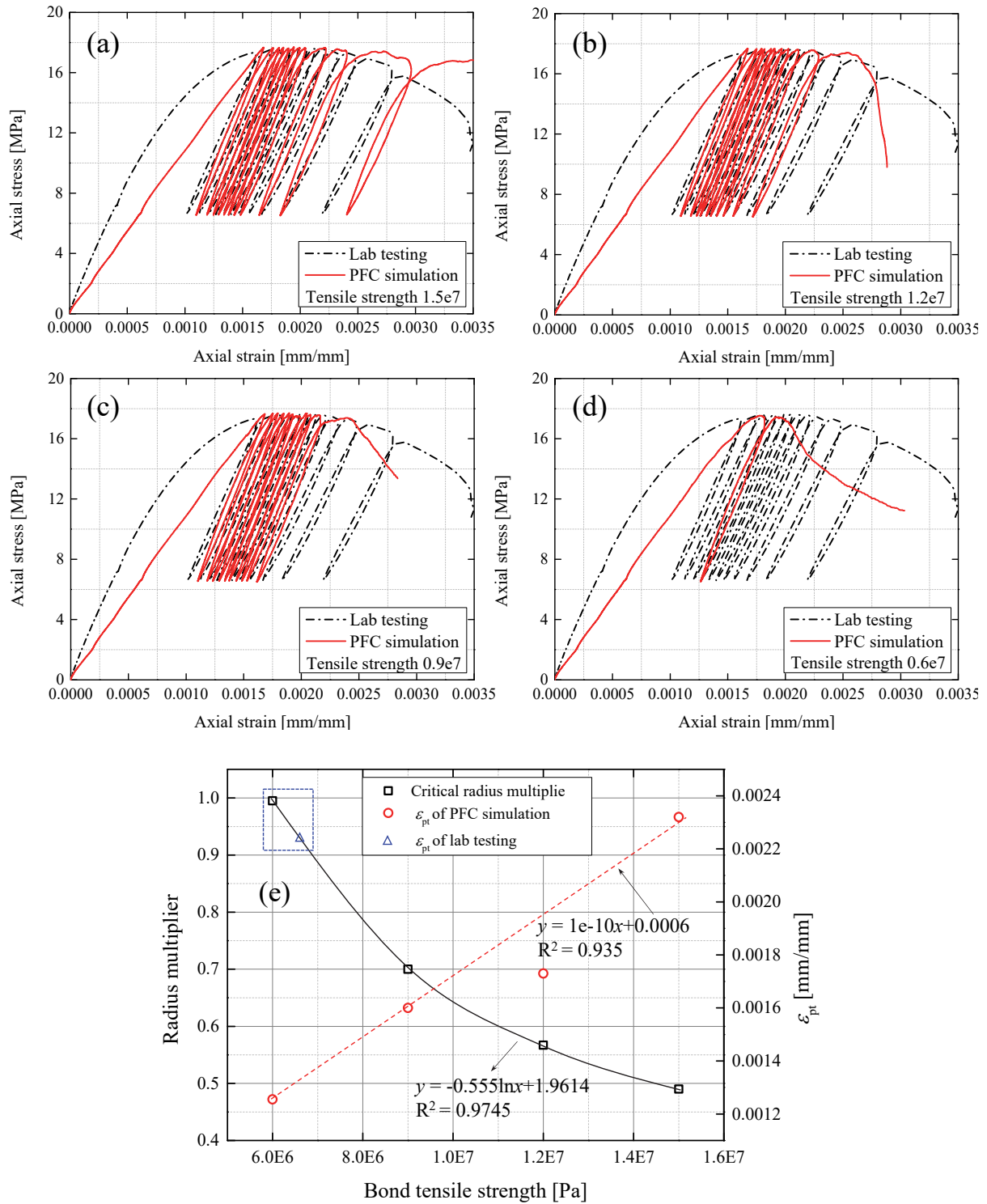
Figure 4.17 Stress-strain curves with different tensile strength values (a) 1.5e7 Pa (b) 1.2e7 Pa (c) 0.9e7 Pa (d) 0.6e7 Pa and (e) relation between bond tensile strength, ε_{pt} and critical value of λ

97

4.3.2.5 Calibration of fatigue life

The fatigue life N is defined as total number of load cycles until the sample fails. It is controlled by cyclic load level, tensile strength of bonds and critical value of λ (value at failure). When specific bond tensile strength and cyclic load level are applied, the critical value of λ is the unique unknown quantity, and it needs to be assigned to predict or calibrate fatigue life. The approach to determine critical value of radius multiplier is similar to the simulation of static fatigue which is proposed by Potyondy (2007). In detail, a constant load which is equal to the upper limit of cyclic load level is applied to the sample. Then the bond diameter gradually decreases following a linear function up to failure. Finally, the critical value of λ with respect to applied cyclic load level and tensile strength can be obtained.

4.3.3 Simulation results based on single-level fatigue testing

Test data from four samples (Sample S1-1, S1-3, S1-5 and S1-7) are selected from 16 artificial rock (concrete) samples to calibrate the numerical model. Load level and physical properties are documented in Table 4.2. The simulation results are illustrated in Figure 4.18 to Figure 4.21. S1-7 failed in the first cyclic loading stage, and S1-1, S1-3, S1-5 remained stable in the first cyclic loading stage with 20 cycles. It is obvious that the simulation results fit almost perfect the axial strain evolution. This documents that the NPSC model is capable to reproduce the mechanical fatigue behaviour even under different load levels. It is worth noting that only stiffness parameters of parallel bond (k_n', k_s') have to be changed by a small amount to better fit the modulus of concrete samples caused by the natural scatter of physical properties. The other parameters remained unchanged in the simulations of all four samples. The stress-strain curve of S1-7 shows the 'loose-dense-loose' three-phase characteristics and for S1-1, S1-3, but for S1-5 only the 'loose-dense' two-phase characteristic is observed.

Table 4.2 Loading parameters and material properties for S1-1, S1-3, S1-5 and S1-7

Sample	Length	Diameter	Density	P-wave speed	Load frequency	Cyclic load level
Unit	[mm]	[mm]	[g/cm^3]	[m/s]	[Hz]	[MPa]
S1-1	125.31	50.12	2.10	3481	0.4	6.56 - 15.05
S1-3	125.60	50.21	2.10	3606	0.4	6.56 - 12.36
S1-5	125.74	50.17	2.12	3657	0.4	6.56 - 14.18
S1-7	125.51	50.22	2.10	3730	0.4	6.56 - 16.82
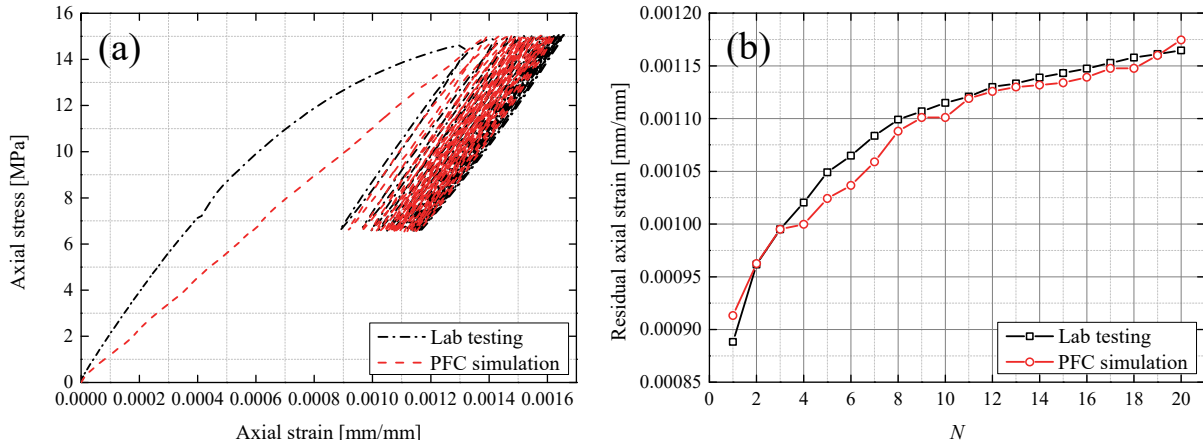
Figure 4.18 Simulation result of S1-1 (a) stress-strain curve (b) evolution of residual axial

strain vs. number of cycles
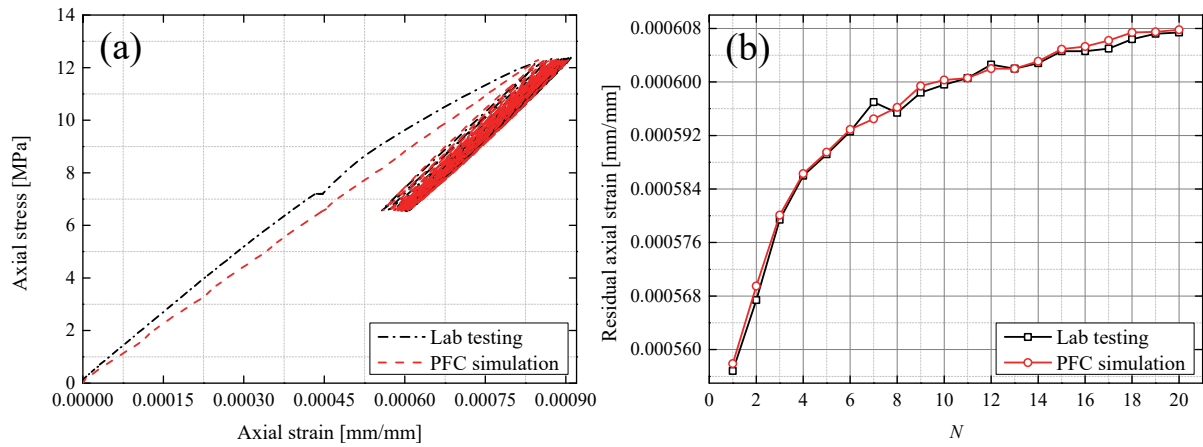
Figure 4.19 Simulation result of S1-3 (a) stress-strain curve (b) evolution of residual axial

strain vs. number of cycles
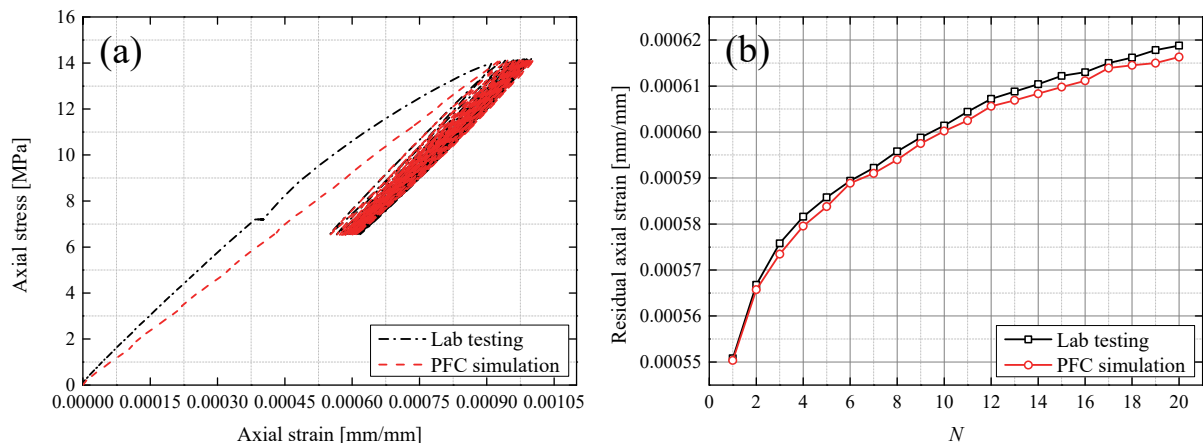
Figure 4.20 Simulation result of S1-5 (a) stress-strain curve (b) evolution of residual axial

strain vs. number of cycles
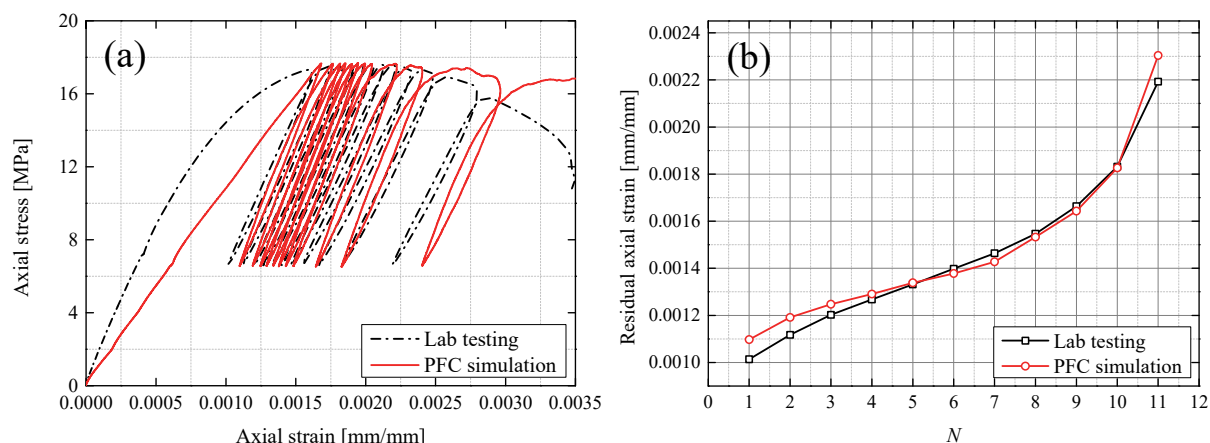
Figure 4.21 Simulation result of S1-7 (a) stress-strain curve (b) evolution of residual axial strain vs. number of cycles

The evolution of the radius multiplier λ for the NPSC model for the four samples is plotted in Figure 4.22. It can be seen that with increasing maximum cyclic load level, the radius multiplier reduction becomes stronger, which demonstrates that the damage evolution is stronger at higher load levels, which is also verified by laboratory tests (Xiao et al. 2010). It is also found that when maximum load level is small, like for S1-3 (65% UCS) and S1-5 (75% UCS), the evolution of λ is almost the same, which indicates that the load level is below the critical fatigue value, always defined as 80% UCS (Rao and Ramana 1992).
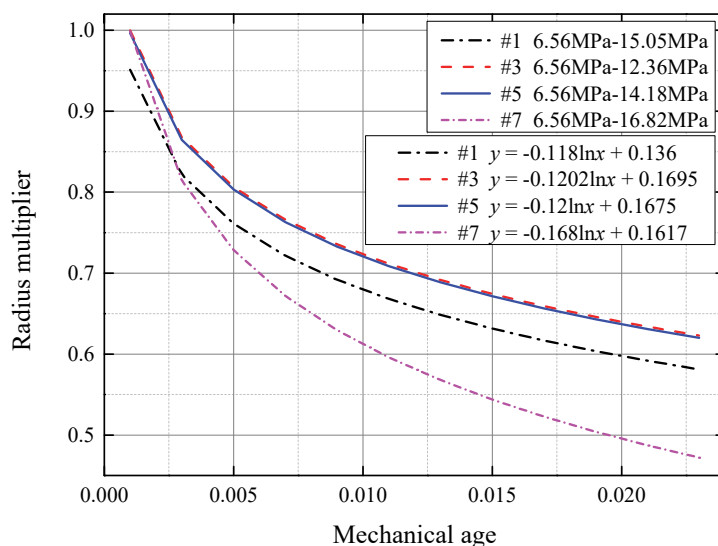
Figure 4.22 Evolution of radius multiplier for S1-1, S1-3, S1-5, and S1-7

4.3.4 Simulation of AE in single-level fatigue testing

Cumulative AE counts and cumulative AE energy are two main indexes to represent the evolution of damage. In LPBM, the bond breakage can explicitly represent the formation and

coalescence of micro cracks (Hazzard and Young 2000; Potyondy and Cundall 2004; Potyondy 2007) and the number of cracks can be used to represent the cumulative AE counts. Figure 4.23 shows the cumulative AE counts for S1-7. The relation between number of cracks and number of cycles N shows linearity in the laboratory tests, but non-linearity is observed in the simulations.
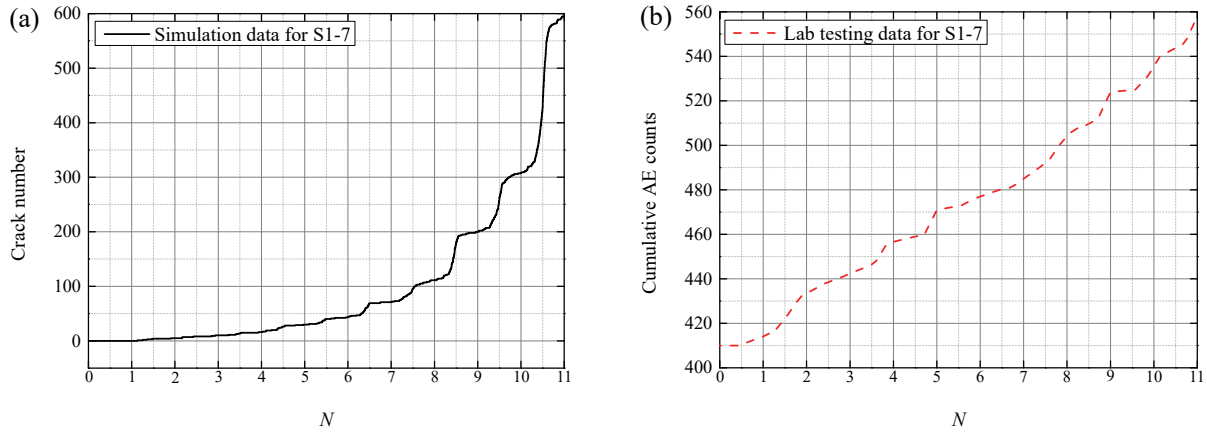
Figure 4.23 (a) number of cracks vs. number of cycles in simulations (b) cumulative AE counts vs. number of cycles in laboratory tests

The LPBM has the advantage of tracking and calculating the energy between particles. When a bond between particles breaks, the bond strain energy E_k will be released and tracked. E_k is updated according to Equation 4.24. A special function is used to accurately track the location of bond breakage and the amount of released energy E_k. Figure 4.24 shows a schematic diagram of AE energy simulation. The area of the circle in the enlarged figure are proportional to the amount of released bond strain energy. The circle centre is the location of the micro crack (source of AE energy). Figure 4.25 illustrates the cumulative E_k and the cumulative AE energy of S1-7 in laboratory tests. The trend of E_k during the simulations is very similar to the trend of cumulative AE energy during laboratory tests, especially the evolution characteristic at the last two cycles before failure.

$$E_k = \frac{1}{2}\left[\frac{F_{pn}^{\;2}}{k_n'A} + \frac{F_{ps}^{\;2}}{k_s'A} + \frac{M_{pn}^{\;2}}{k_s'J} + \frac{M_{ps}^{\;2}}{k_n'I}\right]$$

(4.24)
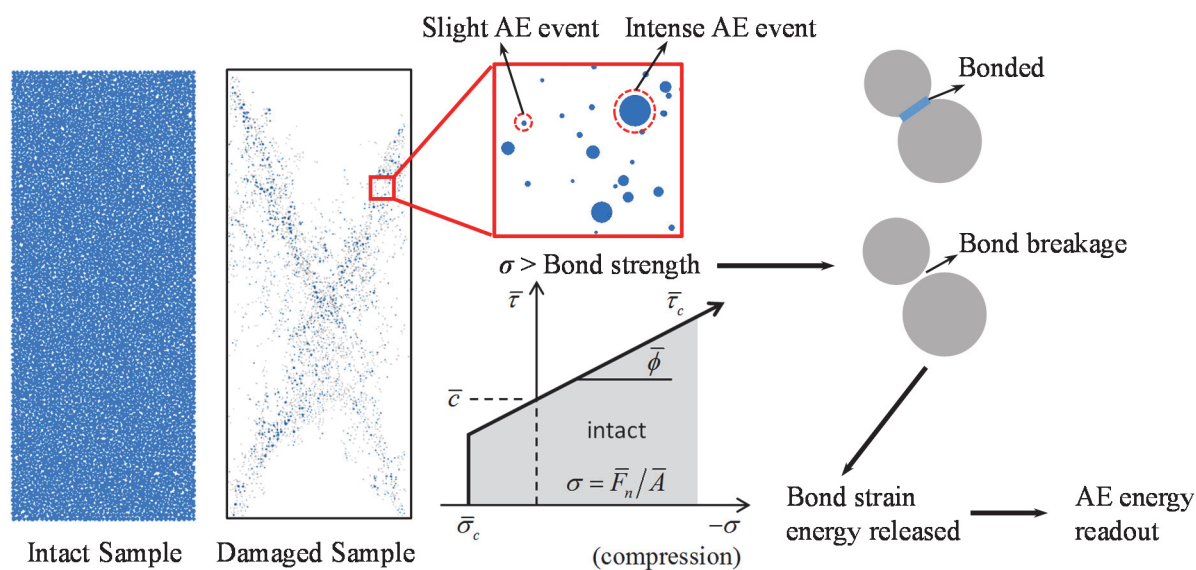
Figure 4.24 Scheme of AE monitoring in numerical simulations
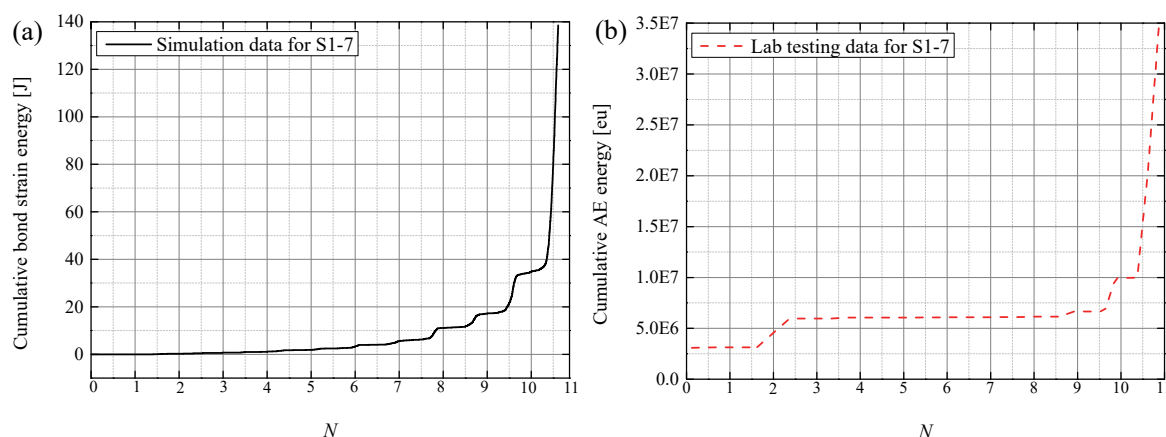
Figure 4.25 (a) cumulative released bond strain energy vs. number of cycles (b) cumulative AE energy vs. number of cycles

4.4 Numerical simulation of multi-level fatigue testing

4.4.1 Multi-level Stress Corrosion (MSC) model

Many laboratory test results document that axial strain rate and dissipated energy are stress-dependent during cyclic loading (Liu and He 2012; Oneschkow 2016; Lei et al. 2017; Liu et al. 2018b; Song et al. 2018a). This indicates that a change of load level (σ_{max}, σ_{min}) has direct influence on the damage during cyclic loading. Namely, the damage of cyclically loaded material is stress-dependent. The basic logic of the MSC model is to quantitatively characterize the damage with respect to the load level during multi-level cyclic loading. For cyclic loading stages in which the sample do not fail, the axial strain rate is quite small compared to the failure stage, the bond diameter remains at a constant value (radius multiplier λ is a constant but not

equal to 1) which represents the stable status of the sample. A smaller constant of λ (less than 1) can lead to larger axial strain rate according to Equation 4.16. The value of λ determines the strain rate during stable cyclic loading stages. The principle of the MSC model with stepwise or continuous increase or decrease of σ_{max} and σ_{min} is illustrated in Figure 4.26. The damage, characterized by reduction of the bond diameter (determined by λ) is also changing. Considering the generality and applicability of the model, a clear and general form of the relation between damage and load levels (σ_{max} and σ_{min}) should be established. Based on the results of multi-level compressive cyclic loading, this section investigates the quantitative relation of damage rate with respect to both, σ_{max} and σ_{min} via numerical simulations.

4.4.2 Application of MSC model in multi-level fatigue testing

Different from the simulation of single-level fatigue testing, the numerical simulation of multi-level fatigue testing is based on PFC^{3D}. A three-dimensional numerical model can more realistically replicate the interactions between grains and better characterize the mechanical behaviour of concrete samples in the laboratory testing.
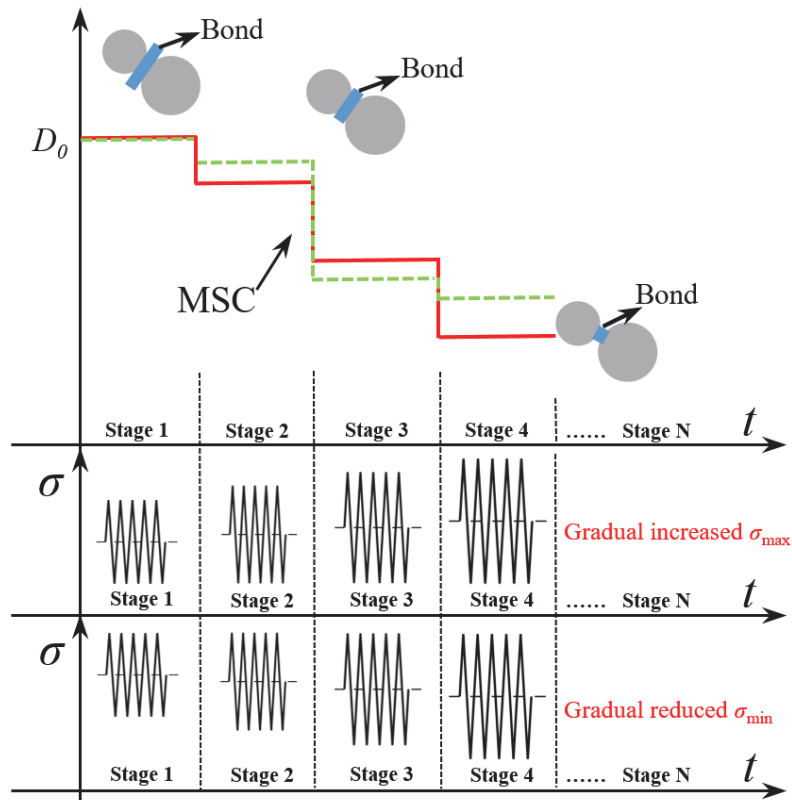
Figure 4.26 Illustration of some potential MSC models

4.4.2.1 Implementation of a 3D stress-controlled cyclic loading system
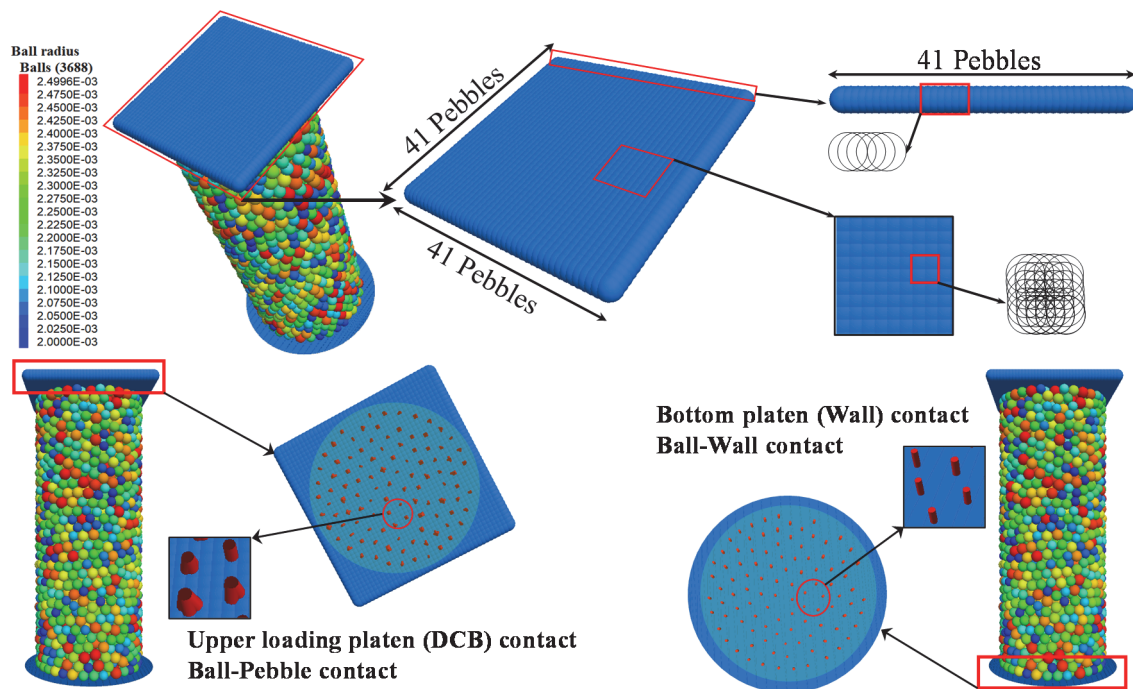
Figure 4.27 Particle based stress-controlled 3D loading system

The stress-controlled 3D cyclic loading system implemented in PFC^{3D} is shown in Figure 4.27. The applied numerical loading strategy is the same as those used in the laboratory tests. A 3D dense clump block-wall (DCB-wall) is generated acting as stiff and unbreakable loading platen. As shown in Figure 4.27, the square shaped DCB is composed of 1681 (41 × 41) pebbles. The distance between two pebbles is 0.25 times the pebble radius. The contacts of the two sample interfaces (upper interface ball-pebble contact and bottom interface ball-wall contact) are also plotted in Figure 4.27. It can be observed that the contact of both interfaces are evenly distributed within the range of the sample section. The contact normal directions are almost vertical to the loading platen, which is consistent with the loading platen used during the laboratory tests (Song et al. 2019d).

4.4.2.2 Stress wave transmission

The numerical model should well reproduce the cyclic waveform to guarantee the accuracy of the stress transmission. Figure 4.28a and Figure 4.28b show the waveforms: laboratory testing vs. numerical simulation. It indicates that the sinusoidal stress waveform is well reproduced in the numerical simulation. Figure 4.28c illustrates that the numerical assembly has the same geometry as the laboratory specimen. Three measure spheres (upper, middle and bottom) are selected to check the vertical (Z-Z direction) stress wave transmission. Figure 4.28d shows the

vertical stress within the three measuring spheres. All the three curves show the sinusoidal shape and document good consistency during the multi-level loading stages. Therefore, Figure 4.28 proves that the vertical stress transmission in the numerical model is almost homogeneous and consistent with the stress-wave in laboratory testing.
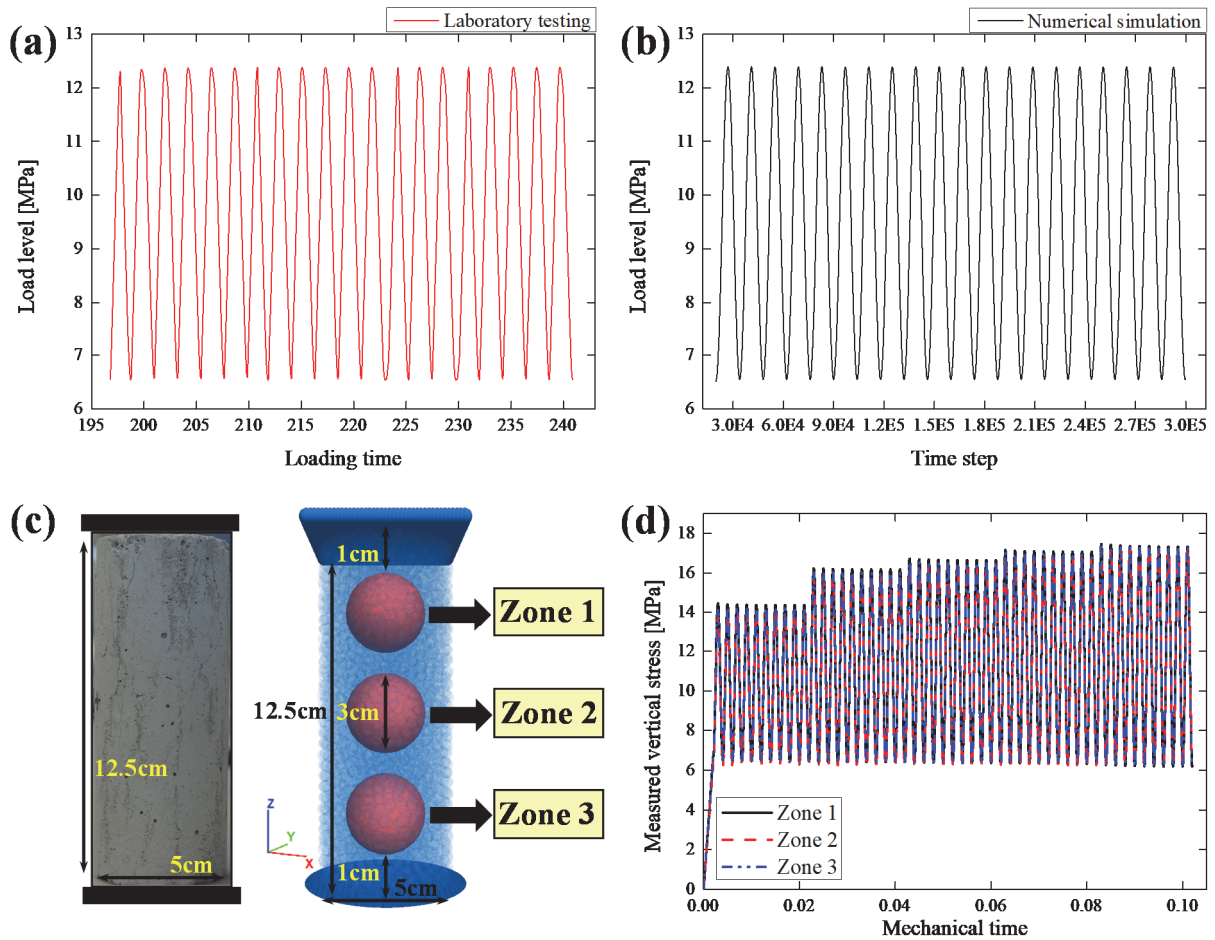
Figure 4.28 (a) stress waveform in laboratory testing (b) stress waveform in numerical simulation (c) layout of three measure circles (d) measured vertical (Z-Z) stress within the three measure circles

4.4.2.3 Micro-parameters assignment

The microscopic parameters of the numerical model are listed in Table 4.3. In order to guarantee the homogeneity of the macroscopic strength of numerical samples, the strength related micro-parameters σ_t, ϕ and f are fixed and only stiffness related parameters (k_n, k_s and k_n', k_s') vary in a limited range to better fit the macroscopic parameters such as Young's modulus and Poisson's ratio. The detailed parameter calibration is similar to that described in section 4.3.2 and is not presented in detail anymore here.

Table 4.3 Microscopic parameters of numerical model

Ball number	Ball radii [m]	Porosity [%]	Density [kg/m³]	k_n [N/m]	k_s [N/m]
3688	2e-3 – 2.5e-3	32	2100	7.8e7 – 8.2e7	3.9e7 – 4.1e7

k_n' [Pa/m]	k_s' [Pa/m]	Tensile strength σ_t	Friction angle ϕ	Friction coefficient	Normal damping
1.8e11 – 3.8e11	9e10 – 1.9e11	1.5e7	26.5	0.5	0.5

Shear damping	Pebble radius [m]	Pebble density [kg/m³]	Pebble overlap [m]	Sample height [m]	Sample radius [m]
0.5	2.6e-3	9000	6.5e-4	0.125	0.025

4.4.3 Simulation results based on multi-level fatigue testing

4.4.3.1 Multi-level cyclic loading with gradual increase of σ_{max}

The simulation with multi-level cyclic loading and gradual increase of σ_{max} is based on three concrete samples (S1-5, S1-12 and S2-13). All three samples experienced at least four cyclic loading stages with different load levels. Physical properties and loading scheme are listed in Table 4.4 and Table 4.5.

Table 4.4 Physical properties of samples S1-5, S1-12 and S2-13

Sample No.	Wave velocity [m/s]		Dyn. elastic modulus [GPa]	Length [mm]	Diameter [mm]	Density [g/cm³]	Mass [g]
	P-wave	S-wave					
S1-5	3657	2260	25.83	125.74	50.17	2.12	527.22
S1-12	3832	2459	30.11	126.09	50.18	2.17	538.90
S2-13	4096	2289	28.75	123.74	50.31	2.16	531.32

Table 4.5 Cyclic loading scheme of samples S1-5, S1-12 and S2-13

Sample No.	Stage 1	Stage 2	Stage 3	Stage 4	Stage 5
	Cyclic load level [MPa]				
S1-5	6.56 – 14.16	6.56 – 16.00	6.56 – 16.44	6.56 – 16.90	6.56 – 17.33
S1-12	6.89 – 16.48	6.89 – 17.46	6.89 – 17.90	6.89 – 18.35	6.89 – 18.81
S2-13	7.12 – 12.37	7.12 – 13.36	7.12 – 14.31	7.12 – 15.29	

For the three specimens, the first ten cycles of each cyclic loading stage are selected to calibrate the numerical model. According to Equation 4.16, the reduction of the bond diameter will lead to an increase of axial strain at the end of each cycle. Namely, a smaller bond diameter will result in a larger residual strain rate during the cyclic loading. Many publications documented that an increase of σ_{max} leads to a larger residual axial strain rate (Liu et al. 2011, 2018b; Lei et al. 2017; He et al. 2018; Song et al. 2018a). A typical stress-strain relation during multi-level cyclic loading of S1-5 (five stages) is shown in Figure 4.29. A preliminary logic for MSC can be established, so that the bond diameter of two bonded particles should decrease to a smaller

value with increasing σ_{max} when a sample experiences several cyclic load levels. It can be observed from Figure 4.29b and Figure 4.29c that, the residual strain rate during the initial stage is quite large compared to the following stages, which is attributed to the fact that the sample shows a compaction effect during the first several cycles of the initial stage. Before the initial cyclic loading stage, the sample is intact and the bond radius multiplier, λ, should start with 1, which represents the undisturbed (undamaged) sample. Therefore, for the initial stage, λ should decrease starting from 1. The NPSC model has revealed that for the initial cyclic loading stage, a logarithmic reduction of bond diameter can best replicate the stress-strain curve. For the MSC model, we adopt a linear reduction to achieve a more general and simpler law in terms of damage evolution during the initial cyclic loading stage.
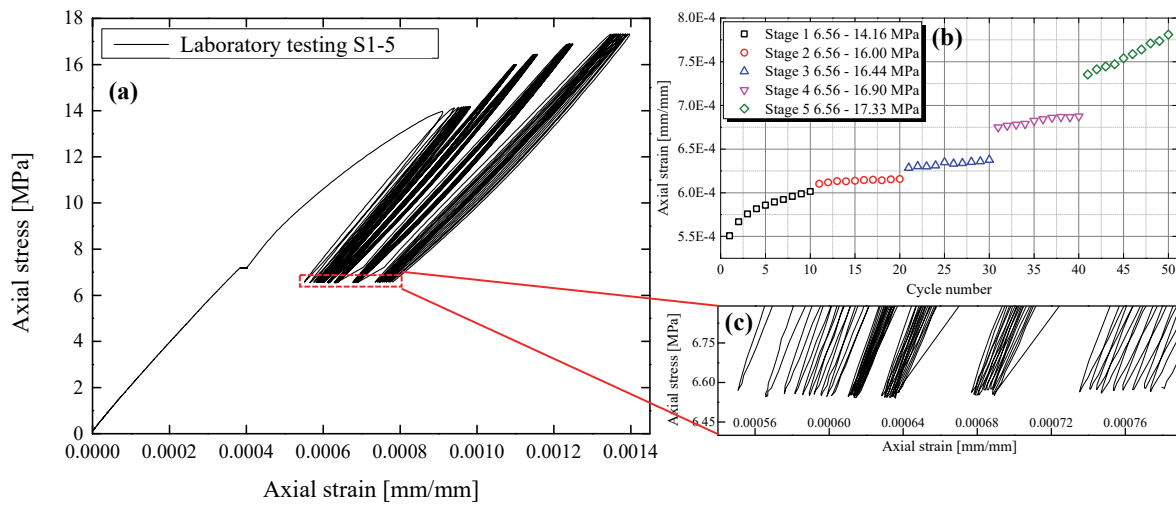
Figure 4.29 (a) stress and strain curves of S1-5 during five cyclic loading stages (b) residual strain evolution during five stages (c) enlarged residual axial strain

For the selected three samples, the evolution of the bond diameter (reduction of radius multiplier λ) with respect to σ_{max} is plotted in Figure 4.30. It is shown that, except for the initial cyclic loading stage, λ of all the three samples remains small and constant with increase of σ_{max} during the following loading stages. The initial cyclic loading stage is described by a linear reduction of λ due to the quite large axial strain rate induced by the compaction effect. A rise of λ is observed from the first to the second loading stage, which is attributed to a sudden drop of the strain rate during the second loading stage. This indicates that the compaction effect has disappeared after the initial loading stage, and the sample enters into the stable stage. Reduction of λ is not the only factor to accelerate the strain rate, the rise of σ_{max} can also contribute to a larger strain rate, as shown by Equation 4.25.

$$d\varepsilon_a/dN = f(D, \sigma_{max}, \lambda)$$

(4.25)

As shown in Figure 4.30, the relation between λ and σ_{max} for all three samples follow an exponential function (the initial stage is not fitted). With continuous increase of σ_{max}, the reduction speed of λ decreases. The stress-strain relations (hysteresis loop) for S1-5, S1-12 and S2-13 are shown in Figure 4.31a to 4.31c. As shown in Figure 4.31, the curves of the simulation (red dashed lines) show good consistency with laboratory test results (solid black lines). It can be observed that during the cyclic loading stages without sample failure, the elastic modulus in different loading stages is almost constant. This documents that damage induced by cyclic loading during the stable stages cannot be obviously reflected by the deterioration of elastic modulus. To more precisely characterize the damage in different loading stages, a more sensitive indicator is adopted: the axial strain rate ($d\varepsilon_a/dN$). The axial strain rate is composed of two parts: first: residual strain rate ($d\varepsilon_{ar}/dN$) and second: peak strain rate ($d\varepsilon_{ap}/dN$).
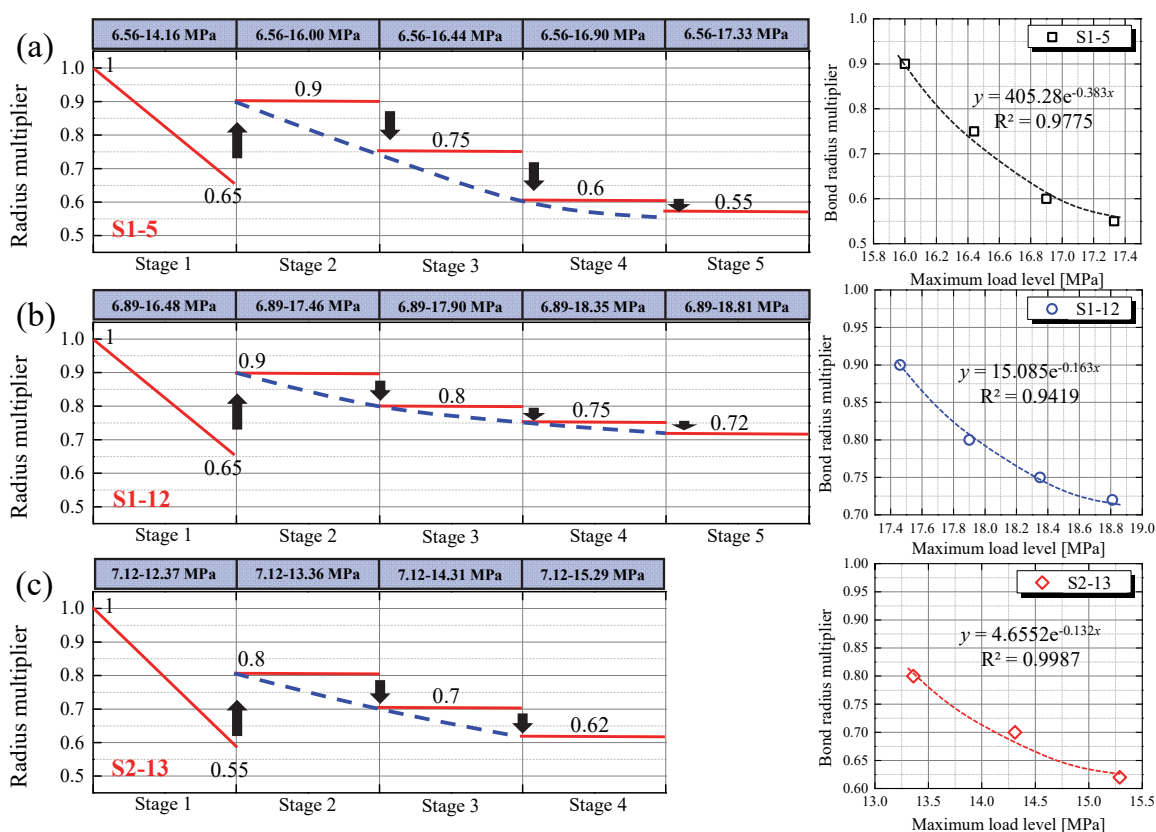
Figure 4.30 Evolution of bond radius multiplier (λ) for (a) S1-5 (b) S1-12 and (c) S2-13
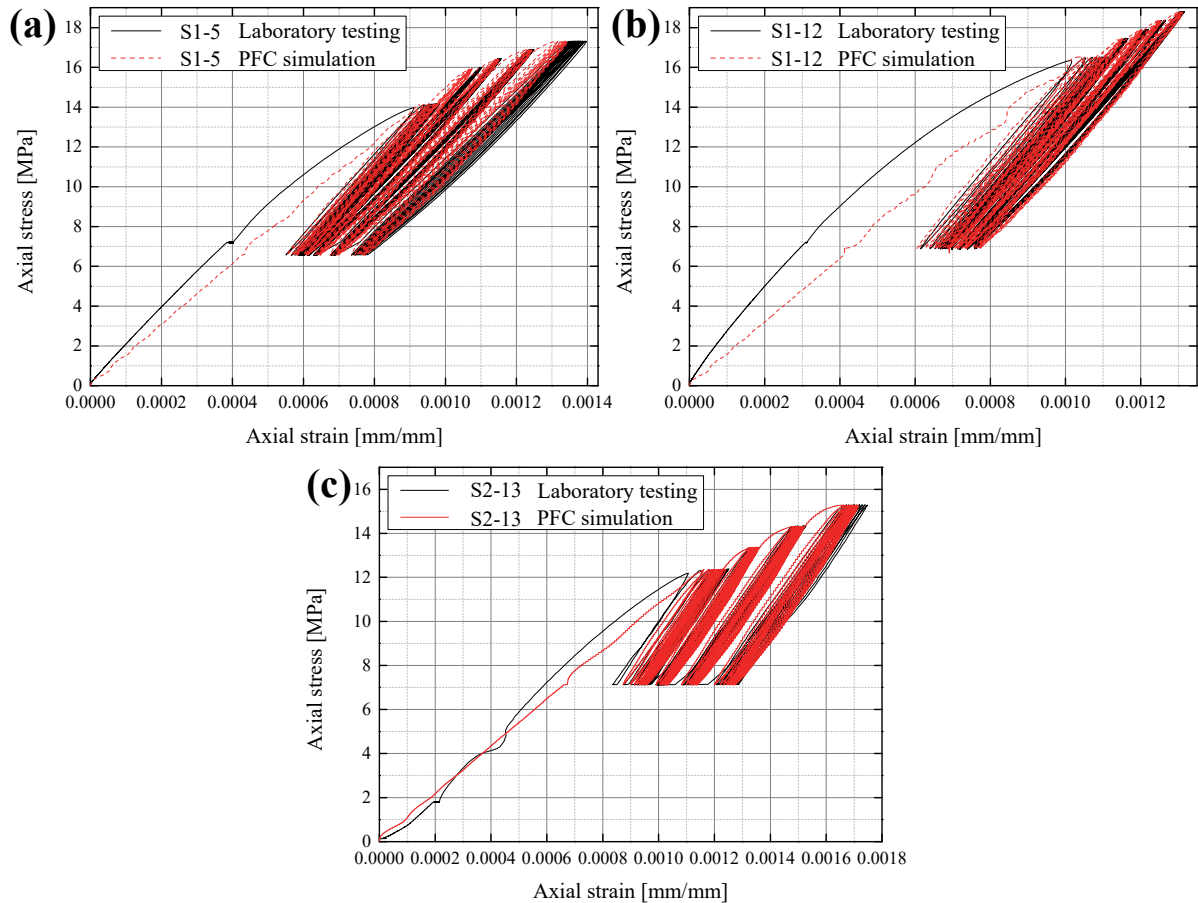
Figure 4.31 Hysteresis loops: laboratory testing and PFC^{3D} simulations for (a) S1-5 (b) S1-12 and (c) S2-13

Figure 4.32 shows the evolution of residual strain (ε_{ar}) and peak strain (ε_{ap}) observed during laboratory tests and numerical simulations for three samples. During each cyclic loading stage, the first ten cycles are selected: S1-5 and S1-12 have 50 cycles in total (5 stages) and S2-13 has 40 cycles (4 stages). Residual and peak strain rate are separately plotted by bar figures for each loading stage. As shown in Figure 4.32a to Figure 4.32f, the numerical simulation results show high consistency in terms of both, strain evolution and strain rate with respect to the laboratory tests. The initial cyclic loading stage always has the largest residual/peak strain rate due to the compaction effect. In the following cyclic loading stages, residual/peak strain rate nonlinearly increase with σ_{max}. The value of σ_{max} for each loading stage is also marked at the top of the bars in Figure 4.32. The good consistency between laboratory tests and numerical simulations demonstrates that the evolution of λ versus σ_{max} (exponential relation between λ and σ_{max}) as presented in Figure 4.30 can well reproduce the behaviour of axial strain at the peak as well as at the end of a cycle. This also verifies that a smaller bond diameter (smaller λ) will result in a larger axial strain rate during the multi-level cyclic loading in the simulations.
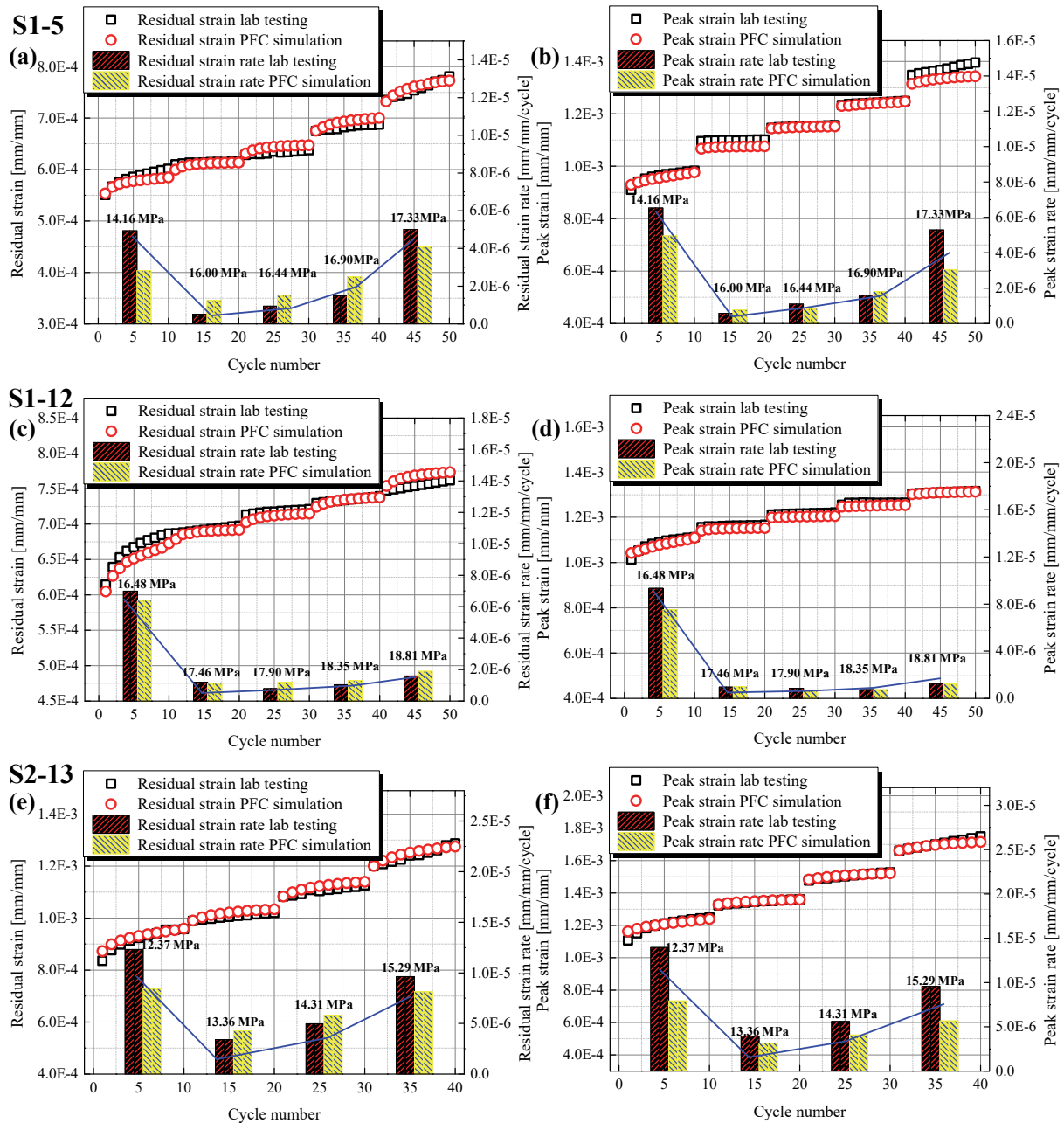
Figure 4.32 (a) residual strain evolution of S1-5 (b) peak strain evolution of S1-5 (c) residual strain evolution of S1-12 (d) peak strain evolution of S1-12 (e) residual strain evolution of S2-13 (f) peak strain evolution of S2-13

Figure 4.33 illustrates the relation between axial stress, λ, and number of cracks for the three samples in the simulations. Sample S1-12 (222 cracks) has obviously more cracks than the other two samples (84 cracks for S1-5 and 10 cracks for S2-13). This is because σ_{max} of S1-12 (18.81 MPa) is larger than those of S1-5 (17.33 MPa) and S2-13 (15.29 MPa). For S1-5 and S1-12, the number of cracks suddenly increases at the final cyclic loading stage whereas for S2-13 it remains at the same number after the initial stage. This demonstrates that the small

value of σ_{max} for S2-13 has less effect on cracks compared with the other samples which have larger σ_{max}. For S1-12, it is observed that during the initial cyclic loading stage, the number of cracks quickly rises and reaches 151, which counts for 68% of the total number of cracks at the end, whereas for the other two samples, the ratio of cracks formed at the initial cyclic loading stage is much lower than for S1-12. This indicates that the damage of the initial cyclic loading stage for S1-12 is quite large. This results from the large σ_{max} during the initial cyclic loading stage (16.48 MPa for S1-12). The smaller σ_{max} during the initial cyclic loading stage (14.16 MPa for S1-5 and 12.37 MPa for S2-13) results in fewer cracks and smaller initial damage.
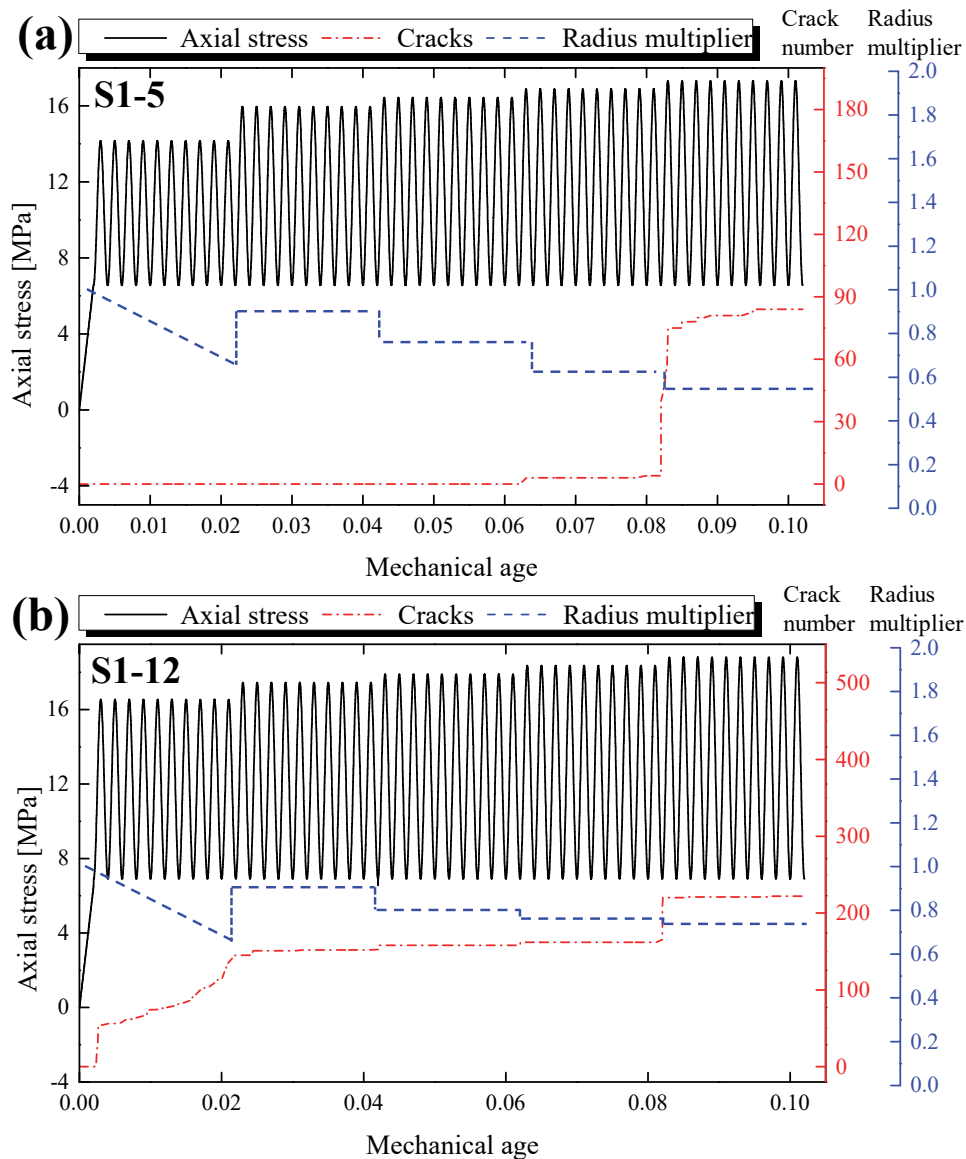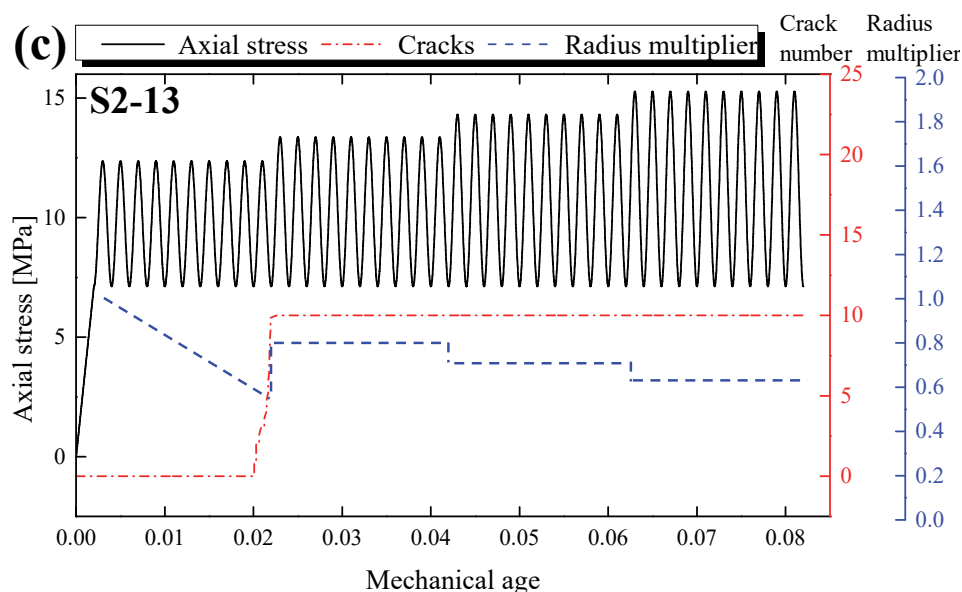
Figure 4.33 Relation between axial stress, radius multiplier and number of cracks for (a) S1-5 (b) S1-12 (c) S2-13

4.4.3.2 Multi-level cyclic loading with gradual decrease of σ_{min}

The simulation on multi-level cyclic loading with gradual decrease of σ_{min} is based on two concrete samples (S1-8 and S2-14). The two samples experienced five cyclic loading stages with fixed σ_{max} and gradual decreasing σ_{min}. Physical properties and loading scheme are listed in Table 4.6 and Table 4.7.

Table 4.6 Physical and geometrical properties of sample S1-8 and S2-14

Sample No.	Wave velocity [m/s]		Dyn. elastic modulus [GPa]	Length [mm]	Diameter [mm]	Density [g/cm³]	Mass [g]
	P-wave	S-wave					
S1-8	3731	2331	27.39	126.31	50.08	2.14	529.12
S2-14	4046	2323	28.63	123.70	50.45	2.11	521.75

Table 4.7 Cyclic loading scheme for S1-8 and S2-14

Sample No.	Stage 1	Stage 2	Stage 3	Stage 4	Stage 5
	Cyclic load level [MPa]				
S1-8	8.32 – 16.88	7.42 – 16.88	6.56 – 16.88	5.67 – 16.88	4.86 – 16.88
S2-14	7.13 – 15.29	6.15– 15.29	5.21 – 15.29	4.31 – 15.29	3.34 – 15.29

The evolution of λ during the multi cyclic loading stages for S1-8 and S2-14 is illustrated in Figure 4.34. Unlike the evolution tendency of λ (see Figure 4.30), best fitting between laboratory tests and numerical simulations requires that the value of λ remains constant during the different cyclic loading stages (except for the initial cyclic loading stage) when σ_{min} continuously decreases and σ_{max} is fixed. According to the laboratory test results, the effect of

σ_{min} on axial strain evolution and strain rate is not as sensitive and obvious than σ_{max}. The constant value of λ can reproduce the behaviour of strain evolution which varies in a relatively limited range. Another observation is that the value of λ during the loading stages with decreasing σ_{min} and fixed σ_{max} is always larger compared to loading stages with increasing σ_{max} and fixed σ_{min}. This indicates that the damage resulting from decreasing σ_{min} is much lower than for increasing σ_{max}.
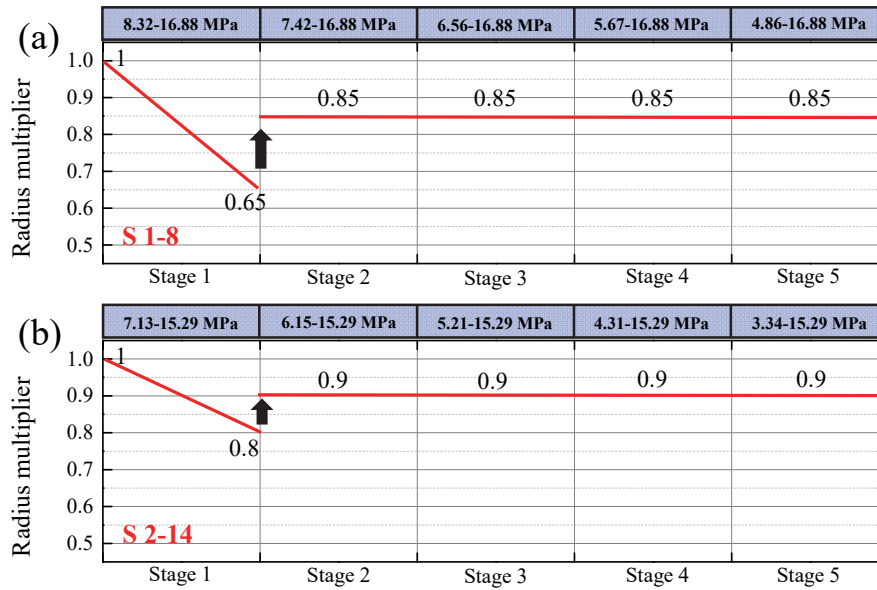
Figure 4.34 Evolution of bond radius multiplier (λ) for (a) S1-8 (b) S2-14

The hysteresis loops of laboratory tests and numerical simulations are illustrated in Figure 4.35. Figure 4.35a and Figure 4.35g show the hysteresis loops of all five stages. Some overlaps in Figure 4.35a and Figure 4.35g can lead to an unclear picture of detailed hysteresis loops in each different loading stage. Therefore, Figure 4.35b - Figure 4.35f show the hysteresis loops of laboratory tests and numerical simulation for S1-8 for the five cyclic loading stages. Plots of detailed loops for S2-14 are shown in Figure 4.35h to Figure 4.35l. It is known that based on the evolution strategy of λ (see Figure 4.34), the hysteresis loop of numerical simulation is highly consistent with the laboratory test results. As shown in Figure 4.35, the elastic modulus of S1-8 and S2-14 is not influenced by reduction of σ_{min}. The characteristics of the hysteresis loop shape can be also replicated by the simulations. It is observed that with decrease of σ_{min}, the enclosed area of a single loop grows, which means that the energy dissipated during one cycle increases when σ_{min} decreases. This is also consistent with laboratory test results. The conclusion can be drawn that, when λ is fixed, reduction of σ_{min} in the simulation will lead to more obvious hysteresis behaviour.
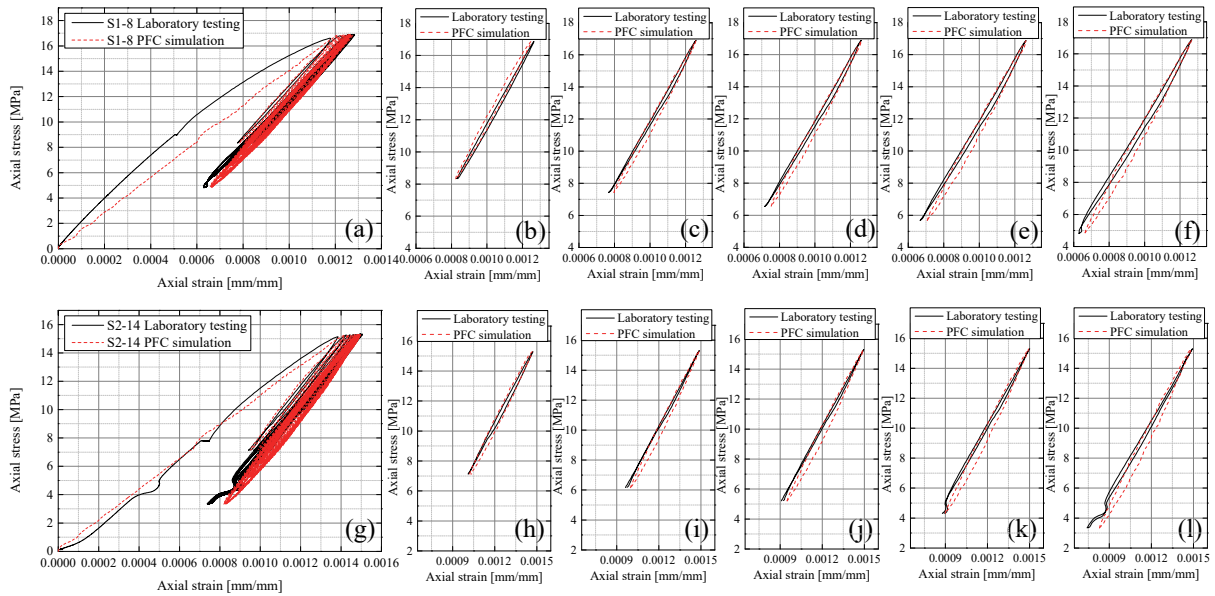
Figure 4.35 Stress-axial strain loop of S1-8 (a) five stages (b) 1st stage (c) 2nd stage (d) 3rd stage (e) 4th stage (f) 5th stage; Stress-axial strain loop of S2-14 (g) five stages (h) 1st stage (i) 2nd stage (j) 3rd stage (k) 4th stage (l) 5th stage

Similar to Figure 4.32, the evolution of axial strain and strain rate for S1-8 and S2-14 is analysed and discussed in Figure 4.36. Laboratory testing and simulation reveal quite similar patterns in terms of peak and residual strain evolution tendency. As indicated by the bars in Figure 4.36, peak and residual strain rate show a substantial drop after the initial loading stage, followed by fluctuations in a small range with decreasing σ_{min}. The value of σ_{min} for each loading stage is marked above the bars. In terms of hysteresis loop and strain evolution, the relation between λ and σ_{min} as proposed in Figure 4.34 is quite effective to reproduce the main mechanical behaviour of the concrete sample when exposed to loading where σ_{min} decreases and σ_{max} is fixed.
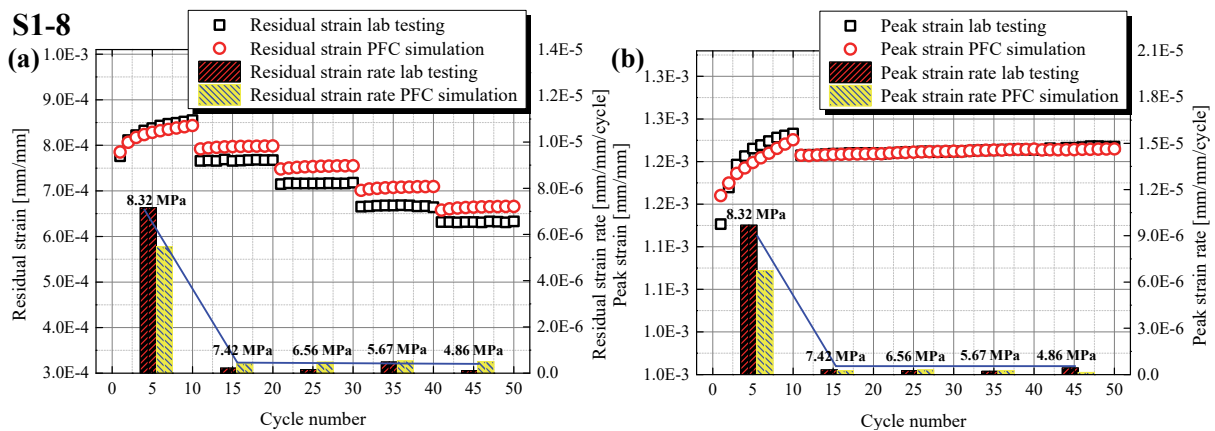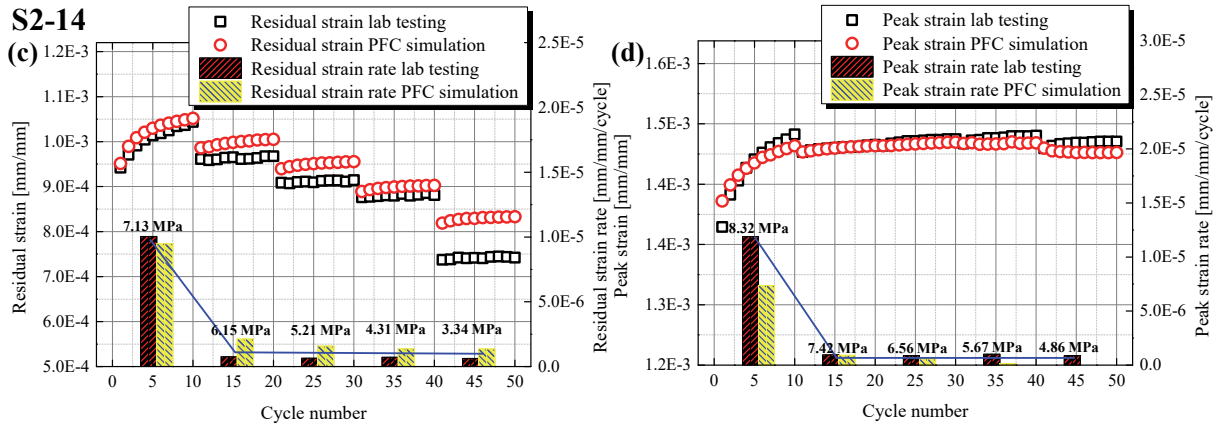
Figure 4.36 (a) residual strain evolution of S1-8 (b) peak strain evolution of S1-8 (c) residual strain evolution of S2-14 (d) peak strain evolution of S2-14

4.4.3.3 Multi-level cyclic loading with both, gradual decrease of σ_{min} and increase of σ_{max}

Sections 4.4.3.1 and 4.4.3.2 have presented the MSC model with samples subjected to two different cyclic loading strategies during multi-level stages. When σ_{min} is fixed and σ_{max} gradually increases, the results of laboratory tests and numerical simulation show good agreement when the bond diameter (radius multiplier λ) decreases following an exponential law. When σ_{max} is fixed and σ_{min} gradually decreases, the simulation shows good agreement when the bond diameter remains constant after the initial cyclic loading stage. This is the basic logic of the MSC model.

In order to validate the MSC model under the condition that σ_{min} decreases and σ_{max} increases, laboratory results of sample S1-10 are used. The properties of S1-10 are shown in Table 4.8 and the loading scheme in Table 4.9. Sample S1-10 experienced six cyclic loading stages and two loading strategies as discussed in sections 4.4.3.1 and 4.4.3.2. From stage one to three, σ_{max} is fixed and σ_{min} decreases; from stage four to stage six, σ_{min} is fixed and σ_{max} increases.

Table 4.8 Physical and geometrical properties of sample S1-10

Sample	Wave velocity [m/s]		Dynamic elastic modulus	Length	Diameter	Density	Mass
No.	P-wave	S-wave	[GPa]	[mm]	[mm]	[g/cm^3]	[g]
S1-10	3790	2432	29.52	125.76	50.14	2.17	538.41

Table 4.9 Cyclic loading scheme of S1-10

Sample	Stage 1	Stage 2	Stage 3	Stage 4	Stage 5	Stage 6
No.				Cyclic load level [MPa]		
S1-10	4.85 – 16.87	3.11 – 16.87	1.43 – 16.87	1.43 – 17.78	1.43 – 18.24	1.43 – 18.67

Based on the MSC model, Figure 4.37 shows the evolution of λ during the six cyclic loading stages. In the initial stage, λ follows a linear reducing from 1 to 0.8, which can better replicate the compaction effect during the initial cyclic loading stage. Then λ remains constant with a value of 0.9 during the second and third cyclic loading stages, which corresponds to the condition of fixed σ_{max} and decreasing σ_{min}, λ starts to reduce in an exponential manner with gradual increasing σ_{max}.
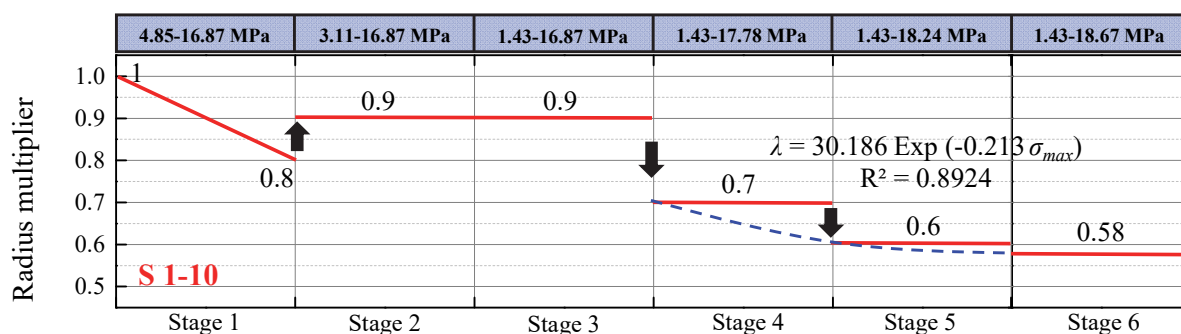
Figure 4.37 Evolution of bond radius multiplier (λ) for S1-10

Figure 4.38a shows the hysteresis loop of S1-10 for both, laboratory test and numerical simulation. Figure 4.38b shows residual strain evolution and residual strain rate. As shown in Figure 4.38b, the residual strain rate remains almost constant when σ_{min} deceases and σ_{max} is fixed, whereas the residual strain rate obviously increases when σ_{max} starts to rise. The comparison between laboratory testing and numerical simulation proves that the MSC model can well reproduce the stress-strain behaviour and the change of residual strain rate when a concrete sample is subjected to multi-level and different cyclic loading strategies.
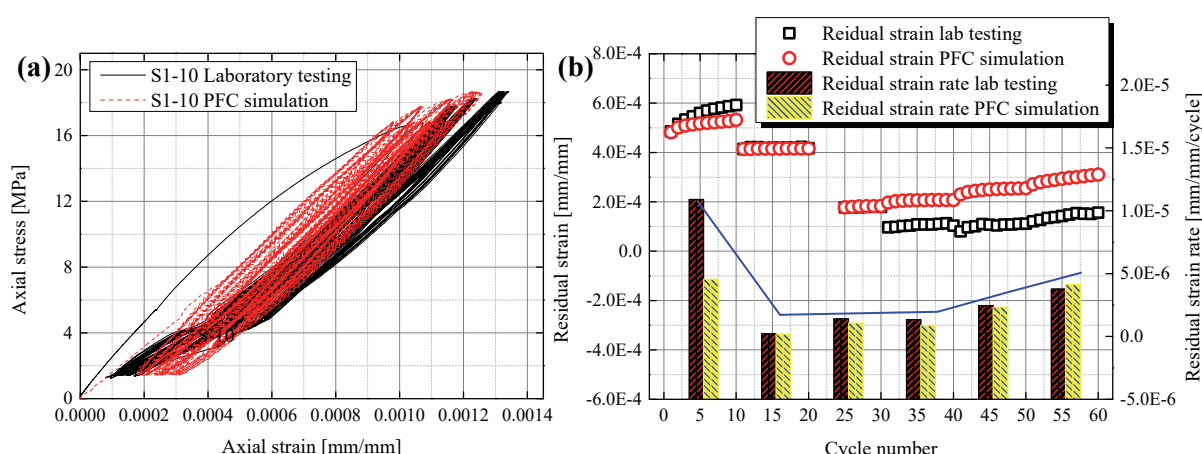
Figure 4.38 (a) stress-strain loop of five stages of S1-10 (b) residual strain evolution of S1-10

Figure 4.39 documents the crack evolution during all the six cyclic loading stages. During the first three cyclic loading stages, the crack grow rate is moderate. For the stages four to six, the

116

number of cracks increases much faster due to the gradual rise of σ_{max}. This is one of the reasons leading to the larger strain rate as shown in Figure 4.38b, the other reason is the reduction of λ from 0.7 to 0.58.
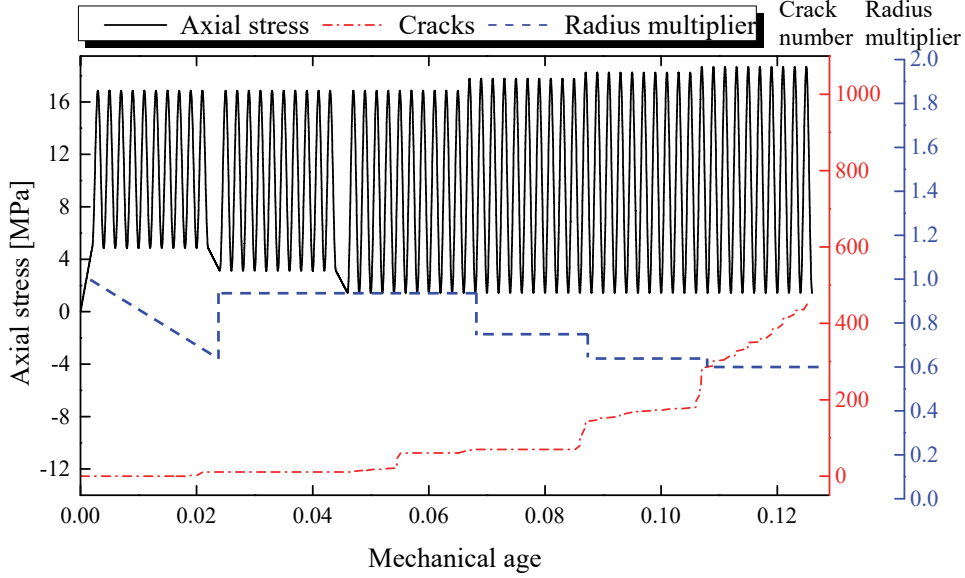
Figure 4.39 Relation between axial stress, radius multiplier and number of cracks for S1-10

4.4.4 Simulation of AE in multi-level fatigue testing

The acoustic emission (AE) technology is often used during laboratory cyclic testing as an effective failure precursor (Cai et al. 2007; Fan et al. 2017; Zhang et al. 2018; Li et al. 2019). During the simulations the bond breakages can be precisely tracked. The number of broken bonds are often related to the number of micro cracks (Hazzard and Young 2000). The AE energy in the PFC simulations is related to the bond strain energy (E_k). It is stored in the parallel bonds of the LPBM. The determination of E_k is shown in Equation 4.26. When the bond breaks, E_k will be released, therefore E_k represents a physical mechanism similar to a real AE event in a laboratory test. The process diagram in Figure 4.40 shows the logic to collect cumulative AE energy during simulations.

$$E_k = \frac{1}{2}\left[\frac{F_{pn}^{2}}{k_n'A} + \frac{F_{ps}^{2}}{k_s'A} + \frac{M_t^{2}}{k_s'J} + \frac{M_b^{2}}{k_n'I}\right]$$

$$F_{pn} = F_{pn} + k_n'A\Delta\delta_n$$

$$F_{ps} = F_{ps} - k_s'A\Delta\delta_s$$

$$M_t = M_t - k_s'J\Delta\theta_t$$

$$M_b = M_b - k_n'I\Delta\theta_b$$

(4.26)
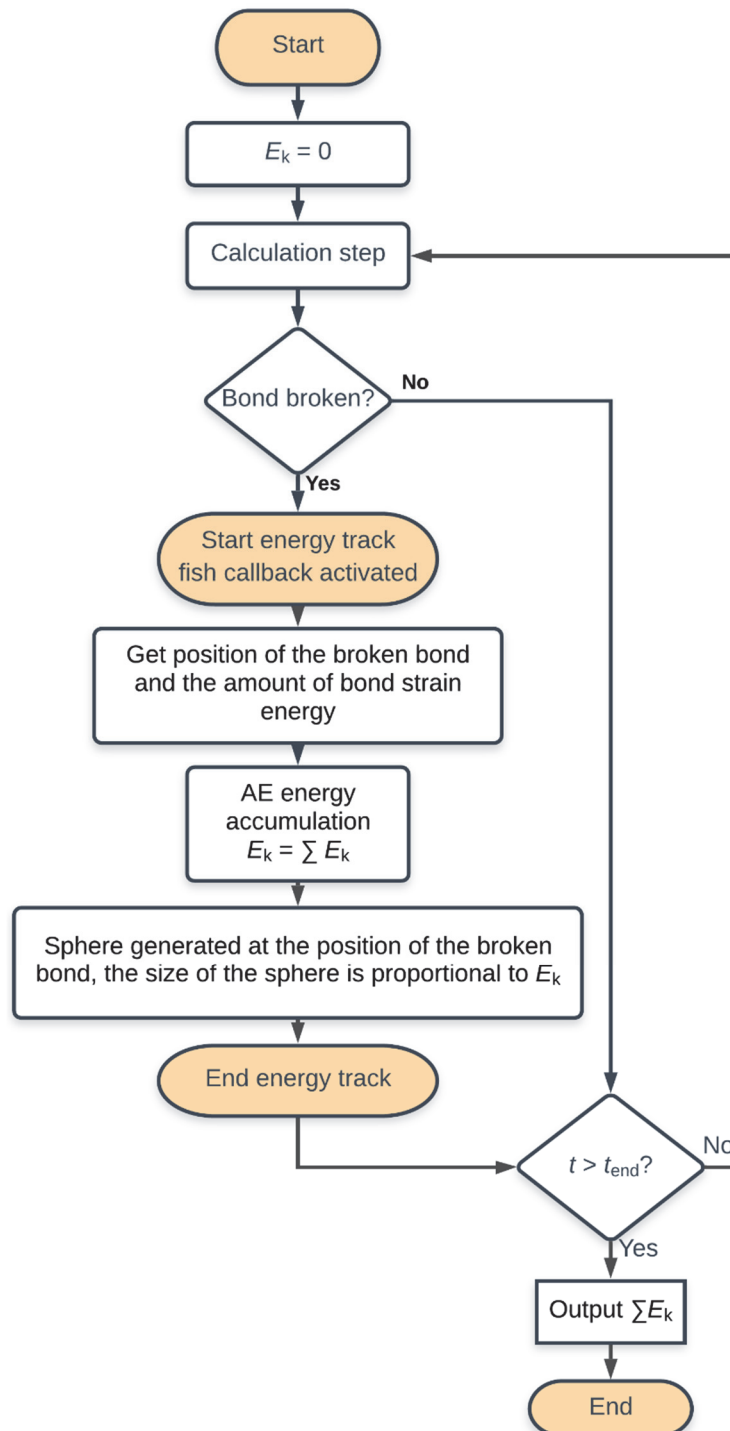
Figure 4.40 Process diagram of AE energy monitoring

Figure 4.41a and Figure 4.41b illustrate the number of cumulative AE hits and cumulative AE energy observed during laboratory testing and numerical simulation with six cyclic loading stages for S1-10. The cumulative AE hits observed during laboratory testing show three parts: the first and the sixth stage show a larger growth rate than the stages two to five. In the numerical simulations, the fast increase of AE hits during the initial stage is not reflected due

to the fact that almost no bonds are broken during the first cyclic loading stage. This is due to the fact that a sphere used in PFC simulations is much larger than the actual mineral grains of the concrete. The larger slope during the sixth stage is consistent with laboratory results which indicates that a large number of cracks emerge during this stage. The curves of the cumulative AE energies (laboratory testing and simulation) show much better agreement than the AE hits. Even though the AE hits in laboratory testing during the initial cyclic loading are large, the cumulative AE energy is small only holds a relatively small amount. Later the AE energy shows a stepwise increase which is also duplicated in the simulations. For both, laboratory testing and simulation, the largest increase rate of AE energy occurs in the sixth stage.
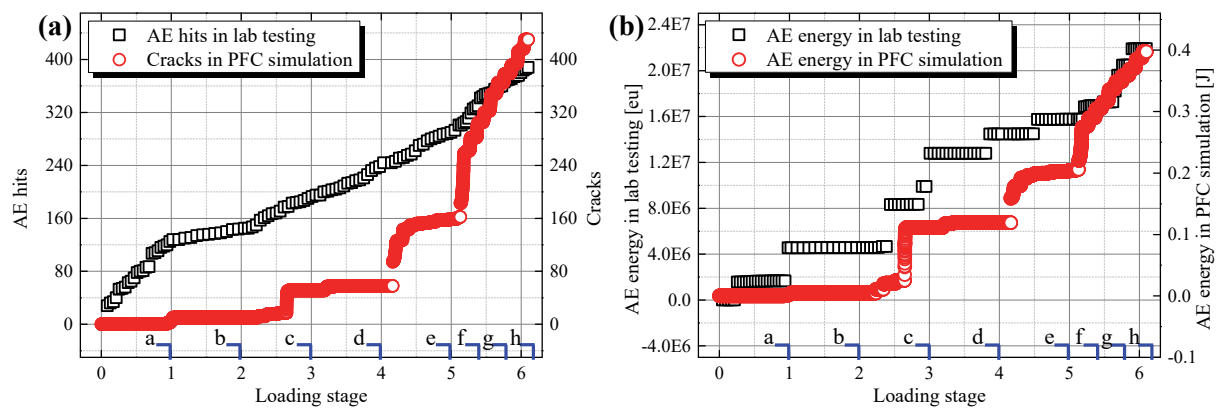
Figure 4.41 (a) cumulative AE hits: laboratory testing and simulation (b) cumulative AE energy: laboratory testing and simulation

The 3D spatial distribution of broken bonds and AE energy for S1-10 is illustrated in Figure 4.42 and Figure 4.43, respectively. Eight stages are selected to reflect the evolution of crack distribution and AE energy. These eight stages correspond to the eight points in time marked in Figure 4.41 (point a - point h). Figure 4.42 precisely reflects the location of AE events (bond breakage). However, the AE energy cannot be characterized quantitatively. The spheres in Figure 4.43 are proportional to the amount of released bond strain energy E_k. The sphere centre is the position of the broken bond (source of AE energy). The two enlarged areas in Figure 4.43 emitted large energy (strong events) and small energy (small events), respectively.
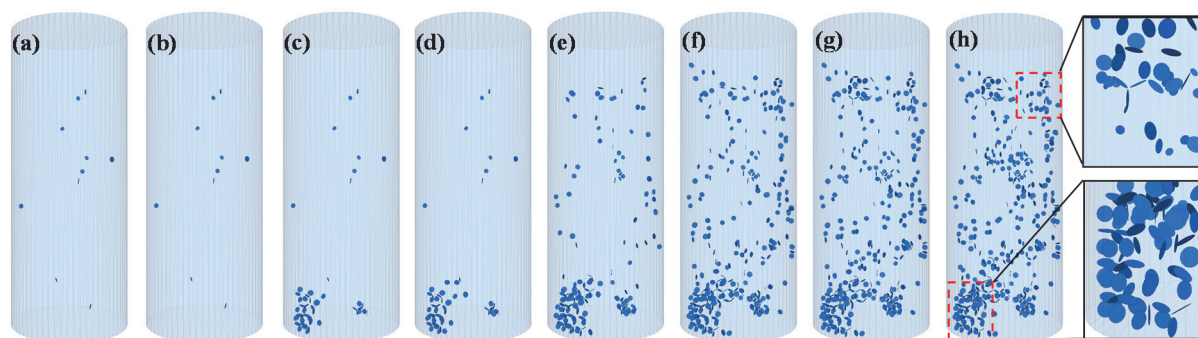
Figure 4.42 Crack evolution of S1-10 during the simulation for points in time (a) - (h) according to Figure 4.41
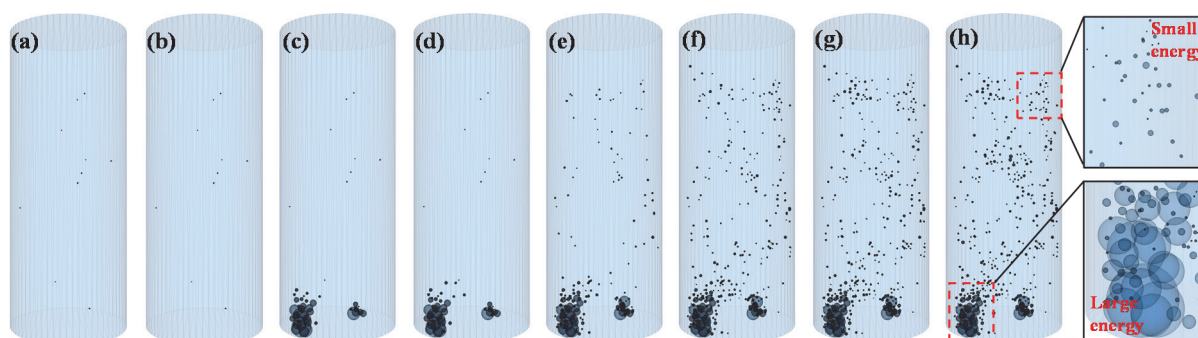
Figure 4.43 AE energy evolution S1-10 during the simulation for points in time (a) - (h) according to Figure 4.41

4.5 Conclusions

Based on the LPBM in PFC^{2D}, the NPSC model is proposed to simulate the mechanical behaviour of concrete subjected to single-level cyclic loading. The time-dependent damage during fatigue tests is reflected by the nonlinear reduction in bond diameter between two bonded particles. Based on PFC^{3D}, the MSC model is proposed to simulate the mechanical behaviour of concrete subjected to multi-level cyclic loading and calibrated on laboratory tests. The MSC model considers the quantitative relation of the time and stress dependent damage with respect to the maximum and minimum load during cyclic loading. The damage in the numerical model is characterized by reducing the bond diameter. The damage during the multi-level cyclic loading is a time-stress-dependent variable. The following conclusions can be drawn:

1. The stress-controlled loading is realized by adoption of a dense clump block wall (DCB-wall). The stress-controlled loading is capable to simulate different load levels under monotonic and repeated loading. Applicability and effectiveness of stress-controlled loading

are validated through uniaxial compressive cyclic loading tests. The stress wave transmission during the stress-controlled loading regime is homogenous and is consistent with laboratory testing.

2. Based on the calibration of laboratory tests, it is found that the PSC model has limited effect on simulating the fatigue characteristics of concrete. The proposed NPSC model is capable to reproduce the mechanical fatigue behaviour including damage of rock-like materials under single-level cyclic loading. The logarithmic function in NPSC model gives the best fit with laboratory test results. The reduction speed of bond diameter increases with increasing maximum cyclic load level.

3. The proposed MSC model is capable to reproduce the mechanical fatigue behaviour of concrete materials under multi-level cyclic loading. The main logic of the MSC model is that for the initial cyclic loading stage, the bond diameter follows a linear reduction due to the compaction effect in laboratory testing. For the consecutive cyclic loading stages where σ_{max} increases and σ_{min} is fixed, the bond diameters remain constant during each loading stage. For further stages, the bond diameter reduces following an exponential function with respect to σ_{max}. For the consecutive cyclic loading stages where σ_{min} decreases and σ_{max} is fixed, the bond diameter remains constant after the initial cyclic loading stage. This indicates that the damage effect induced by an increase of σ_{max} is more pronounced than a decrease of σ_{min} during multi-level cyclic loading.

4. The evolution of axial strain, peak/residual strain rate, and the shape of hysteresis loop in numerical simulation adopting the MSC model are compared and calibrated via laboratory test results. Laboratory testing and numerical simulations show a quite similar pattern.

5. A three-dimensional numerical AE monitoring system is proposed for PFC³ᴰ. The cumulative AE energy can be precisely and quantitatively characterized by the release of the bond strain energy. The results of cumulative AE energy measured during laboratory tests and PFC simulations show a high consistency during multi-level cyclic loading.

5. Hysteresis energy based fatigue prediction method

5.1 Hysteresis energy based fatigue indicators

For brittle geo-materials, the phase shift between stress and strain is distinctive in fatigue loading tests (Vasseva 1993; Mayergoyz 2003; Ibarra et al. 2005; Xi et al. 2006; Tutuncu et al. 2012; Hu et al. 2018; Song et al. 2018b; Zhang et al. 2020). At the loading stage, the phase shift between stress and strain can be zero, positive or negative. However, at the unloading stage, the stress is always ahead of strain (Xi et al. 2006). If the phase shift is zero, the material is completely elastic and there is no hysteresis. Hence, the value of phase shift can reflect the degree of deviation from elasticity. When the plastic damage is large, the phase shift between stress and strain is obvious. Three typical stress-strain curves obtained by fatigue loading tests are plotted in Figure 5.1. In Figure 5.1a, the three types of stress-strain curves represent (a) elasticity (b) moderate hysteresis and (c) obvious hysteresis, where points A, B, C are the maximum stress points and A', B', C' are maximum strain points. When hysteresis appears, the maximum stress and strain values do not coincide, like plotted in Figure 5.1b. Only use the phase shift to evaluate the degree of hysteresis is not comprehensive and accurate enough, because it cannot quantitatively characterize the effect of stress and strain on hysteresis. Therefore, the hysteresis energy density (HED) is defined as the work done from maximum stress value (B) to maximum strain value (B'), see purple area in Figure 5.1c. See also corresponding Equation 5.1, where the ε_1 and ε_2 are the corresponding strains as shown in Figure 5.1c. The dissipated energy density (U_d) is defined as the area of the hysteresis loop within one single cycle, see pink area in Figure 5.1c and corresponding Equation 5.2. The hysteresis energy ratio (HER) is defined as the value of HED/U_d, which represents the percentage of hysteresis energy in U_d. Therefore, HER is a damage variable characterizing the degree of hysteresis by considering the effect of stress and strain. The hysteresis occurrence ratio (HOR) is defined as the number of cycles with hysteresis (N_h) divided by the total selected cycle number (N_w): HOR= N_h/N_w. According to the loading scheme, 50 cycles are the least number of cycles for a single cyclic loading stage, so N_w in our investigations is 50 cycles for convenient comparison between different specimens. For other tests, N_w can be chosen arbitrary, but should contain enough cycles to get a reliable data base. HOR is a variable to evaluate the occurrence probability of hysteresis.

$$\text{HED} = \int_{\varepsilon_1}^{\varepsilon_2} \sigma d\varepsilon$$

(5.1)

$$U_d = \int \sigma d\varepsilon$$

<div align="right">(5.2)</div>
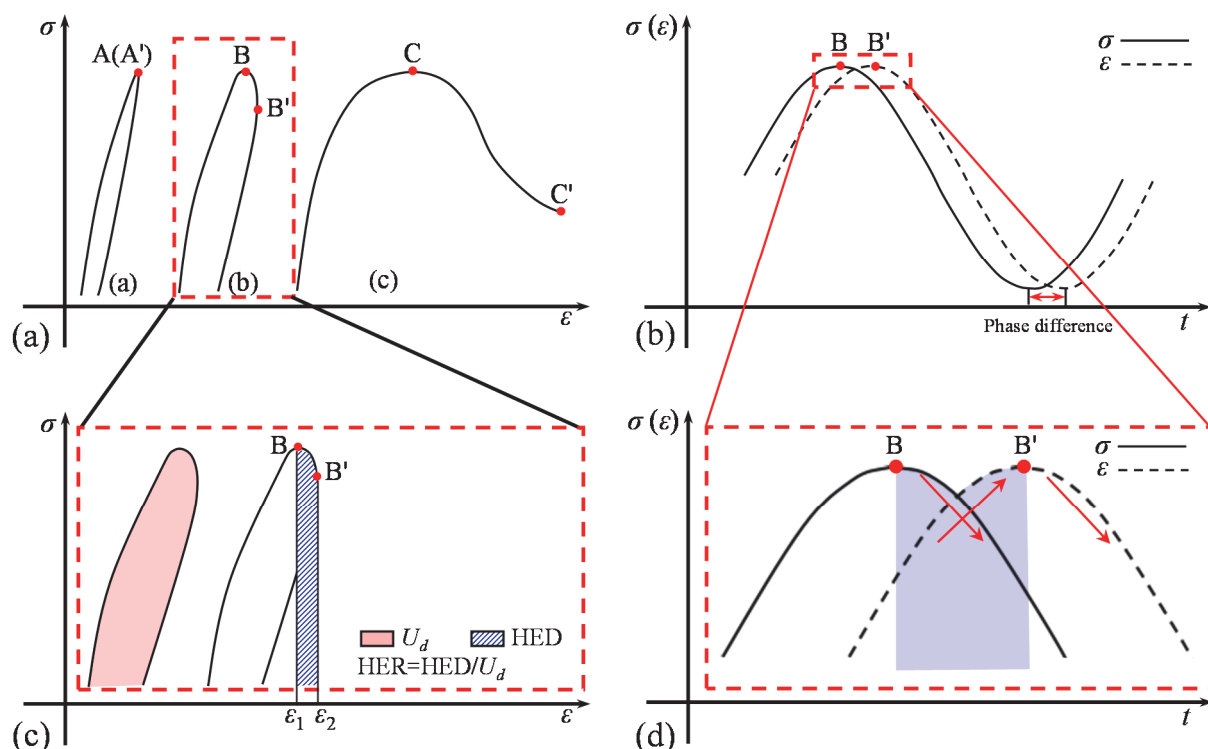
Figure 5.1 (a) three typical stress-strain hysteresis loops (b) hysteresis of stress and strain (c) schematic diagram of U_d, HED and HER (d) enlarged diagram for stress-strain hysteresis

5.2 Laboratory test results

5.2.1 Analysis of HOR

As plotted in Figure 5.2, 40 cyclic loading stages belonging to 9 samples are selected to analyse HOR. Due to the fact that only Series 1 is analysed and Series 2 is not considered in Chapter 5, the symbol '#' is used to represent the sample number of Series 1 for convenience, namely #3 in this chapter means sample S1-3 as described in Chapter 3. #1 S1 in Figure 5.2 represents the first cyclic loading stage of sample #1, #5 S2 represents the second cyclic loading stage of sample #5 and so on. During stable loading stages (samples are not broken), the first 50 cycles are used for evaluation to get a robust data set. According to Figure 5.2, there are 9 stages with failure (marked by letter F) with respect to 9 different samples. Based on the 9 failure stages, it can be observed that when HOR is smaller than 75% (see green dashed line in Figure 5.2), concrete samples are not broken independent on load levels and loading strategies. Therefore, a value of 75% is defined as first critical value which is used to define a safety threshold. In

addition, when HOR is larger than 95% (see blue dashed line in Figure 5.2), all the concrete samples are broken and therefore, 95% is defined as second critical value which is used to define the extremely dangerous threshold. Figure 5.3 illustrates the safe and dangerous regions based on HOR. When HOR is located in the safe region (green area), concrete samples will not fail in the current cyclic loading stage. When HOR is located in the dangerous range (blue grid filled area), concrete samples have relatively high possibility to break. When HOR is in the extremely dangerous region (marked with red vertical lines), the concrete sample is extremely prone to fail within the next few cycles.
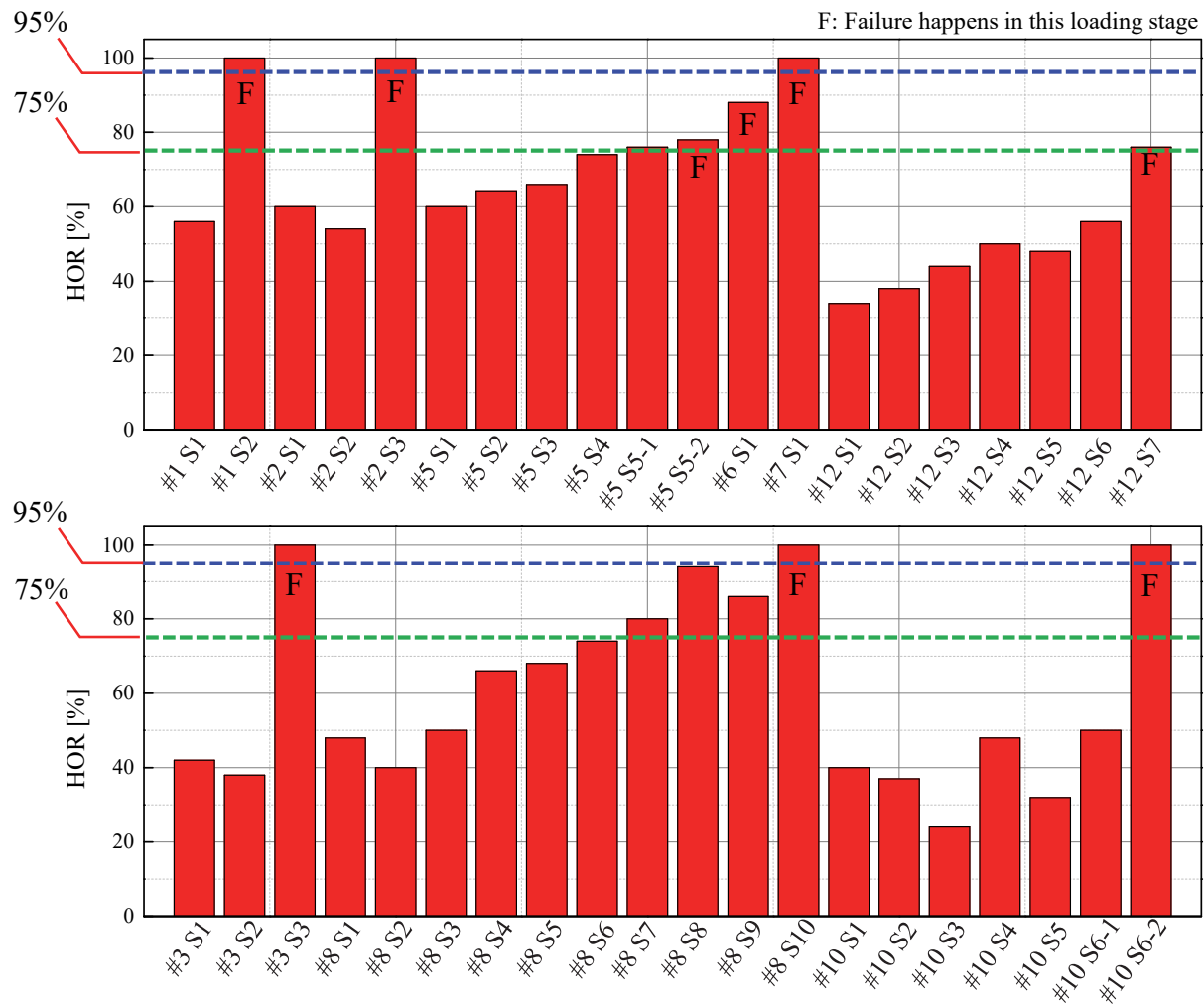
Figure 5.2 HOR of 40 cyclic loading stages for different concrete samples
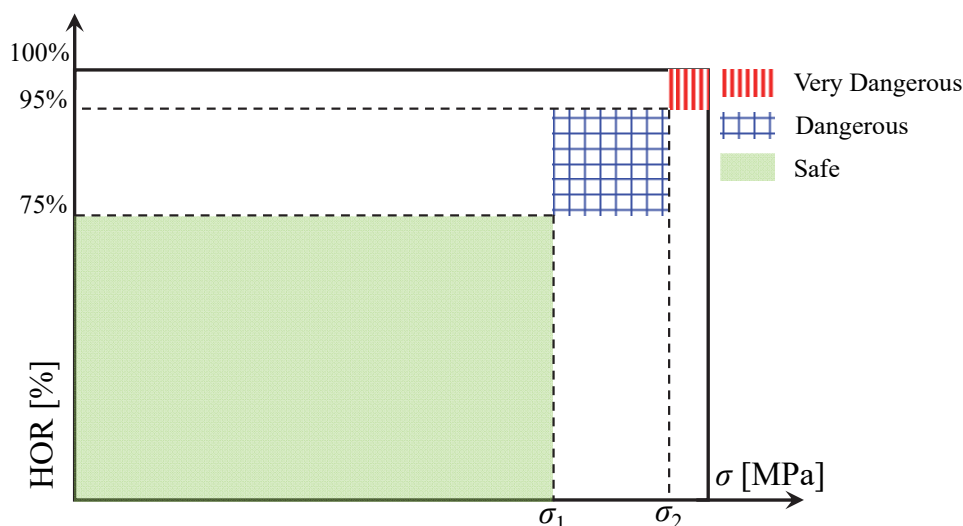
Figure 5.3 Safety prediction based on HOR

In Chapter 3, it is concluded that the accumulated dissipated energy (U_a) has a direct relationship with maximum cyclic load level (σ_{max}), minimum cyclic load level (σ_{min}) and loading frequency (f). Thereupon, the effect of σ_{max}, σ_{min} and f on HOR is investigated and the laboratory results are plotted in Figure 5.4.
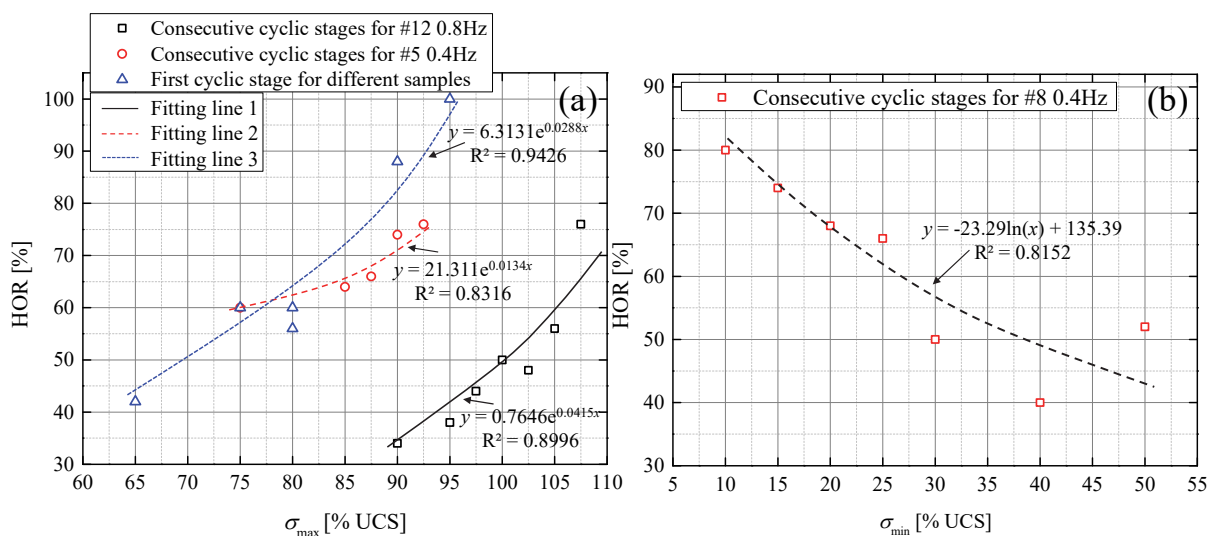
Figure 5.4 (a) effect of σ_{max} and f on HOR (b) effect of σ_{min} on HOR

According to the detailed loading strategies documented in Table 3.2, Figure 5.4a illustrates the effect of σ_{max} on the evolution of HOR. #12 and #5 experienced 7 and 5 consecutive cyclic loading stages, respectively, and represent the progressively increasing σ_{max} when σ_{min} is fixed to 0.4 UCS. The data can be well fitted by exponential functions which coincide with the relation between dissipated energy and σ_{max} in our former research. The blue triangular symbols in Figure 5.4a represent data of the first cyclic loading stages of different samples with different

σ_{max}. As documented in Figure 5.4a, the fitting line for the first cyclic loading stage has a steeper slope than #5 and #12. This indicates that gently and progressively increasing σ_{max} in the consecutive cyclic loading stages (red and black symbols in Figure 5.4a) will reduce the growth rate of HOR compared to the single cyclic loading stage (blue symbols in Figure 5.4a). In Chapter 3, it is also documented that a slowly, but gradually increase of σ_{max} reduces the growth rate of the accumulated dissipated energy. This phenomenon can be explained from the viewpoint that the gradual increment of σ_{max} will consolidate the sample and enhance the elasticity of the concrete. As the loading frequency of #12 is two times that of #5, the slope of the fitting line for #12 is steeper than that for #5. This demonstrates that increasing loading frequency may increase the speed of HOR increment when σ_{max} is progressively enhanced. For #8, σ_{max} is fixed and σ_{min} is gradually reduced from 0.5 UCS to 0.1 UCS. The effect of σ_{min} on HOR is illustrated in Figure 5.4b. The data can be fitted by a logarithmic function which is again coincident with the relation between dissipated energy and σ_{min} in (see Chapter 3). To sum up, increasing of σ_{max} and reduction of σ_{min} will increase the value of HOR which also increases the failure probability. This indicates that the effect of σ_{max} and σ_{min} on dissipated energy and HOR have similarities.

As shown in Table 3.2, #8 and #10 experienced two types of loading: firstly fixing σ_{max} and gradually decreasing σ_{min}, then fixing σ_{min} and increasing σ_{max}. Hence, both σ_{max} and σ_{min} changed during the cyclic loading. During the fatigue test, ultrasonic P-wave speed is measured to monitor the damage evolution. Figure 5.5 illustrates the evolution of P-wave speed and HOR for #8 and #10 during the cyclic loading. Many researchers have found that the evolution of P-wave speed is directly related to the occurrence of hysteresis. Reduction of P-wave speed is always associated with a pronounced hysteresis phenomenon. It can be observed that, when σ_{max} is fixed, decrease of σ_{min} results in gentle reduction of P-wave speed and HOR moderately increases at the same time. In the second loading strategy, the reduction of P-wave speed is more obvious with increase σ_{max}. This demonstrates that σ_{max} is more dominant than σ_{min} in terms of damage evolution. HOR also experiences a sudden rise due to the increase of σ_{max}, however, different from evolution of P-wave speed, a subsequent reduction of HOR is observed after the first increasing of σ_{max}. This indicates that increase of σ_{max} will interrupt the balanced status of hysteresis in the former loading strategy. The concrete shows a self-adapting mechanism when new value of σ_{max} is applied.
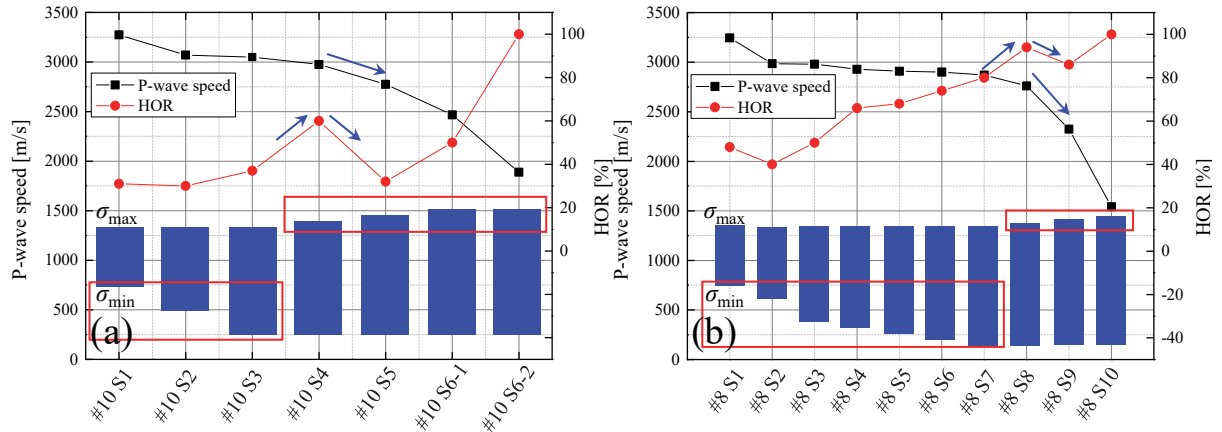
Figure 5.5 HOR and P-wave speed evolution for (a) #10 (b) #8

5.2.2 Analysis of HER

HOR describes the safety based on the occurrence probability of hysteresis and therefore serves as a failure indicator for concrete subjected to cyclic loading. However, if HOR has reached the second critical value and the concrete has entered the extremely dangerous region, a second failure indicator is needed at that moment for more accurate prediction of failure. HER can meet the requirement of a second failure indicator and has the following advantages: 1. HER is dimensionless with a range between [0 - 1]. 2. HER has a distinctive physical meaning and reflects both, the hysteresis energy and the dissipated energy. Apart from HER, the accumulated hysteresis energy (AHE) is also available to continuously reflect the evolution of hysteresis. AHE refers to the cumulative HED up to a given cycle number. The corresponding equation to calculate AHE is shown in Equation 5.3. The slope of curve AHE versus N represents the change of hysteresis energy with ongoing cycling.

$$\mathrm{AHE} = \sum_{1}^{N} \mathrm{HED}$$

(5.3)

HER versus number of loading cycles for 9 samples are shown in Figure 5.6 to Figure 5.13. In cyclic loading stages without failure, the first 50 cycles are selected to analyse AHE and HER. When the concrete samples are not broken, it is obviously that HER is smaller than the critical value which is equal to 0.3 in this research (see the blue lines in Figure 5.6 to Figure 5.13). As shown in Figure 5.10, #6 and #7 are the only two samples that have experienced only a single cyclic loading stage up to the failure. AHE of #6 and #7 show the three-stage characteristics with same evolution tendency of axial strain (ε_a) and accumulated dissipated energy (U_a) in Chapter 3. However, the curves of HER for #6 and #7 only show a two-stage characteristic: 1.

phase with small value (HER < 0.3) and 2. phase with large value (HER > 0.3). This demonstrates the advantage of HER as failure indicator because there is no need to identify the third stage compared to failure indicators which have a three-stage characteristic, such as dissipated energy or axial strain. Except for #6 and #7, as shown in Figure 5.9, Figure 5.11, Figure 5.12 and Figure 5.13, the samples which experienced multi-cyclic loading stages (#5, #12, #10 and #8) also show the two-stage characteristic in terms of HER. This indicates that the two-stage characteristic of HER is a general feature for both, single and multi-stage cyclic loading. In addition, for multi-stage cyclic loading, it can be observed that the scatter of HER in the first several cyclic loading stages is larger than in the later ones. It also manifests that the elasticity of the concrete is enhanced with the gradual increase of cyclic load level. This explains the result in Figure 5.4a that progressive increase σ_{max} at lower cyclic load level results in a smaller slope of HOR (red dashed line in Figure 5.4a) compared to samples subjected to higher cyclic load level in the first cyclic loading stage (blue dashed line in Figure 5.4a).

Figure 5.6 AHE and HER versus load cycles for (a) #1 S1 (b) #1 S2

Figure 5.7 AHE and HER versus load cycles for (a) #2 S1 (b) #2 S2 (c) #2 S3

Figure 5.8 AHE and HER versus load cycles for (a) #3 S1 (b) #3 S2 (c) #3 S3

130

Figure 5.9 AHE and HER versus load cycles for (a) #5 S1 (b) #5 S2 (c) #5 S3 (d) #5 S4 (e) #5 S5-1 (f) #5 S5-2
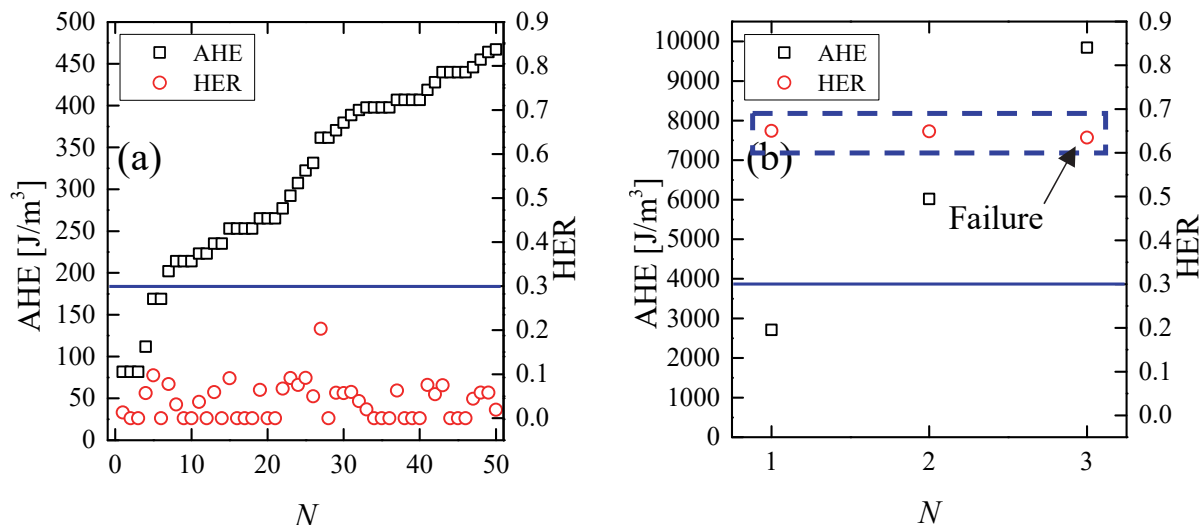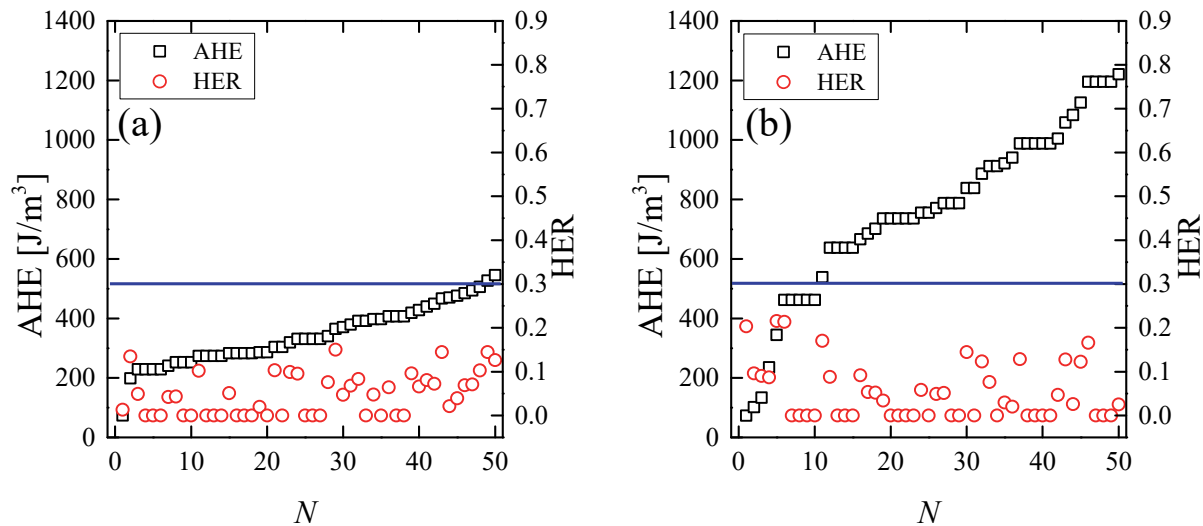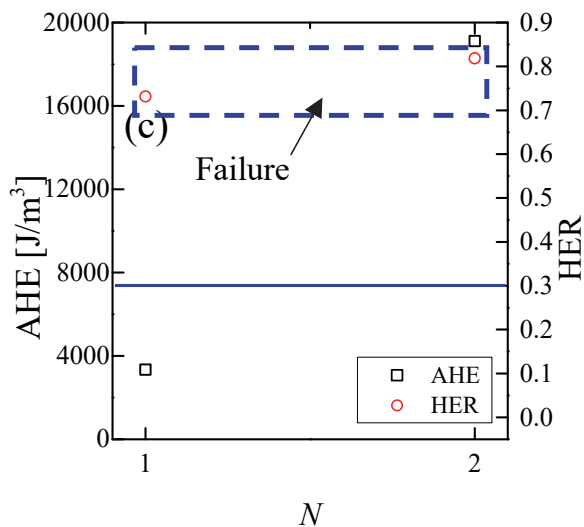
Figure 5.10 AHE and HER versus load cycles for (a) #7 S1 (b) #6 S1

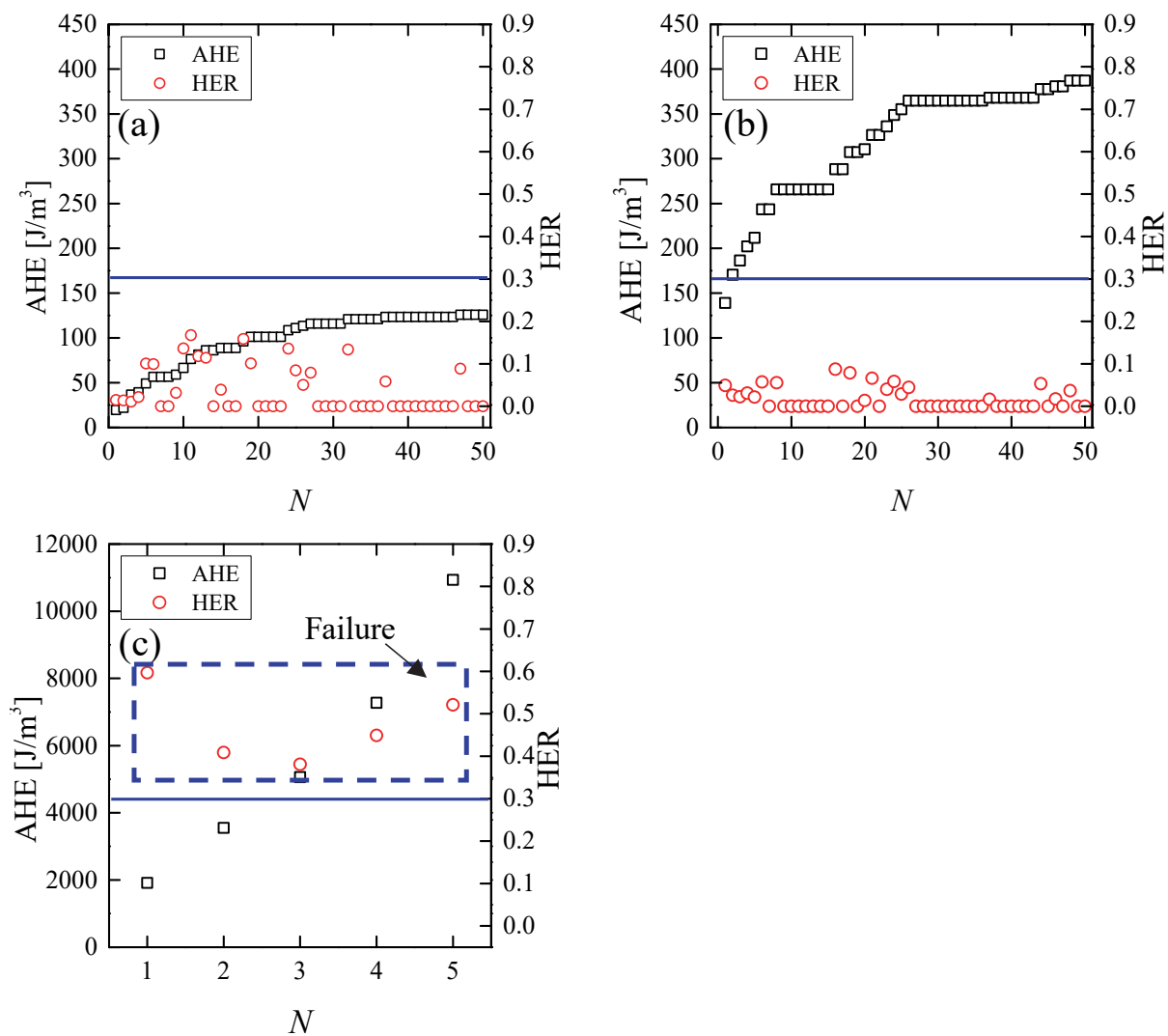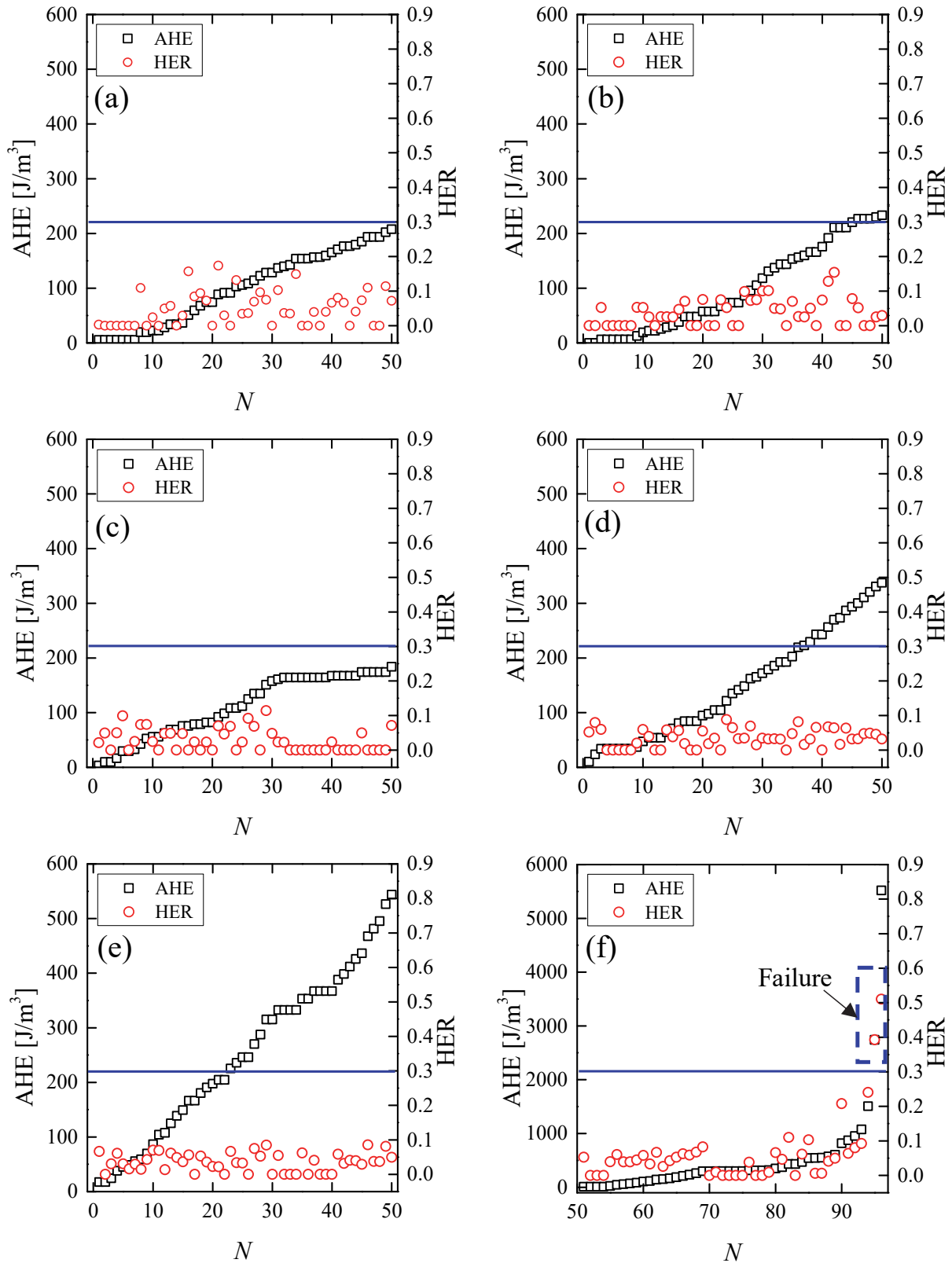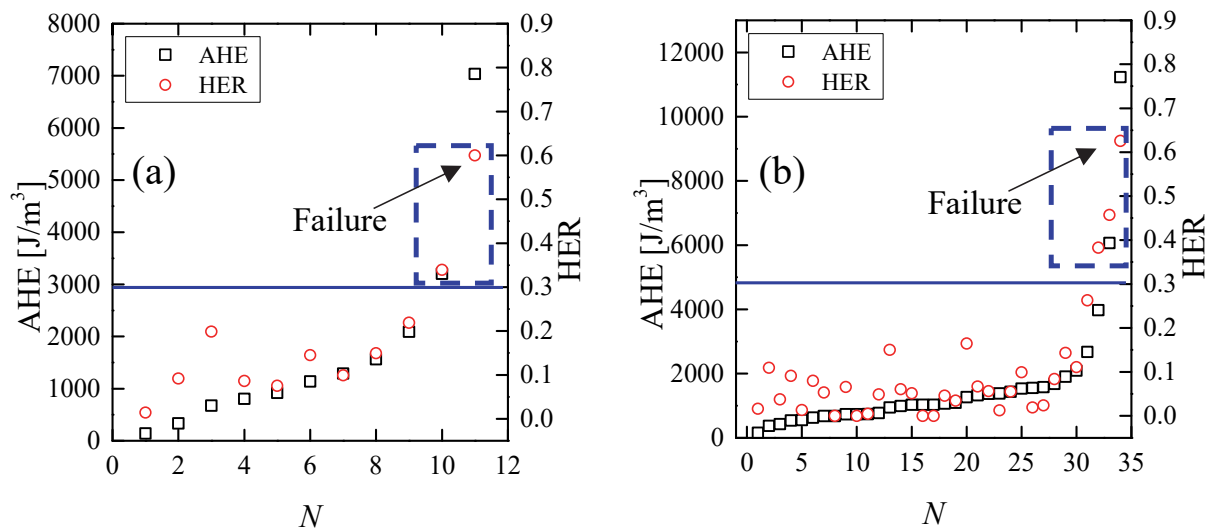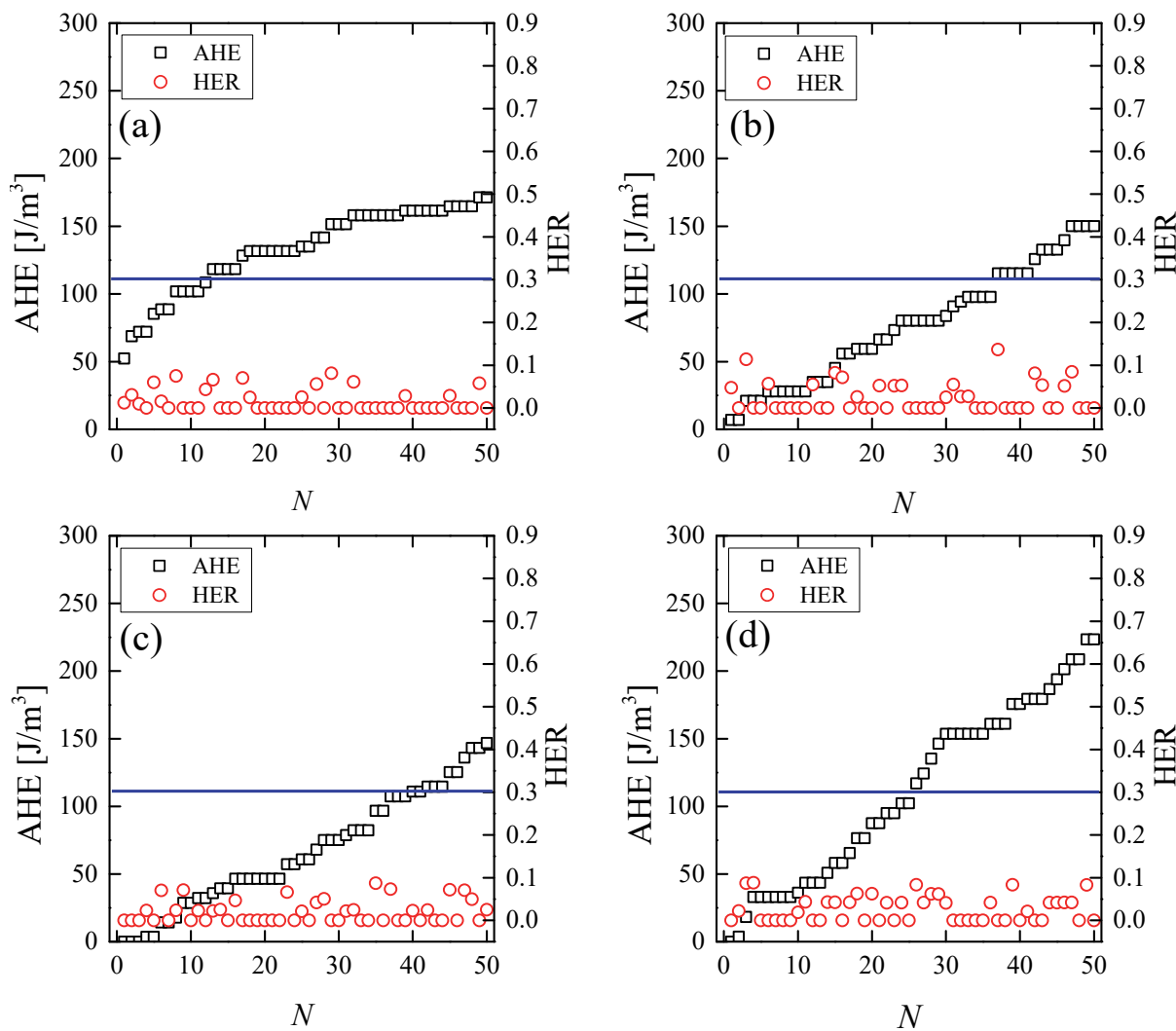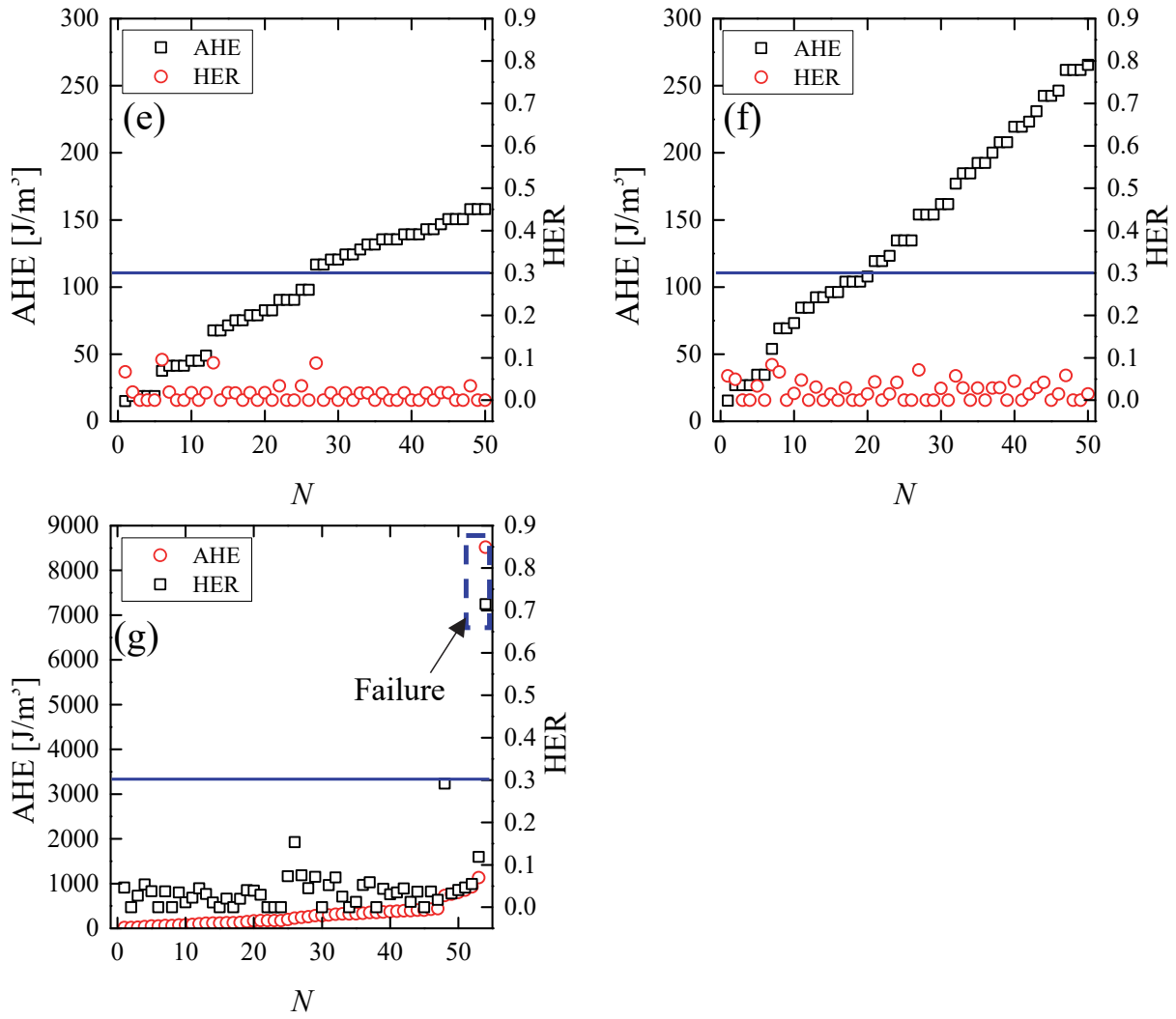**Figure 5.11** AHE and HER versus load cycles for (a) #12 S1 (b) #12 S2 (c) #12 S3 (d) #12 S4 (e) #12 S5 (f) #12 S6 (g) #12 S7
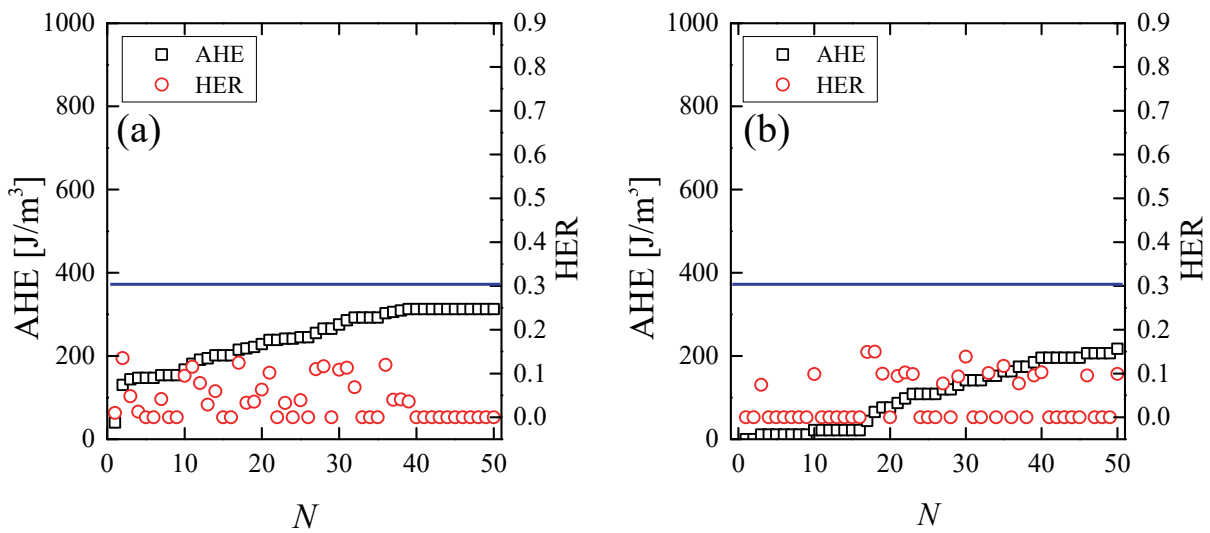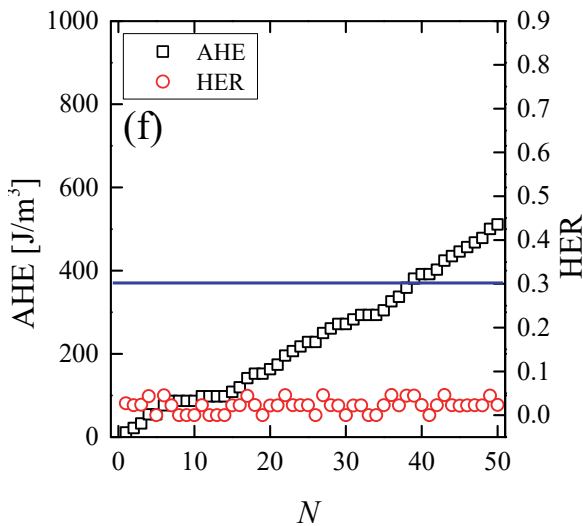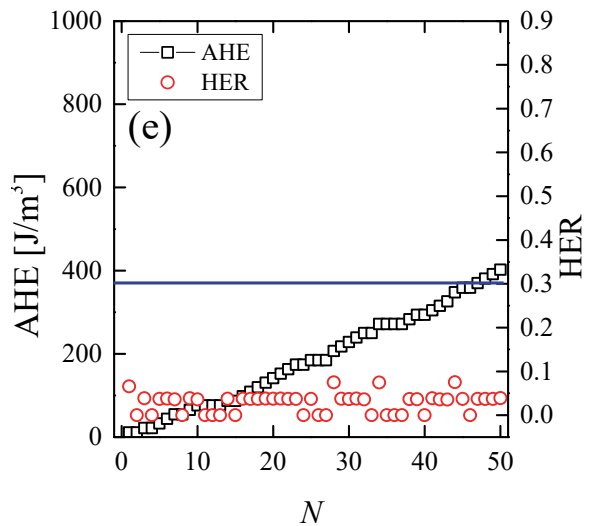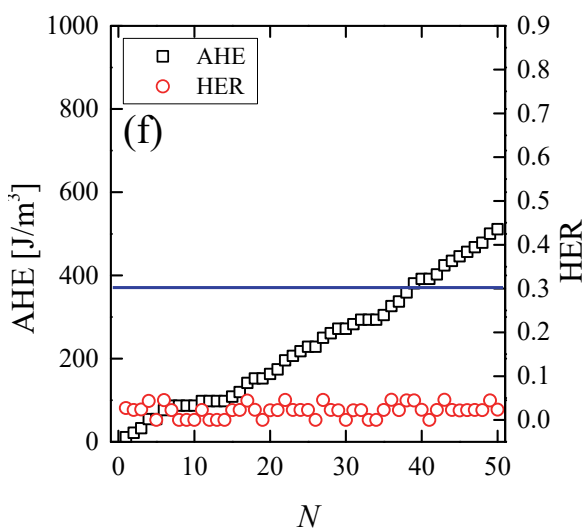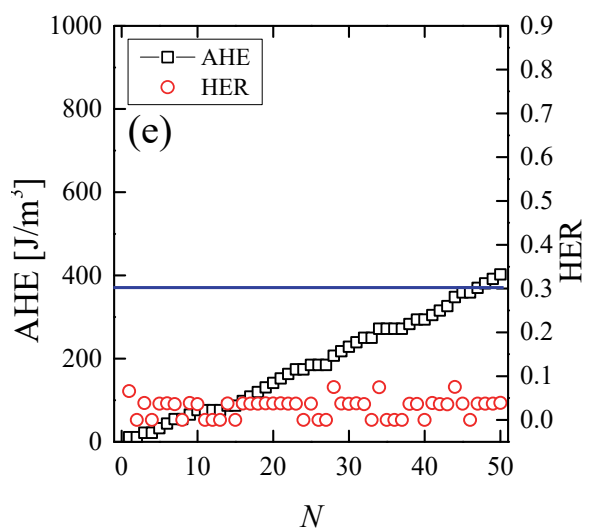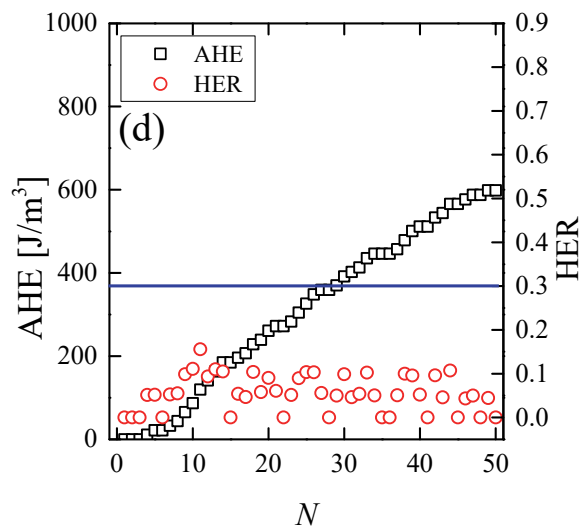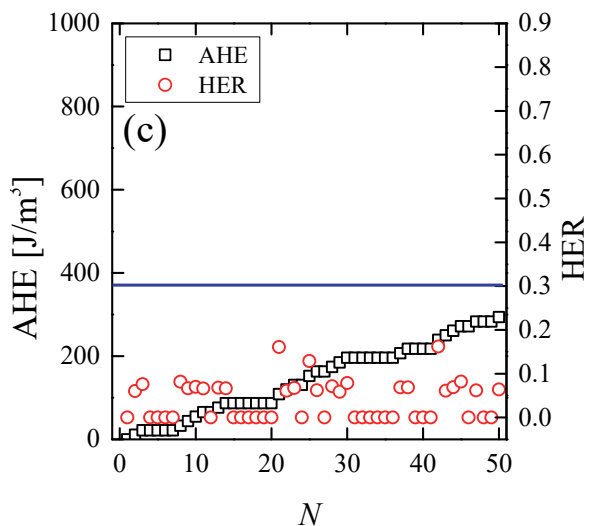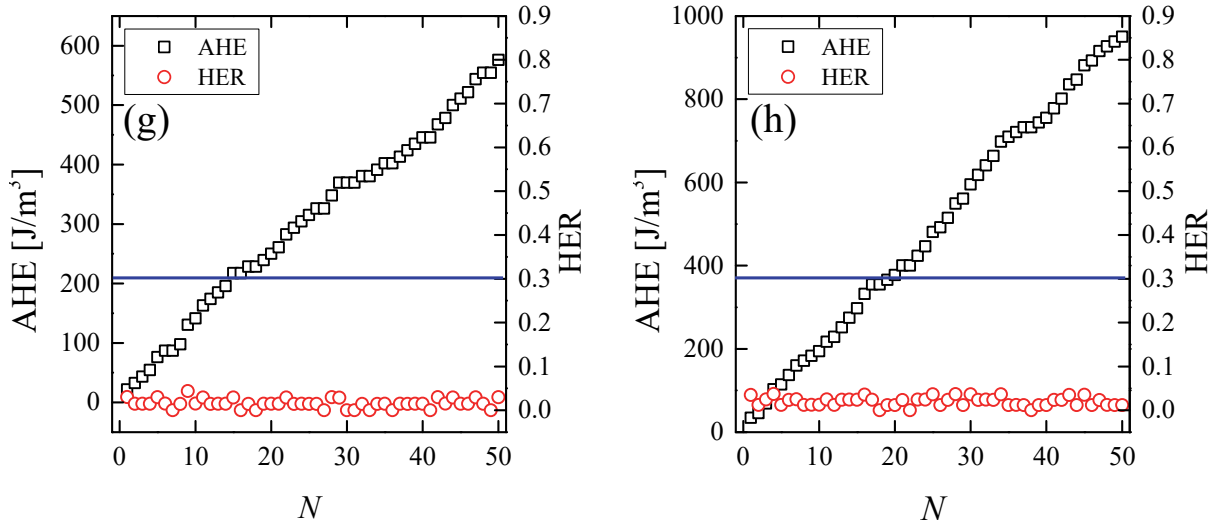
Figure 5.12 AHE and HER versus load cycles for (a) #8 S1 (b) #8 S2 (c) #8 S3 (d) #8 S4 (e) #8 S5 (f) #8 S6 (g) #8 S7 (h) #8 S8 (i) #8 S9 (j) #8 S10
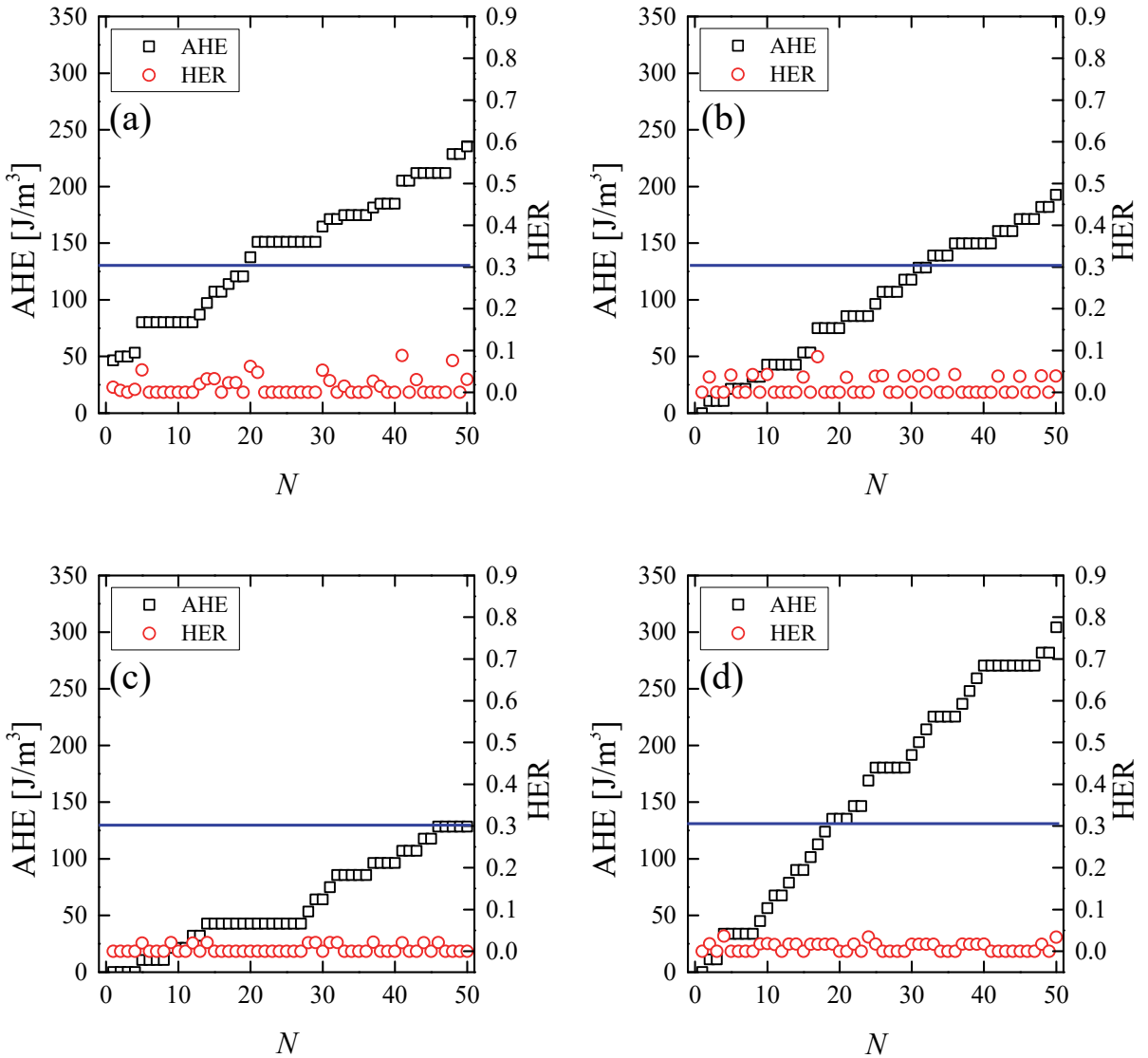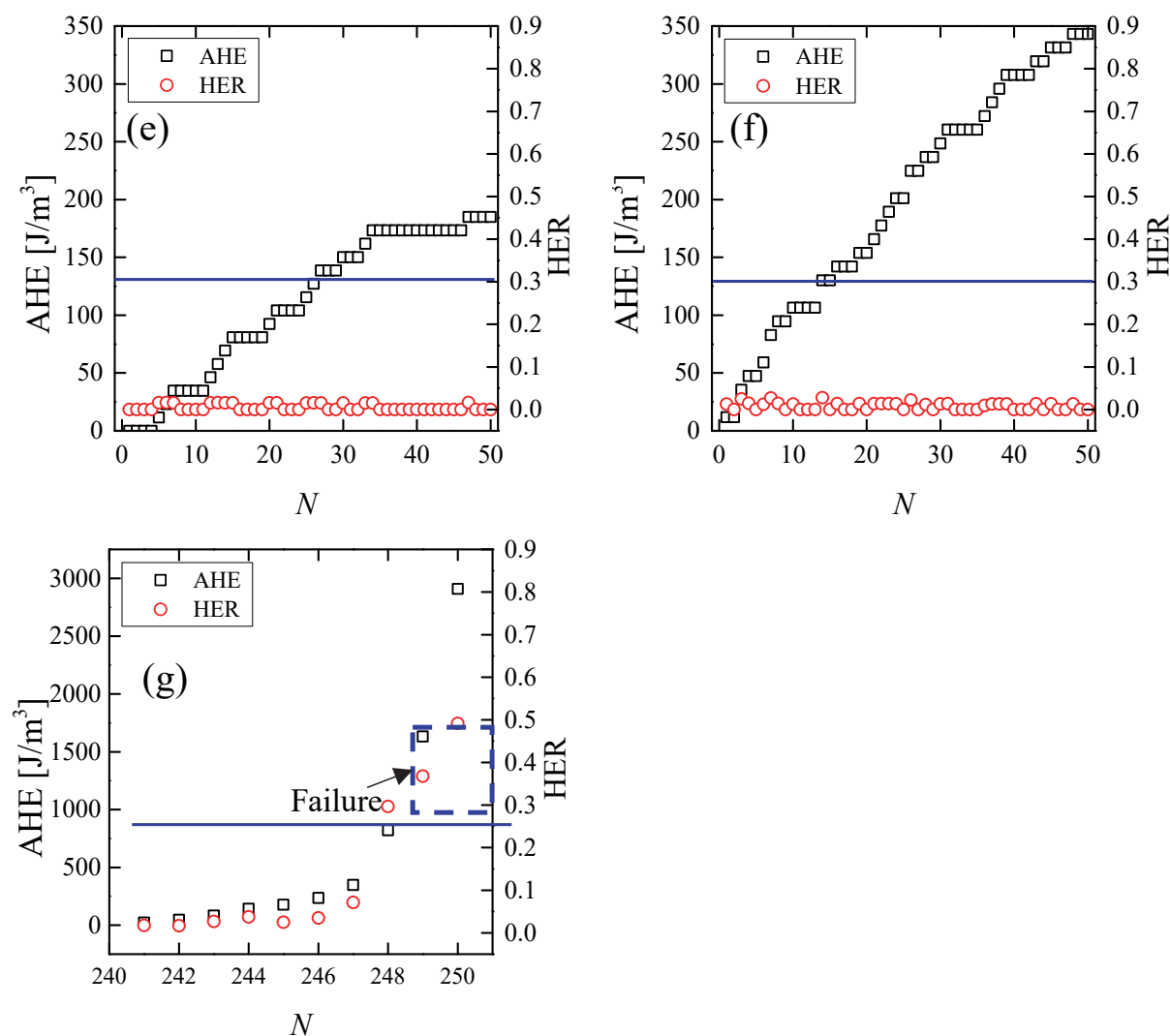
Figure 5.13 AHE and HER versus load cycles for (a) #10 S1 (b) #10 S2 (c) #10 S3 (d) #10 S4 (e) #10 S5 (f) #10 S6-1 (g) #10 S6-2

As described in Chapter 3, in the framework of the dissipated energy method, U_a reflects the evolution of the cumulative dissipated energy. The slope of the curve U_a/N versus N represents the speed of energy dissipation. Figure 5.14 illustrates the effect of σ_{max} and loading frequency on U_a/N and AHE/N. The relation between U_a/N and σ_{max} can be fitted by an exponential function. According to Table 3.2, #5 experienced 5 consecutive cyclic loading stages with σ_{max} increasing from 0.75 UCS to 0.925 UCS and #12 experienced 7 consecutive loading stages with σ_{max} increasing from 0.9 UCS to 1.075 UCS. As shown in Figure 5.14a, the speed of energy dissipation in the first cyclic loading stage (blue triangular symbols) is larger than in the following ones with gradually increasing σ_{max} (red round symbols for #5 and black square symbols for #12). The influence of loading frequency on U_a/N is limited under the condition that loading frequency is increased from 0.4 Hz to 0.8 Hz. The curves shown in Figure 5.14a

136

are very similar to those shown in Figure 5.14b. The relation between AHE/N and σ_{max} also follows an exponential relation. The gradual increase of σ_{max} starting from a smaller value can reduce the growth rate of AHE. A smaller growth rate of AHE is beneficial to the stability of concrete.
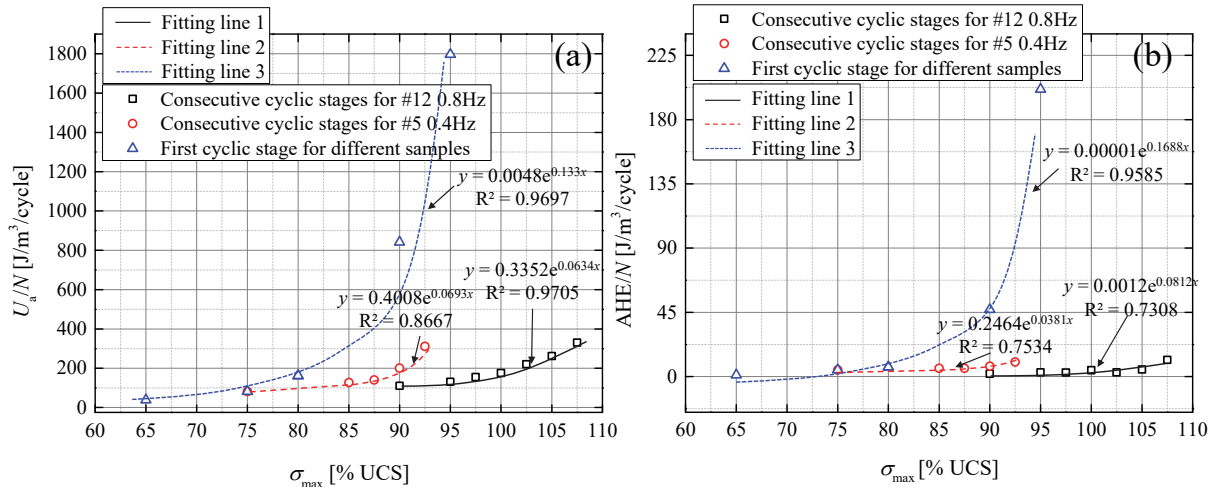
Figure 5.14 (a) effect of σ_{max} and f on U_a/N (b) effect of σ_{max} and f on AHE/N

Figure 5.15 illustrates the effect of σ_{min} on cumulated speed of U_a and AHE. The relation between U_a/N, AHE/N and σ_{min} follows a logarithmic relation. The effect of σ_{min} on U_a/N and AHE/N is not that obvious compared to σ_{max}. This indicates that σ_{max} has a more dominant influence on the damage evolution than σ_{min} which is coincident with the results shown in Figure 5.5.
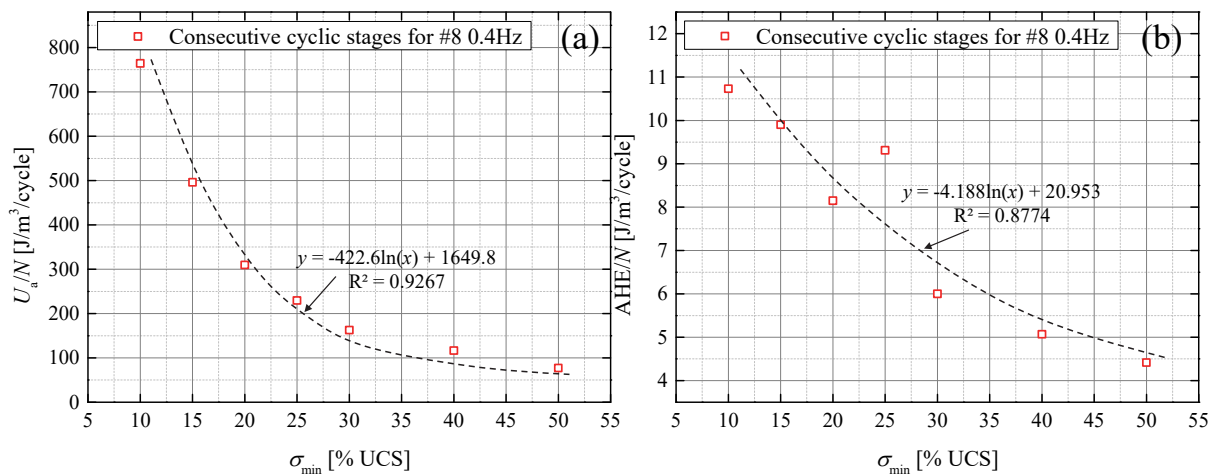
Figure 5.15 (a) effect of σ_{min} on U_a/N (b) effect of σ_{min} of on AHE/N

5.3 In situ application of the fatigue prediction method

The proposed two-step approach is more like a real-time monitoring method. The critical values for HOR and HER do not include the load levels directly. This indicates that the proposed prediction method has a more general applicability than other common methods (such as the S-N curve). In laboratory testing or field applications, two independent but synchronized channels should record peak stress and peak strain during one cycle. An automatic recognition program should be inserted in the testing system to detect whether peak stress point and peak strain point are coincident or not. If the two points are not coincident, N_h will be determined. The method is illustrated in Figure 5.16.
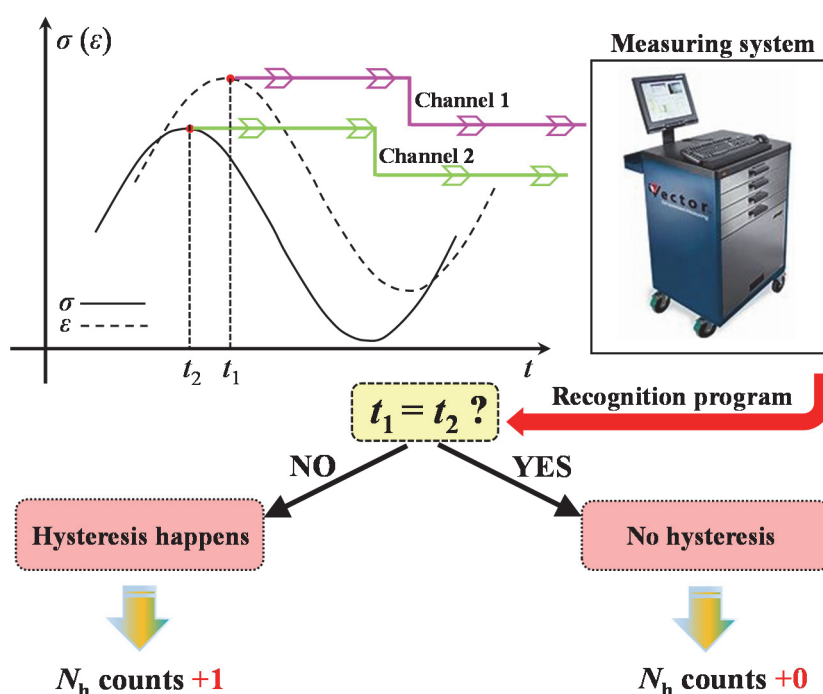
Figure 5.16 Scheme to illustrate the determination of N_h during laboratory testing or in-situ application

The two-step analysis described above can be applied in engineering practice as follows (see also Figure 5.17). First, perform laboratory tests with samples of the specific material (e.g. concrete or rock) to define critical (limit, threshold) values for HOR and HER. Second, determine actual HOR and HER values by stress and strain measurements in-situ. This can be done continuously or - in a more economical way – only at several points in time. Finally, actual values have to be compared with the critical values to classify the current state and safety of the construction element. The two-step prediction approach seems to provide a more precise

failure criterion compared to other classical approaches. More detailed investigations are necessary to proof if the proposed approach is robust.
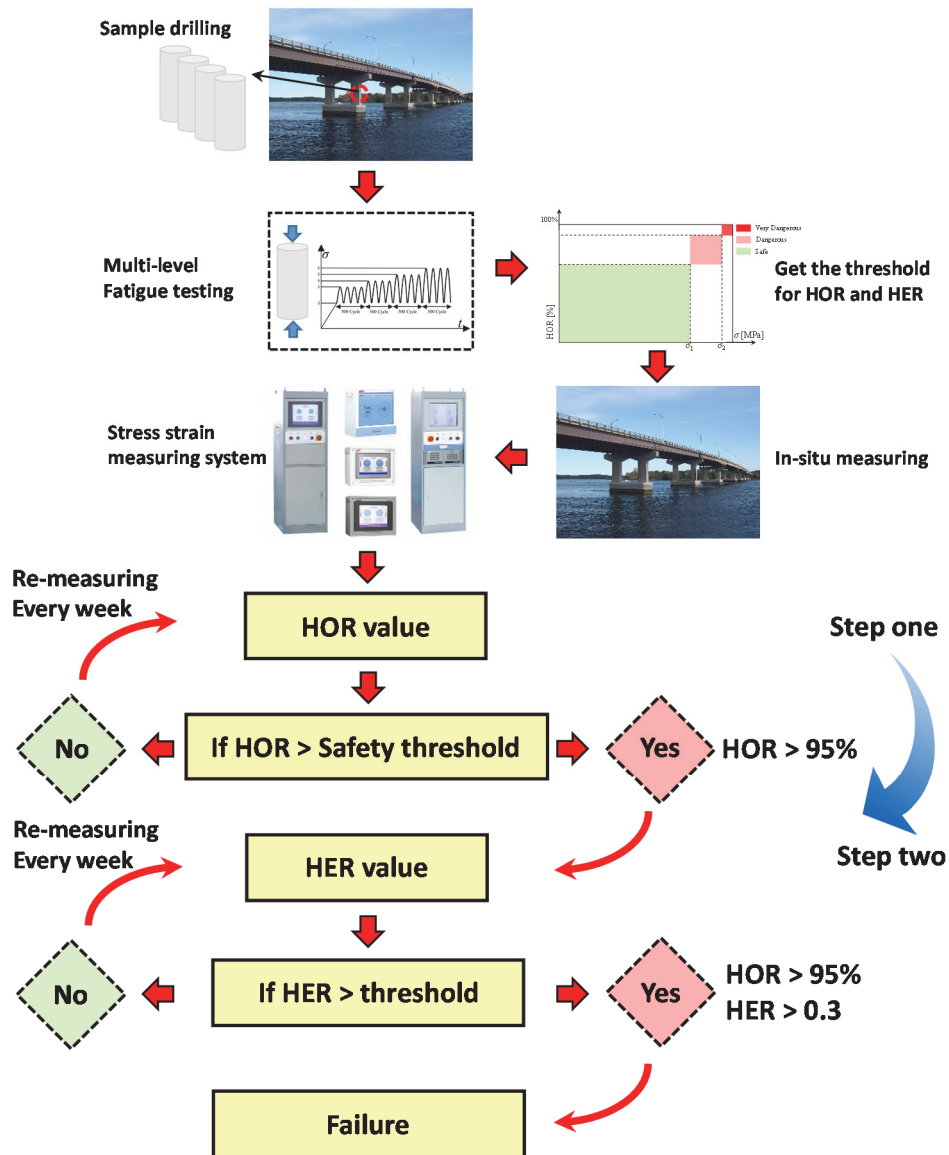
Figure 5.17 Flow chart of two-step prediction approach for engineering applications

5.4 Conclusions

As a fatigue damage indicator, HOR has two critical values. The two critical values for the specific concrete we used in laboratory testing are 75% and 95%. When HOR is under 75%, the concrete has no risk to fail, when HOR is between 75% and 95%, the concrete has the possibility to break, when HOR is larger than 95%, the concrete is extremely prone to fail already in the current cyclic loading stage. In addition, if HOR is larger than 75% and HER is larger than 0.3 at the same time, the concrete will fail within next few cycles. All the tested 9

concrete samples confirmed this statement. It is worth noting that the critical values of HOR and HER are material specific parameters. For different materials, fatigue testing should be conducted to get the specific critical values for HOR and HER. Due to the in general similar material behaviour of concrete and brittle rocks it can be assumed, that the proposed two-step approach can also be applied in rock mechanics. To get reliable and robust values for HOR and HER it is suggested to perform at least 50 cycles in each load level. It is also suggested that the time interval between the two consecutive data points should be small enough. In our laboratory testing, the time interval between two data points is as small as 0.02 seconds.

6. Conclusions and outlook

6.1 Main conclusions

In this thesis, the fatigue behaviour of concrete subjected to compressive cyclic loading has been investigated based on laboratory tests and numerical simulations. In laboratory testing, single and multi-level cyclic loading regimes were carried out. The evolution of axial/radial strain, dissipated energy, acoustic emission (AE) characteristics, ultrasonic wave speed and dynamic response behaviours are analysed. In the numerical simulations, the **N**onlinear **P**arallel-bonded **S**tress **C**orrosion (NPSC) model and the **M**ulti-level **S**tress **C**orrosion (MSC) model were proposed to replicate the mechanical behaviour of concrete samples under single-level and multi-level cyclic loading. Based on the **L**inear **P**arallel **B**onded **M**odel (LPBM), AE events and AE energy are simulated and calibrated on the data set obtained from laboratory testing. A real time fatigue prediction method is proposed based on the hysteresis damage indicator. The main conclusions of this thesis are:

1. The evolution of damage indicators in terms of continuum damage mechanics and dissipated energy can be well described by an exponential relation in case of fixed minimum load level and varying maximum load level and can be well fitted by a logarithmic relation for a fixed maximum load level and varying minimum load level. The effect of maximum load level on cumulative AE counts and P-wave speed is more obvious than minimum load level.

2. The axial strain for cyclically loaded concrete specimens is inhomogeneous. Top and bottom parts of the samples are influenced by the stiffness contrast and the dynamic effect of direct loading, whereas the middle part is not influenced. The maximum load level has an obvious effect on axial and lateral strain rate and follows an exponential relation. At peak strength the strain rate in the middle part is larger than that in the top and bottom parts.

3. The energy dissipation of samples is also inhomogeneous when subjected to cyclic loading. At small load levels, top, middle and bottom parts have almost the same amount of dissipated energy. The disparity of energy dissipation between middle part and top/bottom part increases with increasing load level and reaches the peak value at ultimate strength. The maximum load level has a more pronounced effect on energy dissipation than the minimum load level does.

4. A P-wave ratio is proposed as ratio of P-wave speed measured at the middle and top part of the concrete sample, respectively. The P-wave ratio evolution shows three stages and its peak

point is an effective precursor to predict the fatigue failure of concrete. Monotonically loaded concrete specimens show smaller axial and lateral strain compared to cyclically loaded samples at peak strength of the last cycle. The release of stored energy for samples failing after monotonic loading leads to larger macroscopic and persistent cracks. Due to enhanced energy absorption during cyclic loading, the failure patterns of cyclically loaded concrete samples typically show smaller and more evenly distributed cracks.

5. For specimens which failed during the first fatigue loading stage, hysteresis in the direction vertical to loading is more obvious than in loading directions. The hysteresis time shows a sudden rise when the specimen is close to failure. **D**ynamic **R**esponse **R**atio (DRR) experiences an initial increase and then drops to a lower value at failure. The maximum load level of the first cyclic loading stage has an approximately linear relation with DRR and hysteresis time. The hysteresis time increases with maximum load level whereas DRR shows an opposite trend. For specimens which experienced multi-loading stages, a slight increase of the maximum load level can reduce the hysteresis time and increase DRR. The hysteresis time shows a strong nonlinear rise when the maximum load level is close to the fatigue strength. The evolution with respect to the DRR of lateral strain is well consistent with the four-phase trend of P-wave speed during the cyclic loading. The trend with respect to hysteresis time of lateral strain has strong similarity with the evolution of cumulative AE counts. DRR and hysteresis time of lateral strain can be used as damage variables when ultrasonic and AE monitoring are not available. The maximum load level has more pronounced effect on DRR and hysteresis time than the minimum load level.

6. Based on the LPBM in PFC^{2D}, the NPSC model is proposed to simulate the mechanical behaviour of concrete subjected to single-level cyclic loading. The time-dependent damage during fatigue tests is reflected by the nonlinear reduction in bond diameter between two bonded particles. The logarithmic function in NPSC model gives the best fit with laboratory test results. Based on PFC^{3D}, the MSC model is proposed to simulate the mechanical behaviour of concrete subjected to multi-level cyclic loading and calibrated on laboratory tests. The MSC model considers the quantitative relation of the time and stress dependent damage with respect to the maximum and minimum load during cyclic loading. The logic of the MSC model is that for the initial cyclic loading stage. The bond diameter follows a linear reduction due to the compaction effect in laboratory testing. For the consecutive cyclic loading stages where maximum load level increases and minimum load level is fixed, the bond diameters remain

constant during each loading stage. For further different stages, the bond diameter reduces following an exponential function with respect to the maximum load level. For the consecutive cyclic loading stages in which minimum load level decreases and maximum load level is fixed, the bond diameter remains constant after the initial cyclic loading stage.

7. The stress-controlled loading is realized by use of a dense clump block wall (DCB-wall) in both, PFC^{2D} and PFC^{3D} numerical simulations. The stress-controlled loading is capable to simulate different load levels under monotonic and repeated loading. The applicability and effectiveness of stress-controlled loading are validated through uniaxial compressive cyclic loading tests. The stress wave transmission during the stress-controlled loading is homogenous and consistent with laboratory tests.

8. The evolution of axial strain, peak/residual strain rate, and the shape of hysteresis loop in numerical simulations using the MSC model are compared and calibrated via laboratory test results. Laboratory tests and numerical simulations show quite similar pattern. A 3D AE monitoring system is proposed for PFC^{3D}. The cumulative AE energy can be precisely and quantitatively characterized by the release of the bond strain energy in LPBM. The results of cumulative AE energy measured in laboratory tests and PFC simulations show high consistency during multi-level cyclic loading.

9. A real time fatigue failure prediction method is proposed based on the **H**ysteresis **O**ccurrence **R**atio (HOR) and **H**ysteresis **E**nergy **R**atio (HER). HOR has two critical values. The two critical values for the specific concrete we used in laboratory testing are 75% and 95%. When HOR is under 75%, the concrete has no risk to fail, when HOR is between 75% and 95%, the concrete has the possibility to fail, when HOR is larger than 95%, the concrete is extremely prone to fail already in the current cyclic loading stage. In addition, if HOR is larger than 75% and HER is larger than 0.3 at the same time, the concrete will fail within next few cycles. It is worth noting that the critical values of HOR and HER are material specific parameters. For different materials, fatigue testing should be conducted to get the specific critical values for HOR and HER. It is also suggested that the time interval between two consecutive data points should be small enough. In our laboratory testing, the time interval between two data points is as small as 0.02 seconds.

6.2 Recommendations for future research

Based on the current research, future work should cover the following aspects:

1. The fatigue behaviour of concrete subjected to more complex stresses should be considered, such as triaxial fatigue testing, static - dynamic coupled fatigue testing, compression - tension fatigue testing.

2. Thermo-mechanical coupled fatigue testing is also a promising research direction.

3. Random cyclic loading should be considered because it is closer to loading in-situ.

4. The numerical model can be up-graded by more details at the microscopic level. Shapes of particles should be considered in a more realistic manner to duplicate actual mineral grains in concrete material or rocks.

Reference

Aïtcin PC (2003) The durability characteristics of high performance concrete: a review. Cem Concr Compos 25:409–420. doi: https://doi.org/10.1016/S0958-9465(02)00081-1

Albert W (1838) Uber Treibseile am Harz. Arch fuer Mineral Geognosie, Bergbau und Huttenkd 10:215–234.

Alderliesten R, Rans C (2009) The meaning of threshold fatigue in fibre metal laminates. Int J Fatigue 31:213–222. doi: https://doi.org/10.1016/j.ijfatigue.2008.09.008

Alliche A (2004) Damage model for fatigue loading of concrete. Int J Fatigue 26:915–921. doi: http://dx.doi.org/10.1016/j.ijfatigue.2004.02.006

Anderson T (2005) Fracture mechanics: fundamentals and applications, third edition.

Bagde MN, Petroš V (2005) Fatigue properties of intact sandstone samples subjected to dynamic uniaxial cyclical loading. Int J Rock Mech Min Sci 42:237–250. doi: http://dx.doi.org/10.1016/j.ijrmms.2004.08.008

Bagde MN, Petroš V (2009) Fatigue and dynamic energy behaviour of rock subjected to cyclical loading. Int J Rock Mech Min Sci 46:200–209. doi: http://dx.doi.org/10.1016/j.ijrmms.2008.05.002

Bahaaddini M, Sharrock G, Hebblewhite BK (2013) Numerical direct shear tests to model the shear behaviour of rock joints. Comput Geotech 51:101–115. doi: 10.1016/j.compgeo.2013.02.003

Baluch MH, Al-Gadhib AH, Khan AR, Shaalan A (2003) CDM model for residual strength of concrete under cyclic compression. Cem Concr Compos 25:503–512. doi: http://dx.doi.org/10.1016/S0958-9465(02)00090-2

Belytschko T, Black T (1999) Elastic crack growth in finite elements with minimal remeshing. Int J Numer Methods Eng 45:601–620. doi: 10.1002/(SICI)1097-0207(19990620)45:5<601::AID-NME598>3.0.CO;2-S

Bernard S, Balla VK, Bose S, Bandyopadhyay A (2011) Rotating bending fatigue response of laser processed porous NiTi alloy. Mater Sci Eng C 31:815–820. doi: https://doi.org/10.1016/j.msec.2010.12.007

145

Bhattacharya B, Ellingwood B (1998) Continuum damage mechanics analysis of fatigue crack initiation. Int J Fatigue 20:631–639. doi: 10.1016/S0142-1123(98)00032-2

Borja RI (2013) Plasticity modeling & computation. Springer Berlin Heidelberg

Boukpeti N, Lehane B, Carraro JAH (2014) Strain accumulation procedure during staged cyclic loading of carbonate sediments. In: Proceedings of the ASME 2014 33rd International Conference on Ocean, Offshore and Arctic Engineering. San Francisco, p 23692

Braithwaite F (1854) On the fatigue and consequent fracture of metals. In: Minutes of the Proceedings of the Institution of Civil Engineers. London, pp 463–474

Bumanis G, Dembovska L, Korjakins A, Bajare D (2018) Applicability of freeze-thaw resistance testing methods for high strength concrete at extreme −52.5 °C and standard −18 °C testing conditions. Case Stud Constr Mater 8:139–149. doi: https://doi.org/10.1016/j.cscm.2018.01.003

Cai M, Kaiser PK, Morioka H, et al (2007) FLAC/PFC coupled numerical simulation of AE in large-scale underground excavations. Int J Rock Mech Min Sci 44:550–564. doi: https://doi.org/10.1016/j.ijrmms.2006.09.013

Cerfontaine B, Collin F (2018) Cyclic and fatigue behaviour of rock materials: review, interpretation and research perspectives. Rock Mech Rock Eng 51:391–414. doi: 10.1007/s00603-017-1337-5

Chaboche JL (1988a) Continuum damage mechanics: part I—general concepts. J Appl Mech 55:59–64. doi: 10.1115/1.3173661

Chaboche JL (1988b) Continuum damage mechanics: part II—damage growth, crack initiation, and crack growth. J Appl Mech 55:65–72. doi: 10.1115/1.3173662

Chang SH, Yun KJ, Lee CI (2002) Modeling of fracture and damage in rock by the bonded-particle model. Geosystem Eng 5:113–120. doi: 10.1080/12269328.2002.10541196

Chen TC, Yeung MR, Mori N (2004) Effect of water saturation on deterioration of welded tuff due to freeze-thaw action. Cold Reg Sci Technol 38:127–136. doi: https://doi.org/10.1016/j.coldregions.2003.10.001

Chen W, Konietzky H (2014) Simulation of heterogeneity, creep, damage and lifetime for loaded brittle rocks. Tectonophysics 633:164–175. doi: https://doi.org/10.1016/j.tecto.2014.06.033

Chen X, Huang Y, Chen C, et al (2017) Experimental study and analytical modeling on hysteresis behavior of plain concrete in uniaxial cyclic tension. Int J Fatigue 96:261–269. doi: 10.1016/j.ijfatigue.2016.12.002

Chen Y, Ji C, Zhang C, et al (2019) Analysis for post-impact tensile-tensile fatigue damage of 2024-T3 sheets based on tests, digital image correlation (DIC) technique and finite element simulation. Int J Fatigue 122:125–140. doi: https://doi.org/10.1016/j.ijfatigue.2019.01.010

Cho N, Martin CD, Sego DC (2007) A clumped particle model for rock. Int J Rock Mech Min Sci 44:997–1010. doi: 10.1016/j.ijrmms.2007.02.002

Cundall PA, Strack ODL (1979) A discrete numerical model for granular assemblies. Géotechnique 29:47–65. doi: 10.1680/geot.1979.29.1.47

Dang W, Konietzky H, Frühwirt T (2017) Direct shear behavior of planar joints under cyclic normal load conditions: effect of different cyclic normal force amplitudes. Rock Mech. Rock Eng. 50:3101–3107.

Dang W, Konietzky H, Frühwirt T (2016) Direct shear behavior of a plane joint under dynamic normal load (DNL) conditions. Eng Geol 213:133–141. doi: 10.1016/j.enggeo.2016.08.016

Dattoma V, Giancane S (2013) Evaluation of energy of fatigue damage into GFRC through digital image correlation and thermography. Compos Part B Eng 47:283–289. doi: http://dx.doi.org/10.1016/j.compositesb.2012.10.030

Dib G, Roy S, Ramuhalli P, Chai J (2019) In-situ fatigue monitoring procedure using nonlinear ultrasonic surface waves considering the nonlinear effects in the measurement system. Nucl Eng Technol 51:867–876. doi: https://doi.org/10.1016/j.net.2018.12.003

Ding X, Ma T, Gao W (2017) Morphological characterization and mechanical analysis for coarse aggregate skeleton of asphalt mixture based on discrete-element modeling. Constr Build Mater 154:1048–1061. doi: https://doi.org/10.1016/j.conbuildmat.2017.08.008

Dirik H, Yalçinkaya T (2018) Crack path and life prediction under mixed mode cyclic variable amplitude loading through XFEM. Int J Fatigue 114:34–50. doi: https://doi.org/10.1016/j.ijfatigue.2018.04.026

Dowell RK, Seible F, Wilson EL (1998) Pivot hysteresis model for reinforced concrete members. ACI Struct J 95:607–617. doi: 10.14359/575

Erarslan N, Alehossein H, Williams DJ (2014) Tensile fracture strength of brisbane tuff by static and cyclic loading tests. Rock Mech Rock Eng 47:1135–1151. doi: 10.1007/s00603-013-0469-5

Erdogan F, Ratwani M (1970) Fatigue and fracture of cylindrical shells containing a circumferential crack. Int J Fract Mech 6:379–392. doi: 10.1007/BF00182626

Eskandari H, Kim HS (2017) A theory for mathematical framework and fatigue damage function for the S-N plane. In: Fatigue and Fracture Test Planning, Test Data Acquisitions and Analysis.

Fairhurst C (1964) On the validity of the 'Brazilian' test for brittle materials. Int J Rock Mech Min Sci Geomech Abstr 1:535–546. doi: https://doi.org/10.1016/0148-9062(64)90060-9

Fan J, Chen J, Jiang D, et al (2017) Discontinuous cyclic loading tests of salt with acoustic emission monitoring. Int J Fatigue 94:140–144. doi: 10.1016/j.ijfatigue.2016.09.016

Fan X, Hu S, Lu J, Wei C (2016) Acoustic emission properties of concrete on dynamic tensile test. Constr Build Mater 114:66–75. doi: https://doi.org/10.1016/j.conbuildmat.2016.03.065

Fathi A, Moradian Z, Rivard P, Ballivy G (2016) Shear mechanism of rock joints under pre-peak cyclic loading condition. Int J Rock Mech Min Sci 83:197–210. doi: https://doi.org/10.1016/j.ijrmms.2016.01.009

Feng SZ, Li W (2018) An accurate and efficient algorithm for the simulation of fatigue crack growth based on XFEM and combined approximations. Appl Math Model 55:600–615. doi: https://doi.org/10.1016/j.apm.2017.11.015

Feng X-T, Young RP, Reyes-Montes JM, et al (2019) ISRM suggested method for in situ acoustic emission monitoring of the fracturing process in rock masses. Rock Mech Rock Eng. doi: 10.1007/s00603-019-01774-z

Feng Y, Chi X, Wang W, et al (2008) Fast computing for LURR of earthquake prediction. Pure Appl Geophys 165:749–759. doi: 10.1007/s00024-008-0313-0

Freiman SW (1984) Effects of chemical environments on slow crack growth in glasses and ceramics. J Geophys Res Solid Earth 89:4072–4076. doi: 10.1029/JB089iB06p04072

Frost NE, Dugdale DS (1958) The propagation of fatigue cracks in sheet specimens. J Mech Phys Solids 6:92–110. doi: 10.1016/0022-5096(58)90018-8

Ge X (1987) Study on deformation and strength behavior of the large-sized triaxial rock samples under cyclic loading. Chinese J Rock Soil Mech 8:11–19.

Ge X, Jiang Y, Lu R, Ren J (2003) Testing study on fatigue deformation law of rock under cyclic loading. Chinese J Rock Mech Eng 22:1591–1585.

Ge X, Lu Y (1992) tudy on fatigue damage and irreversible deformation law of rock under cyclic. Chinese J Geotechical Eng 14:56–60.

Geranmayeh Vaneghi R, Ferdosi B, Okoth AD, Kuek B (2018) Strength degradation of sandstone and granodiorite under uniaxial cyclic loading. J Rock Mech Geotech Eng 10:117–126. doi: 10.1016/j.jrmge.2017.09.005

Ghuzlan KA, Carpenter SH (2006) Fatigue damage analysis in asphalt concrete mixtures using the dissipated energy approach. Can J Civ Eng 33:890–901.

Goel S, Singh SP, Singh P (2012) Flexural fatigue strength and failure probability of Self Compacting Fibre Reinforced Concrete beams. Eng Struct 40:131–140. doi: https://doi.org/10.1016/j.engstruct.2012.02.035

Griffith AA (1921) The phenomena of rupture and flow in solids. Philos Trans R Soc A Math Phys Eng Sci 221:163–198. doi: 10.1098/rsta.1921.0006

Grossi CM, Brimblecombe P, Harris I (2007) Predicting long term freeze–thaw risks on Europe built heritage and archaeological sites in a changing climate. Sci Total Environ 377:273–281. doi: https://doi.org/10.1016/j.scitotenv.2007.02.014

Han Z, Weatherley D, Puscasu R (2017) A relationship between tensile strength and loading stress governing the onset of mode I crack propagation obtained via numerical investigations using a bonded particle model. Int J Numer Anal Methods Geomech. doi:

10.1002/nag.2710

Hanif A, Usman M, Lu Z, et al (2018) Flexural fatigue behavior of thin laminated cementitious composites incorporating cenosphere fillers. Mater Des 140:267–277. doi: https://doi.org/10.1016/j.matdes.2017.12.003

Hazzard JF, Young RP (2000) Simulating acoustic emissions in bonded-particle models of rock. Int J Rock Mech Min Sci 37:867–872. doi: https://doi.org/10.1016/S1365-1609(00)00017-4

He J, Pan J, Wang A (2014) Acoustic emission characteristic of coal specimen under triaxial cyclic loading and unloading. J China Coal Soc 39:84–90.

He M, Huang B, Zhu C, et al (2018) Energy dissipation-based method for fatigue life prediction of rock salt. Rock Mech Rock Eng 51:1447–1455. doi: 10.1007/s00603-018-1402-8

Head A. (1953) The growth of fatigue cracks. London, Edinburgh, Dublin Philos Mag J Sci 44:925–938.

Henry HAL (2007) Soil freeze–thaw cycle experiments: Trends, methodological weaknesses and suggested improvements. Soil Biol Biochem 39:977–986. doi: https://doi.org/10.1016/j.soilbio.2006.11.017

Horii H, Shin HC, Pallewatta TM (1992) Mechanism of fatigue crack growth in concrete. Cem Concr Compos 14:83–89. doi: 10.1016/0958-9465(92)90002-D

Hu X, Lu Q, Xu Z, et al (2018) Compressive stress-strain relation of recycled aggregate concrete under cyclic loading. Constr Build Mater 193:72–83. doi: https://doi.org/10.1016/j.conbuildmat.2018.10.137

Hudson JA, Brown ET, Rummel F (1972) The controlled failure of rock discs and rings loaded in diametral compression. Int J Rock Mech Min Sci Geomech Abstr 9:241–248. doi: https://doi.org/10.1016/0148-9062(72)90025-3

Ibarra LF, Medina RA, Krawinkler H (2005) Hysteretic models that incorporate strength and stiffness deterioration. Earthq Eng Struct Dyn 34:1489–1511. doi: 10.1002/eqe.495

Infante-García D, Qian G, Miguélez H, Giner E (2019) Analysis of the effect of out-of-phase biaxial fatigue loads on crack paths in cruciform specimens using XFEM. Int J Fatigue

123:87–95. doi: https://doi.org/10.1016/j.ijfatigue.2019.01.019

Inglis C (1913) Stresses in a plate due to the presence of cracks and sharp corners. SPIE Milestone Ser 221:3–17.

Irwin G (1956) Onset of fast crack propagation in high strength steel and aluminum alloys. In: Sagamore Research Conference Proceedings. pp 289–305

Irwin G (1957) Analysis of stresses and strains near the end of a crack traversing a plate. J Appl Mech ASME 24:351–369.

Isailović I, Wistuba MP (2018) Asphalt mixture layers' interface bonding properties under monotonic and cyclic loading. Constr Build Mater 168:590–597. doi: https://doi.org/10.1016/j.conbuildmat.2018.02.149

ISRM (1978) Suggested methods for determining tensile strength of rock materials. Int J Rock Mech Min Sci Geomech Abstr 15:99–103.

Itasca Consulting Group Inc. (2014) PFC 5.0 (Particle Flow Code) documentation. Minneapolis

Jia C, Xu W, Wang R, et al (2018) Characterization of the deformation behavior of fine-grained sandstone by triaxial cyclic loading. Constr Build Mater 162:113–123. doi: https://doi.org/10.1016/j.conbuildmat.2017.12.001

Jia H, Wang E, Song D, et al (2019) Precursory changes in wave velocity for coal and rock samples under cyclic loading. Results Phys 12:432–434. doi: 10.1016/j.rinp.2018.11.096

Jiang F, Liu R, Zhang D (1994) A fatigue damage function based on energy analysis. J Harbin Eng Univ 15:25–30.

Jing L, Stephansson O, Nordlund E (1993) Study of rock joints under cyclic loading conditions. Rock Mech Rock Eng 26:215–232. doi: 10.1007/BF01040116

Ju Y, Wang Y, Dong H, Yang Y (2018) Numerical analysis of the hydrofracturing behaviour of heterogeneous glutenite considering hydro-mechanical coupling effects based on bonded particle models. Int J Numer Anal Methods Geomech. doi: 10.1002/nag.2801

Kanninen MF, Popelar CA, Saunders H (1988) Advanced fracture mechanics. J Vib Acoust Stress Reliab Des 110:419. doi: 10.1115/1.3269540

Khanlari G, Abdilor Y (2015) Influence of wet-dry, freeze-thaw, and heat-cool cycles on the physical and mechanical properties of upper red sandstones in central Iran. Bull Eng Geol Environ 74:1287–1300. doi: 10.1007/s10064-014-0691-8

Kim J, Son S, Rye T, Soriano G (2015) Effects of cyclic shear stress and average shear stress on the cyclic loading failure of marine silty sand. Lowl Technol Int 17:19–26.

Komoróczi A, Abe S, Urai JL (2013) Meshless numerical modeling of brittle--viscous deformation: first results on boudinage and hydrofracturing using a coupling of discrete element method (DEM) and smoothed particle hydrodynamics (SPH). Comput Geosci 17:373–390. doi: 10.1007/s10596-012-9335-x

Kulatilake PHSW, Malama B, Wang J (2001) Physical and particle flow modeling of jointed rock block behavior under uniaxial loading. Int J Rock Mech Min Sci 38:641–657. doi: 10.1016/S1365-1609(01)00025-9

Kumar S, Singh I V, Mishra BK (2015) A homogenized XFEM approach to simulate fatigue crack growth problems. Comput Struct 150:1–22. doi: https://doi.org/10.1016/j.compstruc.2014.12.008

Le KN, Ghayoomi M (2017) Cyclic direct simple shear test to measure strain-dependent dynamic properties of unsaturated sand. Geotech Test J 40:381–395. doi: 10.1520/GTJ20160128

Lee H-J, Daniel JS, Richard KY (2000) Continuum damage mechanics-based fatigue model of asphalt concrete. J Mater Civ Eng 12:105–112.

Lee MK, Barr BIG (2004) An overview of the fatigue behaviour of plain and fibre reinforced concrete. Cem Concr Compos 26:299–305. doi: 10.1016/S0958-9465(02)00139-7

Lei D, Zhang P, He J, et al (2017) Fatigue life prediction method of concrete based on energy dissipation. Constr Build Mater 145:419–425. doi: http://dx.doi.org/10.1016/j.conbuildmat.2017.04.030

Leng J, Liao C, Ye G, Jeng D-S (2018) Laboratory study for soil structure effect on marine clay response subjected to cyclic loads. Ocean Eng 147:45–50. doi: https://doi.org/10.1016/j.oceaneng.2017.10.020

Li B, Rosa LG (2016) Prediction models of intrinsic fatigue threshold in metal alloys examined

by experimental data. Int J Fatigue 82:616–623. doi: https://doi.org/10.1016/j.ijfatigue.2015.09.018

Li D, Wang E, Kong X, et al (2019) Damage precursor of construction rocks under uniaxial cyclic loading tests analyzed by acoustic emission. Constr Build Mater 206:169–178. doi: https://doi.org/10.1016/j.conbuildmat.2019.02.074

Li D, Wong LNY (2013) The Brazilian disc test for rock mechanics applications: review and new insights. Rock Mech Rock Eng 46:269–287. doi: 10.1007/s00603-012-0257-7

Li J, Konietzky H, Frühwirt T (2017a) Voronoi-based DEM simulation approach for sandstone considering grain structure and pore size. Rock Mech Rock Eng 50:2749–2761. doi: 10.1007/s00603-017-1257-4

Li Z, Wang YH, Ma CH, Mok CMB (2017b) Experimental characterization and 3D DEM simulation of bond breakages in artificially cemented sands with different bond strengths when subjected to triaxial shearing. Acta Geotech. doi: 10.1007/s11440-017-0593-6

Liang J, Nie X, Masud M, et al (2017) A study on the simulation method for fatigue damage behavior of reinforced concrete structures. Eng Struct 150:25–38. doi: https://doi.org/10.1016/j.engstruct.2017.07.001

Ling Y, Shantz C, Mahadevan S, Sankararaman S (2011) Stochastic prediction of fatigue loading using real-time monitoring data. Int J Fatigue 33:868–879. doi: 10.1016/j.ijfatigue.2011.01.015

Liu E, He S (2012) Effects of cyclic dynamic loading on the mechanical properties of intact rock samples under confining pressure conditions. Eng Geol 125:81–91. doi: 10.1016/j.enggeo.2011.11.007

Liu E, He S, Xue X, Xu J (2011) Dynamic properties of intact rock samples subjected to cyclic loading under confining pressure conditions. Rock Mech Rock Eng 44:629–634. doi: 10.1007/s00603-011-0151-8

Liu G, Sun W, Lowinger SM, et al (2018a) Coupled flow network and discrete element modeling of injection-induced crack propagation and coalescence in brittle rock. Acta Geotech. doi: 10.1007/s11440-018-0682-1

Liu X, Dai F, Zhang R, Liu J (2015) Static and dynamic uniaxial compression tests on coal

rock considering the bedding directivity. Environ Earth Sci 73:5933–5949. doi: 10.1007/s12665-015-4106-3

Liu Y, Dai F, Xu N, et al (2018b) Experimental and numerical investigation on the tensile fatigue properties of rocks using the cyclic flattened Brazilian disc method. Soil Dyn Earthq Eng 105:68–82. doi: https://doi.org/10.1016/j.soildyn.2017.11.025

Liu Y, Dai F, Zhao T, Xu N wen (2017) Numerical investigation of the dynamic properties of intermittent jointed rock models subjected to cyclic uniaxial compression. Rock Mech Rock Eng 50:89–112. doi: 10.1515/jpem-2016-0229

Llavori I, Esnaola JA, Zabala A, et al (2018) Fretting: Review on the Numerical Simulation and Modeling of Wear, Fatigue and Fracture. In: Contact and Fracture Mechanics.

Love AEH (1906) A treatise on the mathematical theory of elasticity. Dover Publ New York 662.

Ma L, Liu X, Wang M, et al (2013) Experimental investigation of the mechanical properties of rock salt under triaxial cyclic loading. Int J Rock Mech Min Sci 62:34–41. doi: https://doi.org/10.1016/j.ijrmms.2013.04.003

Ma T, Zhang Y, Zhang D, et al (2016) Influences by air voids on fatigue life of asphalt mixture based on discrete element method. Constr Build Mater 126:785–799. doi: https://doi.org/10.1016/j.conbuildmat.2016.09.045

Maxwell JC (1865) A dynamical theory of the electromagnetic field. Philos Trans R Soc London 155:459–512. doi: 10.1098/rstl.1865.0008

Mayergoyz ID (2003) Mathematical models of hysteresis and their applications. Springer

McConnell J (1850) On the deterioration of railway axles. In: Proceedings of the Institution of Mechanical Engineers. London, pp 3–14

McEvily A., Illg W (1958) The rate of crack propagation in two aluminum alloys. NASA Technical Note 4394.

Miner M (1945) Cumulative damage in fatigue. J Appl Mech 12:159–164.

Minto TA, de Oliveira VMCA, Voorwald HJC (2017) Plasma immersion ion implantation: Influence on the rotating bending fatigue strength of AA 7050-T7451 aluminum alloy. Int

J Fatigue 103:17–27. doi: https://doi.org/10.1016/j.ijfatigue.2017.05.002

Momeni A, Karakus M, Khanlari GR, Heidari M (2015) Effects of cyclic loading on the mechanical properties of a granite. Int J Rock Mech Min Sci 77:89–96. doi: http://dx.doi.org/10.1016/j.ijrmms.2015.03.029

Naderi M, Khonsari MM (2013) On the role of damage energy in the fatigue degradation characterization of a composite laminate. Compos Part B Eng 45:528–537. doi: http://dx.doi.org/10.1016/j.compositesb.2012.07.028

Nesládek M, Španiel M (2017) An Abaqus plugin for fatigue predictions. Adv Eng Softw 103:1–11. doi: https://doi.org/10.1016/j.advengsoft.2016.10.008

Nguyen NHT, Bui HH, Kodikara J, et al (2019) A discrete element modelling approach for fatigue damage growth in cemented materials. Int J Plast 112:68–88. doi: https://doi.org/10.1016/j.ijplas.2018.08.007

Nguyen O, Repetto EA, Ortiz M, Radovitzky RA (2001) A cohesive model of fatigue crack growth. Int J Fract 110:351–369. doi: 10.1023/A:1010839522926

Nikfam MR, Zeinoddini M, Aghebati F, Arghaei AA (2019) Experimental and XFEM modelling of high cycle fatigue crack growth in steel welded T-joints. Int J Mech Sci 153–154:178–193. doi: https://doi.org/10.1016/j.ijmecsci.2019.01.040

Ohtsu M, Watanabe H (2001) Quantitative damage estimation of concrete by acoustic emission. Constr Build Mater 15:217–224. doi: 10.1016/S0950-0618(00)00071-4

Oliveira PJV, Correia AAS, Cajada JCA (2018) Effect of the type of soil on the cyclic behaviour of chemically stabilised soils unreinforced and reinforced with polypropylene fibres. Soil Dyn Earthq Eng 115:336–343. doi: https://doi.org/10.1016/j.soildyn.2018.09.005

Oneschkow N (2016) Fatigue behaviour of high-strength concrete with respect to strain and stiffness. Int J Fatigue 87:38–49. doi: http://dx.doi.org/10.1016/j.ijfatigue.2016.01.008

Özbek A (2014) Investigation of the effects of wetting-drying and freezing-thawing cycles on some physical and mechanical properties of selected ignimbrites. Bull Eng Geol Environ 73:595–609. doi: 10.1007/s10064-013-0519-y

Özdeş H, Tiryakioğlu M, Eason PD (2017) On estimating axial high cycle fatigue behavior by rotating beam fatigue testing: Application to A356 aluminum alloy castings. Mater Sci Eng A 697:95–100. doi: https://doi.org/10.1016/j.msea.2017.05.008

Pandey VB, Singh I V, Mishra BK, et al (2019) A new framework based on continuum damage mechanics and XFEM for high cycle fatigue crack growth simulations. Eng Fract Mech 206:172–200. doi: https://doi.org/10.1016/j.engfracmech.2018.11.021

Pantelides CP (2014) Rehabilitation of cracked aluminum components using fiber-reinforced polymer (FRP) composites. In: Karbhari VM (ed) Rehabilitation of Metallic Civil Infrastructure Using Fiber Reinforced Polymer (FRP) Composites. Woodhead Publishing, pp 201–214

Paris P, Director A, Erdogan F (1963) A critical analysis of crack propagation laws. J Basic Eng 85:528–533.

Park B, Min K-B (2015) Bonded-particle discrete element modeling of mechanical behavior of transversely isotropic rock. Int J Rock Mech Min Sci 76:243–255. doi: http://dx.doi.org/10.1016/j.ijrmms.2015.03.014

Polder RB, Peelen WHA (2002) Characterisation of chloride transport and reinforcement corrosion in concrete under cyclic wetting and drying by electrical resistivity. Cem Concr Compos 24:427–435. doi: https://doi.org/10.1016/S0958-9465(01)00074-9

Potyondy DO (2007) Simulating stress corrosion with a bonded-particle model for rock. Int J Rock Mech Min Sci 44:677–691. doi: 10.1016/j.ijrmms.2006.10.002

Potyondy DO (2015) The bonded-particle model as a tool for rock mechanics research and application: current trends and future directions. Geosystem Eng. 18:1–28.

Potyondy DO, Cundall PA (2004) A bonded-particle model for rock. Int J Rock Mech Min Sci 41:1329–1364. doi: http://dx.doi.org/10.1016/j.ijrmms.2004.09.011

Qi J, Vermeer PA, Cheng G (2006) A review of the influence of freeze-thaw cycles on soil geotechnical properties. Permafr Periglac Process 17:245–252. doi: 10.1002/ppp.559

Qin C, Zhang C (2011) Numerical study of dynamic behavior of concrete by meso-scale particle element modeling. Int J Impact Eng 38:1011–1021. doi: 10.1016/j.ijimpeng.2011.07.004

Ramakrishnan V, Malhotra VM, Langley WS (2005) Comparative evaluation of flexural fatigue behavior of high-volume fly ash and plain concrete. In: SP-229: Qlty of Conc Struct and Recent Advances in Conc Matls & Testing: An Intl Conf Honoring V. Mohan Malhotra. pp 351–368

Rankine W (1842) On the causes of the unexpected breakage of the journals of railway axles, and on the means of preventing such accidents by observing the law of continuity in their construction. In: Minutes of the Proceedings of the Institution of Civil Engineers. pp 105–108

Rao MVMS, Ramana Y V (1992) A study of progressive failure of rock under cyclic loading by ultrasonic and AE monitoring techniques. Rock Mech Rock Eng 25:237–251. doi: 10.1007/BF01041806

Ray S, Kishen JMC (2010) Fatigue crack propagation model for plain concrete – An analogy with population growth. Eng Fract Mech 77:3418–3433. doi: https://doi.org/10.1016/j.engfracmech.2010.09.008

Reinhardt HW, Cornelissen HAW (1984) Post-peak cyclic behaviour of concrete in uniaxial tensile and alternating tensile and compressive loading. Cem Concr Res 14:263–270. doi: https://doi.org/10.1016/0008-8846(84)90113-3

Sadd MH, Tai Q, Shukla A (1993) Contact law effects on wave propagation in particulate materials using distinct element modeling. Int J Non Linear Mech 28:251–265. doi: https://doi.org/10.1016/0020-7462(93)90061-O

Schmidtke RH, Lajtai EZ (1985) The long-term strength of lac du bonnet granite. Int J Rock Mech Min Sci Geomech Abstr 22:461–465. doi: https://doi.org/10.1016/0148-9062(85)90010-5

Schöpfer MPJ, Childs C (2013) The orientation and dilatancy of shear bands in a bonded particle model for rock. Int J Rock Mech Min Sci 57:75–88. doi: 10.1016/j.ijrmms.2012.07.019

Schütz W (1996) A history of fatigue. Eng. Fract. Mech. 54:263–300.

Semnani SJ, Borja RI (2017) Quantifying the heterogeneity of shale through statistical combination of imaging across scales. Acta Geotech. doi: 10.1007/s11440-017-0576-7

Sengupta P, Li B (2014) Hysteresis behavior of reinforced concrete walls. J Struct Eng 140:04014030. doi: 10.1061/(ASCE)ST.1943-541X.0000927

Shabani P, Taheri-Behrooz F, Maleki S, Hasheminasab M (2019) Life prediction of a notched composite ring using progressive fatigue damage models. Compos Part B Eng 165:754–763. doi: https://doi.org/10.1016/j.compositesb.2019.02.031

Shadman M, Ziari H (2017) Laboratory evaluation of fatigue life characteristics of polymer modified porous asphalt: A dissipated energy approach. Constr Build Mater 138:434–440. doi: http://dx.doi.org/10.1016/j.conbuildmat.2017.02.043

Shang H, Yi TY, Guo X (2014) Study on strength and ultrasonic velocity of air-entrained concrete and plain concrete in cold environment. Adv Mater Sci Eng 2014:1–7.

Shang J, Yokota Y, Zhao Z, Dang W (2018) DEM simulation of mortar-bolt interface behaviour subjected to shearing. Constr Build Mater 185:120–137. doi: 10.1016/j.conbuildmat.2018.07.044

Shen S, Airey GD, Carpenter SH, Huang H (2006) A dissipated energy approach to fatigue evaluation. Road Mater Pavement Des 7:47–69. doi: 10.3166/rmpd.7.47-69

Shimadzu (2017) Worldwide most efficient very high cycle fatigue testing system. https://www.shimadzu.de/worldwide-most-efficient-very-high-cycle-fatigue-testing-system.

Simon KM, Kishen JMC (2017) A multiscale approach for modeling fatigue crack growth in concrete. Int J Fatigue 98:1–13. doi: https://doi.org/10.1016/j.ijfatigue.2017.01.007

Sinaie S, Ngo TD, Nguyen VP (2018) A discrete element model of concrete for cyclic loading. Comput Struct 196:173–185. doi: https://doi.org/10.1016/j.compstruc.2017.11.014

Singh SP, Kaushik SK (2003) Fatigue strength of steel fibre reinforced concrete in flexure. Cem Concr Compos 25:779–786. doi: 10.1016/S0958-9465(02)00102-6

Singh SP, Sharma UK (2007) Flexural fatigue strength of steel fibrous concrete beams. Adv Struct Eng 10:197–207. doi: 10.1260/136943307780429761

Sohel KMA, Al-Jabri K, Zhang MH, Liew JYR (2018) Flexural fatigue behavior of ultra-lightweight cement composite and high strength lightweight aggregate concrete. Constr

Build Mater 173:90–100. doi: https://doi.org/10.1016/j.conbuildmat.2018.03.276

Song Z, Frühwirt T, Konietzky H (2018a) Characteristics of dissipated energy of concrete subjected to cyclic loading. Constr Build Mater 168:47–60. doi: https://doi.org/10.1016/j.conbuildmat.2018.02.076

Song Z, Frühwirt T, Konietzky H (2019a) Inhomogeneous mechanical behaviour of concrete subjected to monotonic and cyclic loading. Int J Fatigue 105383. doi: https://doi.org/10.1016/j.ijfatigue.2019.105383

Song Z, Konietzky H (2019) A particle-based numerical investigation on longwall top coal caving mining. Arab J Geosci 12:556. doi: 10.1007/s12517-019-4743-z

Song Z, Konietzky H, Frühwirt T (2019b) Hysteresis and dynamic response features of concrete exposed to repeated multilevel compressive loading. J Mater Civ Eng 31:04019066. doi: 10.1061/(ASCE)MT.1943-5533.0002703

Song Z, Konietzky H, Frühwirt T (2018b) Hysteresis energy-based failure indicators for concrete and brittle rocks under the condition of fatigue loading. Int J Fatigue 114:298–310. doi: 10.1016/J.IJFATIGUE.2018.06.001

Song Z, Konietzky H, Herbst M (2019c) Bonded-particle model-based simulation of artificial rock subjected to cyclic loading. Acta Geotech 14:955–971. doi: 10.1007/s11440-018-0723-9

Song Z, Konietzky H, Herbst M (2019d) Three-dimensional particle model based numerical simulation on multi-level compressive cyclic loading of concrete. Constr Build Mater 225:661–677. doi: https://doi.org/10.1016/j.conbuildmat.2019.07.260

Song Z, Wei W, Zhang J (2018c) Numerical investigation of effect of particle shape on isolated extracted zone (IEZ) in block caving. Arab J Geosci 11:310. doi: 10.1007/s12517-018-3669-1

Stahl M, Konietzky H (2011) Discrete element simulation of ballast and gravel under special consideration of grain-shape, grain-size and relative density. Granul Matter 13:417–428. doi: 10.1007/s10035-010-0239-y

Sumner PD, Loubser MJ (2008) Experimental sandstone weathering using different wetting and drying moisture amplitudes. Earth Surf Process Landforms 33:985–990. doi:

10.1002/esp.1586

Sun B, Zhu Z, Shi C, Luo Z (2017) Dynamic mechanical behavior and fatigue damage evolution of sandstone under cyclic loading. Int J Rock Mech Min Sci 94:82–89. doi: 10.1016/j.ijrmms.2017.03.003

Surendran M, Natarajan S, Palani GS, Bordas SPA (2019) Linear smoothed extended finite element method for fatigue crack growth simulations. Eng Fract Mech 206:551–564. doi: https://doi.org/10.1016/j.engfracmech.2018.11.011

Suresh S (1998) Fatigue of materials. Cambridge University Press

Swab JJ, Yu J, Gamble R, Kilczewski S (2011) Analysis of the diametral compression method for determining the tensile strength of transparent magnesium aluminate spinel. Int J Fract 172:187–192. doi: 10.1007/s10704-011-9655-1

Tan X, Chen W, Yang J, Cao J (2011) Laboratory investigations on the mechanical properties degradation of granite under freeze–thaw cycles. Cold Reg Sci Technol 68:130–138. doi: https://doi.org/10.1016/j.coldregions.2011.05.007

Tarefder RA, Bateman D, Swamy AK (2013) Comparison of fatigue failure criterion in flexural fatigue test. Int J Fatigue 55:213–219. doi: https://doi.org/10.1016/j.ijfatigue.2013.07.004

Tazoe K, Hamada S, Noguchi H (2017) Fatigue crack growth behavior of JIS SCM440 steel near fatigue threshold in 9-MPa hydrogen gas environment. Int J Hydrogen Energy 42:13158–13170. doi: https://doi.org/10.1016/j.ijhydene.2017.03.223

Tepfers R, Hedberg B, Szczekocki G (1984) Absorption of energy in fatigue loading of plain concrete. Matériaux Constr 17:59–64.

Tong X, Wang D, Xu H (1989) Investigation of cyclic hysteresis energy in fatigue failure process. Int J Fatigue 11:353–359. doi: http://dx.doi.org/10.1016/0142-1123(89)90062-5

Turon A, Bak B, Lindgaard E, et al (2015) Interface elements for fatigue-driven delaminations in advanced composite materials. In: Camanho PP, Hallett SR (eds) Numerical Modelling of Failure in Advanced Composite Materials. Woodhead Publishing, pp 73–91

Tutuncu AN, Podio AL, Sharma MM (2012) Nonlinear viscoelastic behavior of sedimentary rocks, Part II: Hysteresis effects and influence of type of fluid on elastic moduli.

Vasseva E (1993) Nonlinear dynamic analysis of reinforced concrete frames. Nat Hazards 7:279–290. doi: 10.1007/BF00662651

Vassilopoulos AP, Shahverdi M, Keller T (2015) Mode I fatigue and fracture behavior of adhesively-bonded pultruded glass fiber-reinforced polymer (GFRP) composite joints. In: Vassilopoulos AP (ed) Fatigue and Fracture of Adhesively-Bonded Composite Joints. Woodhead Publishing, pp 149–186

Vervoort A, Min KB, Konietzky H, et al (2014) Failure of transversely isotropic rock under Brazilian test conditions. Int J Rock Mech Min Sci 70:343–352. doi: 10.1016/j.ijrmms.2014.04.006

Vicentini D, Crocombe A, Barroso A, et al (2014) Fatigue crack initiation and damage characterization in Brazilian test specimens for adhesive joints. J Adhes Sci Technol 28:1418–1431. doi: 10.1080/01694243.2012.698099

Vojtek T, Žák S, Pokluda J (2018) Quantitative analysis of intrinsic mode III fatigue thresholds in bcc metals. Int J Fatigue 115:35–41. doi: https://doi.org/10.1016/j.ijfatigue.2018.04.022

Wang D, Ma W, Niu Y, et al (2007) Effects of cyclic freezing and thawing on mechanical properties of Qinghai–Tibet clay. Cold Reg Sci Technol 48:34–43. doi: https://doi.org/10.1016/j.coldregions.2006.09.008

Wang Q, Xing L (1999) Determination of fracture toughness KIC by using the flattened Brazilian disk specimen for rocks. Eng Fract Mech 64:193–201. doi: https://doi.org/10.1016/S0013-7944(99)00065-X

Wang QZ, Jia XM, Kou SQ, et al (2004) The flattened Brazilian disc specimen used for testing elastic modulus, tensile strength and fracture toughness of brittle rocks: analytical and numerical results. Int J Rock Mech Min Sci 41:245–253. doi: https://doi.org/10.1016/S1365-1609(03)00093-5

Wang Y, Wang C, Bahia H (2017) Comparison of the fatigue failure behaviour for asphalt binder using both cyclic and monotonic loading modes. Constr Build Mater 151:767–774. doi: https://doi.org/10.1016/j.conbuildmat.2017.06.144

Wang Z, Li S, Qiao L, Zhang Q (2015) Finite element analysis of the hydro-mechanical

behavior of an underground crude oil storage facility in granite subject to cyclic loading during operation. Int J Rock Mech Min Sci 73:70–81. doi: 10.1016/j.ijrmms.2014.09.018

Wiederhorn SM, Fuller ER, Thomson R (1980) Micromechanisms of crack growth in ceramics and glasses in corrosive environments. Met Sci 14:450–458. doi: 10.1179/msc.1980.14.8-9.450

Wöhler A (1870) Über die Festigkeitsversuche mit Eisen und Stahl. Zeitschrift für Bauwes 20:73–106.

Xi D, Chen Y, Tao Y, Liu Y (2006) Nonlinear elastic hysteric characteristics of rocks. Chinese J Rock Mech Eng 25:1086–1093.

Xiao J-Q, Ding D-X, Jiang F-L, Xu G (2010) Fatigue damage variable and evolution of rock subjected to cyclic loading. Int J Rock Mech Min Sci 47:461–468. doi: http://dx.doi.org/10.1016/j.ijrmms.2009.11.003

Xiao J-Q, Ding D-X, Xu G, Jiang F-L (2009) Inverted S-shaped model for nonlinear fatigue damage of rock. Int J Rock Mech Min Sci 46:643–648. doi: http://dx.doi.org/10.1016/j.ijrmms.2008.11.002

Xie H, Ju Y, Li L (2005) Criteria for strength and structural failure of rocks based on energy dissipation and energy release principles. Chinese J Rock Mech Eng 24:3003–3010.

Xie H, Peng R, Ju Y (2004) Energy dissipation of rock deformation and fracture. Chinese J Rock Mech Eng 23:3565–3570.

Xu J (2016) Mechanics of fatigue. Science Press, Beijing

Xu J, Tang Y, Zhou J (2017) Effect of drying-wetting cycles on aggregate breakdown for yellow-brown earths in karst areas. Geoenvironmental Disasters 4:20. doi: 10.1186/s40677-017-0084-y

Xu T, Zhou G, Heap MJ, et al (2018) The modeling of time-dependent deformation and fracturing of brittle rocks under varying confining and pore pressures. Rock Mech Rock Eng 51:3241–3263. doi: 10.1007/s00603-018-1491-4

Yang B, Mall S, Ravi-Chandar K (2001) A cohesive zone model for fatigue crack growth in quasibrittle materials. Int J Solids Struct 38:3927–3944. doi:

https://doi.org/10.1016/S0020-7683(00)00253-5

Yang SQ, Ranjith PG, Huang YH, et al (2015) Experimental investigation on mechanical damage characteristics of sandstone under triaxial cyclic loading. Geophys J Int 201:662–682. doi: 10.1093/gji/ggv023

Yassini E, Mirzaei M, Alimi A, Rahaeifard M (2016) Investigation of the fatigue behavior of adhesive bonding of the lithium disilicate glass ceramic with three resin cements using rotating fatigue method. J Mech Behav Biomed Mater 61:62–69. doi: https://doi.org/10.1016/j.jmbbm.2016.01.013

Yin XC, Yu HZ, Kukshenko V, et al (2004) Load-unload response ratio (LURR), accelerating moment/energy release (AM/ER) and state vector saltation as precursors to failure of rock specimens. Pure Appl Geophys 161:2405–2416. doi: 10.1007/s00024-004-2572-8

Yin XC, Zhang LP, Zhang Y, et al (2008) The newest developments of load-unload response ratio (LURR). Pure Appl Geophys 165:711–722. doi: 10.1007/s00024-008-0314-z

Yoon JS, Zang A, Stephansson O (2012) Simulating fracture and friction of Aue granite under confined asymmetric compressive test using clumped particle model. Int J Rock Mech Min Sci 49:68–83. doi: 10.1016/j.ijrmms.2011.11.004

York J (1842) An account of a series of experiments on the comparative strength of solid and hollow axles. In: Minutes of the Proceedings of the Institution of Civil Engineers. London, pp 105–108

Zerbst U, Madia M, Vormwald M, Beier HT (2018) Fatigue strength and fracture mechanics – A general perspective. Eng Fract Mech 198:2–23. doi: https://doi.org/10.1016/j.engfracmech.2017.04.030

Zhang J he, Wang J, Chai L sha (2017) Factors influencing hysteresis characteristics of concrete dam deformation. Water Sci Eng 10:166–174. doi: 10.1016/j.wse.2017.03.007

Zhang L, Zhuang J (2011) An improved version of the load/unload response ratio method for forecasting strong after shocks. Tectonophysics 509:191–197. doi: 10.1016/J.TECTO.2011.06.008

Zhang M, Dou L, Konietzky H, et al (2020) Cyclic fatigue characteristics of strong burst-prone coal: Experimental insights from energy dissipation, hysteresis and micro-seismicity. Int

J Fatigue 133:105429. doi: https://doi.org/10.1016/j.ijfatigue.2019.105429

Zhang QB, Zhao J (2014) A review of dynamic experimental techniques and mechanical behaviour of rock materials. Rock Mech Rock Eng 47:1411–1478. doi: 10.1007/s00603-013-0463-y

Zhang S, Lai Y, Zhang X, et al (2004) Study on the damage propagation of surrounding rock from a cold-region tunnel under freeze–thaw cycle condition. Tunn Undergr Sp Technol 19:295–302. doi: https://doi.org/10.1016/j.tust.2003.11.011

Zhang X, Shan W, Zhang Z, Li B (2018) AE monitoring of reinforced concrete squat wall subjected to cyclic loading with information entropy-based analysis. Eng Struct 165:359–367. doi: https://doi.org/10.1016/j.engstruct.2018.03.059

Zhao C, Koseki J, Sasaki T (2018) Image based local deformation measurement of saturated sand specimen in undrained cyclic triaxial tests. Soils Found 58:1313–1325. doi: https://doi.org/10.1016/j.sandf.2018.07.008

Zhao W, Huang R, Yan M (2015) Study on the deformation and failure modes of rock mass containing concentrated parallel joints with different spacing and number based on smooth joint model in PFC. Arab J Geosci 8:7887–7897. doi: 10.1007/s12517-015-1801-z

Zheng M, Li P, Yang J, et al (2019) Fatigue character comparison between high modulus asphalt concrete and matrix asphalt concrete. Constr Build Mater 206:655–664. doi: https://doi.org/10.1016/j.conbuildmat.2019.01.170

Zhou Z, Cai X, Chen L, et al (2017) Influence of cyclic wetting and drying on physical and dynamic compressive properties of sandstone. Eng Geol 220:1–12. doi: https://doi.org/10.1016/j.enggeo.2017.01.017